Universidad Carlos III de Madrid

Departamento de Física

Doppler Reflectometry in the TJ-II Stellarator: Design of an Optimized Doppler Reflectometer and its Application to Turbulence and Radial Electric Field Studies

Tesis Doctoral

Presentada por:

Tim Happel

Dirigida por:

Dra. Teresa Estrada

Asociación Euratom-Ciemat para Fusión
Avda. Complutense 22, 28040, Madrid

Madrid, Octubre de 2010

'Tim, en esta vida, nada tiene sentido.'

Teresa Estrada, at the time of finishing the thesis

Contents

Chapter 1

Introduction

For several decades magnetic confinement of high-temperature plasmas has been investigated with the objective of building a burning fusion reactor. One of the main obstacles in reaching this goal is the energy and particle losses caused by radial transport processes in the plasma. Therefore, the identification and reduction of this radial transport is a demanding challenge faced by theoretical and experimental physicists.

The transport processes in toroidal plasmas can be grouped into two categories, i.e. neoclassical and turbulent transport. Neoclassical theory is an extension of classical theory to include the toroidal geometry of magnetic confinement fusion experiments, which results in new particle drifts and magnetic field mirror effects, which trap particles and lead to an increased collision frequency. Neoclassical transport is an ubiquitous process, since it depends on the existence of background gradients in the plasma and Coulomb collisions between particles.

The second type of transport, turbulent or anomalous transport, is fundamentally different from neoclassical transport due to the fact that the described particle losses are caused by microinstabilities. These microinstabilities occur irregularly in the plasma, hence turbulent transport is an intermittent process rather than a continuous one. The particle and energy losses observed in toroidal fusion plasmas are believed to be mainly caused by turbulent transport, making it one of the dominant fields of investigation of the fusion community in the last few decades.

Plasma turbulence can basically be described as the incoherent motion of the plasma which arises from small-scale fluctuations in parameters such as plasma density, temperature, potential, and the magnetic field. Gradients in the plasma parameters are the driving forces of the turbulence, which leads to the conclusion that the better the plasma confinement (stronger gradients), the higher the turbulence level. However, this is not completely true: the discovery of the H-mode confinement regime in 1982 showed that the plasma can spontaneously self-organize and enter a mode of improved confinement (L-H transition), characterized by a steepening of plasma gradients accompanied by a significant reduction of the level of fluctuations and turbulent transport.

This discovery led to an immense effort, from both the theoretical and the experimental sides, in trying to understand the L-H transition and the reduced turbulence level in the H-mode confinement regime. After more than a quarter century of active

research, the prevailing paradigm to explain the turbulence level reduction consists in turbulence suppression via sheared flows. However, although these flows are observed in H-mode plasmas, their generation mechanisms are still unknown. Several candidates involving the edge pressure gradient or turbulence driven mean and oscillating flows exist, but elucidation is still pending.

These questions push forward the continuous development of new diagnostics which are capable of measuring the involved magnitudes. One of these diagnostics is Doppler reflectometry, a rather new diagnostic based on the scattering of electromagnetic waves off density fluctuations. Doppler reflectometry combines the scale-selectivity of scattering experiments with the radial localization of reflectometry. During the last ten years it has proven to be a powerful technique to measure the perpendicular velocity of density fluctuations $u_\perp$, the radial electric field E_r, and the perpendicular wave number spectrum $S(k_\perp)$ in magnetically confined fusion plasmas. A major advantage of Doppler reflectometry is the possibility to measure the edge density gradient region, where several other diagnostics (Langmuir probes, heavy ion beam probes) struggle to obtain measurements.

H-mode plasmas have been observed in the TJ-II stellarator since 2008 with lithium coated walls and neutral beam injection heating. The resultant plasma characteristics are comparable to other devices, i.e. an increase of the energy confinement time τ_E, decreases in H_α radiation and in the density turbulence level, and a steepening of the edge density profile gradient.

In this work the design of an optimized Doppler reflectometer for the TJ-II stellarator and its application to turbulence and radial electric field studies is illustrated. In the Doppler reflectometer design, special consideration is paid to the fact that the TJ-II plasma is complex, i.e. three-dimensional and highly shaped, which results in the need for an optimization of the system in terms of alignment to the magnetic field and microwave beam focusing.

The experimental part dedicates particular emphasis to a comparison between equilibrium L- and H-mode plasmas. Both perpendicular velocity profiles of density fluctuations and perpendicular wavenumber spectra of density turbulence in L- and H-modes are compared.

The dynamics of the L-H transition is investigated on fast timescales with special attention to oscillating sheared flows and the coupling between density turbulence and sheared flows, magnitudes which are measured simultaneously by Doppler reflectometry.

Chapter 2

Turbulence and Radial Electric Fields in Toroidal Fusion Plasmas

In this chapter, the term turbulence is introduced, along with its properties and impact on magnetic confinement fusion. Furthermore, the sheared flow mechanism, commonly accepted to cause turbulence suppression, is presented. In this context it is appropriate to give a short overview of how sheared flows can be generated by the plasma itself and through external mechanisms. Therefore at the end of the chapter the terms of perpendicular velocities and radial electric fields, central measurement magnitudes in this work, are explained.

2.1 Turbulence

Turbulence is an ubiquitous phenomenon in fluids, gases and plasmas as soon as the fluid or gas is subject to external forces [1]. These can be boundaries or obstacles the gas is passing, artificially injected energy through the propeller of ships or aircrafts, or the forces acting on the plasma due to the gradients produced when it is confined by a magnetic field. The basic equation to describe turbulence in incompressible neutral fluids ($\nabla \cdot \mathbf{u} = 0$) is the *Navier-Stokes* equation,

$$\rho_m \left(\frac{\partial \mathbf{u}}{\partial t} + (\mathbf{u} \cdot \nabla)\mathbf{u} \right) = -\nabla p + \nu \Delta \mathbf{u}, \tag{2.1}$$

where ρ_m is the mass density, $\mathbf{u}$ is the velocity field, p the pressure and ν the viscosity. If L is the characteristic scale of the system, U_0 its characteristic velocity, a characteristic time $T = L/U_0$ is defined. A transition to dimensionless magnitudes can be obtained by defining primed magnitudes $\mathbf{x}' = \mathbf{x}/L$, $\mathbf{u}' = \mathbf{u}/U_0$, $t' = t/T$ and $p' = p/\rho_m U^2$, resulting in spatial and temporal derivatives of the form $\nabla' = L\nabla$ and $\partial/\partial t' = (L/U_0)\partial/\partial t$. Substituting magnitudes in (2.1) by their primed equivalents, the dimensionless form of the Navier-Stokes equation is

$$\frac{\partial \mathbf{u}'}{\partial t'} + (\mathbf{u}' \cdot \nabla')\mathbf{u}' = -\nabla' p' + \frac{1}{R_e}\Delta' \mathbf{u}', \tag{2.2}$$

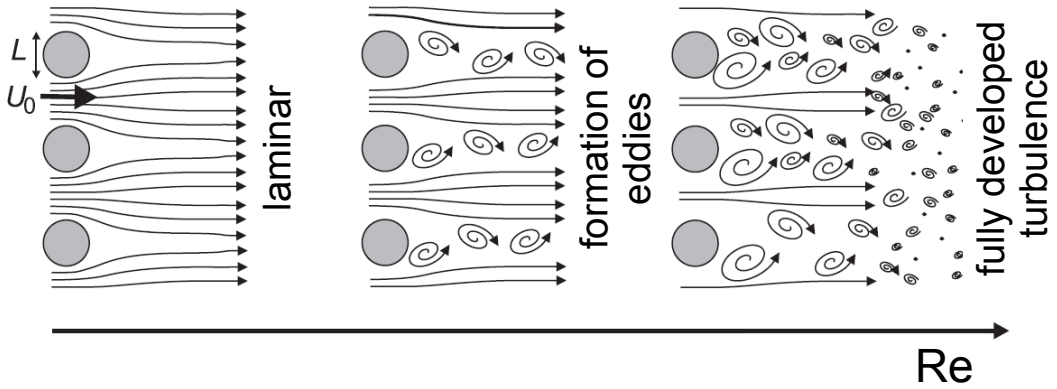

Figure 2.1: Schematic visualization of a flow at different Reynolds numbers, increasing from left to right. The flow goes over from laminar to turbulent passing an intermediate stage where eddies and Kármán vortex streets are formed. Taken from Ref. [2].

where the *Reynolds number* is defined

$$R_e = \frac{U_0 L \rho_m}{\nu} \tag{2.3}$$

and describes the degree of turbulence of the system by relating the non-linear behavior with the viscous damping. Indeed, (2.2) shows that a flow is completely characterized by its Reynolds number. Two systems that have different L, U_0, ρ_m and ν can be *dimensionally similar* if their R_e are the same, i.e. they will show the same dynamical properties.

Fig. 2.1 shows the different flow states for increasing R_e from left to right. On the left, R_e is low and the flow is laminar. In the middle, an intermediate R_e causes the formation of eddies and Kármán vortex streets. The fully developed turbulence at high R_e is depicted on the right, where eddies are formed which feed energy into smaller eddies and no clear structures can be seen. It was only in 1941 that a theory appeared which explained the transfer of energy from larger into smaller eddies on basis of a dimensional analysis, explained further below.

It should be mentioned that a magnetically confined fusion plasma is a more complex system than the neutral fluid mentioned here. In a plasma, at least two fluids exist (electrons and ions), which interact on each other. These fluids can act back on the magnetic field, i.e. slightly move the obstacles considered static from before. This results in an extremely complex system of interactions. Nevertheless, although the neutral fluid picture is used here as a schematic description, it gives a basic (visual) understanding of turbulence.

2.1.1 Turbulence in Magnetically Confined Fusion Plasmas

In magnetically confined toroidal plasmas, nested so-called *flux surfaces* are formed by the magnetic field $\mathbf{B}$. In general, the magnetic field has two components, a toroidal component B_φ and a poloidal component B_θ, where φ and θ are the toroidal and

poloidal angles, respectively. In the tokamak concept, B_φ is produced by toroidal field coils, while B_θ is obtained by inducing a toroidal plasma current. For more information on tokamaks, the reader is referred to [3]. In the stellarator, both B_φ and B_θ are obtained through a complex arrangement of magnetic coils [4]. In the present work the stellarator TJ-II [5] is used, for details on its coil configuration see chapter 4.

In a plasma in force equilibrium ($\nabla p = \mathbf{j} \times \mathbf{B}$, p: pressure, $\mathbf{j}$: (diamagnetic) current), plasma parameters on the magnetic flux surfaces are nearly constant since the charged particles in a plasma can move freely along the magnetic field lines, hence parallel transport is fast. Perpendicular to the flux surfaces, however, the transport is slow due to the Lorentz force, and so gradients (in density, temperature, etc.) are formed. It will be seen later (cf sec. 2.3) that flows will be present in a plasma as soon as it is confined. These have impact on the Reynolds-number (2.3), and the system can go into a turbulent state, causing fluctuations in plasma density, temperature, potential, or even the magnetic field. These fluctuations can give rise to microinstabilities, which are believed to be responsible for the so-called *turbulent* or *anomalous transport* (anomalous: Greek for "defiance of laws").

Note that the decoupling of parallel and perpendicular directions through the magnetic field has the effect that as a first approximation, plasma movements perpendicular to the magnetic field can be seen as two-dimensional (2D). This has effect on turbulence spectra, as will be seen below.

2.1.2 Spectral Properties of Turbulence

When thinking about turbulence in a fluid, one automatically thinks about movements in random directions and different scales incorporated in the problem, as indicated on the right hand side (rhs) of fig. 2.1, where eddies of different sizes are schematically displayed. Due to the number of variables incorporated in the problem, an analytical solution is not feasible. In principle, the calculation of the evolution of a turbulent system with computer simulations is possible, since the governing equations and initial conditions are known. However, simulations of systems at high R_e are extremely CPU consuming and will not be possible until many generations of computers have passed. Still, a statistical (global) description can be used to characterize the turbulence and to try to make predictions on the turbulence behavior, which is important for example in weather forecasts or financial evolution predictions.

An important question when looking at a turbulent system, e.g. a fluid, is how much turbulence energy is contained in each scale. But this is only a momentary characterization of the system. The scales in the system are of interest and can change in its temporal evolution. In nature the sizes of involved objects can grow (e.g. formation of clouds out of individual water drops) or shrink (e.g. breaking apart of large rocks through collisions in an avalanche). These rearrangements are generally labeled *cascades*, where the cascade towards smaller scales is called *direct cascade*, and the one towards larger scales *inverse cascade*. Joining the two pictures, the energy contained in each scale, and the formation of larger or smaller structures, the question arises how the energy is transferred between the different scales. This is fundamentally different

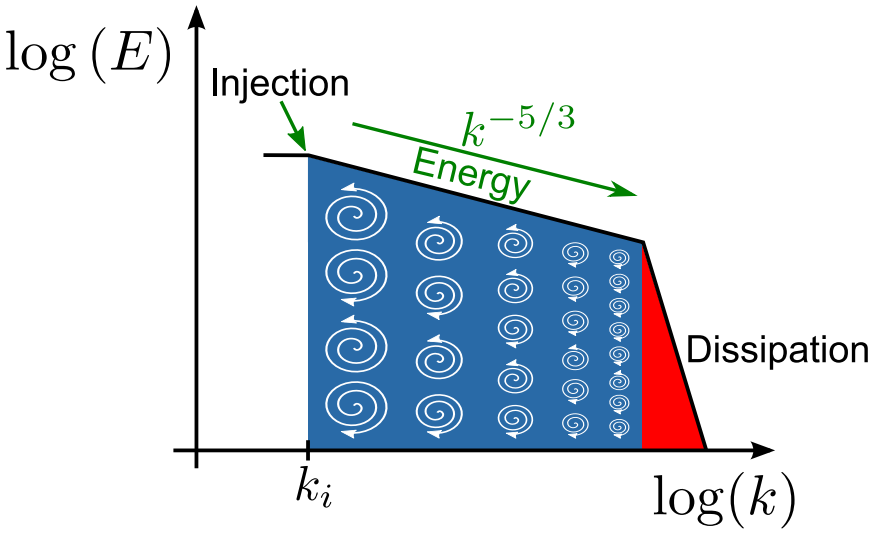

Figure 2.2: Schematic drawing of the spectral energy of 3D Navier Stokes turbulence. The direct cascade transfers energy to smaller scales.

depending on whether two or three-dimensional (2D or 3D) turbulence is considered.

3D Turbulence

One of the most established theories is obtained via a dimensional analysis and was first published in 1941 by Kolmogorov, therefore called the *Kolmogorov-41* or *K41*-theory [6, 7]. In this work homogeneous, isotropic 3D turbulence is assumed. The key contribution of the K41-theory is the idea of a multiscale nature of turbulence, where the properties of a turbulent cascade are controlled by an energy transfer rate. Fig. 2.2 schematically plots the energy per unit wavenumber against the structure scale. Eddies are schematically shown to indicate the size of the structures, which is decreasing towards higher k. The basic idea is that energy is injected into the system at some large scale (*injection scale* k_i), then transferred towards smaller scales (*inertial range*), and ultimately dissipated through viscosity (*dissipative range*). Note that in the Navier-Stokes equation (2.1), the viscosity goes with k^2 ($\nabla^2\mathbf{u}$), hence dissipative effects dominate at small scales. The important wavenumber range where dissipation dominates is sometimes called the *viscous cutoff* [8]. In the K41-theory it is assumed that injection scale and dissipative range are separated in k-space. Since no energy is transferred into the system in the inertial range, the turbulent energy is conserved. For self-similar and isotropic Navier-Stokes turbulence, the K41-theory predicts for the spectral energy per unit wave number

$$E_k = C\epsilon^{2/3}k^{-5/3}, \tag{2.4}$$

where C is the Kolmogorov constant and ϵ is the energy transfer rate. The spectral index predicted by (2.4) is $\alpha = -5/3$ and has been confirmed by a number of experiments in fluids (see e.g. [9–11]).

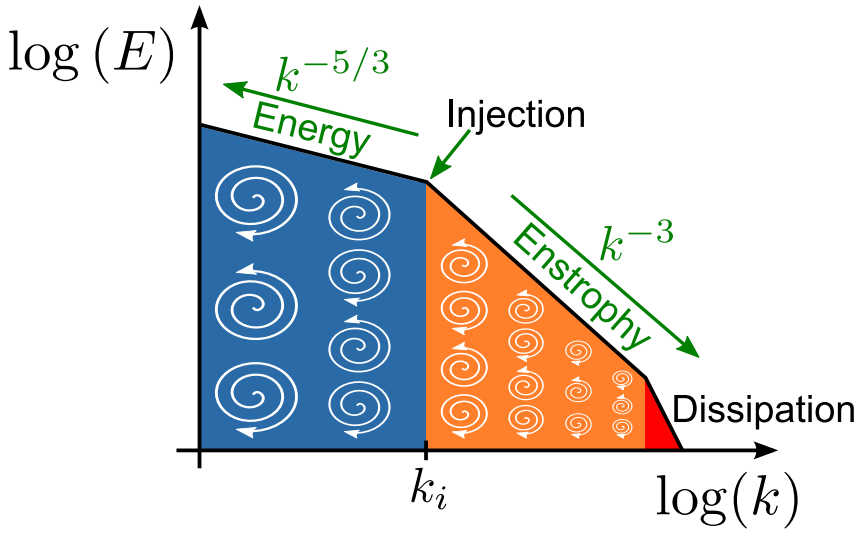

Figure 2.3: Schematic drawing of the spectral energy of 2D Navier Stokes turbulence. The dual cascade transfers energy to larger and enstrophy to smaller scales.

2D Turbulence

The essential difference between 3D and 2D turbulence is that in 2D, the effect of vorticity stretching is absent (Kraichnan, 1967: "In two dimensions, the vorticity constraint drastically changes matters."), resulting in the conservation of enstrophy. The principal consequence is that energy is transferred towards smaller wavenumbers and enstrophy towards higher wavenumbers, each with different spectral indices.

A schematic drawing of a theoretical wavenumber spectrum of two-dimensional Navier-Stokes turbulence is shown in fig. 2.3. In 2D turbulence, if energy is injected at one scale k_i (*injection*), two inertial ranges form. Energy is transferred from the injection scale towards larger scales and enstrophy is transferred towards smaller scales. The two directions are called *inverse cascade* for energy and *direct cascade* for enstrophy transfer. Therefore, the name *dual cascade* is often used in the context of 2D turbulence. At high k, the energy is dissipated and thus contributes to the total energy in the system. The spectral indices α are different for the two inertial ranges. The inverse cascade is characterized by $\alpha = -5/3$ while the direct cascade shows $\alpha = -3$. The latter spectral index was modified with a logarithmic correction in a paper by Kraichnan in 1971 taking into account the nonlocality of interactions [12].

Fig. 2.4 shows a turbulence wavenumber spectrum measured in a 2D fluid [13]. Experimentally, a 2D fluid is realized by a thin ($<$ 1 cm thick), but wide ($>$ 10×10 cm^2) layer where movement is mainly horizontal. Small test particles are introduced on the surface and their movement is recorded by a video camera. The excitation of turbulence is then done via an array of magnets below the fluid interacting with a current flowing through the fluid layer, resulting in $\mathbf{j} \times \mathbf{B}$-driven vortices which interact to produce the turbulent flow. For details the reader is referred to Refs. [13–16].

However, the description above only holds under certain assumptions, the most basic of them is that a neutral fluid is considered. In magnetized plasmas, as stated

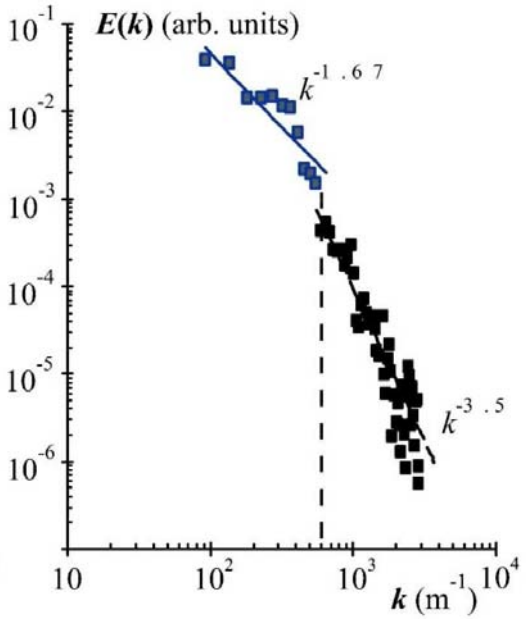

Figure 2.4: Experimental wavenumber spectrum measured in a 2D fluid. The injection scale k_i is marked by the vertical dashed line. Taken from [13].

above, two or more fluids can interact and even act back on the magnetic field. Furthermore, the probability density function (PDF) of the turbulent fluctuations has to be Gaussian, which has been shown not to be the case in several fusion experiments. In recent experiments skewed PDFs were measured and the structures were labeled blobs (positive perturbations) in the confinement region and holes (negative perturbations) in the scrape-off layer (SOL) [17–19]. This was also confirmed by simulations, which show that PDFs are non-Gaussian for 2D interchange, but almost Gaussian for 2D-ITG (ion-temperature-gradient) turbulence [20].

2.2 Turbulence Suppression

Since the discovery of the low to high confinement (L-H) transition in the ASDEX tokamak in 1982 by Wagner *et al.* [21], exceptional efforts have been undertaken to understand the improved confinement regime and the transition into it. The H-mode improved confinement is intrinsically connected to reduced cross-field losses of particles and energy, caused by so-called *transport barriers*. In many experiments, these transport barriers show similar properties, among them a location close to the plasma edge and sheared poloidal plasma flows. In the following the H-mode confinement regime is introduced, followed by a brief introduction to the theory of turbulence suppression by shear flows.

2.2.1 The H-mode Confinement Regime

H-mode plasmas are characterized by their improved (high, H) confinement properties with respect to (w.r.t.) the normal (low, L) confinement plasmas. In general, H-mode plasmas are obtained when the plasma heating power P exceeds a heating power threshold P_{th}, which depends mainly on plasma line-averaged density $\langle n_e \rangle$, magnetic field strength B and plasma surface area S [22]. The type of heating (ohmic, electron cyclotron resonance heating (ECRH), neutral beam injection (NBI)) is not relevant. The fact that this power threshold exists excites pronounced physics interest in the H-mode: it is worth mentioning that when going into H-mode the system self-organizes into a higher energy state with reduced turbulence and transport, although an additional energy source (heating) is applied to it.

A plasma in H-mode exhibits steep gradients in density n, temperature T and radial electric field E_r, and the turbulence level is strongly reduced. A reduced amount of radial particle flux Γ is registered by H_α (D_α) monitors, interrupted sometimes by strong particle exhaust events, the so-called *ELM*s (Edge Localized Modes), which are grouped by their different characteristics in type I, II and III ELMs. The steepening of gradients and reduced radial particle flux lead to an increase of the energy confinement time τ_{E} by a factor of $2-3$. Although the H-mode confinement regime has been known for more than a quarter century and experimental evidence strongly suggests that the radial electric field E_r plays an important role in H-mode physics, it is still not clear whether the strong E_r and its spatial derivative $\mathrm{d}E_r/\mathrm{d}r = E_r'$ are a consequence of the L-H transition, or rather a cause. This is because the self-organization of the plasma into H-mode happens on a fast (turbulent) timescale, making it difficult to distinguish cause and effect.

The first theoretical connection between the H-mode confinement regime and the radial electric field E_r was suggested by Itoh and Itoh [23]. Their model is based on a bifurcation in E_r which causes another bifurcation in the particle flux and convective energy loss in the plasma edge ($|a-r| \lesssim \rho_{\mathrm{p},i}$, a is the minor plasma radius, r is the minor radius and $\rho_{\mathrm{p},i}$ is the ion poloidal gyroradius). In 1990, the mechanism of turbulence suppression by sheared flows was first proposed in order to explain the L-H transition by Biglari *et al.* [24]. In this work a sufficiently sheared E_r can cause sheared plasma flows which can tear apart turbulent eddies, reducing their radial correlation length and thus reducing turbulent transport. Nowadays, this theory is the prevailing picture explaining H-mode reduced turbulent transport due to accumulated experimental evidence. Shortly after Biglari *et al.* published their work, it was realized that turbulence itself could modify the average plasma flow profile through Reynolds stress [25], which implies that E_r or flow profiles and turbulence have to be calculated self-consistently. In 1994, Diamond *et al.* proposed the first self-regulating model in which turbulence and shear flows were coupled [26]. This work established a link between the turbulence level and shear flows through the Reynolds stress. The power threshold was theoretically explained in terms of the net energy input rate, which has to exceed the flow damping rate, giving a power threshold for the H-mode confinement. The model shows characteristics of the *predator-prey* model [27], in which the

flow shear is analogous to the predator species and the fluctuation level to the prey species. Recent H-mode theories also include the effect of oscillating sheared electric fields, the so-called *Zonal Flows (ZF)* as a cause for the L-H transition [28–30].

Despite the above mentioned efforts, still no theoretical model exists which can explain in detail the H-mode confinement regime, in fact the question for the mechanism which generates the strong E_r observed in H-mode plasmas is seen as one of the fundamental open issues confronting the fusion community. In general, theoretical models try to find sinks and sources for the radial force balance equation (cf sec. 2.3) to explain the strong E_r' found in H-mode plasmas compared to L-mode plasmas.

2.2.2 Shear Flows

In order to explain the suppression of turbulence by velocity shearing, first basic attempts were made by Lehnert in 1966 by analytically applying a spatially varying velocity field to flute disturbances [31]. With regard to L-H transitions, in 1990, Biglari, Diamond and Terry published a letter showing analytically that a possible turbulence quench mechanism is a sufficiently strong shear in the radial electric field E_r [24] (For a review, see [32]). An important result of this work is that the turbulence suppression does not depend on the sign of either E_r or its associated radial shear $\mathrm{d}E_r/\mathrm{d}r = E_r'$. In mathematical form, the above criterion can be written

$$\left|\frac{E_r'}{B_\varphi}\right| > \frac{\Delta\omega_t}{k_\theta L_r} \tag{2.5}$$

where $\Delta\omega_t$ is the turbulence decorrelation frequency, B_φ is the toroidal field, L_r is the radial correlation length of the turbulent structures with poloidal wavenumber k_θ. This criterion is often called the *BDT-criterion*. Indeed, (2.5) shows that the larger the turbulent structures (L_r), the less radial electric field shear is necessary to tear them apart. A first experimental confirmation of the paradigm was provided by Groebner *et al.* in 1990 in the DIII-D tokamak [33]. But the theory is not only applicable to plasmas, it has been confirmed to be active in 2D fluids, where self-generated and externally applied sheared flows are shown to lead to a turbulence suppression in agreement with the BDT theory [15].

A schematic visualization of the shear decorrelation mechanism is shown in fig. 2.5. The gray circle represents a turbulent structure which is put into a velocity field. The velocity u_y affects the structure. On the left hand side (lhs), no shear is present ($u_y' = 0$), hence the structure is convected upwards without any change to its shape. The drawing in the middle shows the same turbulent structure affected by weak shear (u_y' weak). It is stretched and tilted, but still the correlation length L_r is not changed. However, if a strong velocity shear is present (u_y' strong, rhs), the turbulent structure is torn apart, resulting in smaller structures, with the effect that L_r decreases. This means that (2.5) is not satisfied anymore, so no further turbulence suppression will occur. It can be said that the turbulent structure size is now in balance with the velocity shear strength.

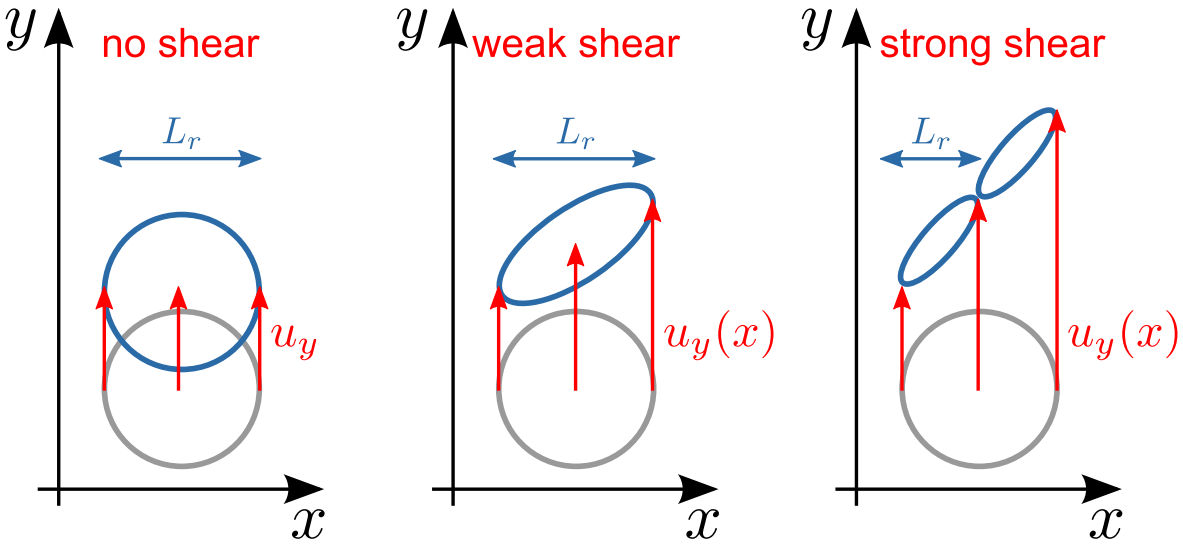

Figure 2.5: Schematic drawing illustrating turbulence decorrelation. Without shear, the turbulent structure is convected upwards but retains its shape. As the shear increases, the structure is stretched and eventually, when the shear is strong enough, torn apart, reducing the turbulence correlation length.

In fig. 2.6 a gyrofluid simulation result by Scott [34] is depicted. From left to right the imposed u' increases. The (ion temperature) turbulent structures are affected by the velocity shear, and in the rightmost plot, structures have small radial size (L_r small) but are elongated in the vertical direction, and the velocity shear acts like a transport barrier.

2.2.3 Zonal Flows

Zonal flows (ZFs) are low frequency (up to some kHz) $n = m = 0$ (n, m: toroidal and poloidal mode numbers, respectively) electrostatic fluctuations with finite radial wavenumber k_r [28–30] (therefore sometimes called *band-like* sheared flows). Since they are poloidally symmetric, they do not drive radial transport. ZFs gain their energy from all types of microinstabilities, and regulate the amplitude of the latter by shearing them. Since ZFs are electrostatic fluctuations, the caused velocity shear is time-varying. Mathematically, this effect can be described as a predator-prey system [27], in which the turbulence is the prey and the ZF is the predator.

A possible interaction between ZFs and mean sheared flows is subject to recent research. Due to the fact that ZFs depend on turbulence and that a mean flow shear can suppress turbulence, a suppression of turbulence by a mean flow shear will result in a ZF suppression as well. Indeed, a recent theory states that ZFs can lower the L-H transition threshold by quenching the turbulence, followed by a gradient buildup in the plasma, which can drive a mean flow shear which itself suppresses turbulence and thus the ZF that helped the plasma to enter into H-mode in the first place [35].

Another consequence of ZFs is the so-called *Dimits shift* [36]. It describes the effect that ITG turbulence is stable even slightly above the linear critical gradient R/L_T,

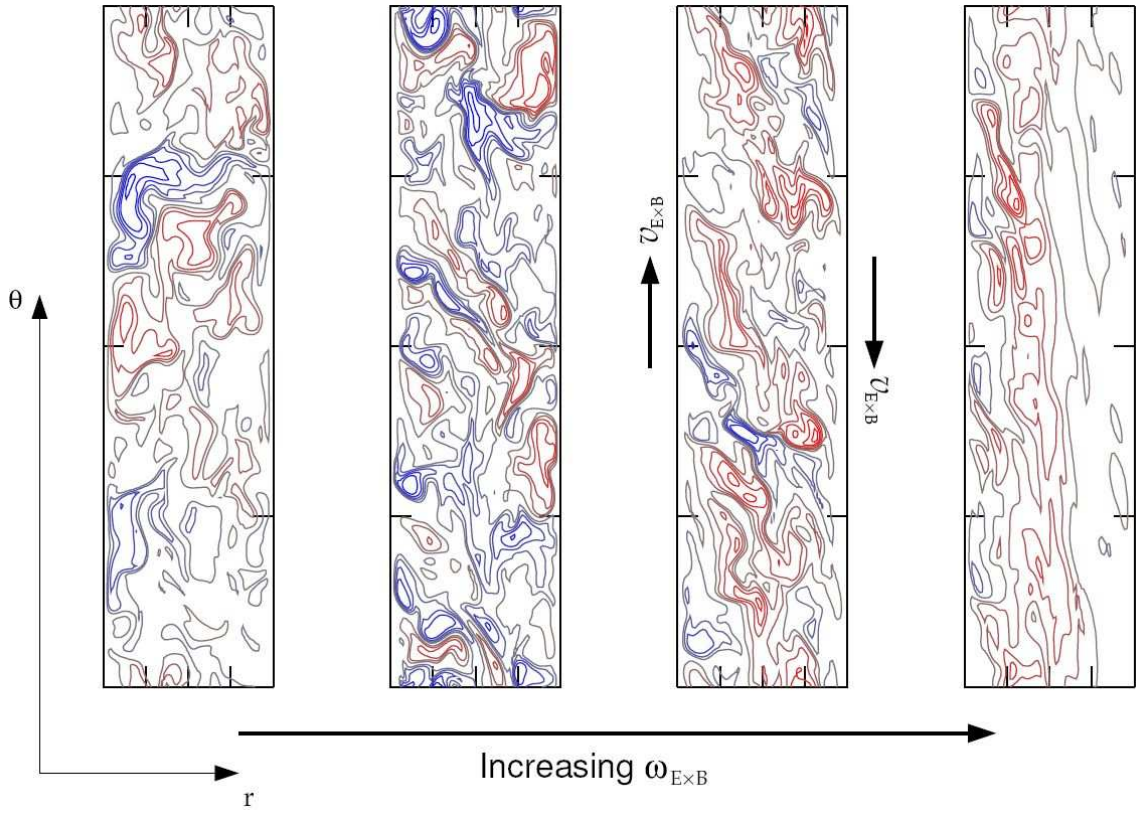

Figure 2.6: Gyrofluid simulation of turbulence decorrelation due to background imposed $E \times B$ shear flow [34]. Ion temperature fluctuations are plotted. From left to right, the velocity shear increases.

because ZFs limit the eddy size and thus transport. The effective critical gradient is upshifted, hence the name.

2.3 The Radial Electric Field

The importance of the radial electric field E_r in magnetic confinement fusion was not recognized until in 1988 Itoh and Itoh introduced E_r into the discussion to explain the H-mode confinement regime [23], later followed by the inclusion of its shear in 1990 by Biglari [24]. From then until today, increased effort has been undertaken to measure E_r in tokamaks and stellarators. The BDT theory predicts that if the E_r shear is strong, it can drive perpendicular plasma shear flows that break turbulent structures into smaller ones, thus reducing radial correlation lengths and suppressing turbulence.

To calculate the plasma flows perpendicular to the magnetic field, the momentum equation without external forces or friction is considered. Furthermore, an equilibrium solution is desired, so that temporal derivatives are zero. This leads to

$$\rho(\mathbf{E} + \mathbf{v} \times \mathbf{B}) - \nabla p = 0. \tag{2.6}$$

Here, $\rho = nq$ is the charge density, $\mathbf{E}$ and $\mathbf{B}$ are electric and magnetic fields, respectively, and $\mathbf{v}$ is the plasma flow. Multiplication from the right with $\mathbf{B}$ and for flows perpendicular to $\mathbf{B}$

$$(\mathbf{v} \times \mathbf{B}) \times \mathbf{B} = -B^2\mathbf{v} + (\mathbf{B} \cdot \mathbf{v})\mathbf{B} = -B^2\mathbf{v}_\perp \tag{2.7}$$

leads to a formula for the perpendicular velocity of the plasma:

$$\mathbf{v}_\perp = \frac{\mathbf{E} \times \mathbf{B}}{B^2} - \frac{\nabla p \times \mathbf{B}}{\rho B^2}. \tag{2.8}$$

This formula states that in a plasma confined in a magnetic field, flows will be present. The two terms on the rhs are the $E \times B$-*velocity*

$$\mathbf{v}_{E\times B} = \frac{\mathbf{E} \times \mathbf{B}}{B^2} \tag{2.9}$$

and the *diamagnetic velocity*

$$\mathbf{v}_{\text{dia}} = -\frac{\nabla p \times \mathbf{B}}{\rho B^2}. \tag{2.10}$$

Since $\mathbf{v}_{E\times B}$ is charge-independent, it does not produce any currents in the plasma. However, this is not true if for instance due to collisions one plasma species is hampered in its movement. Then the other species will carry a current in the plasma. The diamagnetic velocity $\mathbf{v}_{\text{dia}}$, due to its charge-dependence, produces a current in the plasma, called *diamagnetic current*

$$\mathbf{j}_{\text{dia}} = \rho(\mathbf{v}_{\text{dia},i} - \mathbf{v}_{\text{dia},e}). \tag{2.11}$$

Writing (2.9) in component form and solving for E_r a simple expression for the $\mathbf{v}_{E\times B}$-contribution of the radial electric field is obtained

$$E_r = v_{E\times B} B. \tag{2.12}$$

The radial electric field can be obtained from the radial force balance for any plasma species α

$$E_r = v_{\theta,\alpha} B_\varphi - v_{\varphi,\alpha} B_\theta - \frac{1}{\rho_\alpha}\frac{\mathrm{d}p_\alpha}{\mathrm{d}r}, \tag{2.13}$$

where $v_{\theta,\alpha}, v_{\varphi,\alpha}, \rho_\alpha$ and p_α are the poloidal and toroidal velocities, charge density and pressure of species α. The last term on the rhs is often called the *diamagnetic contribution* to E_r. Principal factors determining the E_r structure are poloidal and toroidal driving forces (momentum input from NBI, neoclassical fluxes, ion orbit losses, etc.) and their counterparts, the damping forces, like parallel and perpendicular viscosities. Note that a velocity shear in both poloidal and toroidal directions can contribute to an E_r shear.

2.3.1 Measurement of the Radial Electric Field

Experimentally, a measurement of E_r is particularly challenging. The measurement is possible in the edge plasma and scrape-off layer by emissive [37] or ball-pen [38] probes, which measure the plasma potential ϕ_p. Taking the derivative $-\mathrm{d}\phi_\mathrm{p}/\mathrm{d}r = -\phi_\mathrm{p}'$ ($\mathrm{d}x/\mathrm{d}r \equiv x'$ for all magnitudes x in the following) gives E_r. However, emissive probes are fragile and have limited lifetime, in particular in large-scale experiments with high temperatures. Ball-pen probes are promising, but only usable around the separatrix. Another type of probes is the Langmuir probe, which measures the floating potential ϕ_fl. Often E_r is calculated from radially separated probes, and a possible electron temperature contribution to ϕ_fl is neglected, which can lead to problems in the measurement interpretation [39, 40].

Another diagnostic capable of measuring E_r is the Heavy Ion Beam Probe (HIBP), which measures the radial ϕ_p profile. Using $E_r = -\phi_\mathrm{p}'$, a radial electric field profile is obtained. A drawback of HIBP systems is that their signal quality depends on the plasma density, meaning that in the edge plasma, which is of particular importance for H-mode research, they lack accuracy. Furthermore, HIBP system are complex and expensive, hampering their feasibility for many – in particular small-scale – laboratories.

Apart from these two methods, (2.13) can be used to calculate E_r from measurements of v_θ, v_φ and p' through charge exchange recombination spectroscopy (CXRS) [41]. Spectroscopy lacks spatial and especially temporal resolution, so this method is not optimum when trying to measure fast processes, e.g. the dynamics of the L-H transition [42]. All terms of (2.13) have to be measured for the same species α, be it ions or some impurity. Apart from that, the installation of both poloidal and toroidal CXRS lines of sight is complex and presents great challenges to the experimentalist.

Doppler reflectometry, discussed in the following, is a relatively cost-effective diagnostic capable of measuring the perpendicular velocity of density fluctuations $u_\perp$, E_r (for details see sec. 3.3) and density turbulence wavenumber spectra $S(k_\perp)$. Therefore it offers an attractive alternative to the cited issues and is a valuable tool for the investigation of turbulence and the interplay between (sheared) flows and the level of turbulence in fusion plasmas.

Chapter 3

Doppler Reflectometry

Doppler reflectometry (DR), also called *Doppler backscattering* (DBS), is a diagnostic tool first used in the late 1990's [43–45] which is capable of providing measurements of the perpendicular velocity of density fluctuations $u_\perp$ and their wavenumber spectra $S(k_\perp)$, where $k_\perp$ is the turbulence perpendicular wavenumber. With the addition of very basic and almost always satisfied assumptions, it is possible to deduce the radial electric field E_r from the perpendicular velocity. An important point is that measurements can be made on fast timescales, which allows for the calculation of fluctuating perpendicular velocities $\tilde{u}_\perp$, fluctuating radial electric fields $\tilde{E}_r$ and turbulence level $\tilde{n}_e$ simultaneously.

3.1 History

Conventional reflectometers are based on the fact that electromagnetic waves are reflected by the plasma at a so-called *cutoff-density* n_c, which depends on the wave frequency f_0 and, for X-mode measurements, on the magnetic field strength B. Usually, the frequencies necessary to probe fusion plasmas are in the microwave frequency range (1 – 100 GHz). The phase ϕ of the reflected wave is compared to a reference wave and gives information on the cutoff-layer position in the plasma.

From the early 1990's on, it was observed that the phase ϕ of reflectometer measurements did not fluctuate around a mean value, as was expected due to radial movements of the cutoff layer. Instead it increased or decreased monotonically, with ϕ reaching net values corresponding to cutoff layer movements larger than the system size, which could not be real. The first one to make measurements (on JET) and document the effect was Sips in 1991 [46], calling it *phase runaway* (PRA). He also noted that the PRA was due to density fluctuations, and it was seen that in H-mode the PRA disappeared. However, Sips provided no physical interpretation of the effect, instead he attributed it to a phase meter problem at low signal level (due to fluctuations). To overcome the problem, he installed high-pass filters which allowed the measurements of fluctuations only on timescales smaller than 0.2 ms, which removed the PRA, but with the drawback to lose the information on density fluctuations with frequencies below 5 kHz.

The correct interpretation of Bragg backscattering off moving density fluctuations was first given by Sánchez *et al.* at the first International Reflectometry Workshop (IRW1) in Abingdon, UK, in March 1992 [47]. The heterodyne reflectometry signals measured in the W7-AS stellarator allowed for the calculation of complex amplitude spectra, and the PRA was shown to be related to asymmetries in the spectra. Two interpretations were proposed, (i) symmetric moving plasma perturbations with an antenna misalignment or (ii) asymmetric moving plasma perturbations. The conclusions from Sánchez *et al.* from W7-AS were confirmed by Hanson *et al.* for measurements on the ATF torsatron in September 1992 [48].

One year later, in 1993, as a side-product in a different context, Mazzucato and Nazikian derived a formula for the Doppler shift in the frequency spectrum caused by enhanced scattering off density fluctuations at the cutoff layer [49]. They proposed that *"... the plasma rotation may be inferred from the Doppler shift in the peak of the frequency spectrum."*

In the following years the observation of PRA was confirmed by many groups on several experiments [50–56], where a connection between turbulence level and the existence of the PRA was deduced in almost all cases. Bulanin and Korneev showed that the sign of the PRA reversed when the plasma entered H-mode in TUMAN-3, and attributed the effect to a possible velocity shear in H-mode [51]. Brañas *et al.* showed that in W7-AS H-mode plasmas the PRA completely vanished, interrupted by short reappearances during ELMs. In addition, when the magnetic field was reversed, the phase derivative changed sign, a proof that radially moving density fluctuations were not responsible for the PRA [56].

The first two-dimensional (2D) full-wave simulations were done by Irby *et al.*, where the effect of poloidally propagating density fluctuations on the phase evolution was confirmed [57]. Using the previously developed physical optics model [58, 59], Conway investigated the effects of asymmetric reflectometer configurations and asymmetric density perturbations [60]. In this context he showed that phase ramping or PRA only occurs when a threshold turbulence level – its value depends on several parameters – is surpassed.

At this point it seemed to be only a matter of time until the first Doppler reflectometers were developed. PRA had been observed and explained in theory and simulation and it had been proposed that PRA could be exploited to deduce the perpendicular velocity of plasma density fluctuations.

The first measurements with deliberately tilted antennas that showed finite Doppler shifts f_{D} clearly separated from 0 kHz were presented in March 1999 at the 4$^{\mathrm{th}}$ International Reflectometry Workshop in Cadarache, France, by Hirsch *et al.* for W7-AS [43] and Zou *et al.* for Tore Supra [44]. It was then when Zou *et al.* showed the first perpendicular wavenumber spectrum ever measured with Doppler reflectometry [44]. Bulanin did similar measurements on TUMAN-3M with tilted antenna beams [45], However, in his experiments the antenna setup was not optimized and the Doppler peak was not separated from the reflection component of the spectrum, so that the interpretation of the data was not straightforward. In the years following 1999, several Doppler reflectometers were designed for different tokamak and stellarator experiments [61–65].

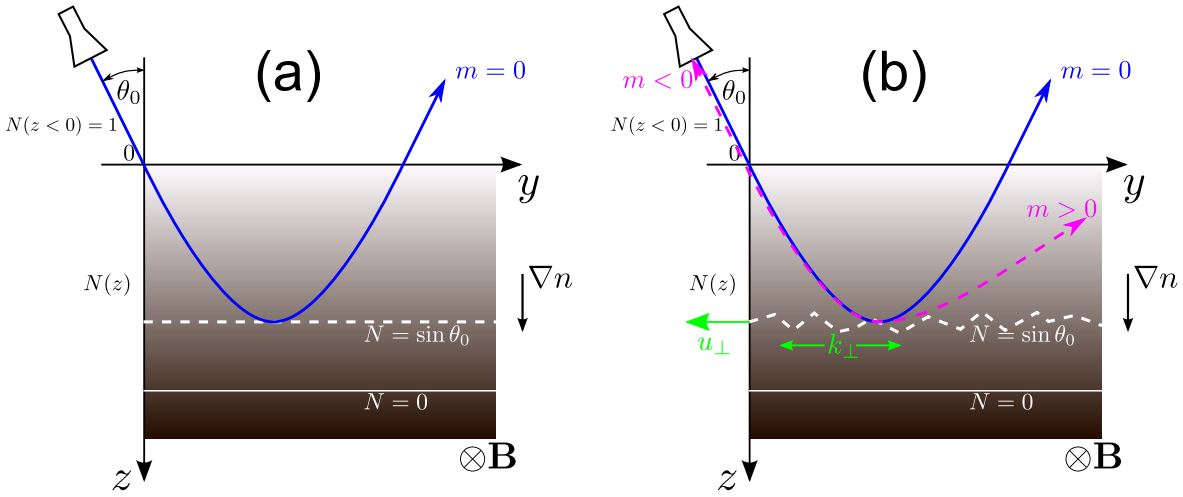

Figure 3.1: Oblique incidence of a microwave beam in a slab plasma (a) without and (b) with the presence of turbulence at the cutoff layer.

The new systems had better spectral resolution and Doppler shifts of several MHz were obtained. Dedicated 2D full wave simulations show that optimized systems with Gaussian beams are reliable in f_D and $S(k_\perp)$ measurements [66, 67].

3.2 Theoretical Background

In the following, the physical processes involved in Doppler reflectometry and the spectral resolution of a Doppler backscattering experiment are explained. These are important points indispensable in the design process of a Doppler reflectometer.

3.2.1 Physical Mechanism

In contrast to conventional reflectometry, where the microwave beam is launched perpendicular to the cutoff layer in the plasma, in Doppler reflectometry the microwave beam is launched obliquely with respect to the cutoff layer normal. The following description for the case without turbulence is based on the derivation given in Ref. [68]. In fig. 3.1(a) a plasma slab in the y-z-plane is indicated, with the density gradient pointing downward in z-direction. The magnetic field points into the page. For $z < 0$, there is no plasma, hence the refractive index $N(z < 0) = 1$, i.e. the wave (indicated by a blue line) travels in a straight line in vacuum. The wave vector is $\mathbf{k} = \omega/c\,(0, \sin\theta_0, \cos\theta_0)$. As the wave enters into the plasma at $z = 0$, the refractive index starts to decrease and the wave vector is modified according to the local dispersion relation in the plasma. As indicated in fig. 3.1(a) the wave direction is modified as the cutoff layer is approached. At the cutoff layer the refractive index takes on its minimum value $N = \sin\theta_0$, k_z changes sign and the wave travels out of the plasma again. In the case of fig. 3.1(a), with a flat cutoff layer, the wave is reflected and no scattering takes place.

The situation is different when the cutoff layer is corrugated as schematically displayed in fig. 3.1(b). Due to the corrugations, scattering will take place, as indicated by the magenta dashed line. If the turbulence scale $k_\perp$ at the cutoff layer matches the *Bragg condition*

$$k_\perp = 2k_0 \sin\theta_0, \tag{3.1}$$

the -1$^{\text{st}}$ order scattering will return to the antenna (*Bragg backscattering*). Typically, Doppler reflectometers cover a perpendicular wavenumber range of $k_\perp = 3$ – 20 cm^{-1}, values where the typical wavenumber spectra in magnetic confinement fusion experiments are finite, i.e. fluctuations at these scales are normally present.

The spectrum of the backscattered wave is Doppler shifted, the value of the Doppler shift depends on the velocity of the plasma turbulence and on its wave number

$$\omega_{\text{D}} = \mathbf{u}\cdot\mathbf{k} = u_\perp k_\perp + u_\parallel k_\parallel + u_r k_r. \tag{3.2}$$

In general, Doppler reflectometers are optimized in a way that they are only sensitive to $k_\perp$ and not $k_\parallel$ by aligning them perpendicular to the magnetic field $\mathbf{B}$. Additionally, in magnetically confined plasmas it is usually assumed that $k_\perp \gg k_\parallel$ and $u_\perp < u_\parallel$, in a way that the second term on the rhs of (3.2) is negligible with respect to the first one [69]. $k_\perp/k_\parallel$ was experimentally shown to be close to 200 in the stellarator experiment TJ-K [70], about 100 – 200 in TEXT [71, 72] and roughly 30 in TFTR [73]. About a quarter century ago, these measurements were extremely challenging, so generally upper bounds for $k_\parallel$ were provided, with the result $k_\perp > k_\parallel$ [74, 75], but which did not rule out $k_\perp \gg k_\parallel$. Numerically $k_\perp \gg k_\parallel$ was confirmed for plasma edge turbulence simulations with TEXT parameters [72]. If in addition to the above the turbulence does not displace itself radially [48, 62, 76], the third term vanishes, and (3.2) can be written

$$\omega_{\text{D}} = u_\perp k_\perp. \tag{3.3}$$

The perpendicular wavenumber of density turbulence $k_\perp = 2k_{\perp,i}$ is obtained through ray tracing, which gives $k_{\perp,i}$, the wavenumber of the incident ray. With the measurement of the Doppler shift, the perpendicular velocity of density fluctuations can be calculated.

It should be mentioned that the typical density turbulence timescales are ~ 10 μs, which defines a lower limit for the measurement of the Doppler shift of a spectrum. This makes Doppler reflectometry a well-suited diagnostic for temporally resolved analysis of perpendicular velocity and density fluctuation behavior. In particular, Doppler reflectometry is important to investigate transient phenomena like L-H transitions on short timescales. This fact is underlined by the ability to measure $u_\perp$ or E_r (DC and fluctuating) and $\tilde{n}_e$ simultaneously.

The radial localization of the backscattering process is provided both by the Bragg condition and the swelling of the wave electric field close to the cutoff layer [77]. At the backscattering layer, $k_{\perp,i}$ takes on its minimum value. Since $k_\perp = 2k_{\perp,i}$ is also minimum, the highest density fluctuation level is expected (see wavenumber spectra in sec. 2.1.2). The radial resolution of the diagnostic depends strongly on the density profile gradient and can be optimized by optimizing the spectral resolution of the

system [78] (see next section). A ray tracing analysis of the radial localization is done in sec. 5.7.2.

3.2.2 Spectral Resolution

Scattering of electromagnetic waves is an established method for the investigation of density fluctuations. In every scattering experiment, the wavenumber investigated depends on the volume illuminated by the electromagnetic wave. The density fluctuations in a volume V can be expressed in wavenumber space by

$$\tilde{n}(\mathbf{k},t) = \int_V n(\mathbf{r},t) e^{i\mathbf{k}\cdot\mathbf{r}} \mathrm{d}\mathbf{r}. \tag{3.4}$$

As stated above, the Bragg condition determines the perpendicular wavenumber of density turbulence $k_\perp$ selected by the antenna. The spectral (wavenumber) resolution Δk of a system determines the wavenumber interval to be measured, centered at $k_\perp$. This can be interpreted as a bandpass filter in wavenumber space. Holzhauer and Massig showed that the spectral resolution Δk for a gaussian beam is inversely proportional to the beam size w [79],

$$\Delta k = \frac{2\sqrt{2}}{w}, \tag{3.5}$$

a factor which has to be modified for cutoff-layer curvature yielding the spectral resolution of a Doppler reflectometer [80, 81]

$$\Delta k_\perp = \frac{2\sqrt{2}}{w} \sqrt{1 + \left(\frac{w^2 k_0}{\rho_{\mathrm{eff}}} \right)^2}, \tag{3.6}$$

with ρ_{eff} the *effective radius of curvature* within the spot size, defined

$$\rho_{\mathrm{eff}} = \frac{R_\mathrm{C} R_\mathrm{B}}{R_\mathrm{C} + R_\mathrm{B}}, \tag{3.7}$$

with R_B and R_C the radii of curvature of the microwave beam and cutoff layer, respectively. Note that if the beam waist is at the cutoff layer ($R_\mathrm{B} \to \infty$), then $\rho_{\mathrm{eff}} \to R_\mathrm{C}$, i.e. the effective radius of curvature reduces to the plasma curvature R_C. If in addition a plasma slab is treated ($\rho_{\mathrm{eff}} \to \infty$), then the square root in (3.6) is unity and (3.5) is recovered.

The optimum beam size is obtained by setting the first derivative of (3.6) to zero, which yields after some basic calculus

$$w_{\mathrm{opt}} = \sqrt{\frac{\rho_{\mathrm{eff}}}{k_0}}. \tag{3.8}$$

The spectral resolution dependence on the beam size in the plasma is illustrated in fig. 3.2. In (a), the probing beam frequency is $f_0 = 50$ GHz for all curves and plane beam wavefronts are assumed in the plasma ($R_\mathrm{B} \to \infty$), therefore $\rho_{\mathrm{eff}} = R_\mathrm{C}$. In

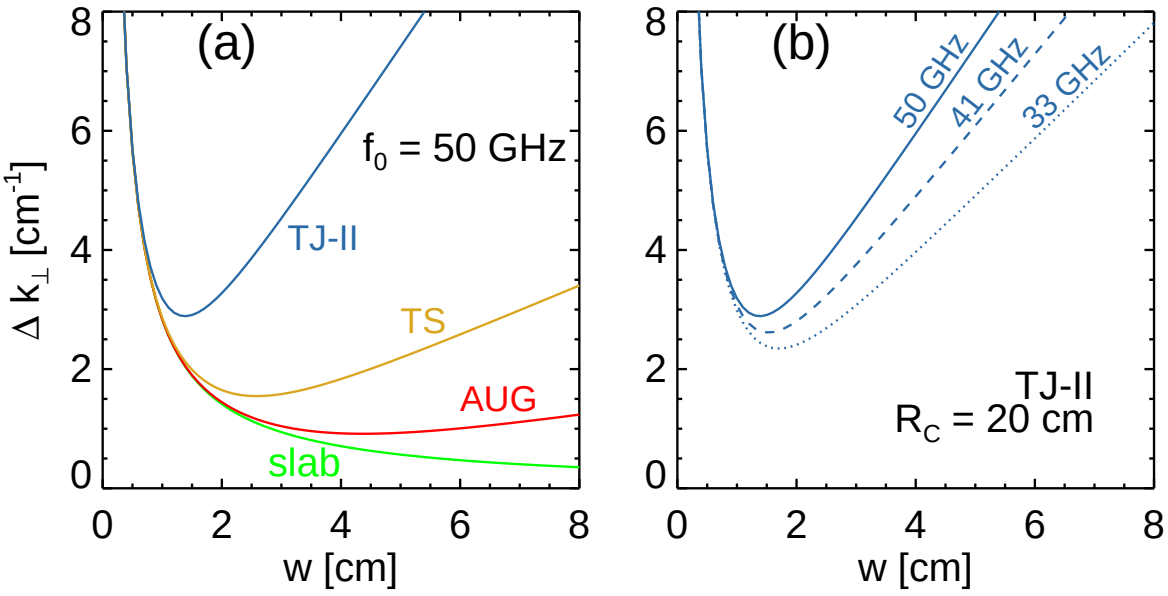

Figure 3.2: Spectral resolution dependence on beam size for $R_B \to \infty$ (waist at cutoff layer). (a) At fixed microwave frequency ($f_0 = 50$ GHz) but for different magnetic confinement fusion experiments, i.e. different R_C (slab: ∞, AUG (ASDEX Upgrade): 2.0 m, TS (Tore Supra): 0.7 m, TJ-II: 0.2 m). (b) In TJ-II for different probing beam frequencies.

consequence, the cutoff layer curvature is the only free parameter. In the slab case, the larger the beam spot, the better the spectral resolution. For the ASDEX Upgrade case (AUG), $R_C = 2.0$ m was used [82]. Here the spectral resolution can be minimized by using a beam spot size of around 4 cm. For Tore Supra (TS, $R_C = 0.7$ m), the beam size should be smaller. For TJ-II ($R_C = 0.2$ m), an optimum beam waist of roughly 1.5 cm should be used.

Fig. 3.2(a) underlines the particular importance of a well-defined beam spot size w for the stellarator TJ-II. It is crucial that w lies in the range of 1.5 cm, and in particular a beam size smaller than this value should be avoided, since the spectral resolution deteriorates more rapidly towards smaller w than towards larger ones. Note also that in the plot a beam waist in the plasma is assumed, i.e. to obtain a situation like the one in fig. 3.2(a), the beam has to be focused to the backscattering region.

The frequency dependence of $\Delta k_\perp$ on w is visualized for the TJ-II case with plane wavefronts in the backscattering region in fig. 3.2(b). As is expected from (3.8), for lower frequencies w_{opt} becomes larger. Furthermore, better spectral resolution can be obtained with lower frequencies. The optimum Doppler reflectometer configuration in TJ-II is one which provides a focused beam in the plasma with decreasing spot size for increasing probing beam frequencies. For a detailed description of the Doppler reflectometer design for TJ-II and hardware details the reader is referred to chapter 5.

3.3 The Perpendicular Velocity of Density Fluctuations

The perpendicular velocity $u_\perp$ measured by Doppler reflectometry is a composition of the plasma background $E \times B$-velocity $v_{E\times B}$ and the phase velocity of the density fluctuations $v_{\rm ph}$

$$u_\perp = v_{E\times B} + v_{\rm ph}. \tag{3.9}$$

The phase velocity of density fluctuations $v_{\rm ph}$ can be interpreted as the velocity with which the density fluctuations move in the plasma frame. If $v_{\rm ph}$ is negligible compared to $v_{E\times B}$,

$$v_{\rm ph} \ll v_{E\times B}, \tag{3.10}$$

(3.9) reduces to $u_\perp = v_{E\times B}$. With knowledge of the magnetic field B the radial electric field can be calculated

$$E_r = u_\perp B. \tag{3.11}$$

In general, it is difficult to show that $v_{\rm ph} \ll v_{E\times B}$. Nevertheless, by comparison with diagnostics that measure E_r it can in principle be shown that the inequality holds. Comparative studies using Doppler reflectometry have been done in TJ-II, where E_r calculated with (3.11) was compared to the one obtained with the heavy ion beam probe [83] (for details see sec. 5.8.4), which measures directly the plasma potential $\phi_{\rm p}$, hence $E_r = -\nabla\phi_{\rm p}$ can be obtained. The inequality (3.10) was confirmed for ECRH and NBI heated L-mode plasmas. Comparisons with spectroscopy in W7-AS [61] and with Langmuir probes in ASDEX Upgrade [19] support the applicability of (3.10).

Chapter 4

Experiment Description

In this chapter, the TJ-II stellarator and the diagnostics with impact on this work will be introduced.

4.1 The TJ-II Stellarator

TJ-II is a 4-period heliac-type stellarator [5] which started operation in 1997 in Madrid, Spain. It has a major radius of $R_0 = 1.5$ m and an average minor plasma radius of $\langle a \rangle \leq 0.2$ m. The on-axis magnetic field strength is $B_0 \leq 1$ T. A sketch of the coil system, plasma and vacuum vessel of the experiment is shown in fig. 4.1. There are 32 toroidal field coils (TF, brown), 4 vertical field coils (VF, green), one circular (CC, blue) and one helical (HX, turquoise) coil, following the helical law

$$R_{\mathrm{HX}} = r_{\mathrm{HX}}^{\mathrm{sw}} \cos(-4\varphi), \tag{4.1}$$
$$Z_{\mathrm{HX}} = r_{\mathrm{HX}}^{\mathrm{sw}} \sin(-4\varphi), \tag{4.2}$$

where φ is the toroidal angle and $r_{\mathrm{HX}}^{\mathrm{sw}} = 0.07$ m is the swing radius of the helical coil. The toroidal field coils (radius $r_{\mathrm{TF}} = 0.4$ m) follow the same helical law, with a swing radius of $r_{\mathrm{TF}}^{\mathrm{sw}} = 0.28$ m. The ensemble circular and helical coil form the so-called *central conductor*. The central conductor is of major importance, since the total current in it defines the plasma volume and the current in the helical coil has large impact on the rotational transform. The configuration of the currents is generally labeled I_{CC}_I_{HX}_I_{VF}, and denotes the currents in the different coils in terms of 100 A. So $I_{\mathrm{CC}} = 100$ stands for a current of 10 kA in the circular coil. Note that I_{TF} is absent in the configuration denomination, because its value is determined by the requirement of $B_0 = 0.95$ T at the toroidal heating position, the resonance condition for electron cyclotron heating. The standard configuration of TJ-II is 100_44_64. Due to the four periods, TJ-II is divided into four sectors (A, B, C, D), each one of 90°, which are identical in terms of physics (flux surfaces are equivalent). The eight ports per sector are labeled in counterclockwise direction, so the ports in sector A are labeled A1 to A8, those in Sector B are labeled B1 to B8 and so on (for clarification see fig. 4.1). In the following, because of the fourfold symmetry and for simplicity, the letter identifying

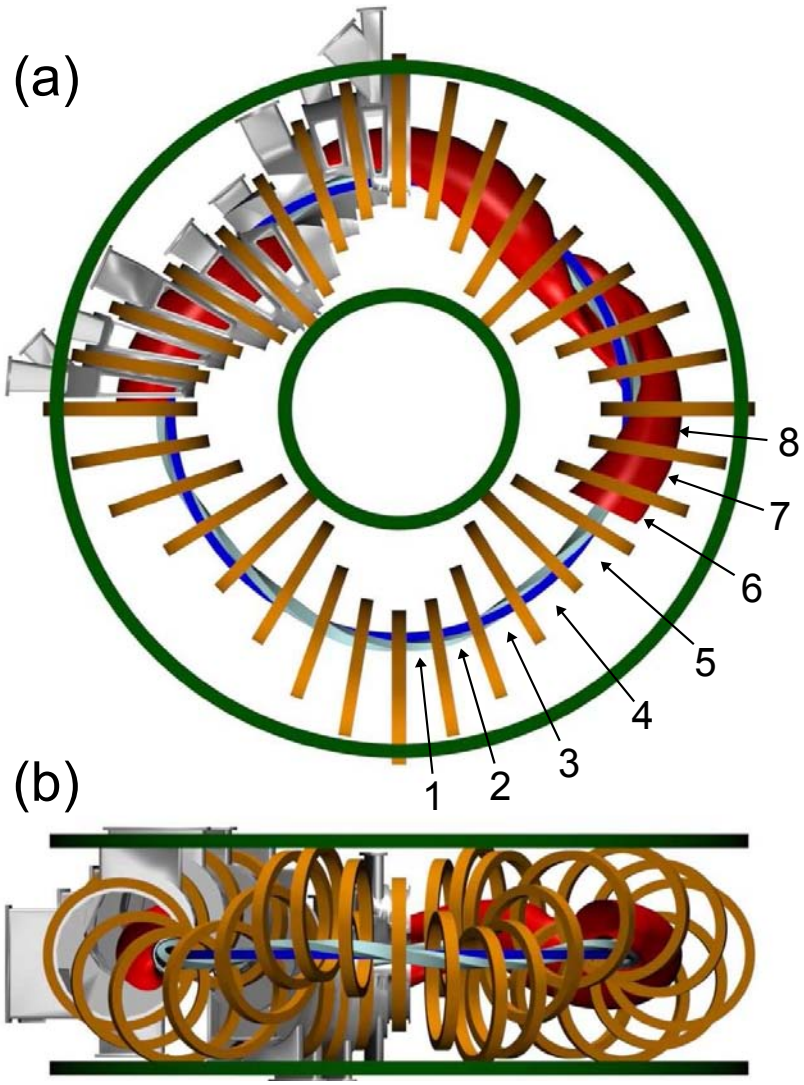

Figure 4.1: (a) Top-down view and (b) lateral view of the TJ-II coil system, plasma (red) and vacuum vessel (gray). The port numbering is indicated. For details refer to the text.

the sector will be discarded. Because of stellarator symmetry, the flux surfaces at φ are the same as those at $90° - \varphi$ mirrored at $Z = 0$ for $\varphi < 90°$. About 200° of the total plasma is depicted in fig. 4.1. On the lower rhs of fig. 4.1(a) the plasma is above the central conductor and then winds in clockwise direction around the central conductor with increasing φ. The cut through the plasma on the rhs is at the position where the Doppler reflectometer is installed ($\varphi = 67.1°$, port 6).

In fig. 4.2 the flux surfaces (red) for the magnetic standard configuration of TJ-II are shown for increasing toroidal angles indicated in the upper left corner of each plot. The axis ranges are the same in all plots. The stellarator symmetry mentioned above can be observed e.g. at $\varphi = 30°$ and 60°. Note that with increasing toroidal angle φ, the plasma winds clockwise around the central conductor, indicated by the $\oplus$ symbol at $R - R_0 = Z = 0$. The winding of the plasma around the central conductor can

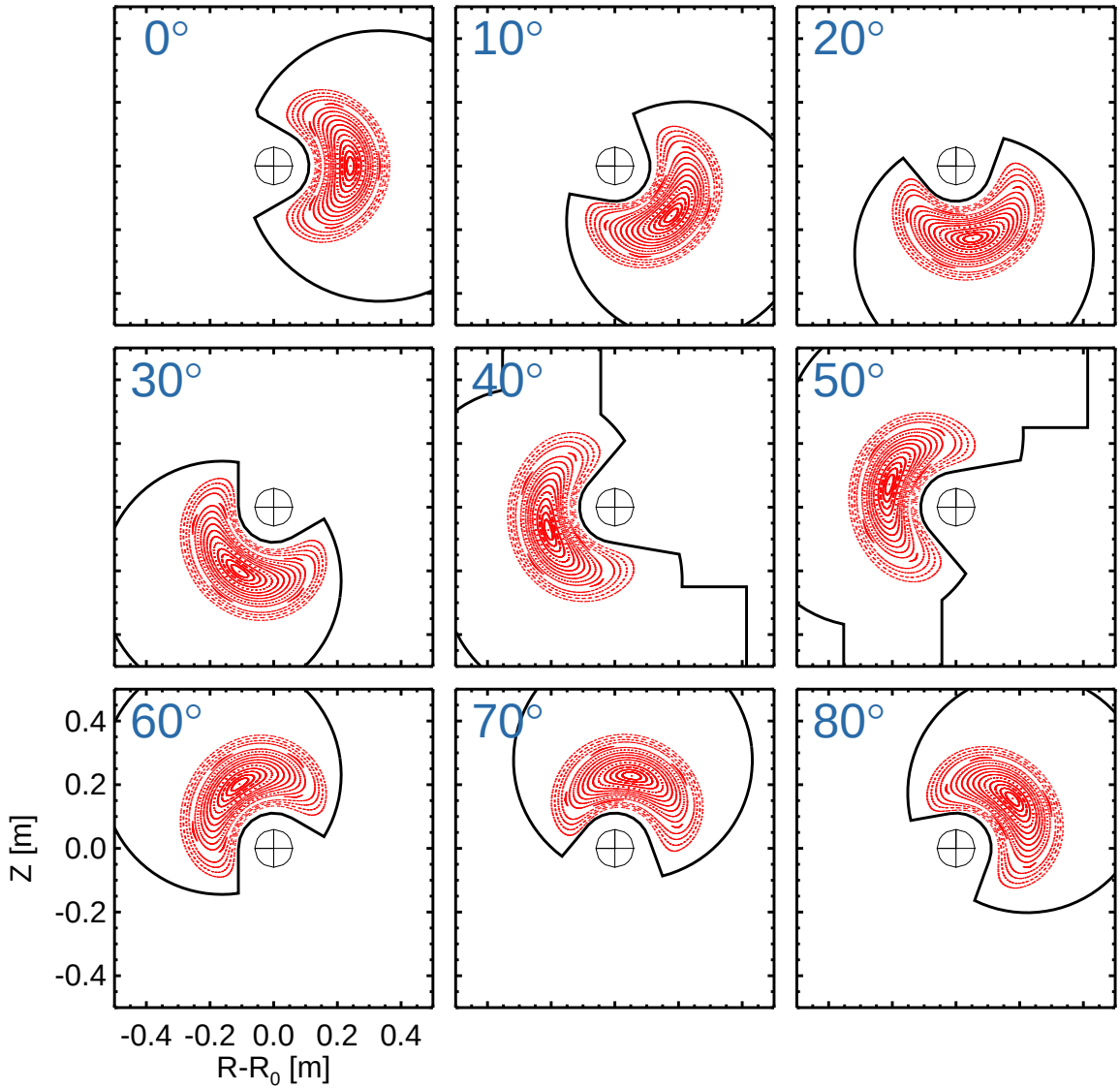

Figure 4.2: Flux surfaces for the standard configuration of TJ-II at different toroidal angles indicated in the upper left corner of each plot. The axis ranges are the same in all plots.

also be observed in fig. 4.1. Note the magnetic island ($n/m = 8/5$) in the flux surfaces at approximately 3/4 of the plasma radius, an important feature of the standard configuration.

TJ-II possesses a high magnetic configuration flexibility, illustrated in the vacuum ι-profiles of some configurations in fig. 4.3. ι denotes the number of poloidal turns during one toroidal turn by a traced magnetic field line. By changing the current in the different coils, the radial positions of rationals (several of them are indicated by the dashed lines) can be controlled, allowing the study of their impact on magnetic confinement or transport barrier formation. Major results are that rational ι-values can facilitate the transition from L- to H-mode [83] and that they tend to increase E_r in their vicinity [84]. When low order rationals are located in the plasma core ($\rho \approx 0.3$,

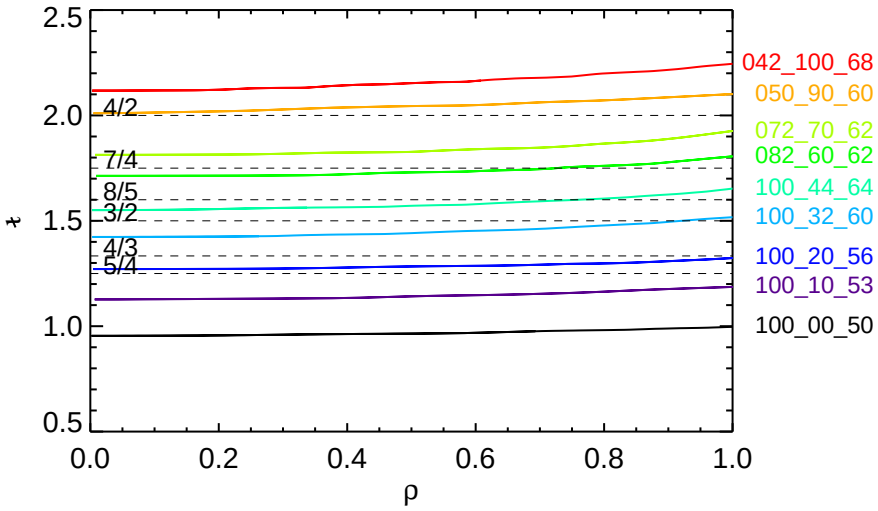

Figure 4.3: Vacuum ι range in TJ-II. $\iota(0)$ can take any value from 0.9 to 2.2. In all configurations, ι increases with the normalized flux radius ρ and the magnetic shear is low. The labels of the curves are in the standard notation (see text). Important rational n/m values are indicated. The 8/5-rational is at $\rho \approx 0.75$ in the standard configuration.

with $\rho = r/a$ the effective radius of the plasma, a the minor plasma radius), an electron internal transport barrier (eITB) may form [85–87]. $\iota(0)$ can take any value between 0.9 and 2.2, and increases with ρ. In all the configurations, the magnetic shear is low. The plasma volume varies with the configuration between 0.3 and 1.1 m^3 ($a = 0.1 - 0.2$ m), depending mainly on the sum of the currents in CC and HX.

The plasma discharges of TJ-II last for up to 300 ms, with hydrogen or helium as working gas. Heating systems include electron cyclotron resonance and neutral beam injection heating (ECRH and NBI). ECR heating is achieved using 2 gyrotrons heating at the second harmonic with $f = 53.2$ GHz and a power of $P_{\mathrm{ECRH}} = 300$ kW each. In ECRH-plasmas, the density profile is normally flat or even hollow [88], due to pump-out of the electrons [86], and the electron temperature profile is peaked. The maximum density in ECRH plasmas is limited by the cutoff-density, which is 1.75×10^{19} m^{-3} for the TJ-II system. The electron temperature in ECRH plasmas reaches $T_{e,\max}^{\mathrm{ECRH}} \approx 2$ keV.

parameter	value		
major radius	R_0	$=$	1.5 m
average minor radius	$\langle a \rangle$	$\leq$	0.2 m
magnetic field strength	B	$\leq$	1 T
rotational transform	$\iota(0)$	$\approx$	0.9 - 2.2
electron density (ECRH)	$n_{e,\max}^{\mathrm{ECRH}}$	$\approx$	1.5×10^{19} m^{-3}
electron density (NBI)	$n_{e,\max}^{\mathrm{NBI}}$	$\approx$	8×10^{19} m^{-3}
peak electron temperature	$T_{e,\max}$	$\approx$	2 keV
ion temperature	T_i	$\approx$	150 eV

Table 4.1: Characteristics of TJ-II and the parameters of the produced plasmas.

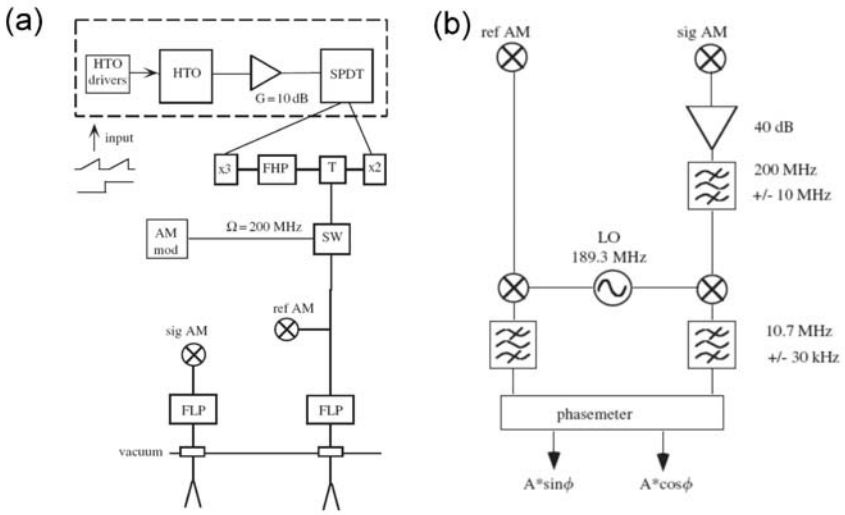

Figure 4.4: (a) Circuit diagram of the AM reflectometer. Microwave frequencies are obtained by doubling and tripling of the oscillator signal. (b) The AM receiver detection system uses an intermediate frequency of 10.7 MHz.

In NBI discharges (two NBI injectors with 1 MW each), the density profile is peaked with maximum values of $n_{e,\max}^{\mathrm{NBI}} \approx 8 \times 10^{19}$ m^{-3}. The characteristics of TJ-II and parameters of the produced plasmas are summarized in Tab. 4.1.

4.2 The AM Profile Reflectometer

A short description of the AM profile reflectometer is given in this section, for more detailed information the reader is referred to [89]. The density profiles measured with this system are used as input for the ray-tracing code `TRUBA` (cf sec. 5.7) to calculate ρ and $k_\perp$ of the Doppler reflectometer measurement. The system works in X-mode and measures at a toroidal angle of $\varphi = 45°$, entering the vessel through port A4TOP. The frequency range is 25 – 50 GHz (sweep time: 1 ms) and densities of $n_e = 0.03 - 1.00 \times 10^{19}$ m^{-3} are covered. Normally, a frequency of 50 GHz would allow for densities up to 1.50×10^{19} m^{-3}, but in general the reflected signal close to 50 GHz is noisy and cannot be used for profile reconstruction. The range of frequencies is obtained by employing a hyper-abrupt varactor-tuned oscillator (12 - 18 GHz) and doubling and tripling its frequency, as shown in fig. 4.4(a). The signal is then amplitude modulated (AM) at 200 MHz and a reference signal is split by a directional coupler. Low-pass filters ($f < 50$ GHz) are used to avoid perturbation of the system by the ECRH system which works at 53.2 GHz. The probing beam is sent to the plasma by the emitting antenna. The reflected (phase shifted) signal is received by another antenna and the phase of the AM envelope is measured by a phasemeter (fig. 4.4(b)) by comparing it to the reference signal. The phase information yields the time delay, which itself is the input for the Bottolier-Curtet [90] algorithm to obtain the density profile.

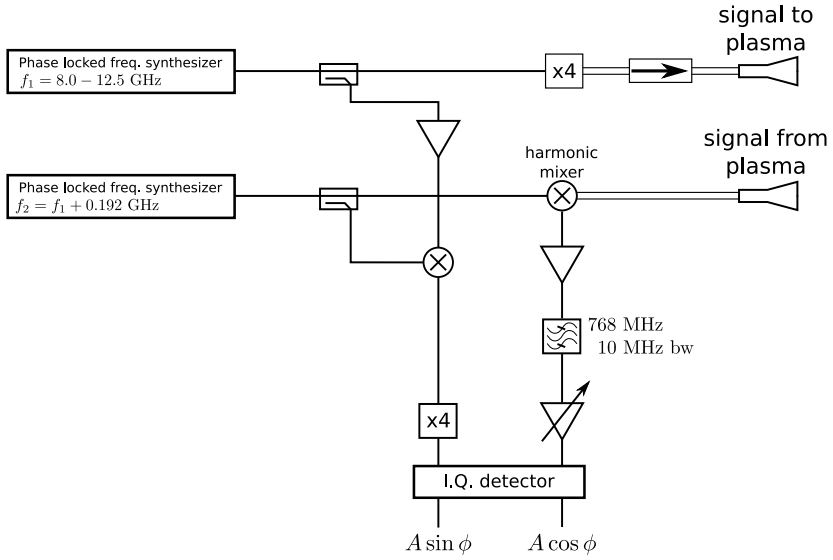

Figure 4.5: Circuit diagram of one channel of the fast frequency hopping reflectometer. The signal received from the plasma is down converted to 768 MHz and heterodyne detection, done by an I.Q. detector, yields the complex amplitude signal which contains the information on the plasma properties. For details refer to the text.

4.3 The Fast Frequency Hopping Reflectometer

The fast frequency hopping reflectometer system [91] was installed in TJ-II until 2008, when the electronics part of the system was moved to be used by the new Doppler reflectometer. The system is a two-channel heterodyne system (for details on heterodyne methods, see the review [92]) working in the frequency range of 33 – 50 GHz (Q-band) in X-mode, resulting in an accessible range of plasma densities of about 0.3 to 1.5×10^{19} m^{-3}. The emitting part of the system is installed at a toroidal position of $\varphi = 85.3°$ and enters the vessel through port B8SIDE. A sketch of the electrical system (one channel) is shown in fig. 4.5. The frequencies of the two channels can be changed independently on a timescale smaller than 1 ms, allowing for the investigation of turbulence and fluctuations with high radial and temporal resolution ($\Delta R < 1$ cm, sampling rate 5 MHz). Each channel uses two independent 8.0 – 12.5 GHz synthesizers, one of which is called the main synthesizer (RF) and the other one local oscillator (LO), which has a frequency offset of 192 MHz.

The RF signal is multiplied by 4 to achieve 33 – 50 GHz and transmitted by a standard horn antenna to the plasma. The returning signal is converted by a harmonic mixer to an intermediate frequency (IF) of 768 MHz, amplified and band pass filtered around 768 MHz with 10 MHz bandwidth. Then it is amplified to the requisite level of the I.Q. detector.

The LO signal is mixed with the RF signal and then multiplied by 4 to attain the necessary 768 MHz, and then fed to the I.Q. detector, which returns the *In-phase (I)* and *Quadrature (Q)* signals containing the amplitude and phase information of the received signal. For details on the $I - Q$ plane and interpretation refer to sec. 6.1.

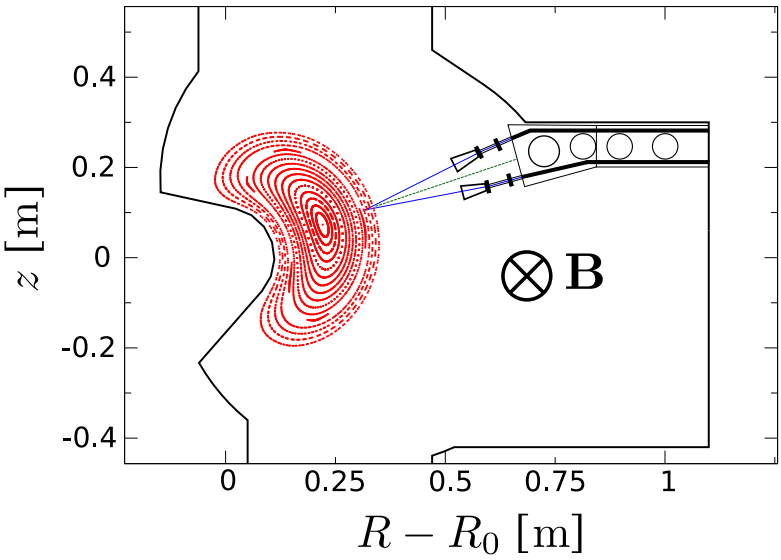

Figure 4.6: Schematic drawing of the frequency hopping fluctuation reflectometer system. The flux surfaces are shown in red, the perpendicular to the LCFS in green and the center of the microwave beam is indicated in blue. The support of the waveguides (close to the vacuum vessel) is shown on the right hand side.

A sketch of the reflectometer system is shown in fig. 4.6. The flux surfaces for the standard configuration are shown in red, and the antenna configuration is almost symmetrical to the perpendicular of the flux surfaces (misalignment about -2°), shown as a green line. The support of the waveguides is made of stainless steel with an inlet of teflon which holds and insulates the waveguides. The misalignment of -2° with respect to the perpendicular to the flux surfaces generates slightly asymmetric spectra of the complex amplitude ($Ae^{i\phi}$) and the complex phase ($e^{i\phi}$). This effect is due to the Doppler shift caused by the perpendicular velocity of the turbulence of the plasma (phase runaway, cf sec. 3.2.1).

4.3.1 Reflectometer Capability to Measure the Sign of the Perpendicular Velocity

The reversal of the edge perpendicular velocity $u_\perp$ in TJ-II can be triggered by the modulation of the line-averaged density $\langle n_e \rangle$ and is closely connected to a threshold value of the collisionality [93]. As stated above, the conventional reflectometer is capable to monitor the sign of the perpendicular velocity of density fluctuations [94,95]. The center of gravity or mean frequency of the power spectrum $S(f)$ of the reflectometer is defined

$$\langle f \rangle = \frac{\int_{-f_{\mathrm{Ny}}}^{f_{\mathrm{Ny}}} f S(f) \mathrm{d}f}{\int_{-f_{\mathrm{Ny}}}^{f_{\mathrm{Ny}}} S(f) \mathrm{d}f}, \tag{4.3}$$

where f_{Ny} is the Nyquist frequency, and reflects the degree of asymmetry of the spectrum.

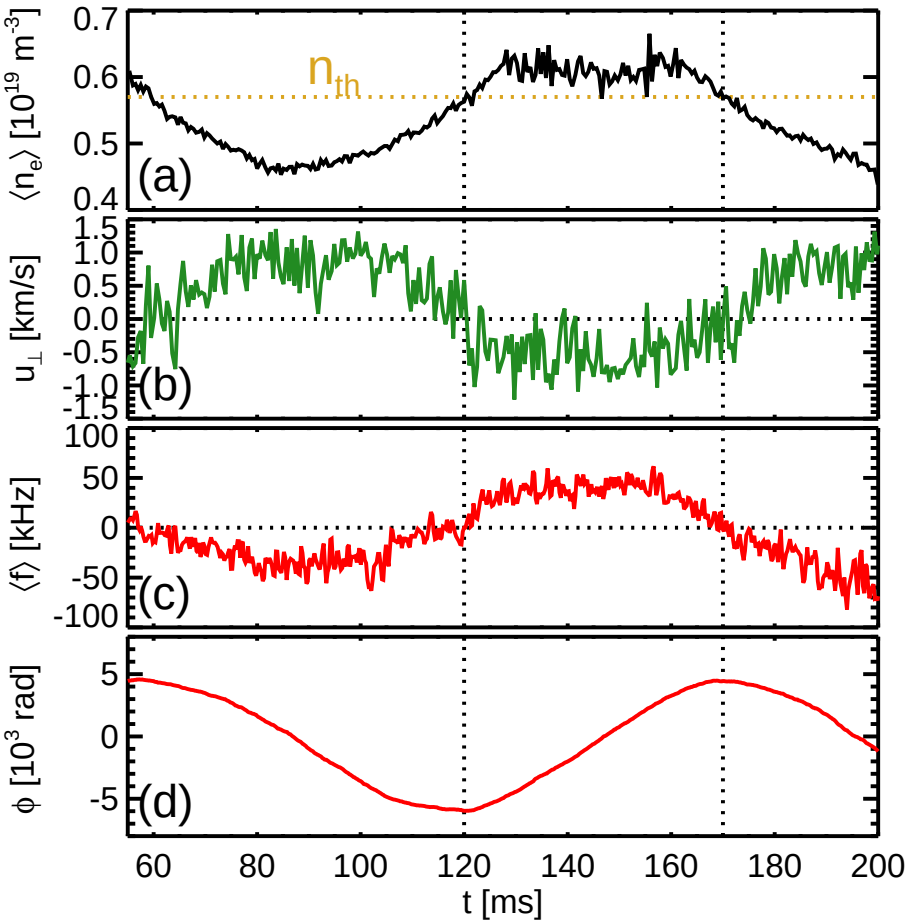

Figure 4.7: (#11285) (a) Time trace of the line-averaged density $\langle n_e \rangle$, crossing twice the threshold density $n_{\mathrm{th}} \approx 0.57 \times 10^{19}$ m^{-3}. (b) Corresponding edge perpendicular velocity measured with Langmuir probes at $\rho \approx 0.9$. (c) The center of gravity $\langle f \rangle$ of the power spectrum of one reflectometer channel measuring at $\rho \approx 0.8$. Negative $\langle f \rangle$ corresponds to positive $u_\perp$ and vice versa. (d) The slope of the reconstructed phase also reflects the sign of the perpendicular velocity.

In fig. 4.7 a discharge with density modulation is shown. In (a), the line-density $\langle n_e \rangle$ crosses the threshold density n_{th} at $t = 120$ ms and goes below again at $t = 170$ ms, which is indicated by dotted vertical lines. The edge perpendicular velocity $u_\perp$ measured with Langmuir probes [96] at $\rho \approx 0.9$ is depicted in (b). $u_\perp$ is positive (ion-diamagnetic direction) when the line-density is below the threshold density ($\langle n_e \rangle < n_{\mathrm{th}}$) and it is negative when the line-density is above the threshold density ($\langle n_e \rangle > n_{\mathrm{th}}$). In (c), the comparison with the center of gravity measurement of the reflectometer is demonstrated. The reflectometer is measuring at $\rho \approx 0.8$. Due to phase-runaway [48, 51], the mean frequency is negative when the perpendicular velocity is positive and vice versa. For comparison, the reconstructed phase ϕ is plotted in (d). The slope is negative for $u_\perp > 0$ and positive for $u_\perp < 0$.

This relation between measurements of Langmuir probes and the reflectometer

demonstrates that although it is not possible to calculate absolute perpendicular velocities from the reflectometer data, it is possible to determine the sign of $u_\perp$. Advantages of the reflectometer to the Langmuir probes are that the reflectometer can measure at more internal positions (up to $\rho \approx 0.6$) and that the temporal resolution of the reconstructed phase is better than the length of the time window required to calculate $u_\perp$ from Langmuir probe measurements.

However physics studies are limited if only the sign of $u_\perp$ can be obtained. In order to study radial electric fields and turbulence behavior and their coupling, it was decided to design a Doppler reflectometer for TJ-II.

Chapter 5

The TJ-II Doppler Reflectometer

One of the two main parts of this thesis was the design of a Doppler reflectometer (DR) for the TJ-II stellarator. The design and optimization of a DR has to be carefully done in order to achieve good spectral resolution and to avoid a possible $k_{\|}$-dependence, which enhances the system reliability [67]. Apart from that, through the optimization process, data analysis is easier and can even be automated (to some degree) if a potential zero-order reflection can be avoided.

5.1 Design of the Doppler Reflectometer

As a first step in the DR design a study was done on the viability of Doppler reflectometry in TJ-II. This included the localization of suitable and available ports, which were found in sector C6. Apart from that, the spectral resolution (cf sec. 3.2.2) had to be optimized by encountering the optimum beam size w_{opt} in the plasma for the respective position of the DR. To accelerate the design process of the system, in the calculation of w_{opt}, the poloidal flux surfaces were preferred to the perpendicular ones. This approximation caused a slight error of w_{opt} resulting in a spectral resolution 2.8% worse. This error is small and comparable to standard error sources, i.e. uncertainties in antenna and mirror fabrication, positioning and alignment of the system. Nevertheless, in the remaining sections, as a guide, the optimum way to design the Doppler reflectometer is illustrated. Differing results caused by considering the poloidal flux surfaces are mentioned throughout the text.

5.1.1 General Considerations

In sec. 3.2.1 it is mentioned that the turbulence scale measured by a DR depends basically on the microwave frequency f_0 and the antenna tilt angle θ_0. The microwave frequency to be used is determined by the plasma density for O-mode and additionally the magnetic field for X-mode operation. Apart from that, a decision has to be taken on the radial range of measurement positions. It is clear that the higher the microwave frequencies, the more internal the measurements while losing the possibility of probing the edge plasma. For the TJ-II DR, X-mode operation was chosen and the target

measurement range was decided to be the (for turbulence investigations) important density gradient region, because it has major influence on the radial electric field (cf eq. (2.13)) and is a driving term for drift wave turbulence. The microwave generator of the conventional reflectometer (see sec. 4.3) provides frequencies $f_0 = 33$ – 50 GHz, suited for these requirements.

There are basically two different ways of changing the turbulence scale measured by Doppler reflectometry through the tilt angle θ_0. One is an alteration of the plasma shape (by moving the plasma or changing the configuration), which changes the angle of incidence of the beam with the cutoff layer [62]. The second way is a movement of the beam, which can be achieved by a motorized antenna [63] or a steerable mirror [97]. In general, a change in plasma shape or position is not desirable, because it can cause changes in plasma properties like confinement, density and temperature gradients, velocities etc. Hence for the TJ-II DR it was decided to make the microwave beam steerable, which technically is achieved with a steerable mirror, explained in detail in sec. 5.4.

In order to be able to measure in perpendicular incidence (conventional reflectometry), the tilt angle of the microwave beam has to be zero degrees, for which (3.1) yields $k_\perp = 0$. In the planning phase of the TJ-II DR it was decided to include this possibility in the design, and even to extend it by allowing the tilt angle to be positive or negative. Apart from the possibility of measuring in conventional reflectometry mode, this provides a way to *calibrate* the DR by searching for the mirror setting where the power spectrum is symmetric.

The TJ-II plasma is highly shaped, an up-down symmetry exists only at toroidal angles $\varphi = 0°$ and $45°$. However, an approximate symmetry can be found if the plasma is mirrored by the line which connects the center of the circular coil ($R - R_0 = Z = 0$) with the center of the helical coil. For simplicity, this line will henceforth be called the *axis of symmetry*. Since the helical coil winds around the circular coil (cf (4.2)), this axis of symmetry depends on the toroidal angle φ. The poloidal angle of the axis of symmetry is $\theta = -4\varphi$. In the design process of the TJ-II DR it was tried to position the system on this axis of symmetry, in order to provide symmetric measurements in the sense that tilt angles of $\pm\theta_0$ provide Doppler shifts f_D of the same magnitude but with different sign.

5.1.2 Toroidal Position

As mentioned in sec. 3.2.1, the optimization of a DR implies the alignment of the system perpendicular to the magnetic field $\mathbf{B}$. To reduce the technical difficulties connected to the three-dimensionality of the stellarator TJ-II, a toroidal position was chosen where the vertical component of the magnetic field B_z vanishes while maintaining the position of the DR on the axis of symmetry of the plasma. Therefore, for each toroidal angle, the vertical magnetic field component on the axis of symmetry at normalized flux radius $\rho = 0.8$ was calculated, in mathematical form (note that ρ is the normalized flux radius, not the radius in a toroidal coordinate system)

$$B_z(\rho = 0.8, \varphi, \theta = -4\varphi) < 10^{-3}\ \mathrm{T}. \tag{5.1}$$

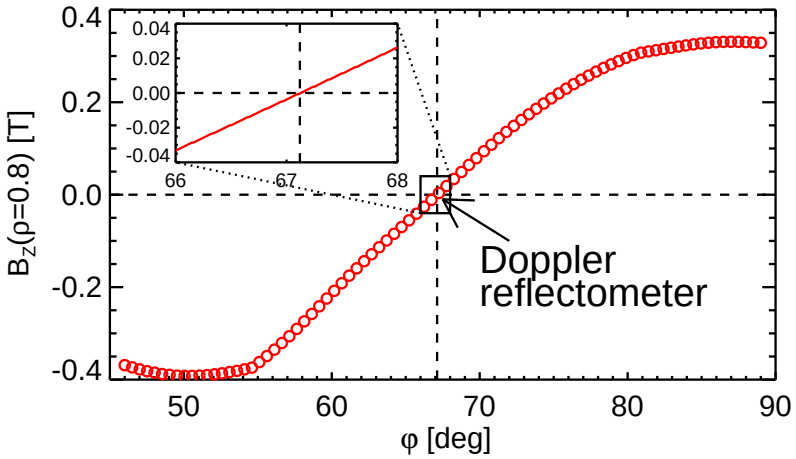

Figure 5.1: Toroidal dependence of $B_z(\rho = 0.8, \varphi, \theta = -4\varphi)$. The inset shows a zoom to the region where $B_z \approx 0$. For details refer to the text.

Fig. 5.1 shows $B_z(\rho = 0.8, \varphi, \theta = -4\varphi)$ for toroidal angles $\varphi = 45° - 90°$. The values of B_z range from -0.4 T at $\varphi \approx 50°$ to 0.35 T at $\varphi \approx 87°$. In the intermediate range of $\varphi = 65° - 70°$, the plasma reaches its maximum vertical position at poloidal angle $\theta \approx 90°$. The inset of fig. 5.1 shows a zoom to the region where $B_z \approx 0$. At toroidal angle $\varphi = 67.1°$ condition (5.1) is fulfilled.

The sector corresponding to $\varphi = 67.1°$ is sector 6. It was decided to install the Doppler reflectometer in sector C6 (and not A6, B6 or D6) due to two reasons: first, sector C is less affected by direct contact with the two NBI injectors, which inject towards sectors B and A, and second, port C6TOP and C6SIDE were vacant at the time of the design, which facilitated substantially the technical design and the installation of the system, explained in detail in sec. 5.6.

In fig. 5.2(a) a top view of sector C of TJ-II is schematically shown. The DR port C6 is indicated by the arrow. In fig. 5.2(b) sector C is plotted showing the outlines of the vacuum vessel (gray) and the circular coil (blue). The poloidal plane for $\varphi = 67.1°$ does not go through the center of port C6, which results in a slight displacement of the DR w.r.t. the port center. In (c), a zoom to the red indicated area from (b) is presented. The magnetic field pitch angle, defined

$$\gamma_p = \tan^{-1}(B_\theta / B_\varphi), \tag{5.2}$$

where B_θ and B_φ are the poloidal and toroidal magnetic field components, respectively, at the design position of the DR is $\gamma_p = 26°$. This angle defines the measurement plane of the DR in TJ-II, which is perpendicular to the magnetic field, indicated by the green line in fig. 5.2(c). To be able to measure in pure X-mode, minimize the Faraday effect and to avoid sensitivity to parallel wave numbers $k_\parallel$, the system has to be aligned accordingly.

Furthermore, in fig. 5.2(c) a new coordinate perpendicular to the magnetic field is introduced, $R_\perp$, which defines the distance of any point in the perpendicular plane to the point where the plane crosses the y-axis, $R_\perp(x = 0) = 0$. Apart from that, a parallel plane (brown line) is defined, which is parallel to the magnetic field in the

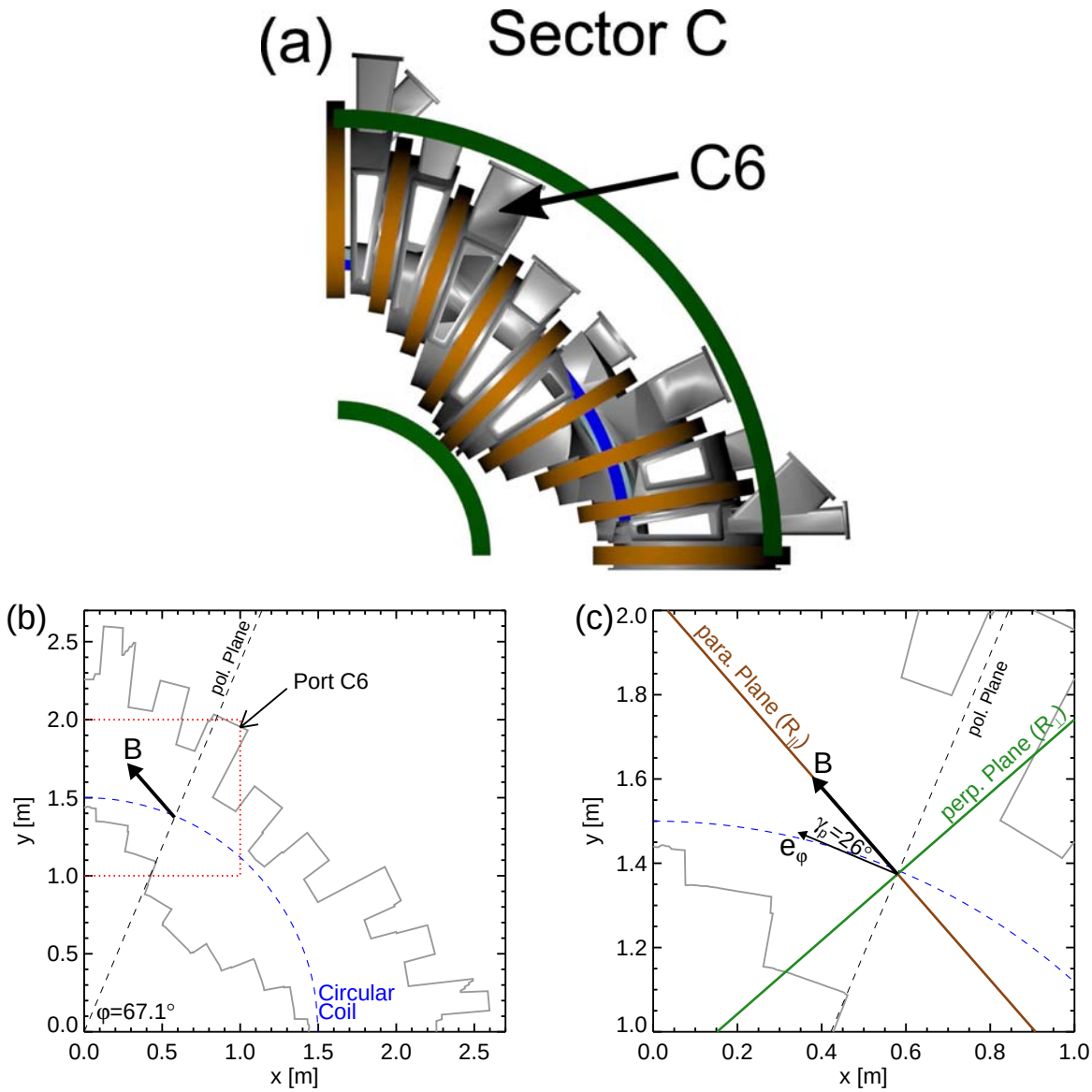

Figure 5.2: (a) Top-down schematic view of sector C of TJ-II with vacuum vessel (gray) and circular coil (blue). The location of ports C6, where the DR is installed, is indicated by the arrow. (b) Plot of the geometry, indicating the magnetic field at the DR measurement position. (c) Zoom to the red indicated region from (b).

point $(\rho = 0.8, \varphi = 67.1°, \theta = -4\varphi)$. Following the definition of the $R_\perp$-coordinate, a coordinate $R_\parallel$ parallel to the magnetic field is defined, with $R_\parallel(x = 0) = 0$.

5.1.3 Flux Surfaces Perpendicular to B

Fig. 5.3(a) shows the poloidal flux surfaces (gray) for the standard configuration at $\varphi = 67.1°$. The axis of symmetry of the plasma (cf sec. 5.1.2) is indicated in green and crosses the helical coil (circle). The design position $\mathbf{x}_{\mathrm{Des}} = (\rho = 0.8, \varphi = 67.1°, \theta =$

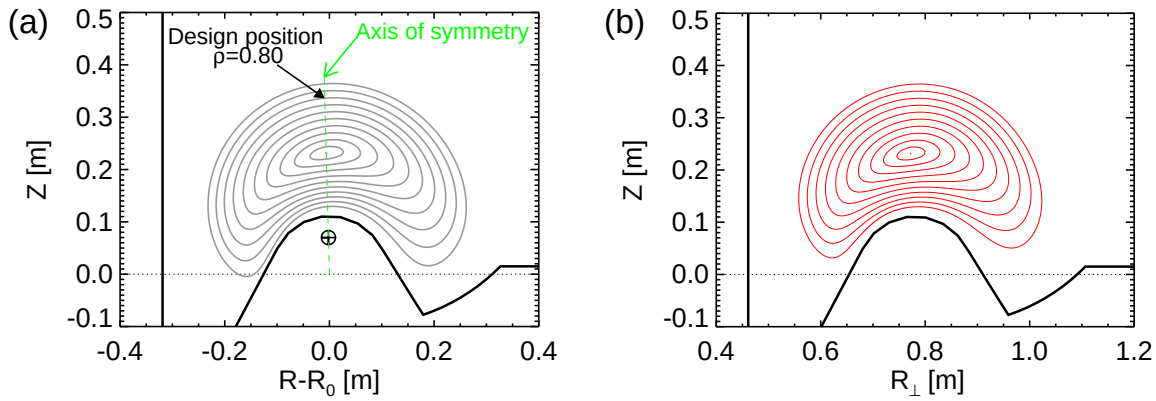

Figure 5.3: (a) Poloidal flux surfaces at $\varphi = 67.1°$ (gray) and vessel wall (black). The axis of symmetry of the plasma and the design position for the DR are indicated. (b) Flux surfaces in the (perpendicular) measurement plane of the DR. For details refer to the text.

91.6°) is the starting point for the calculation of the perpendicular flux surfaces. Therefore, at $\mathbf{x}_{\mathrm{Des}}$ the direction of the magnetic field $\mathbf{B}$ is calculated. The plane which is perpendicular to the magnetic field (cf fig. 5.2(c)) at $\mathbf{x}_{\mathrm{Des}}$ defines a vertical slice (because $B_z = 0$) through the flux surfaces. The result is depicted in fig. 5.3(b). Note the abscissa is labeled $R_\perp$, the perpendicular coordinate defined in sec. 5.1.2.

A visual comparison between poloidal (gray) and perpendicular (red) flux surfaces is depicted in fig. 5.4. Note the perpendicular flux surfaces have been shifted so that the plasma centers overlap. The plot reveals pronounced geometrical differences, but also similarities in the flux surfaces. The closer to $R = 0$, the more similar are the flux surfaces. However, at $R \approx \pm 0.2$ m, perpendicular and poloidal flux surfaces deviate substantially. In the lower horns, the poloidal flux surfaces reach further down than

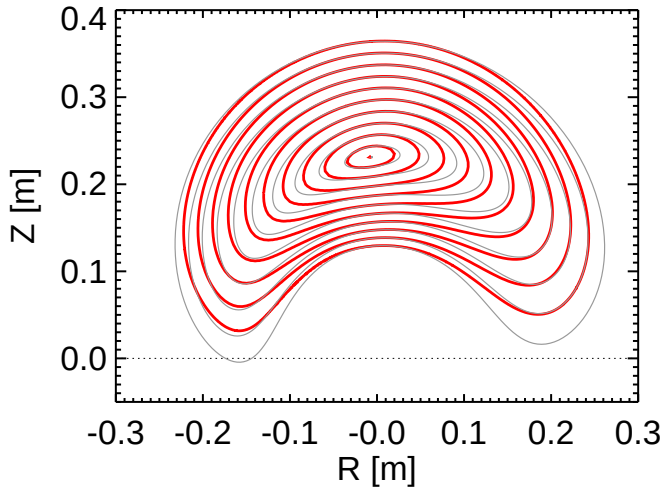

Figure 5.4: Comparison of poloidal flux surfaces at $\varphi = 67.1°$ (gray) and perpendicular flux surfaces (red). The perpendicular cross section of the plasma is smaller than the poloidal cross section.

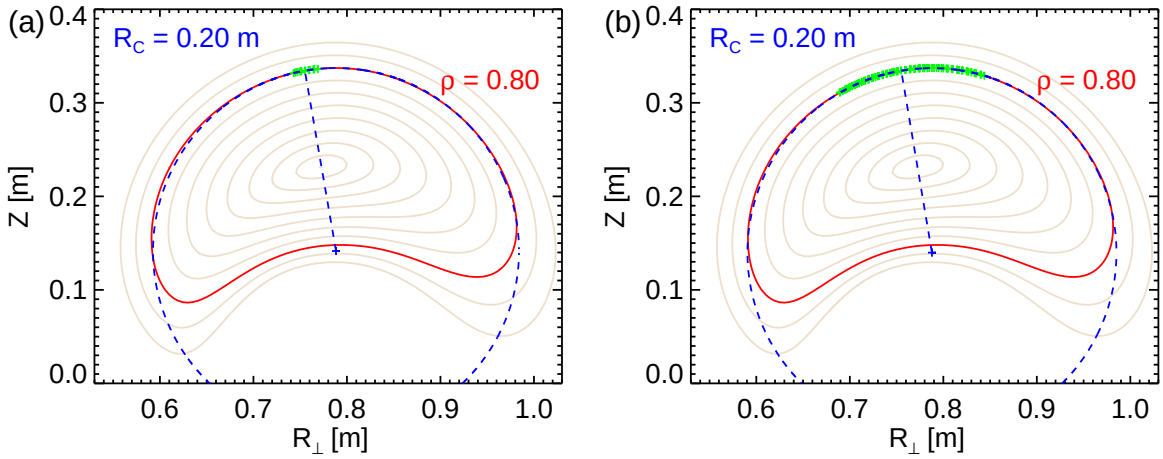

Figure 5.5: Radius of curvature fit (blue) to the perpendicular flux surface $\rho = 0.8$ (red) for (a) a beam-size comparable section of the flux surface (green) and (b) a larger section (green).

the perpendicular ones. At this toroidal position, the perpendicular cross section is smaller than the poloidal cross section, which affects the radius of curvature R_C of the perpendicular flux surfaces, important for the calculation of the spectral resolution of the system in sec. 5.1.5.

5.1.4 Plasma Curvature Radius

The perpendicular flux surfaces from fig. 5.3(b) can be taken to be the cutoff surfaces for the DR, because the magnetic field in the measurement region (edge plasma) is almost constant, so that the radial position of backscattering will depend mainly on the electron density. Since the equilibrium plasma density is constant on the flux surfaces, the latter will be used to calculate R_C of the plasma using the Levenberg-Marquardt method to fit

$$z = \sqrt{R_C^2 - (R_\perp - R_{\perp,0})^2} + z_0 \tag{5.3}$$

to a section comparable to the beam size at the design flux surface ($\rho = 0.8$). Here, R_C, $R_{\perp,0}$ and z_0 are free parameters which define the center $(R_{\perp,0}, z_0)$ and the radius (R_C) of the circle.

Fig. 5.5 shows the result of the fitting of (5.3) to the perpendicular flux surface at $\rho = 0.8$. In (a), the size of the section to be fitted is of a few cm and in (b) a larger part of the flux surface is used for fitting. A curvature radius $R_C = 0.20$ m is obtained independently of the size of the fitting region, reflecting the part of the flux surface under consideration is almost circular. Furthermore, the line connecting the design position at $\rho = 0.8$ and the circle center crosses the plasma center, underlining the near symmetry at the design position.

The information obtained in this section is indispensable to calculate the spectral resolution using (3.6), explained in detail in the next section.

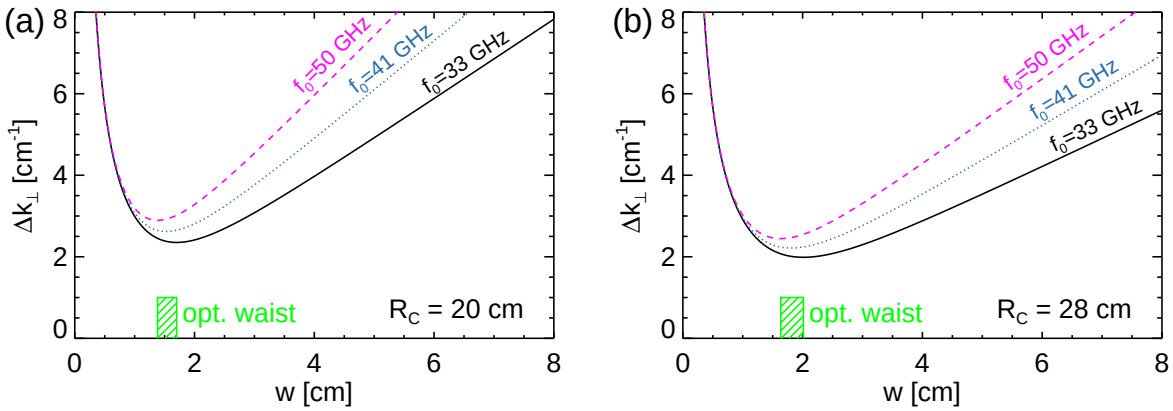

Figure 5.6: Spectral resolution for different frequencies (33, 41, 50 GHz) obtained when using the radius of curvature through (a) perpendicular (R_C = 20 cm) and (b) poloidal (R_C = 28 cm) flux surfaces. The optimum beam waist range for all frequencies is indicated in green.

5.1.5 Spectral Resolution of the System

As shown in sec. 3.2.2, the spectral resolution $\Delta k_\perp$ of a Doppler reflectometer depends on the size of the microwave beam in the plasma w, the wavenumber of the microwave in vacuum k_0 and the effective radius of curvature ρ_{eff} which includes the radii of curvature of the plasma R_C and of the microwave beam R_B. Since the TJ-II plasma curvature is very pronounced, it was decided to design a system with plane beam wavefronts in the plasma ($R_B \to \infty$). In consequence, the effective radius of curvature within the microwave spot ρ_{eff} (cf (3.7)) converges to the plasma curvature radius, $\rho_{\text{eff}} \to R_C$.

Fig. 5.6 plots the spectral resolution against the beam waist in the plasma for different frequencies (33, 41, 50 GHz) and for the perpendicular flux surfaces with (a) $R_C = 20$ cm and the poloidal flux surfaces with (b) $R_C = 28$ cm. In (a), the minimum is located at $w \approx 1.70$ cm for $f_0 = 33$ GHz, and goes towards smaller beam waists for higher frequencies ($w \approx 1.53$ cm for $f_0 = 41$ GHz, $w \approx 1.38$ cm for $f_0 = 50$ GHz). This result is important, because it shows that for the given experimental conditions, the best spectral resolution is obtained with plane beam wavefronts in the plasma and decreasing waists for increasing microwave frequencies. This has immediate impact on the design of antenna and mirror, presented in secs. 5.3 and 5.4, respectively. The optimum beam waists in (b) are slightly larger than the ones in (a), because the plasma curvature is less pronounced when using the poloidal flux surfaces. Since the system design was made following fig. 5.6(b), the beam waists in the plasma are larger than the optimum ones obtained from the perpendicular flux surface calculation (a). Nevertheless, the difference in $\Delta k_\perp$ is only 2.8%. This error is small and comparable to standard error sources, i.e. uncertainties in antenna and mirror fabrication, positioning and alignment of the system.

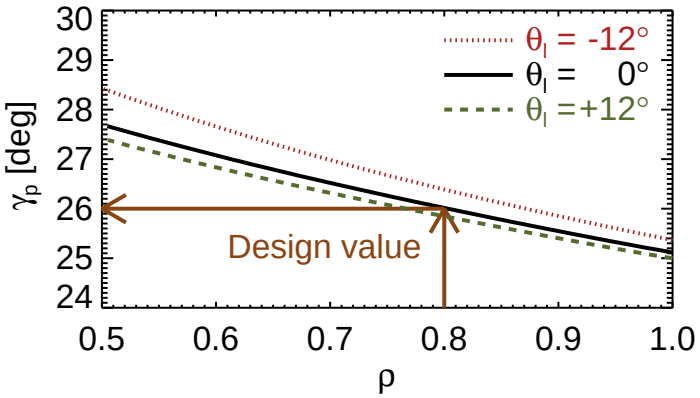

Figure 5.7: Magnetic field pitch angle variation in the radial measurement range of the TJ-II DR for $\theta_l = 0°$ and $\pm 12°$.

5.1.6 Magnetic Field Pitch Angle

Fig. 5.7 shows the radial variation of the magnetic field pitch angle γ_p for three beam tilt angles, one in perpendicular incidence (solid line) and two others with $\pm 12°$ ($+$: dashed line, $-$: dotted line) w.r.t. the perpendicular beam in the radial measurement range of the DR. Straight lines starting from the mirror center are used for the calculation, no beam refraction is taken into account. γ_p varies about 3° from $\rho = 0.5$ to $\rho = 1.0$. This variation is comparable to the variation of the magnetic field direction w.r.t. the measurement plane, which implies that the $k_{\|}$-sensitivity is low in the whole radial measurement range.

5.1.7 Flux Compression / Expansion

Fig. 5.8(a) illustrates that the distance dr between two flux surfaces can vary poloidally. Three representative measurement positions are indicated. In the lower left, the distance dr^{exp} between the two flux surfaces is large, leading to flux expansion. Moving along the flux surfaces in counterclockwise direction, a region close to the central conductor with flux compression (dr^{comp}) is indicated. In the upper part, at the DR measurement position, the distance between flux surfaces is dr^{meas}. Obviously,

$$\mathrm{d}r^{\mathrm{exp}} > \mathrm{d}r^{\mathrm{meas}} > \mathrm{d}r^{\mathrm{comp}}. \tag{5.4}$$

If the plasma moves along the flux surface, its velocity $u_\perp$ will vary depending on the space between flux surfaces. A comparable situation is water passing through a pipe, where the flow velocity is inversely proportional to the square of the pipe radius. Due to the effect of flux compression or expansion, the plasma velocity on a flux surface ($\Psi = \mathrm{const.}$, Ψ normalized magnetic flux) is not constant, but changes depending on the value of $\nabla\Psi$. In the plasma, the stronger $\nabla\Psi$, the closer to each other are the flux surfaces.

Since Doppler reflectometry provides a local measurement of $u_\perp$, in order to compare with other measurements, it is necessary to convert the local measurement to a flux

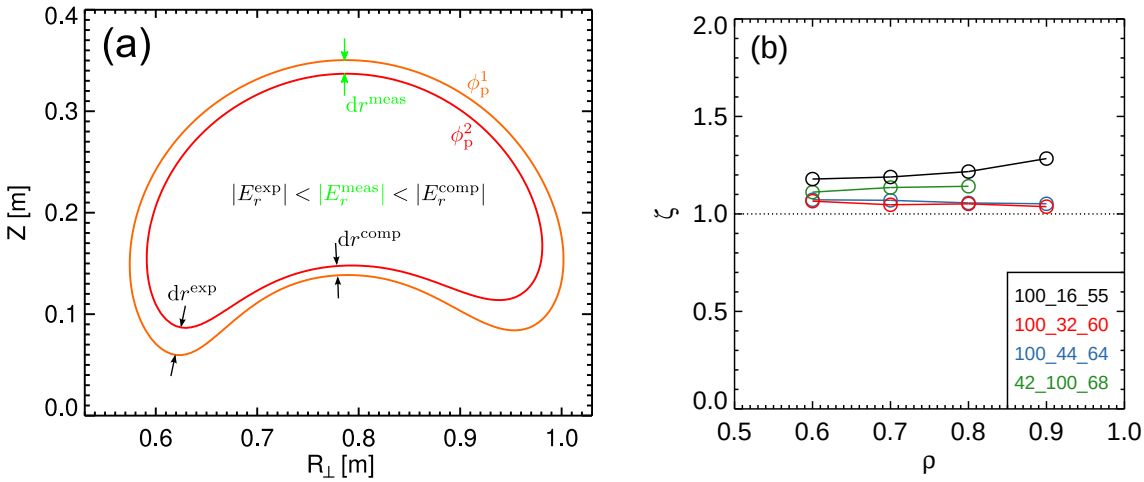

Figure 5.8: (a) Two perpendicular flux surfaces of TJ-II illustrating that the E_r measurement is a local measurement. (b) Radial evolution of the flux compression factor ζ in the DR measurement region calculated for different vacuum magnetic configurations of TJ-II.

surface averaged value. Therefore, the magnitude

$$\zeta = \frac{|\nabla\Psi|}{\langle|\nabla\Psi|\rangle} \tag{5.5}$$

is defined, where $\langle\cdot\rangle$ is the flux surface average. Hence $\zeta > 1$ for flux compression and $\zeta < 1$ for flux expansion. The flux surface averaged perpendicular velocity can then be written

$$\langle u_\perp\rangle = 1/\zeta \cdot u_\perp. \tag{5.6}$$

Note that the correction factor is not squared as in the water pipe example. That is because the above example is calculated for a circular pipe cross-section, which is not the case in the plasma.

The radial ζ profile for different magnetic configurations is depicted in fig. 5.8(b). For all configurations, ζ is close to unity and its radial variation is small. Therefore, in the flux surface averaged measurements throughout this thesis, a value $\zeta = 1.05$ will be used.

Since the plasma potential ϕ_p is assumed constant on a flux surface, the radial electric field measurement depends on the poloidal measurement position. With the above example

$$E_r^{exp} < E_r^{meas} < E_r^{comp}, \tag{5.7}$$

i.e. an E_r measurement depends on its measurement position, and will be largest in zones of flux compression and smallest in zones of flux expansion.

5.1.8 Summary

The above section illustrates the process of theoretical Doppler reflectometer design. A toroidal position for the DR has been found and the optimum beam size at the

cutoff layer has been calculated. Furthermore, the decision has been taken to employ plane wavefronts in the plasma. With those criteria, the theoretical requirements for the TJ-II DR have been established, leading to a feasible hardware design, explained in the following sections.

5.2 General Hardware Considerations

With the information obtained through the theoretical considerations (sec. 5.1) the hardware components to be used in the emitting/receiving part of the Doppler reflectometer can be designed. The main requirements are summarized:

Available space
The toroidal position encountered in sec. 5.1.2 in combination with the complex three-dimensional structure of the magnetic field dictates the alignment of the Doppler reflectometer. The use of top and lateral port is necessary, and due to the port shapes and sizes, the final sizes of mirror and antenna are restricted.

Gaussian beam
There are several types of antennas that provide Gaussian beams, among which are the Gaussian Optics Lens Antennas (GOLA), corrugated horns and specifically designed antennas. GOLAs and corrugated horns are large (up to 1 m for the requirements of the diagnostic). Apart from that, GOLAs are inadequate for vacuum operation. So the choice was made to have an antenna specifically designed for the present requirements.

Beam waist in plasma
The requirement to position the beam waist in the plasma causes the necessity to employ a focusing mirror.

Steerable mirror
To change the turbulence scale measured, the mirror has to be steerable. This complicates the design of the supporting structure and special care has to be taken with the space restrictions due to the operational space.

With these requirements it is clear that the design of the system has to be done carefully both from a physics and a technical point of view. The measures taken to achieve the points above are explained in the following.

5.3 Choked-corrugated Antenna

The antenna of a Doppler reflectometer is one of the crucial parts of the system. Depending on the requirements imposed by the plasma, the antenna has to fulfill a range of demands to obtain the optimum microwave beam. In the following, the requirements, hardware details and beam properties are summarized.

5.3.1 Requirements

As mentioned in sec. 5.1.1, for the TJ-II Doppler reflectometer frequencies ranging from $f_0 = 33 - 50$ GHz are used. From the theory of Gaussian beam propagation (see Ref. [98] and Appendix A), the radius of curvature of the beam can be written

$$R = z + z_c^2/z, \tag{5.8}$$

where z is the coordinate along beam propagation and z_c the confocal distance

$$z_c = \frac{\pi w_0^2}{\lambda_0}. \tag{5.9}$$

These equations show that the frequency of the microwave beam enters into R through the confocal distance. In sec. 5.4 it will be shown that the curvature of an ellipsoidal mirror depends on the radius of curvature of the incoming Gaussian beam R_1. To simplify the design of a mirror suited for the whole frequency range, it is thus important that the antenna produces a Gaussian beam whose waist follows the relation $w_0 \propto \sqrt{\lambda_0}$, resulting in a frequency-independent confocal distance. Hence R_1 will depend only on the distance from antenna to mirror.

Apart form that, the requirements from sec. 5.2 can only be met by certain types of antennas, of which the standard and commercially available ones are either too large for the space requirements of TJ-II (corrugated antennas) or inadequate for vacuum operation (GOLAs). Nevertheless, a patented design of small choked-corrugated horns exists, combining parallel and perpendicular ridges and developed by the Antenna Group of the University of Navarra, Spain. These antennas provide high-quality Gaussian beams [99, 100] and do not employ any vacuum-susceptible parts.

5.3.2 Hardware Details

A sketch of the choked-corrugated antenna specifically designed for the TJ-II Doppler reflectometer is depicted in fig. 5.9. The total length and diameter are 10.4 and 7.8 cm, respectively, values that comply the space requirements imposed by the TJ-II vacuum vessel. The choked part (parallel ridges w.r.t. the beam axis) is located approximately between $l = 1$ and $l = 2$ cm, where l is the coordinate along beam propagation. The rest of the antenna (up to $l = 10.4$ cm) consists of perpendicular ridges. The height of the parallel corrugations is 0.7 mm, with material of 0.3 mm in between and the width of the perpendicular corrugations and the intermediate material is 1.6 and 0.5 mm, respectively. The fabrication process of these small-size ridges is demanding and each part (choked and corrugated) has to be manufactured separately.

The photographs in fig. 5.10 show the choked-corrugated antenna demounted (a) and mounted (b). In (a) the corrugations of both parts can be seen. The choked part is attached to the corrugated part, resulting in the antenna shape in (b).

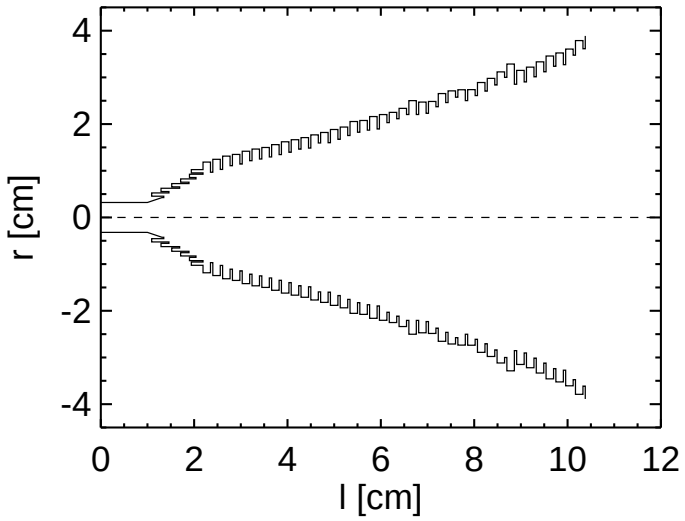

Figure 5.9: Sketch of the choked-corrugated antenna. Length and diameter are 10.4 and 7.8 cm, respectively. Parallel (between $l = 1$ and 2 cm) and perpendicular (up to $l = 10.4$ cm) ridges are visible.

5.3.3 Beam Properties

The beam properties of the antenna are important to obtain reliable results in Doppler reflectometry [101]. Unfortunately, due to time restrictions, it was not possible to measure the antenna characteristics in the laboratory. For this reason the beam properties shown in this section are the results of numerical simulations provided by the developers.

Fig. 5.11(a) shows the simulated far field radiation pattern of the choked-corrugated antenna for $f_0 = 37$ GHz. The design gaussian is shown in light blue. The different co-polarization patterns (0° (black), 45° (green), 90° (brown)) coincide well with the desired power distribution. The different angles are measured w.r.t. the polarization direction of the microwave beam in the antenna, illustrated in fig. 5.11(b). The polar-

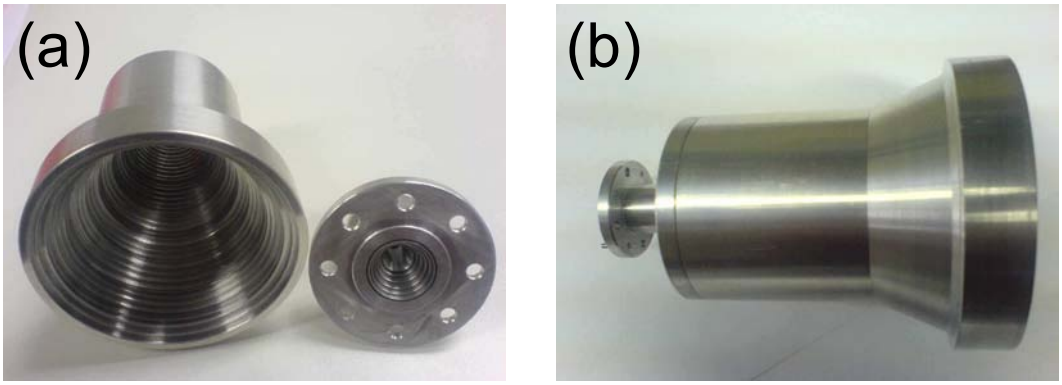

Figure 5.10: Photograph of the choked-corrugated antenna installed as part of the TJ-II Doppler reflectometer. (a) Choked and corrugated parts are fabricated separately. (b) Final assembly.

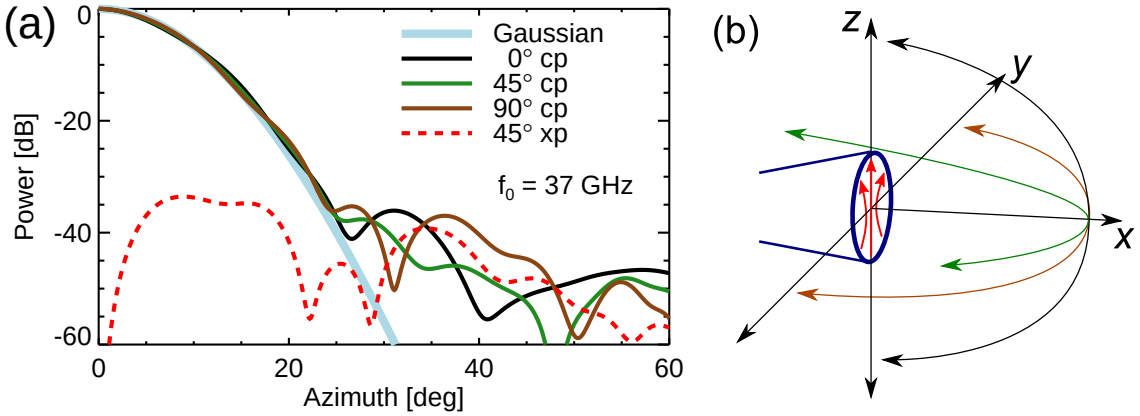

Figure 5.11: (a) Antenna far field radiation pattern for $f_0 = 37$ GHz with design Gaussian beam profile in light blue. All co-polarization simulations follow the Gaussian well, with side lobes below -30 dB. The cross-polarized radiation is below -30 dB as well. (b) Schematic drawing illustrating the different co-polarization curves in (a). For details refer to the text.

ization direction in the antenna mouth is the z-direction. To measure the co-polarized power distribution, another antenna which measures only the desired polarization scans the azimuth moving in different directions: parallel (black), perpendicular (brown) and at 45° degrees (green) w.r.t. to the radiation polarization in the antenna mouth. Since the polarization has non-parallel components away from the center ($y = 0$), the power pattern will be different when scanning in different directions. This is illustrated in fig. 5.11(a). The different co-polarization curves do not coincide perfectly. Nevertheless, the differences are marginal and well below -30 dB. The cross-polarization, measured similar as above, but with an antenna measuring only the non-desired polarized radiation, is also below -30 dB.

Further frequency-dependent characteristics of the antenna are plotted in fig. 5.12. Note that the frequency range of the Doppler reflectometer is 33 – 50 GHz, therefore the regions indicated by the line pattern are not used in operation. In (a), the simulated frequency dependence of the maximum crosspolar power (e.g. maximum of red line in fig. 5.11(a)) is less than -30 dB in the whole frequency range, except for a narrow region around 44.5 GHz.

Another design criterion for the antenna was a beam waist of $w_0 = 1.7\lambda_0$ for $f_0 = 41$ GHz. This results in $w_0(41\text{ GHz}) = 1.24$ cm, which gives the proportionality factor for the beam waist

$$w_0 = 0.1454\sqrt{\lambda_0}, \qquad w_0, \lambda_0 \text{ in m.} \tag{5.10}$$

Fig. 5.12(b) shows the beam waist against the frequency, with the design beam waist indicated by the dashed straight lines. The agreement with the $\sqrt{\lambda_0}$-curve (dashed curve) is not perfect, but the general trend is followed. In particular the frequencies between 44 and 50 GHz show good agreement with the theoretical curve.

The *directivity* D of an antenna (sometimes called *peak directivity*) is a measure of how directional an antenna pattern is, and relates the emitted power density in the desired direction to the emitted power density by an ideal isotropic radiator antenna

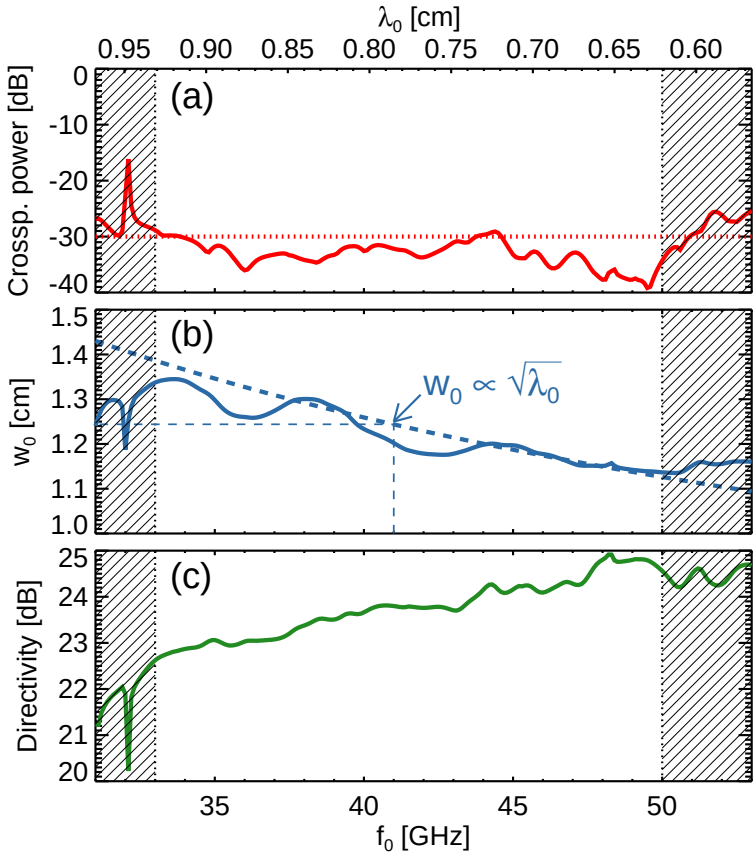

Figure 5.12: Frequency-dependent beam characteristics of the choked-corrugated antenna. The regions marked by the line pattern are out of the frequency range of the microwave electronics (Q-band). (a) The cross-polarization is below -30 dB in almost the whole frequency range. (b) Frequency dependence of the beam waist w_0 with design case (dashed line). (c) The variation in antenna directivity is below 2.5 dB in the whole frequency range.

radiating the same amount of total power. Hence, an antenna emitting the same amount of power in all directions would have $D = 0$ dB. Fig. 5.12(c) shows D of the choked-corrugated antenna, which is between 22.5 and 25.0 dB in the whole Q-band range. Note the small variation of D across the whole frequency band ($\sim$ 2.5 dB), which is of particular importance in the system power calibration in sec. 8.1.

5.4 Ellipsoidal Mirror

To be able to focus the beam to the cutoff layer in order to optimize the spectral resolution of the Doppler reflectometer (sec. 5.1.5), an ellipsoidal mirror was designed. The calculation of the mirror surface, hardware and calibration details are explained in the following.

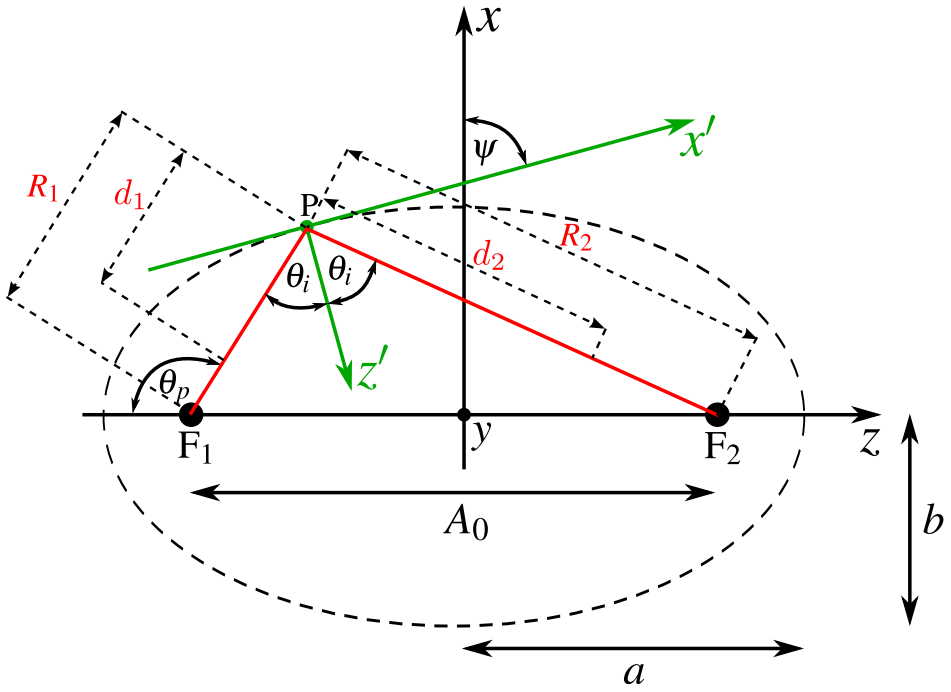

Figure 5.13: Geometry used for the calculation of the ellipsoidal mirror surface. The coordinate system $\{x'y'z'\}$ is rotated by ψ w.r.t. the coordinate system $\{xyz\}$.

5.4.1 Surface Calculation

The design of the ellipsoidal mirror follows mainly the descriptions in [98, 102]. The necessary theoretical background on gaussian beam propagation is given in appendix A. In fig. 5.13 the geometry and the system of coordinates (Cartesian, $\{xyz\}$) used for the derivation of the formulas for the ellipsoidal mirror are shown. y points into the direction of the reader, the ellipsoid is rotationally symmetric about the z-axis. a and b are the major and minor radii, respectively, which define the shape of the ellipse by

$$\frac{x^2+y^2}{b^2}+\frac{z^2}{a^2}=1. \tag{5.11}$$

The eccentricity is defined

$$\epsilon=\sqrt{1-\frac{b^2}{a^2}} \tag{5.12}$$

and ranges from 0 to 1 (supremum). It indicates how elongated the ellipse is, 0 is equivalent to a circle and the approach of 1 results in an elongated ellipse. F_1 and F_2 are the focal points. The distances R_1 and R_2 (equivalent to the radii of curvature of the microwave beam) connecting F_1 and F_2 with any point P lying on the ellipse follow the rule

$$R_1+R_2=2a. \tag{5.13}$$

An equivalent lens focal length l_f can be written as

$$\frac{1}{l_f}=\frac{1}{R_1}+\frac{1}{R_2}. \tag{5.14}$$

l_f can also be calculated (for a detailed derivation the reader is referred to [98])

$$l_f = \frac{d_1}{\eta}\left(1 - \sqrt{1 - \eta\left[1 + \left(\frac{z_c}{d_1}\right)^2\right]}\right), \tag{5.15}$$

where $\eta = 1 - (w_1/w_2)^2$, $z_c = \pi w_1^2/\lambda_0$ the confocal distance and d_1 the distance between the beam waist and the mirror. w_1 and w_2 are the beam waists at d_1 and d_2, respectively.

As seen in fig. 5.13, θ_i is the angle of incidence of the beam and θ_p describes the angle between the beam and the axis of symmetry of the ellipsoid. Using the law of cosines, the distance between the two foci A_0 can be calculated as

$$A_0 = \sqrt{R_1^2 + R_2^2 - 2R_1R_2\cos 2\theta_i}, \tag{5.16}$$

and

$$\theta_p = \pi - \cos^{-1}\left(\frac{R_1^2 + A_0^2 - R_2^2}{2R_1A_0}\right). \tag{5.17}$$

It is now convenient to define a local coordinate system $\{x'y'z'\}$ (shown in green in fig. 5.13). The axis x' is tangential to the ellipse in the point of incidence of the beam P, z' is perpendicular to the surface. It follows from geometry that

$$\psi = \theta_p - \theta_i, \tag{5.18}$$

which is the angle of rotation between the $x'z'$-plane and the xz-plane. The unprimed coordinates can now be expressed in terms of the primed ones, ψ and θ_p:

$$\begin{aligned} x &= x'\cos\psi - z'\sin\psi + R_1\sin\theta_p \\ y &= y' \\ z &= x'\sin\psi + z'\cos\psi - A_0/2 - R_1\cos\theta_p. \end{aligned} \tag{5.19}$$

Substituting these expressions into (5.11) and defining $e \equiv A_0/2$, the section of the ellipse can be calculated as

$$z' = \frac{-B - \sqrt{B^2 - 4AC}}{2A}, \tag{5.20}$$

where

$$\begin{aligned} A &= a^2\sin^2\psi + b^2\cos^2\psi, \\ B &= -2\left[a^2R_1\sin\psi\sin\theta_p + b^2\cos\psi\,(e + R_1\cos\theta_p) + e^2x'\sin\psi\cos\psi\right], \\ C &= a^2(x'\cos\psi + R_1\sin\theta_p)^2 + b^2\left[x'\sin\psi - (e + R_1\cos\theta_p)\right]^2 - a^2b^2 + a^2y'^2. \end{aligned}$$

For small surface extents and incidence angles, this expression can be written as

$$z' = \left(\frac{\cos\theta_i}{4l_f}x'^2 + \frac{1}{4l_f\cos\theta_i}y'^2\right)(1 - cx'), \tag{5.21}$$

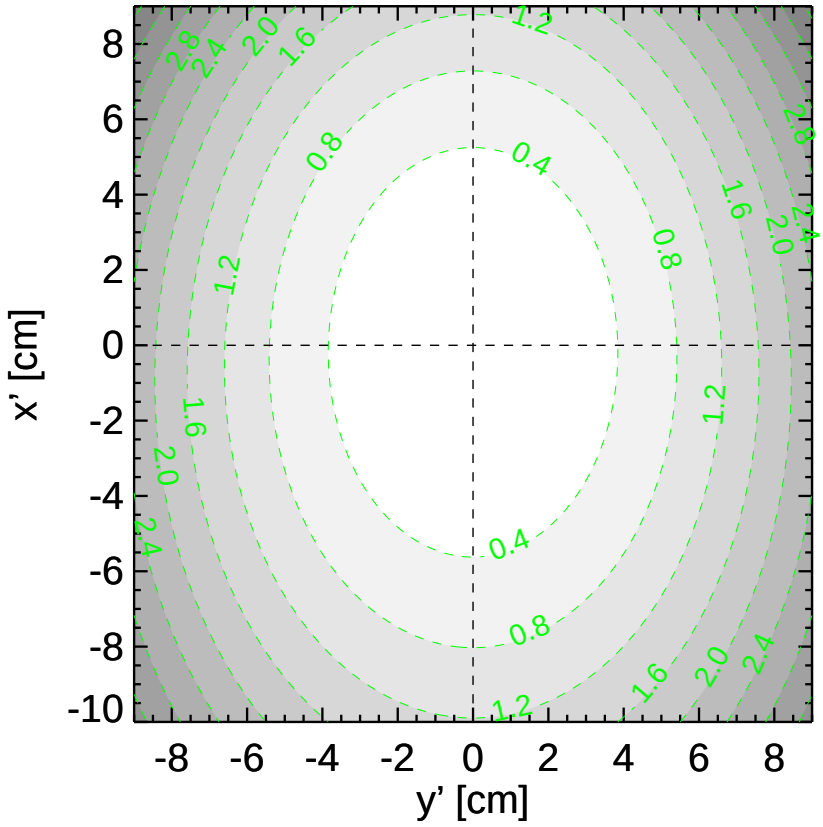

Figure 5.14: Contour plot of the ellipsoidal mirror installed as part of the Doppler reflectometer of TJ-II. The total size is 18×19 cm^2, the axis of rotation is the $x' = 0$ axis.

where

$$c = \frac{\epsilon^2 \sin^2 \psi \cos \psi}{R_1 \sin \theta_p}.$$

A typical design procedure of a mirror ($f, d_1, w_1, w_2, \theta_i$ known) goes as follows: Since the distance between antenna and mirror is known, one can calculate the radius of curvature R_1 at the mirror. (5.15) depends only on w_1, w_2 and d_1 and gives the focal length l_f. By using (5.14), the radius of curvature of the outgoing beam R_2 and thus the position of the outgoing beam waist d_2 can be calculated. The distance between foci is given in (5.16) and this yields θ_p using (5.17), which results in ψ through (5.18). All the required values are now obtained and the surface of the mirror can be calculated with (5.20) or (5.21).

The final design values used to calculate the surface of the mirror are shown in Tab. 5.1. Using these values, the final simplified equation (5.21) for the mirror reads in SI units

$$z' = \left(1.34 \cdot x'^2 + 2.68 \cdot y'^2\right)(1 - 1.25 \cdot x'). \tag{5.22}$$

However, for the final design of the mirror (5.20) was used. A contour plot of the mirror surface is shown in fig. 5.14. Due to space limitations imposed by the vacuum vessel, the final dimensions of the elliptical mirror are 18×19 cm^2. The axis of rotation

parameter	value		
microwave beam frequency	f	=	35 GHz
waist at antenna	w_1	=	1.571 λ
waist in plasma	w_2	=	3.000 λ
configuration			100_44_64
position of cutoff layer	ρ_{cutoff}	=	0.8
distance antenna $\rightarrow$ mirror	d_1	=	0.15 m
distance mirror $\rightarrow$ cutoff	d_2	=	0.20 m
incidence angle	θ_i	=	45.0°
toroidal angle	φ	=	67.1°

Table 5.1: Design parameters for the ellipsoidal mirror of the DR installed in TJ-II.

is the $x' = 0$ axis. While in the y'-direction, the mirror is symmetric, an asymmetry is found in the x'-direction. In the lower half, the 1.2 cm contour line reaches $x' \approx -10$ cm, while in the upper half, it reaches $x' \approx 9$ cm. Furthermore, the upper two corners are more elevated than the lower ones, represented by the dark contour shading.

5.4.2 Fabrication and Calibration

A schematic drawing of the mirror manipulator system is depicted in fig. 5.15. In (a) the magnetic field lies horizontal in the plane while in (b) it points into it. The (upper) non-vacuum part is separated from the (lower) vacuum part through a flange, indicated by the line-pattern area. The non-vacuum part, which is shown again as a photograph in fig. 5.16, is protected against accidental mechanical impact by an acrylic glass housing. Inside, a stepper motor ① is located on top, mounted on a fixture seen on the lhs of (a). The motor turns a leadscrew, which moves a nut ④ up and down. In the schematic fig. 5.15, the nut is shown three times corresponding to three different angular positions of the steerable mirror. Two optical barriers are installed which serve as *upper limit* (*UL*, ③) and *lower limit* (*LL*, ③) between which the nut can be moved. Another optical barrier, called *home* (*H*, ③), is used as the reference position and is situated slightly above LL. This position is particularly important, because each time *the mirror angle w.r.t. the horizontal* θ_{H} (see fig. 5.15) is intended to be reduced, the reference position is approached first and then the mirror is moved to the new value of θ_{H}. This is a precaution to avoid any hysteresis due to up/down movements of the leadscrews. Above UL and below LL are security switches ②, called *upper security* (*US*) and *lower security* (*LS*) that are activated mechanically to protect the system from moving to its mechanical limits in case of failure of the optical limits (UL/LL).

The vacuum part of the system shows the fixture which holds the mirror on the lhs of figs. 5.15(a, b). At the lower end the fixture provides a clamp that sustains the mirror rotatable on its $x' = 0$ axis (cf fig. 5.14). The mirror angle θ_{H} is controlled by a manipulator arm ⑥ connected to a vertically moving nut ⑤.

The system operation goes as follows: the movement of the step motor ① turns the leadscrews of the exterior and in-vessel parts of the system, which are connected

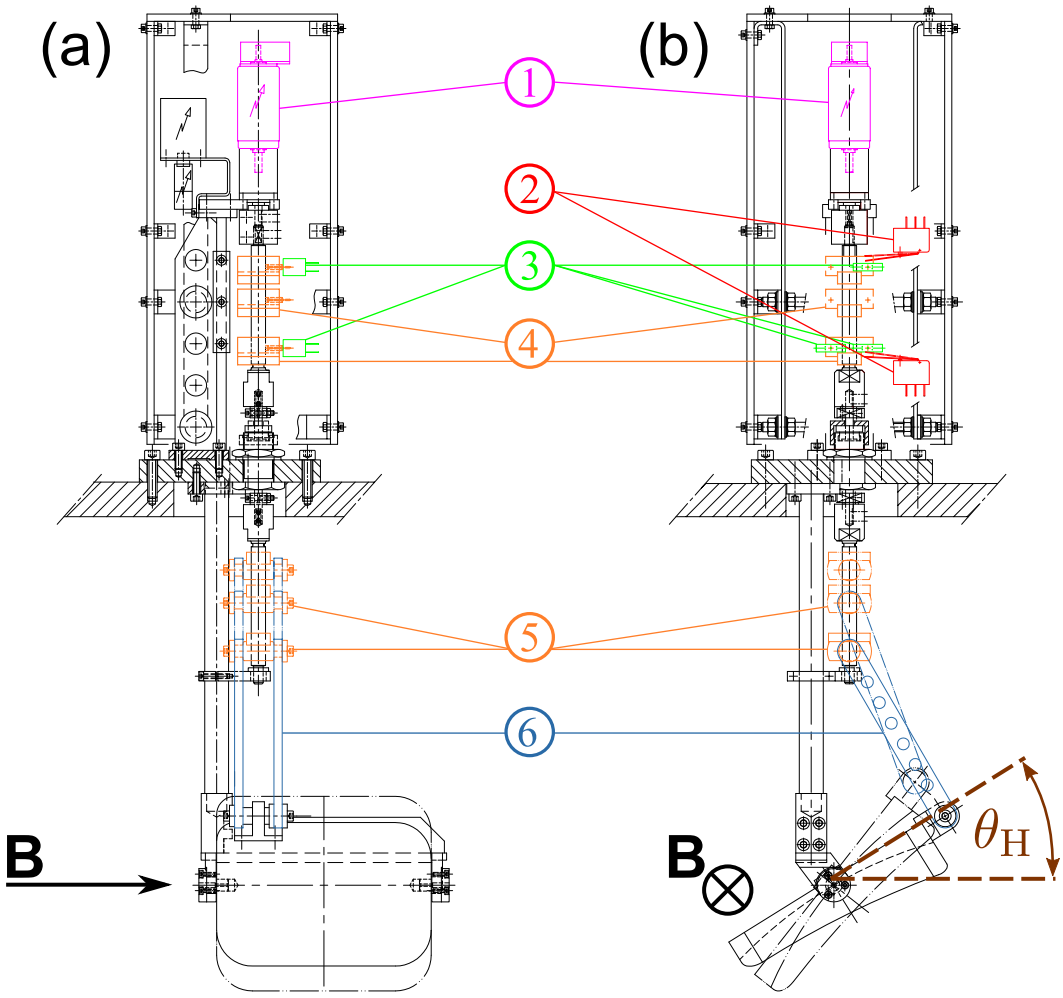

Figure 5.15: Schematic drawing of the mirror manipulator system. The control part and barriers (optical and mechanical) are above the flange (diagonal pattern), the movements are translated to the in-vessel part of the system, causing the mirror rotation w.r.t. the magnetic field direction.

mechanically. The movement of the leadscrews causes a vertical movement of the nuts ④ and ⑤. Hence each position of the exterior nut corresponds to a position of the mirror. With a calibration of the system, a relationship between motor step number and angular position of the mirror can be established.

Fig. 5.17(a) shows a photograph of the mirror and its manipulator system. Note that a 180° rotated view of fig. 5.15(a) is shown. The mirror is in the lower part of the picture with the reflecting surface on the reverse side. The pronounced surface curvature is visible at the lower rim of the mirror. The support arm is located at the extreme right of the mirror. This displacement is due to the toroidal displacement of the mirror from the center of port C6 (cf sec. 5.1.2 and fig. 5.2(b-c)). Going upwards the support arm ends in the vacuum flange. Above the flange the mirror manipulator system electronics with stepper motor and control module are visible. The vacuum part is depicted in (b). The mirror is now seen from its side with the support arm

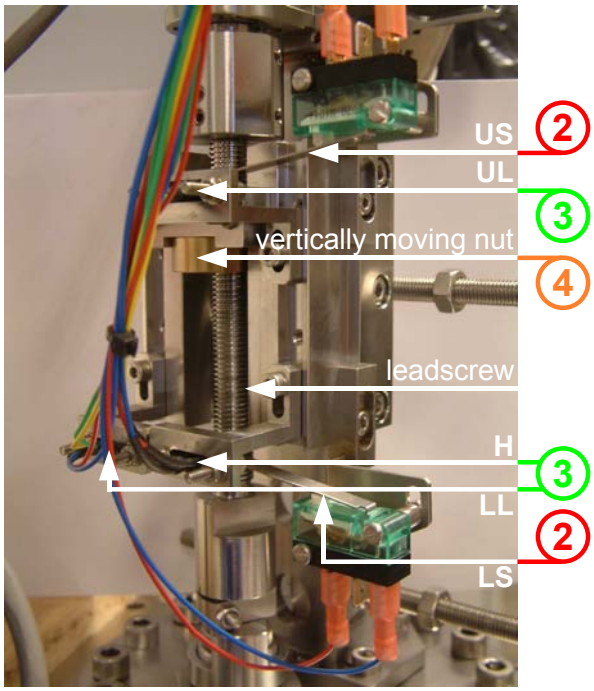

Figure 5.16: Photograph of the mirror manipulator system electronics. The nut is moved by a leadscrew between the lower and upper optical barriers to effect the poloidal movement of the mirror.

on the left. The angular movement is obtained through the manipulator arm which connects the upper part of the mirror with the nut that is moved vertically by the leadscrew. Here the mirror is seen in maintenance position, i.e. the position it has to be in to be taken out of TJ-II or to be put inside. The vertically moving nut is in an upper position and the manipulator arm is almost vertical. During operation, the nut position is lower. The typical operational range is $\theta_{\mathrm{H}} = 32^\circ - 52^\circ$.

The absolute calibration of the mirror angle w.r.t. the horizontal plane θ_{H} is depicted in fig. 5.18(a). To calibrate the mirror, the number of counts qc in the EPOS interface is gradually increased and θ_{H} is measured with a digital spirit level with a precision of $\pm 0.1^\circ$. This is done three times (black, blue and green), but due to the good reproducibility, the points lie on top of each other. The functional dependence from fig. 5.18(a) can be fitted with a fifth-grade polynomial (red curve),

$$\theta_{\mathrm{H}}(qc) = a_5(qc)^5 + a_4(qc)^4 + a_3(qc)^3 + a_2(qc)^2 + a_1(qc) + a_0, \tag{5.23}$$

yielding the coefficients denoted in tab. 5.2. Apart from the fit, in fig. 5.18(a) the operational range of the mirror during plasma operation is indicated. It ranges from $\theta_{\mathrm{H}} = 32^\circ$ to $\theta_{\mathrm{H}} = 52^\circ$. The functional dependence of θ_{H} on qc in this region is almost linear and the slope is weak compared to the higher θ_{H}-range, increasing the precision of the system in this range. The maintenance position is indicated at $\theta_{\mathrm{H}} = 73.5^\circ$ which is close to the upper limit (73.8°). The absolute deviation of the measurement points from the fit is illustrated in fig. 5.18(b), where the deviation is below 0.2° for almost the whole operational range of the system. This uncertainty in the positioning is mostly

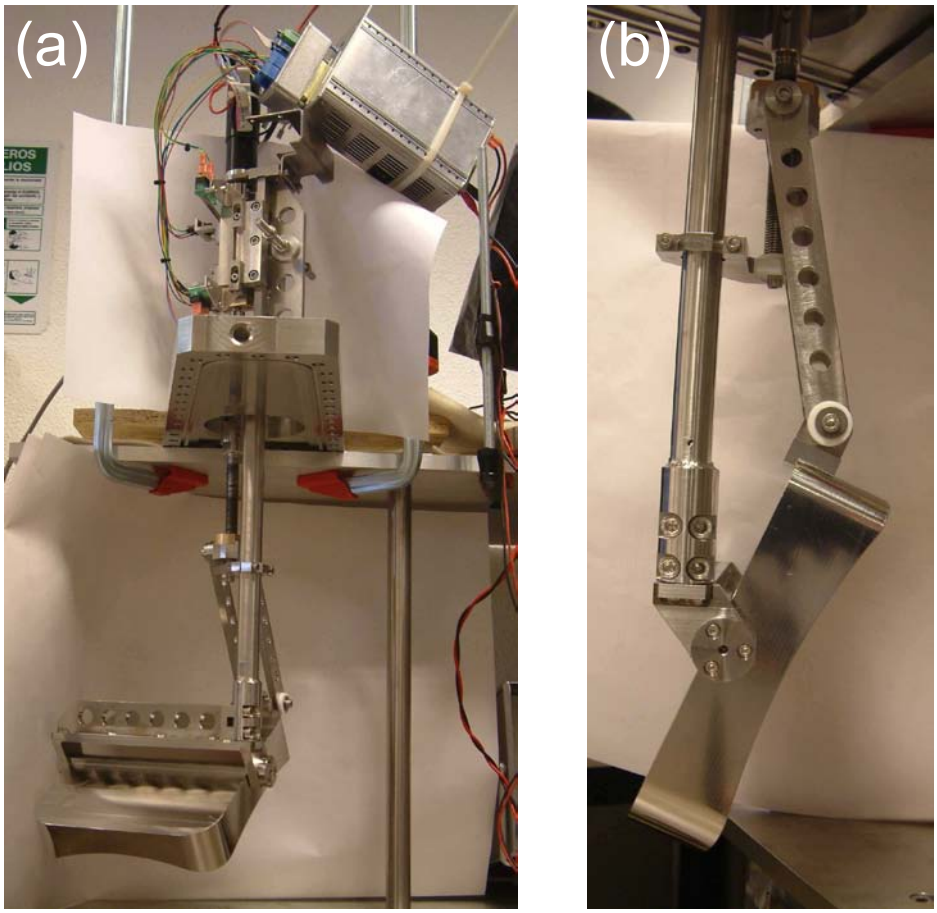

Figure 5.17: (a) Photograph of the mirror, its manipulator system and the electronics. (b) Vacuum part of the system.

due to the fact that the measurement of θ_H in the laboratory is difficult, since a spirit level has to be brought into contact with the mirror. This contact causes a small force acting on the mirror, which can be strong enough to change θ_H by a small amount. In tab. 5.3 θ_H and number of steps qc of the stepper motor of different important positions (limits, switches, home, operational range) are listed.

To move the mirror during operation of TJ-II, a LabView© interface is used which

coefficient	value
a_5	$1.425 \cdot 10^{-33}$
a_4	$-1.996 \cdot 10^{-26}$
a_3	$1.182 \cdot 10^{-19}$
a_2	$-2.239 \cdot 10^{-13}$
a_1	$4.220 \cdot 10^{-6}$
a_0	31.857

Table 5.2: Coefficients of the polynomial fit (5.23).

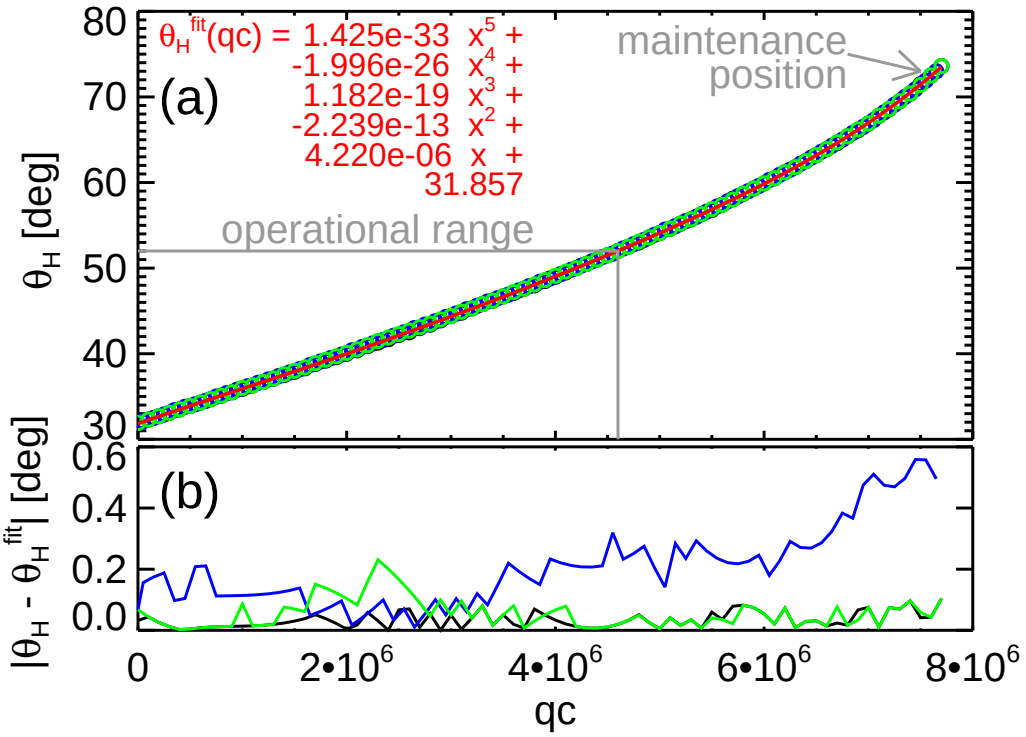

Figure 5.18: (a) Calibration of the mirror angle w.r.t. the horizontal θ_{H} and polynomial fit to the measurements (red). (b) Absolute deviation of the measurement form the fit.

uses the above calibration of the mirror. This remote operation enables changes of θ_{H} on a shot-to-shot basis, e.g. to measure perpendicular wavenumber spectra of density fluctuations (cf sec. 8).

position	θ_{H}	qc
US	75.3°	7,873,000
UL	73.8°	7,734,000
maintenance	73.5°	7,705,000
upper limit in operation	52.0°	4,593,000
lower limit in operation	32.0°	34,000
H	31.9°	0
LL	31.7°	-37,000
LS	31.5°	-84,000

Table 5.3: Important mirror positions with corresponding θ_{H} values and number of steps qc of the stepper motor.

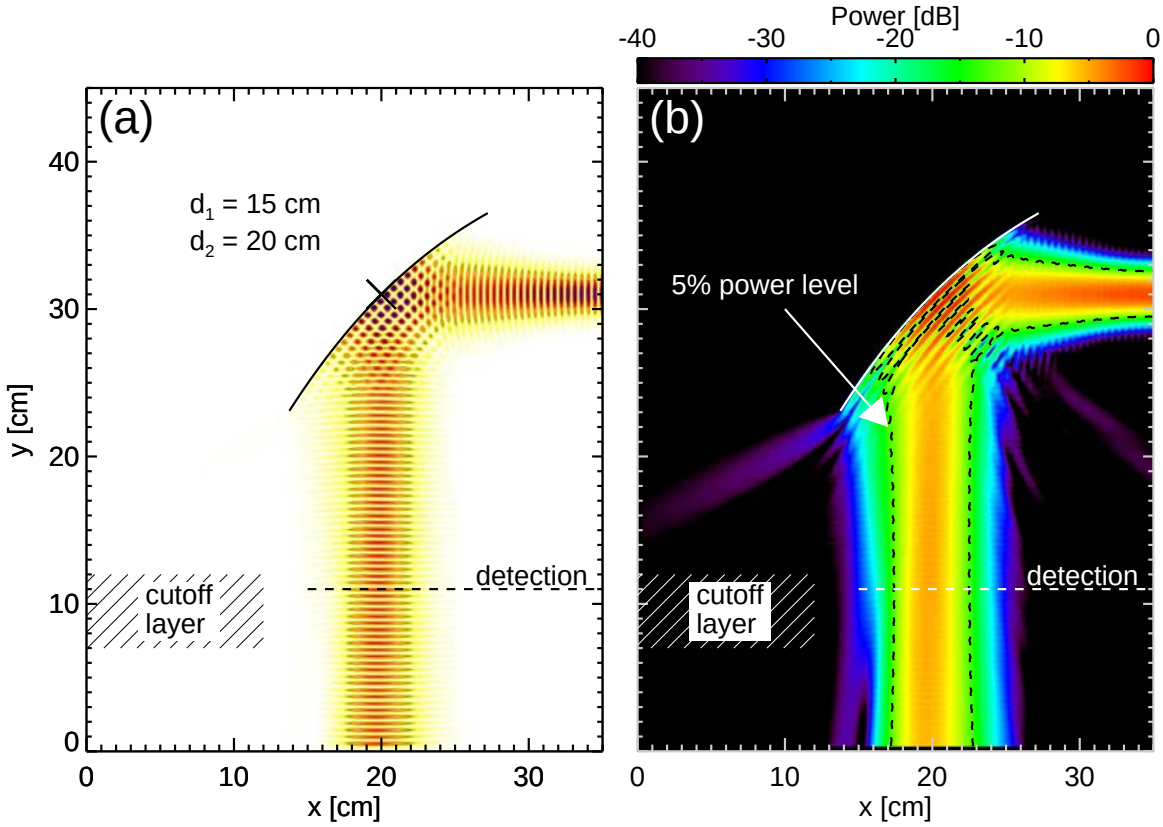

Figure 5.19: (a) Contour plot of the absolute electric field distribution of the microwave beam obtained through 2D full wave simulation. d_1 and d_2 are the distances from antenna to mirror and from mirror to detection plane, respectively. (b) Power distribution of the microwave beam. The 5% power level is indicated by the black dashed contour line. For details refer to the text.

5.5 2D Full Wave Simulation of the System

Since the DR design of secs. 5.1 and 5.2 is not trivial, it is convenient to cross-check the theoretical design of the mirror. Before its fabrication at CIEMAT workshops, simulations using the 2D full wave code by Blanco *et al.* [103] were carried out to test the focusing properties of the configuration and to analyze the beam properties in the plasma.

5.5.1 Focusing Properties

Fig. 5.19 shows the geometry used for the 2D full wave simulations. The simulated area is 35 cm in the x- and 45 cm in the y-direction. The spatial resolution in the calculation is $\Delta x = \Delta y = 3 \times 10^{-2}$ cm, corresponding to 20 points/wavelength at 50 GHz. In the upper part of the plot the mirror is indicated as a solid line, its center is at $(x, y) = (20\text{ cm}, 31\text{ cm})$. Hence the distance from the antenna to the mirror $d_1 = 15$ cm and the distance from mirror to plasma $d_2 = 20$ cm. The $f_0 = 33$ GHz Gaussian beam, corresponding to the beam emitted by the antenna ($w_{0,\,\mathrm{ant}} = 1.39$ cm), is introduced

on the rhs of the graphic. In (a), the absolute value of the electric field distribution is plotted color-coded. The beam is reflected by the mirror towards the plasma and shows convergent beam wavefronts just after being reflected. In the proximity of the plasma cutoff layer indicated by the dashed region and corresponding to $\rho = 0.60$ to 0.85, the beam wavefronts are plane, while for more interior positions ($y \to 0$ cm) the beam diverges. The dashed line at $y = 11$ cm marks the detection plane corresponding to $\rho \approx 0.80$, where the beam properties are analyzed in the following.

In fig. 5.19(b) the logarithm of the power distribution of the beam is plotted in color-scale. To guide the eye, the 5% power level is indicated by the dashed black contour lines. From antenna to mirror, the beam size w grows. As the beam is reflected, several maxima and minima, caused by constructive and destructive interference of incoming and outgoing beam, are observed. The outgoing beam size does not change as much as the incoming beam size, because the beam waist at the cutoff layer is larger than the antenna beam waist. An asymmetry can be observed on the lhs of the outgoing beam, where the power decays more rapidly than on the rhs. This is due to the lost power at the lower end of the mirror, visible in the blue and violet tail going towards the lower left. In order not to interfere with the plasma, the mirror could not be any larger than the one analyzed here. Nevertheless, the lost power is roughly three orders of magnitude less than the beam central power, hence the effect is negligible.

In fig. 5.20 the beam amplitude distribution and the wavefront phase in the detection plane are analyzed for beams with (a) $f_0 = 33$ GHz, (b) $f_0 = 41$ GHz and (c) $f_0 = 49$ GHz. Note that (a) corresponds to the simulation presented in fig. 5.19. The normalized amplitude distribution is shown in dB in the upper row and in linear scale in the middle row. The blue solid line is the desired theoretical Gaussian amplitude distribution while the red line is the simulation result. The dashed vertical lines mark the desired beam waist in the plasma and the dashed horizontal line marks the $1/e$-amplitude. The lower row shows the wavefront phase ϕ obtained through simulation. In (a) ($f_0 = 33$ GHz) the simulation amplitude distribution is close to the desired gaussian, only marginal deviations can be observed on the wings of the distribution. The beam waist obtained through the simulation is $w_0 = 2.7$ cm and compares well to the desired beam waist of $3\lambda_0 \approx 2.7$ cm. The wavefront phase is almost constant along the beam waist, so $R_\mathrm{B} \to \infty$, a criterion assumed in the calculation of the optimum beam size in sec. 5.1.5. In the $f_0 = 41$ GHz case, the amplitude distribution does not overlap with the desired one as well as in (a), but still the beam shape is close to the desired gaussian, with $w_0 = 2.4$ cm compared to a desired $w_0 = 2.2$ cm. Furthermore, the wavefront phase is constant along the beam waist. The 2π change $x = -4$ cm is a fringe jump, not a discontinuity in the wavefront phase. Fig. 5.20(c) depicts the above for $f_0 = 49$ GHz. The deviation of the obtained beam shape from the desired one is stronger in this case, the beam waist is $w_0 = 2.1$ cm, larger than the desired waist of 1.8 cm. Still the wavefront phase is constant along the extension of the beam waist.

The dependence of the optimum beam waist w_opt on the frequency (3.8) is reproduced by the antenna-mirror design of the TJ-II Doppler reflectometer. This is important in order to obtain a good spectral resolution not only for one microwave frequency, but for the whole frequency range of the system. Fig. 5.21 shows the spectral

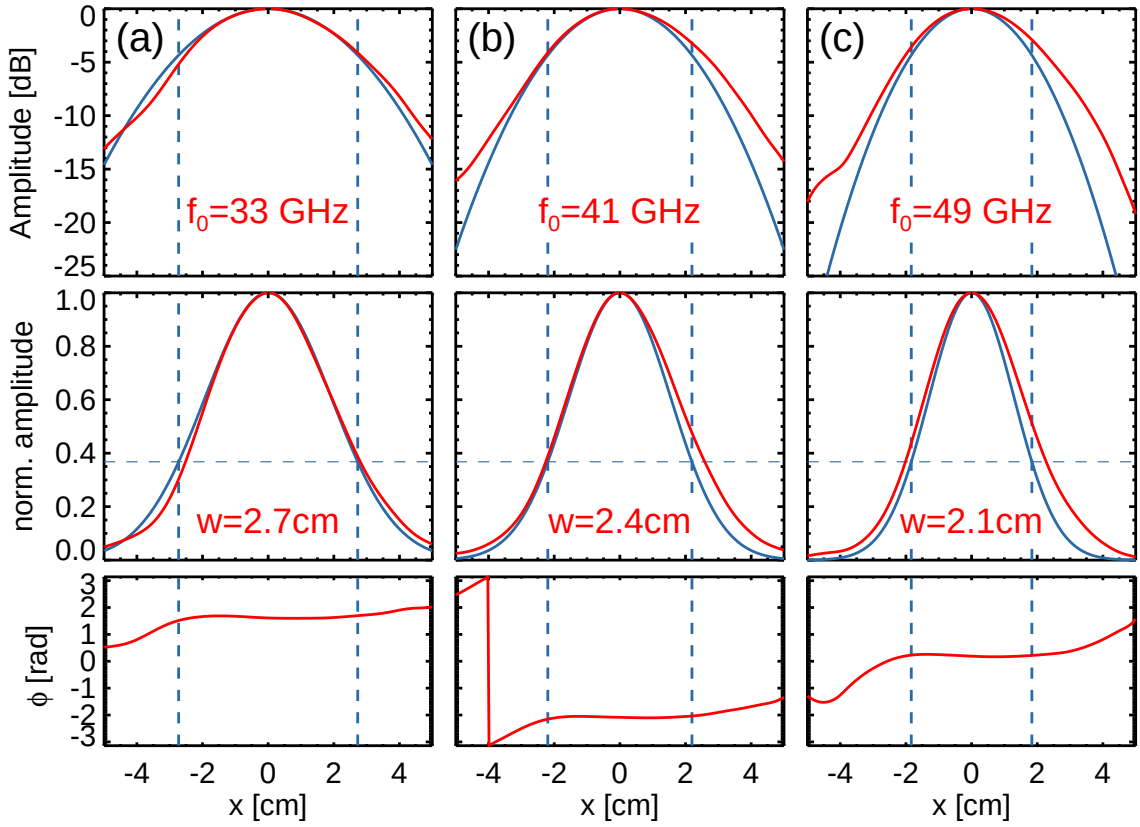

Figure 5.20: 2D full wave simulation results for the beam amplitude distribution (upper and middle row) and phase distribution (lower row) in the detection plane for (a) $f_0 = 33$ GHz, (b) $f_0 = 41$ GHz and (c) $f_0 = 49$ GHz.

resolution dependence on the beam waist in the plasma. The optimum beam waist range is indicated in green. The beam waist radii obtained by 2D full wave simulation (vertical lines) are slightly displaced from the optimum ones towards the more slowly rising flanks of the curves. This was a deliberate design decision since $\Delta k_\perp$ deteriorates more rapidly towards small beam waists. The deterioration of $\Delta k_\perp$ w.r.t. the optimum value is indicated by the line pattern areas, the value of the deterioration is comparable for all frequencies.

5.5.2 Beam Behavior in the Plasma

A 2D full wave calculation in the plane of the perpendicular flux surfaces is shown in fig. 5.22. The absolute electric field distribution is shown. The density profile used is of the form $n_e = n_{e,0}(1 - \rho^\alpha)^\beta$, with $n_{e,0} = 1.7 \times 10^{19}$ m^{-3}, $\alpha = 6$ and $\beta = 7$. Density fluctuations with a fluctuation level of $\tilde{n}_e/n_c = 0.1$, where n_c is the cutoff-density, are randomly introduced. The probing beam frequency is $f_0 = 41$ GHz and the mirror angle $\theta_H = 36°$. The flux surfaces are plotted in red, and in the upper part of the plot the antenna and the ellipsoidal mirror are located. The green lines show ray tracing calculations with the same plasma and probing beam parameters,

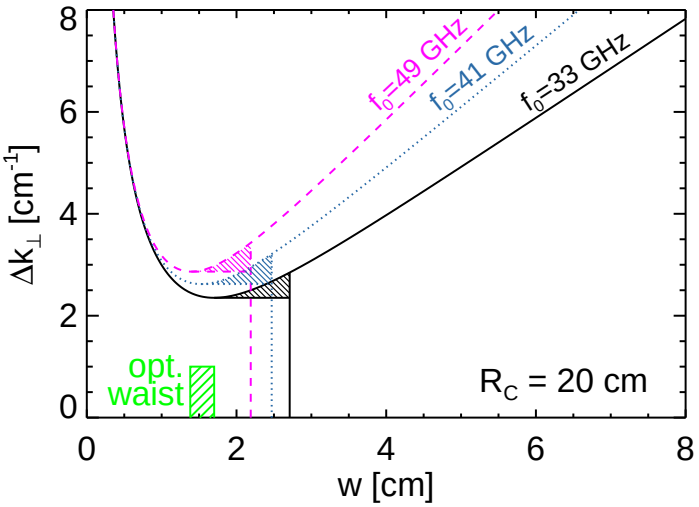

Figure 5.21: Spectral resolution of the TJ-II Doppler reflectometer. The optimum beam waist range is indicated in green. The vertical lines indicate the beam waists obtained by focusing of the beam with the ellipsoidal mirror.

explained in more detail below (sec. 5.7). Following the beam propagation beginning at the antenna mouth, the beam size as well as its wavefront curvature R_B increases. As the beam reaches the ellipsoidal mirror, it is reflected towards the plasma, and close to the mirror the beam wavefronts are convergent. As the beam enters into the plasma, its electric field amplitude grows until it reaches its maximum close at the cutoff layer (here: $\rho \approx 0.75$). The beam is reflected and starts to travel out of the plasma again towards the upper left of the plot.

It is remarkable that the 2D full wave simulation and the 3D ray tracing calculation coincide almost perfectly. The ray tracing calculation is done in the full 3D geometry of TJ-II, taking into account the complex structure of the plasma as it winds around the helical coil. Afterwards, the ray tracing result is projected onto the $R_\perp$-axis. But not only the similarity of the beam propagation is striking, also the point of reflection in the plasma coincides well. As can be observed from the color-coded full wave simulation amplitude, the region of strong electric field is slightly inclined with respect to the flux surfaces, the left extreme being further away from the $\rho = 0.7$ flux surface than the right extreme. Even this inclination is reproduced by the ray tracing calculation, where the right hand ray enters further into the plasma than the left hand ray.

5.5.3 Summary

The above 2D full wave calculations confirm the good adaptation of the hardware components to the plasma characteristics. It has been demonstrated that the focusing properties of the ellipsoidal mirror produce a beam with plane wavefronts in the cutoff layer region ($\rho = 0.60 - 0.85$). Furthermore, the beam waist radii in the plasma decrease with increasing probing beam frequency, a property indispensable for optimum spectral resolution, mathematically described by (3.8). Furthermore, the DR geometry has been

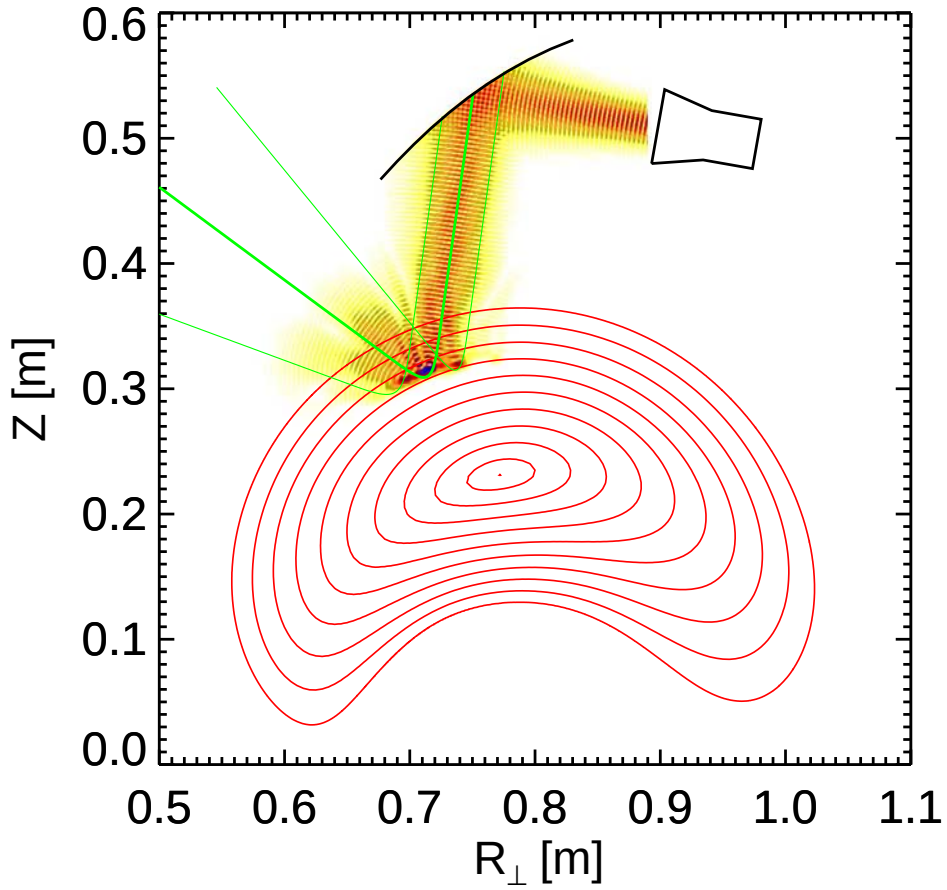

Figure 5.22: 2D full wave calculation showing the absolute electric field distribution in experiment geometry. The flux surfaces are shown in red, antenna and mirror in black and the ray tracing result is overlaid in green.

prepared as input to the 2D full wave code. The shape of the beam is as expected, and the beam shape and amplification of the wave electric field at the cutoff layer coincide spatially with 3D ray tracing calculations, explained in further detail in sec. 5.7.

These results justify the correct theoretical design of the hardware components, and with the information obtained, the system is ready for fabrication and installation into TJ-II.

5.6 Design of the Final Configuration

The design of the final configuration is shown in fig. 5.23. In (a), the top-down view illustrates the alignment of the system w.r.t. the magnetic field. Furthermore, the toroidal displacement of the mirror (yellow) away from the port center (to achieve $B_z = 0$, cf sec. 5.1.2) is visible. In order to align the system as shown, the waveguide and support structure (orange) of the DR had to be placed close to the port wall. The antenna can be seen as a gray cylindrical structure at the end of the waveguide. In the non-vacuum part of the system, the waveguide (red) and the antenna shutter manipu-

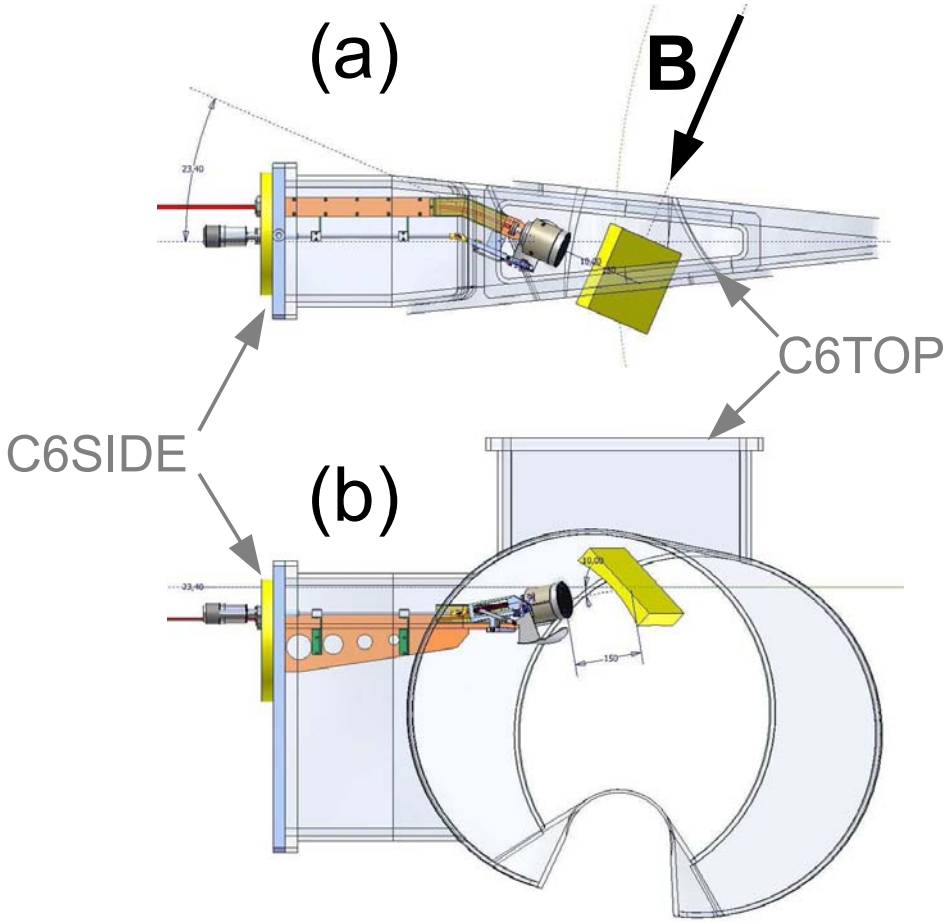

Figure 5.23: Final design of the TJ-II DR. (a) Top-down view illustrating the perpendicular alignment w.r.t. the magnetic field. (b) Lateral view showing the 10° vertical inclination and the antenna shutter. For details refer to the text.

lator are located. In fig. 5.23(b) a lateral view of the system is depicted. The antenna shutter (here open, below antenna) was installed in order to protect the antenna small-size corrugations from impurity accumulation as well as boron and lithium deposition during vessel wall conditioning. The vertical antenna inclination of 10° serves to protect the mirror from the plasma. Apart from that, the distance between plasma and mirror in this configuration is large enough that in case of a mirror manipulator system malfunction the material does not reach the plasma and thus does not hinder plasma operation and require opening the vacuum vessel.

The 10° inclination of the antenna results in a mirror angle $\theta_{\mathrm{H}} = 42.5°$ for perpendicular incidence in the plasma, referred to as θ_{s} in the following, i.e. $\theta_{\mathrm{s}} = 42.5°$. It is convenient to define a so-called *launch angle* θ_{l}, which denotes the beam inclination w.r.t. perpendicular incidence

$$\theta_{\mathrm{l}} = 2(\theta_{\mathrm{H}} - \theta_{\mathrm{s}}), \tag{5.24}$$

where the factor "2" is due to the law of reflection. Since the operational range of the mirror is $\theta_{\mathrm{H}} = 32° - 52°$, the operational range in terms of the launch angle is

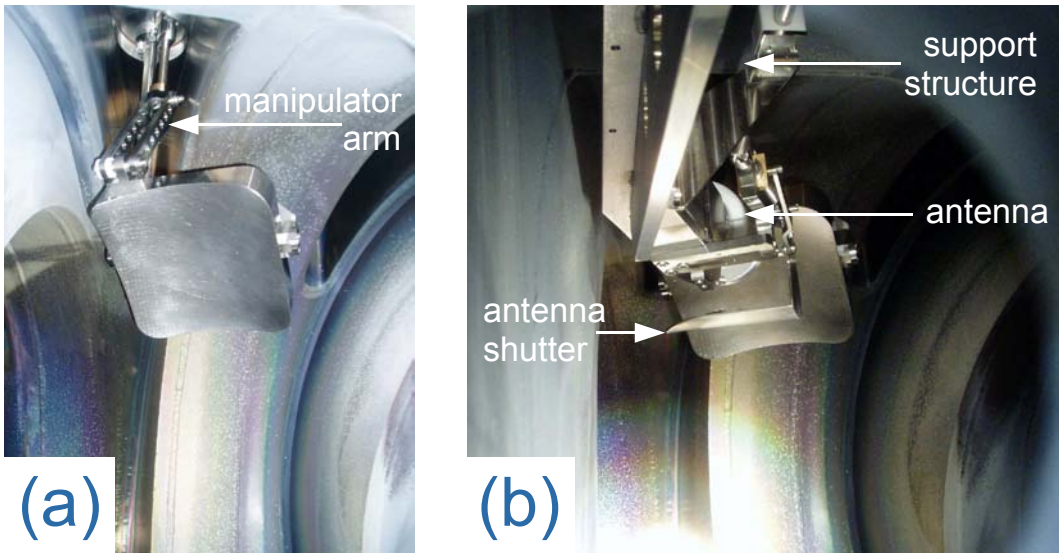

Figure 5.24: In-vessel photographs of the TJ-II DR. (a) The ellipsoidal mirror before the antenna is installed. The manipulator arm is used to change the mirror angle θ_{H}. (b) Antenna and mirror are installed. The antenna shutter is open as in operation.

$\theta_{\mathrm{l}} = (-21°) - (+19°)$.

Since the antenna is used to emit and receive the microwave beam, the received signal has to be decoupled from the transmission line and fed into the detector. This decoupling is done via a directional coupler which was located *outside* the vacuum part of the system in the first operation phase of the system. The result was that a parasitic reflection of the carrier wave was measured which came from the mica window that separated the non-vacuum from the vacuum part of the waveguide. This reflection gave an offset amplitude in the IQ-plane (cf sec. 6.1) and could in some (very few) cases saturate the measurement. This saturation can lead to a *mirror image* of the Doppler peak at reversed frequency $-f_{\mathrm{D}}$. Nevertheless, this does not hinder the measurement of the Doppler shift and thus $u_{\perp}$ measurements. However, due to the power in the mirror peak, height of the *true* Doppler peak is lost and the measurements of the turbulence level are error-prone.

To eliminate the problem, a vacuum directional coupler was installed *inside* the vacuum vessel, which caused a slight modification of the antenna support structure.

Photographs taken on the day the system was installed (January 15, 2009) from the lateral port C6SIDE show the system inside the TJ-II vacuum vessel (fig. 5.24). In (a) the antenna is not yet placed in C6SIDE, so that the ellipsoidal mirror can be seen entirely. In the upper part of the photograph, the support structure enters the vacuum vessel through C6TOP. Connecting support structure and mirror, the manipulator arm is marked in the upper part of the photograph. Here the mirror angle θ_{H} has already been changed from the maintenance position to a position in the operational range. Fig. 5.24(b) shows a similar view as (a), but the antenna has been installed in C6SIDE. The support structure in the upper part of the photograph holds the waveguide, the antenna, and the antenna shutter, which is opened in the photograph.

In the background, the mirror is visible. The photograph shows the DR as it is during plasma operation (mirror position in operational range, antenna shutter open).

5.7 The 3D Ray Tracing Code TRUBA

As pointed out in sec. 3.2.1, an analytical solution to the wave equation cannot be found for complex plasma geometries such as the one encountered in TJ-II. In case of curved plasma geometry, ray [104] or beam [105] tracing has to be used to obtain the (radial) backscattering position, usually called the ray turning point (RTP) ρ_{RTP} and the perpendicular wavenumber of density fluctuations $k_\perp$ the microwave beam is backscattered off [106, 107]. Ray/beam-tracing makes use of the WKB (Wentzel-Kramers-Brillouin) approximation, which is valid for

$$\frac{\lambda_0}{2\pi}\frac{|N'|}{N^2} \ll 1, \tag{5.25}$$

where λ_0 is the wavelength in vacuum and N and N' are the refractive index and its spatial derivative, respectively. Condition (5.25) is not satisfied for steep gradients or low values of the refractive index N. Note that low values of N are intrinsic to perpendicular incidence of the microwave beam, where $N \to 0$ is obtained. This, however, is not the case in Doppler reflectometry, where N is finite at the ray turning point. An equivalent form of writing (5.25) is $\lambda'/2\pi \ll 1$, where λ' is the spatial derivative of the beam wavelength in the plasma. Since the TJ-II plasma curvature is non-negligible ($R_{\mathrm{C}} = 0.20$ m for the DR measuring region), the ray tracing code TRUBA (trubá: Russian for pipe) [108], previously employed for TJ-II plasma heating scenarios [109–111], has been adapted to the DR geometry. TRUBA solves the ray/beam-tracing equations for the full three-dimensional geometry of TJ-II (one run in ray-tracing mode with one traced ray takes about 5 seconds). At each point of the ray trajectory the incident wavenumbers perpendicular ($k_{\perp,i}$) and parallel ($k_{\parallel,i}$) to the magnetic field are calculated. In the following ray-tracing is done in non-relativistic mode, which gives reliable results provided electron temperatures are low. For an estimation of relativistic effects in reflectometry, see Ref. [112]. Running TRUBA in full relativistic mode requires a large amount of CPU time and the difference to non-relativistic calculations is negligible for the temperatures in consideration (< 1 keV).

5.7.1 TRUBA applied to the TJ-II Doppler Reflectometer

Since TRUBA has been adapted to the geometrical configuration of the TJ-II DR, only few inputs are necessary to calculate ρ_{RTP} and $k_\perp$ at ρ_{RTP}. The inputs are the magnetic configuration, the plasma electron density profile $n_e(\rho)$ (analytical or experimental), microwave frequency f_0 and mirror angle θ_{H}. The analytical density profile – if used – is of the form

$$n_e = n_{e,0}(1-\rho^\alpha)^\beta, \tag{5.26}$$

where $n_{e,0}$ is the central density and ρ is the normalized poloidal flux radius. α and β are parameters describing the shape of the profile. In the following examples, an

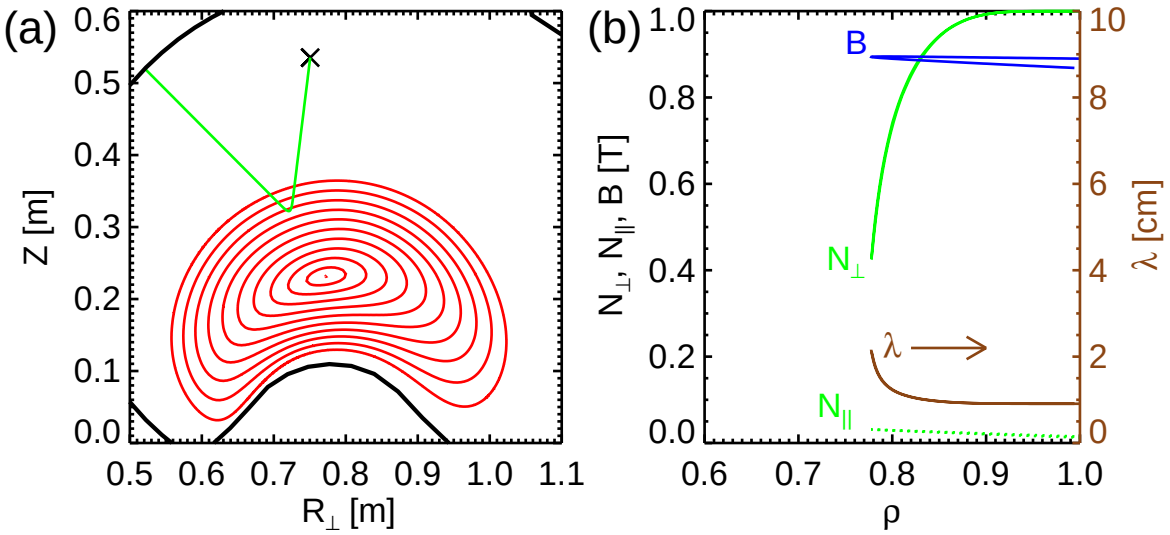

Figure 5.25: Ray tracing results obtained with TRUBA. The density profile (5.26) is used. (a) Ray ($f_0 = 33$ GHz, $\theta_l = -12°$) in the plane of perpendicular flux surfaces. The vessel wall is indicated by a thick line and the perpendicular flux surfaces for the standard configuration are shown in red. The cross in the upper part is the center of the ellipsoidal mirror. (b) Magnitudes along the ray trajectory inside the plasma.

analytical density profile of the form of (5.26) with $n_{e,0} = 1.7 \times 10^{19}$ m^{-3}, $\alpha = 6$ and $\beta = 7$ is used.

A ray tracing calculation for the standard magnetic configuration (100_44_64) with a microwave beam with $f_0 = 33$ GHz and $\theta_l = -12°$ is depicted in fig. 5.25. In (a), the perpendicular flux surfaces (red) and the calculated ray (green) are shown. The ray tracing starts at the mirror center ($x' = y' = 0$ cm in fig. 5.14) and the ray is traced depending on its wavenumber $\mathbf{k}$ towards the plasma. Before it reaches the plasma, the ray travels in a straight line according to vacuum wave propagation. Inside the plasma the electron density increases, the dielectric tensor becomes important and the ray curves and turns around when the refractive index reaches its minimum at the ray turning point. Afterwards the ray travels out of the plasma and eventually hits the wall where the ray-tracing calculation terminates. Fig. 5.25(b) shows the evolution of different ray properties along the trajectory. Note that since the abscissa is the normalized poloidal flux radius of the plasma, the ray enters at $\rho = 1$, propagates towards smaller ρ, turns around and travels out again. The perpendicular component of the refractive index $N_\perp$ (green line) decreases as the ray travels up the density gradient of the plasma, until it reaches its minimum at $\rho_{\mathrm{RTP}} = 0.78$. The parallel component of the refractive index (green dashed line) is negligible throughout the whole ray trajectory. The wavelength of the microwave (brown line) is $\lambda \approx \lambda_0 \approx 0.9$ cm in the edge of the plasma and increases towards the ray turning point, where it achieves a maximum value of about $\lambda = 2$ cm. The absolute value of the magnetic field is slightly increasing as the ray enters into the plasma and is $B \approx 0.9$ T at the ray turning point and on its way out of the plasma. From the ray tracing calculation,

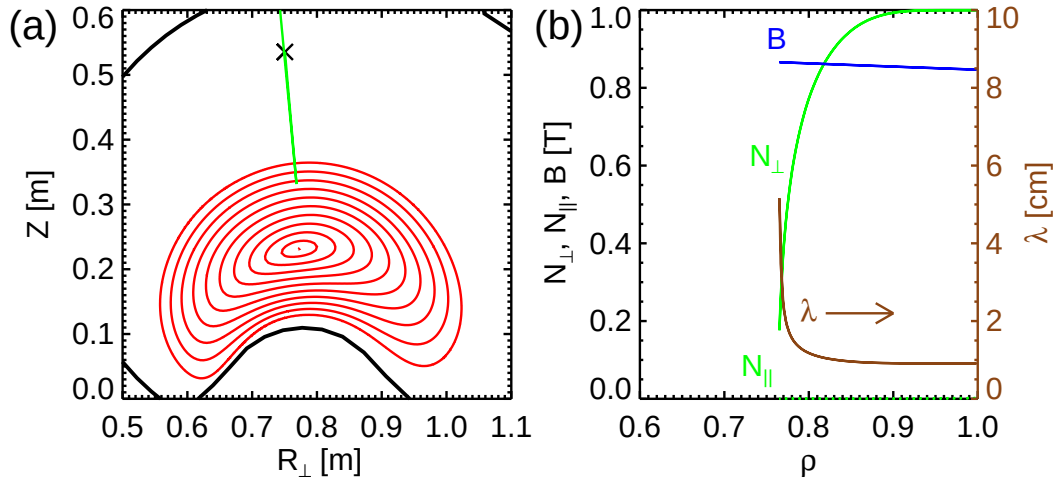

Figure 5.26: (a) Ray ($f_0 = 33$ GHz, $\theta_l \approx 0°$) calculated with TRUBA. (b) Magnitudes along the ray trajectory.

$k_\perp$ of the turbulence is calculated at the ray turning point

$$k_\perp = 2k_{\perp,i} = 2\frac{2\pi f_0}{c}N_\perp, \tag{5.27}$$

where $k_{\perp,i}$ is the perpendicular wavenumber of the microwave ray.

Note that the evolution of $N_\perp$, $N_\parallel$ and λ as the ray leaves the plasma ($\rho = \rho_{\mathrm{RTP}} \rightarrow \rho = 1$) is similar to when it entered ($\rho = 1 \rightarrow \rho = \rho_{\mathrm{RTP}}$), the curves lie on top of each other.

The ray tracing calculation shown in fig. 5.26 shows an almost perpendicular ray ($\theta_l = 0.2°$), i.e. the system operates in conventional reflectometry mode. For a perfectly perpendicular ray with $\theta_l = 0.0°$ TRUBA does not terminate. As mentioned above, numerical problems are encountered when $N \rightarrow 0$. In fig. 5.26(a) the ray enters into the plasma, is reflected at $\rho = 0.76$ and returns to the mirror, indicated by the cross in the upper part of the plot. In fig. 5.26(b) $N_\perp$ decreases towards zero, and has a stronger slope than the $N_\perp$ evolution for the $\theta_l = -12°$ case in fig. 5.25. Note due to the perpendicular incidence the evolution of B is identical on the way into the plasma and out again. $N_\parallel = 0$ because the beam reflection is in the vicinity of the design position of the DR (perpendicular incidence, $\rho = 0.80$).

In fig. 5.27 ray tracing calculations for microwave beams of different frequencies (33, 41, 49 GHz) and $\theta_l = \pm 12°$ are shown for the standard magnetic configuration of TJ-II. The density profile from (5.26) is used. The blue line corresponds to a ray with $f_0 = 33$ GHz and $\theta_l \approx 0°$. A cut perpendicular (a) and parallel (b) to the magnetic field is shown. In (a) the reflected rays for $\theta_l = \pm 12°$ do not return to the antenna, but are deflected towards the vessel wall. This effect assures that the zero-order reflection for the TJ-II DR is negligible in most cases when analyzing the complex amplitude spectra. In (b), only the reflected ray with $\theta_l \approx 0°$ has no component of the wave vector parallel to the magnetic field ($k_\parallel = 0$) because $B_z = 0$. The rays for $\theta_l = -12°$ are deflected to the right, because the magnetic field has a small vertical component

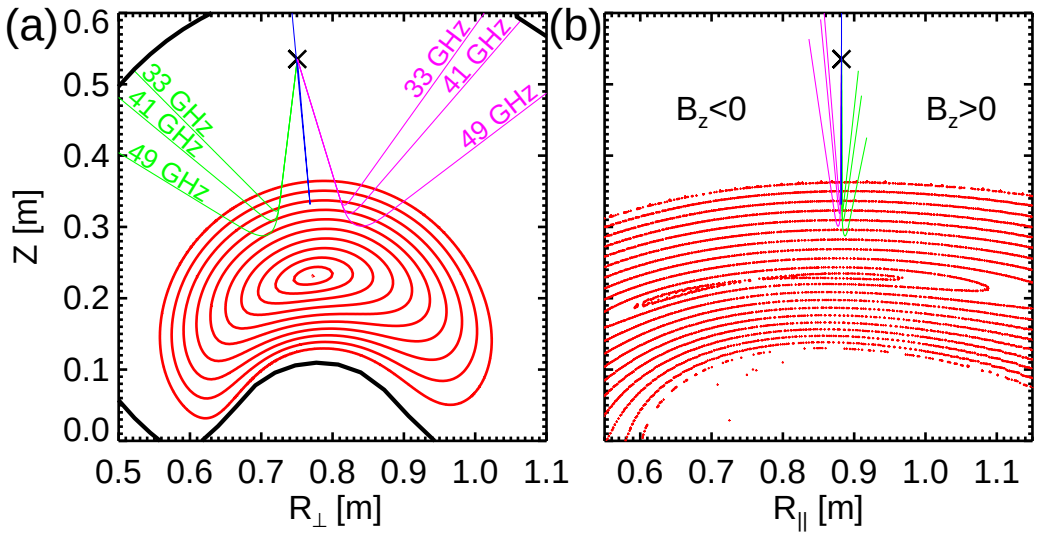

Figure 5.27: Ray tracing calculations for perpendicular incidence at 33 GHz ($\theta_l \approx 0°$, blue line) and different microwave frequencies (33, 41, 49 GHz) for $\theta_l = \pm 12°$ (thin lines) obtained from TRUBA. (a) Perpendicular to the magnetic field and (b) parallel to the magnetic field.

($B_z > 0$). For $\theta_l = +12°$ the rays are deflected towards the left, because $B_z < 0$.

The exact available $k_\perp$-space will depend on the magnetic configuration and density profile, although only slight changes are to be expected. Fig. 5.28(a) shows the density profile used for the ray-tracing calculations. In (b) the $k_\perp$-space is shown for microwave frequencies ranging from 33 – 49 GHz and launch angles $\theta_l = -5°$ to $-21°$. The radial measurement region of the Doppler reflectometer in this plasma is $\rho = 0.55 - 0.77$ and the wavenumber range covered by varying θ_l is $k_\perp = 3 - 15$ cm^{-1}. If it is desired to measure the wavenumber spectrum at a fixed radial position, for each launch angle θ_l the frequency has to be adapted adequately. The same holds for a radial scan at fixed wavenumber (a horizontal cut through fig. 5.28(b)). However, during experiments, this is normally not done since density profiles are usually not available immediately after the discharge. Instead, for fixed θ_l several frequencies are measured, followed by an alteration of θ_l and another scan of frequencies and so on. In this way, the whole perpendicular wavenumber space is spanned, and the analysis is done after the experimental day.

Fig. 5.28(c) shows the parallel wavenumber contribution relative to the perpendicular wavenumber $k_\parallel/k_\perp$. For all the points from (b), the values are below 8%, reflecting the good adaptation of the system to the geometry of the TJ-II magnetic field. Due to the symmetry of the system, the parallel wavenumber contributions for $\theta_l > 0$ are of the same order, while $k_\parallel = 0$ is obtained for perpendicular incidence at $\rho = 0.8$, the design position of the DR (cf fig. 5.26(b)).

5.7.2 Using TRUBA to Estimate Uncertainties

Since the backscattering region in a Doppler backscattering experiment has finite extension, not only one $k_\perp$-value will be probed, but a range of values $k_\perp \pm \Delta k_\perp$, where

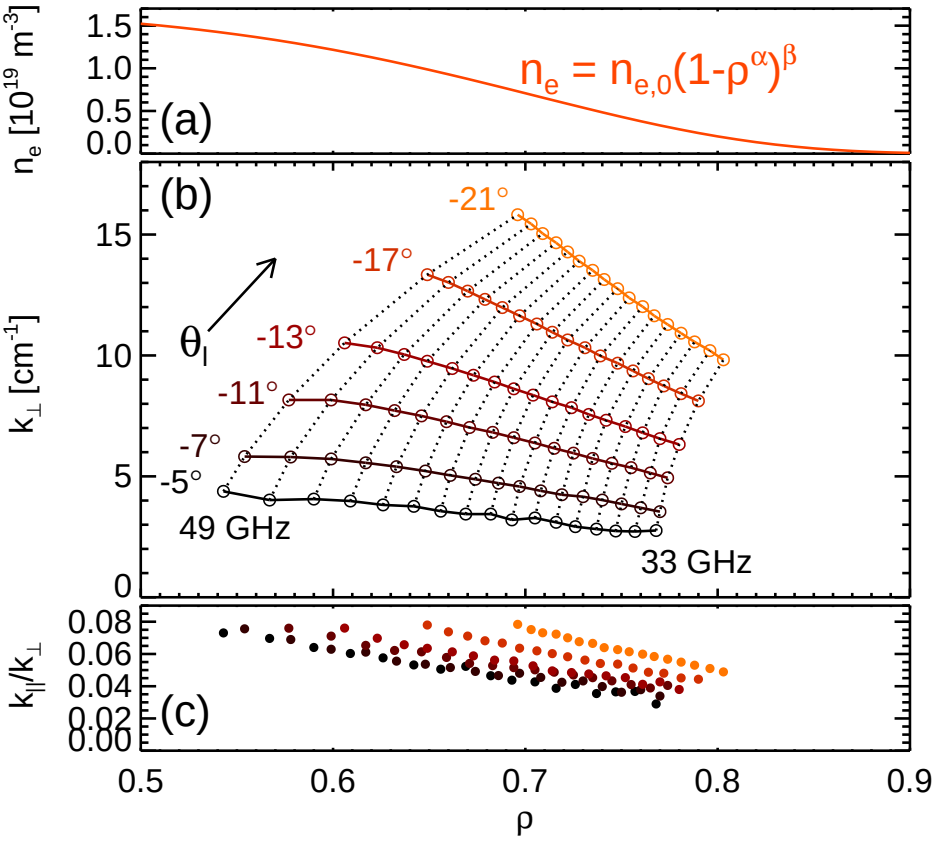

Figure 5.28: (a) Analytical density profile used for the (b) ray-tracing calculation of the $k_\perp$ wavenumber space spanned by the DR. (c) The $k_\parallel$-influence is small. For details refer to the text.

the value of $\Delta k_\perp$ depends on plasma and wavefront curvatures and on the probing beam spot size (cf sec. 3.2.2). Here the weighting of the central $k_\perp$ is maximum, and the weighting function decreases exponentially towards lower and higher values of $k_\perp$ [113]. Naturally, due to the spatial extension the radial measurement position will also be subject to uncertainties. In order to be able to provide uncertainties for the measurements, `TRUBA` can be used not only to trace the probing beam center, but also additional rays which represent the envelope of the microwave beam where the amplitude dropped to $1/e$ of its central value. The envelope is launched from the mirror and in parallel to the central ray. Note that the three rays (central one and envelopes) are independent of each other. Nevertheless, the representation chosen here can give an idea of the beam size in the plasma. For simplicity and illustrative reasons, in the following the combination of central ray and envelopes will be referred to as a *beam*, although the rays do not affect each other. This is not to be confused with beam tracing [105], a technique which allows for interference and diffraction effects.

In fig. 5.29 the central and the envelope rays (labeled 1 and 2) are plotted for $\theta_l = -12°$ and (a) $f_0 = 33$ GHz and (b) $f_0 = 49$ GHz. The mirror center is shown as a cross in the upper part of the plot. As before, the central ray is traced from the mirror center towards the plasma, enters until it reaches ρ_{RTP}, leaves the plasma

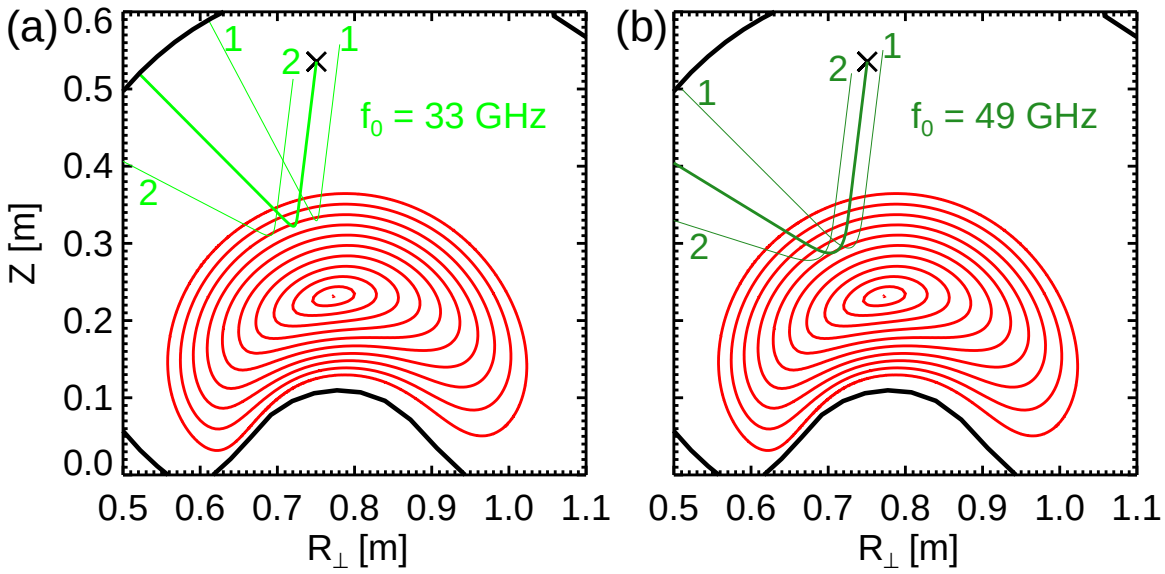

Figure 5.29: Visualization of the beam size to estimate uncertainties in ρ and $k_\perp$ for (a) $f_0 = 33$ GHz and (b) $f_0 = 49$ GHz. The central ray and envelope rays at $1/e$ of the central amplitude value are plotted.

and eventually hits the vessel wall. The envelope rays are launched from the mirror surface, displaced along the mirror according to the antenna beam waist characteristic (5.10). Note that because of the higher probing beam frequency the beam is smaller in (b). The envelope rays enter in parallel to the central ray, and are reflected at their respective ray turning points ρ^1_{RTP} and ρ^2_{RTP}. Since the tilt angles of the envelope rays are different from the central ray tilt angle due to the plasma curvature, ray 1 enters more than the central ray and envelope ray 2: $\rho^1_{\mathrm{RTP}} < \rho_{\mathrm{RTP}} < \rho^2_{\mathrm{RTP}}$. Correspondingly the perpendicular wavenumbers $k^1_{\perp,i}$ and $k^2_{\perp,i}$ of the envelope rays are different. To estimate the uncertainties in ρ_{RTP} and $k_\perp$, the means of the two respective deviations are used:

$$\Delta\rho_{\mathrm{RTP}} = \frac{|\rho_{\mathrm{RTP}} - \rho^1_{\mathrm{RTP}}| + |\rho_{\mathrm{RTP}} - \rho^2_{\mathrm{RTP}}|}{2} \tag{5.28}$$

$$\Delta k_\perp = |k_{\perp,i} - k^1_{\perp,i}| + |k_{\perp,i} - k^2_{\perp,i}|. \tag{5.29}$$

The absence of the factor $1/2$ in (5.29) is due to the relation $k_\perp = 2k_{\perp,i}$. The calculation of error bars in Doppler reflectometry measurements is generally not straightforward and different approaches are used, e.g. assumption of constant errors in f_{D} and θ_0 without the inclusion of the beam size [62,114]. A similar method to the one proposed here but employing beam tracing [106] is used by Hennequin *et al.* in Tore Supra [115]. It has to be noted that these approaches are makeshift solutions that cannot cover the whole physical picture, which includes a variety of effects like fluctuations, forward scattering and reflection, multiple scattering and non-linear effects at large fluctuation amplitude [115].

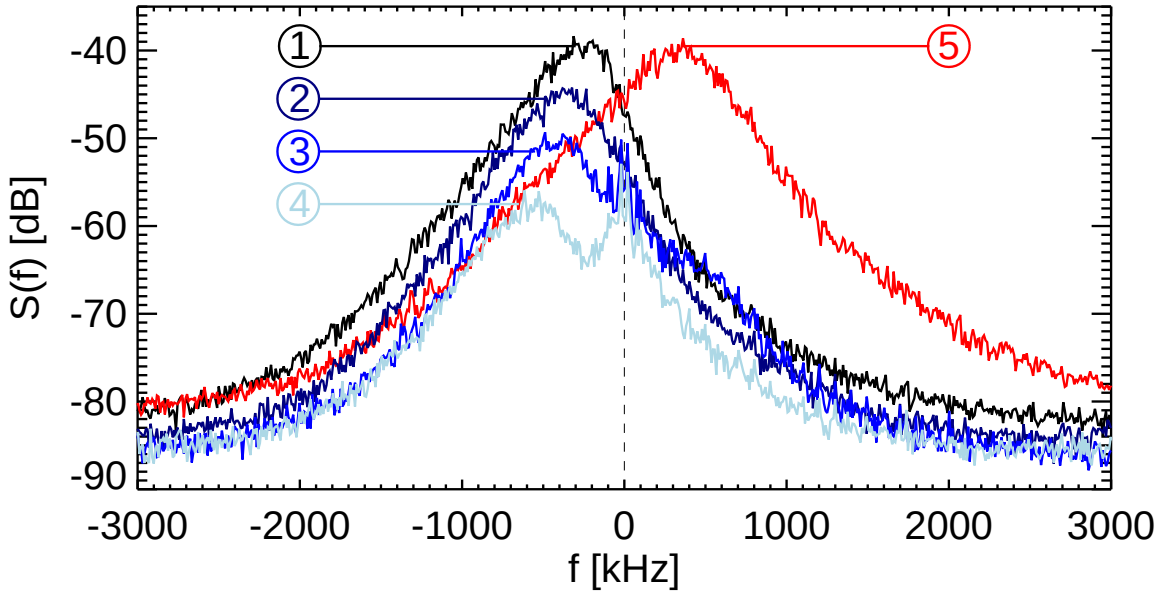

Figure 5.30: (#20277, #20281) Doppler shifted power spectra for four different microwave frequencies for a low-density ECRH plasma ① – ④ and for a higher density ECRH discharge ⑤. The launch angle is $\theta_l = -13°$ in all cases. The Doppler peaks are clearly separated from $f = 0$ kHz.

5.8 Plasma Operation Testing of the Doppler Reflectometer

First experimental results from the TJ-II DR were obtained on February 5, 2009. In the first phase of operation, the reliability of the system was tested.

5.8.1 Doppler Shifted Spectra

Fig. 5.30 shows typical spectra of the complex amplitude signal from the DR for four different microwave frequencies at low density (① - ④: #20281, $\langle n_e \rangle \approx 0.5 \times 10^{19}$ m^{-3}) and one at higher density (⑤: #20277, $\langle n_e \rangle \approx 0.7 \times 10^{19}$ m^{-3}) discharges. Heating of the plasma was done via ECRH with heating power $P_{\mathrm{ECRH}} = 500$ kW and the mirror angle was $\theta_l = -13°$. The Doppler shifted peaks ($m = -1$) are clearly visible in the negative frequency part for low $\langle n_e \rangle$ and in the positive part for high $\langle n_e \rangle$. f_{D} is calculated by fitting a Gaussian to the respective spectrum (cf sec. 6.2 for details). The microwave frequencies used, radial positions of the cutoff layers, perpendicular wavenumbers and deduced perpendicular velocities are shown in tab. 5.4. The uncertainties are calculated following the expressions in sec. 5.7.2 and Gaussian propagation of uncertainties for $\Delta u_\perp$.

No.	f [GHz]	ρ	f_D [kHz]	$k_\perp$ [cm^{-1}]	$u_\perp$ [km/s]
①	33.5	0.82 ± 0.03	-275.9	5.4 ± 1.5	3.2 ± 0.9
②	38.0	0.69 ± 0.04	-382.9	7.0 ± 1.6	3.4 ± 0.8
③	39.5	0.66 ± 0.04	-434.5	7.7 ± 1.7	3.5 ± 0.8
④	41.0	0.63 ± 0.08	-577.9	8.2 ± 1.8	4.4 ± 1.0
⑤	34.0	0.86 ± 0.02	358.0	5.6 ± 1.7	-4.0 ± 1.2

Table 5.4: Deduced perpendicular velocities from the spectra in fig. 5.30. The values of ρ and $k_\perp$ are obtained from `TRUBA` and the perpendicular velocity is calculated by fitting a Gaussian to the respective spectrum. For details refer to the text.

5.8.2 Symmetry of the System

The ability of the system to measure in different types of operation is illustrated in fig. 5.31. Three power spectra are shown for different microwave beam launch angles θ_l. For $\theta_l = 0°$ (blue), the power spectrum is symmetric and the system operates in conventional reflectometry mode. The Doppler shift f_D is negative for $\theta_l = -12°$ (green, $f_0 = 35.0$ GHz) and positive for $\theta_l = +12°$ (magenta, $f_0 = 36.5$ GHz), and the absolute value of f_D is comparable in the two cases. The two $\theta_l = \pm 12$ spectra are not perfect mirror images, which can be due to several reasons, among them are that the two probing frequencies are not the same and the plasmas are slightly different. Nevertheless, the general trend is observed that for comparable plasma conditions measurements with different launch angle signs yield different Doppler peak signs. A striking difference between the spectra of perpendicular and oblique incidence is not only the presence of a Doppler shift in case of oblique incidence. The spectrum

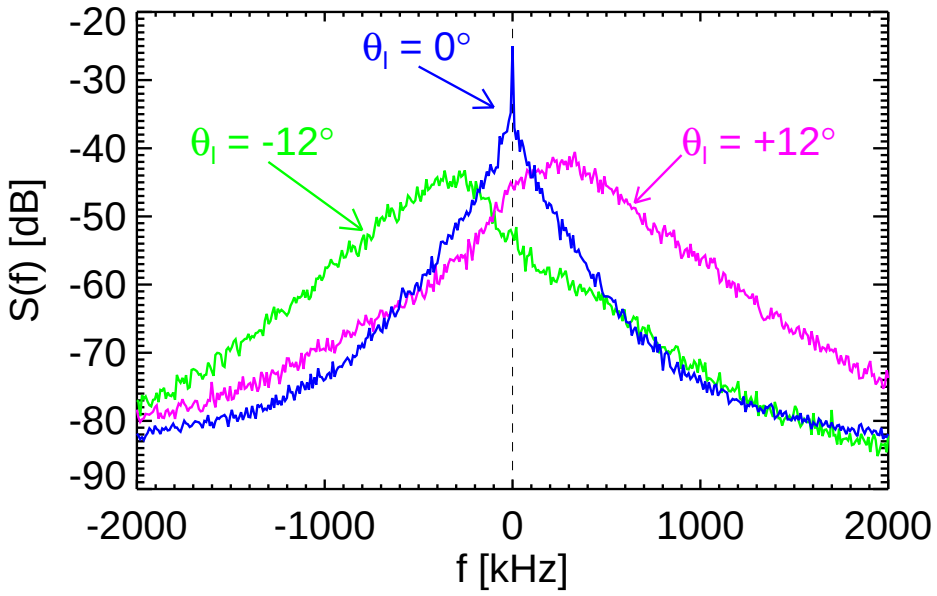

Figure 5.31: (`#20281, #20297, #20361`) Power spectra for different θ_l in comparable plasmas. The $\theta_l = 0°$ spectrum is symmetric, the other two show comparable Doppler shifts with different sign.

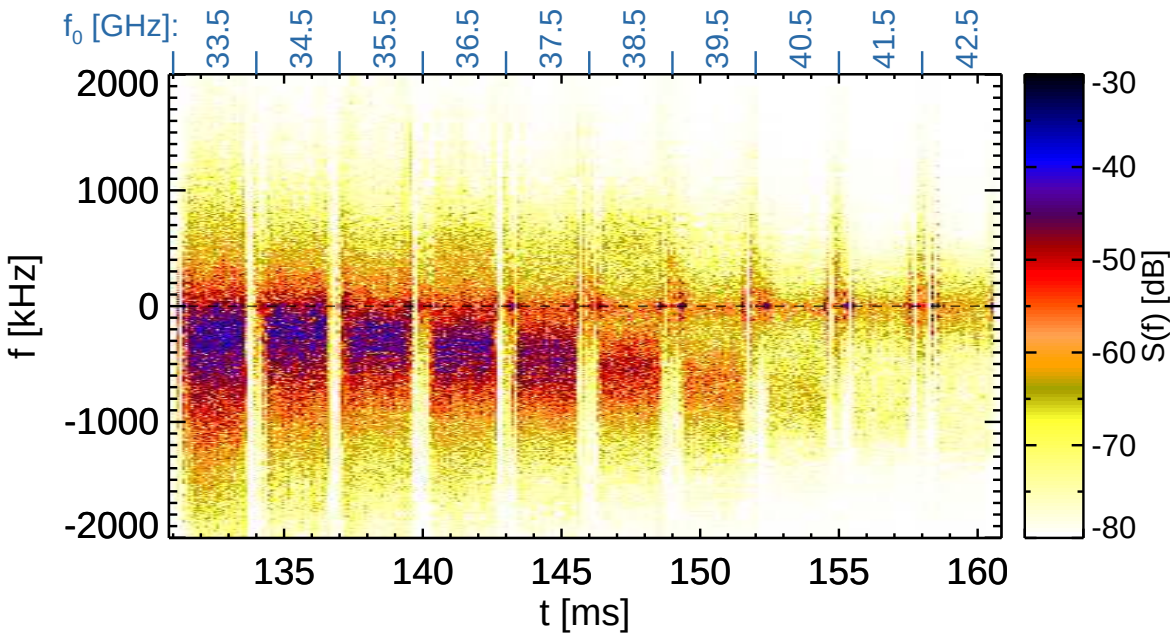

Figure 5.32: (#24102) Spectrogram of the DR during an ECRH discharge. The time window length is 30 ms, ten frequency steps (33.5 – 42.5 GHz) are realized, indicated on top of the plot. For details refer to the text.

for $\theta_l = 0°$ is the spectrum of the direct (zero-order) reflection and is symmetrically broadened due to turbulence and possible cutoff-layer movements.

5.8.3 Perpendicular Velocity Profile

In order to measure radial profiles of the perpendicular velocity $u_\perp$ with the TJ-II DR, either the frequencies of the two reflectometer channels can be scanned during the plasma discharge, or several comparable discharges can be realized and the frequencies changed on a shot-to-shot basis. Usually, the former method is used for ECRH plasmas, because the discharges are usually stationary with constant density during one frequency scan of the DR. ECRH discharges can become non-stationary if $\langle n_e \rangle \gtrsim 0.8 \times 10^{19}$ m^{-3}, which then implies shot-to-shot Doppler reflectometry measurements. The temporal length of a frequency scan can be programmed, typically 10 steps are realized in 30 ms, i.e. 3 ms/step. Hence in a 300 ms plasma, typically ten $u_\perp$ profiles are measured.

A spectrogram of a typical 30 ms frequency scan during an ECRH discharge at low density is shown in fig. 5.32. During the time window, 10 frequency steps are realized with frequencies stepping from $f_0 = 33.5$ GHz (first step) to $f_0 = 42.5$ GHz (last step) with frequency steps of $\Delta f_0 = 1$ GHz (indicated on top of the plot). The spectrogram is interrupted by white stripes of about 1 ms duration which occur when the microwave frequency is switched. The color code represents the amplitude of the spectrum, which is maximum (Doppler peak) at negative frequencies. In general, the amplitude measurement has to be calibrated, because the sensitivity of the system

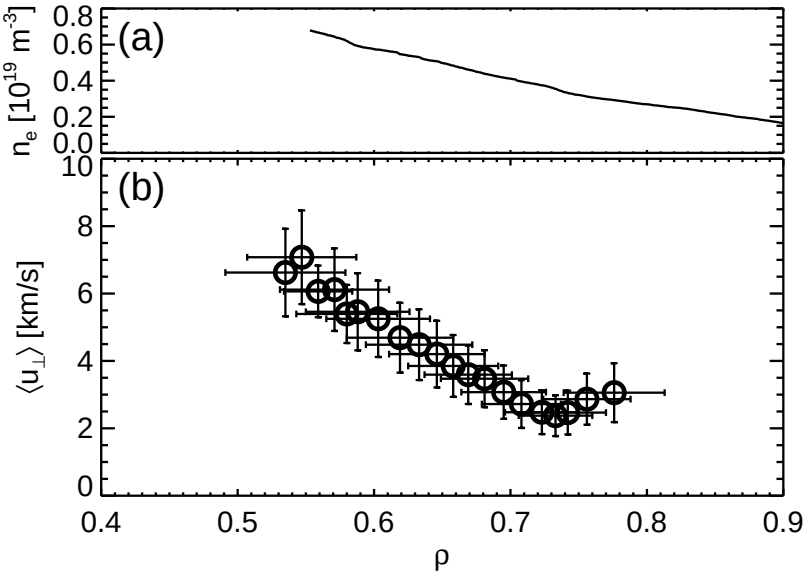

Figure 5.33: (#24102) Low density ECRH plasma ($\langle n_e \rangle \approx 0.5 \times 10^{19}$ m^{-3}) (a) Density profile at $t = 1139$ ms obtained with the AM reflectometer. (b) Profile of the perpendicular velocity of density fluctuations obtained with the DR.

varies with the microwave frequency. However, for microwave channel two (CH2, shown here), the amplitude – frequency response is almost constant, i.e. the color code can be compared between frequency steps, giving an idea of how the density fluctuations decrease at higher f_0, i.e. at more internal measurement positions. This decrease is mainly a mixture of two effects: first, the density fluctuation level decreases from the plasma edge towards the center, and second, a higher $k_\perp$ is measured in the more internal regions of the plasma (cf fig. 5.28). For the spectrum amplitude analysis, the measurement has to be calibrated and the response of each channel (CH1, CH2) to each frequency ($f_0 = 33$ – 50 GHz) has to be known (cf sec. 8.1).

From 130 to 140 ms ($f_0 = 33.5 - 35.5$ GHz) the Doppler shift is rather constant at $f_\mathrm{D} \approx -250$ kHz. Later f_D increases in absolute value, while the amplitude $S(f_\mathrm{D})$ decreases. The perpendicular wavenumbers probed range from $k_\perp = 5.6$ cm^{-1} at $f_0 = 33.5$ GHz to $k_\perp = 9.3$ cm^{-1} at $f_0 = 42.5$ GHz. Throughout the time window, the Doppler shifts f_D are negative, which corresponds to positive $u_\perp$ (ion-diamagnetic direction), a common situation at low line-averaged densities in ECRH plasmas in TJ-II. The exploitation of all frequency steps from fig. 5.32 (for CH2) and those from CH1 gives 20 radial measurement points in a 30 ms time window.

The resulting $\langle u_\perp \rangle$ profile (flux surface averaged, cf sec. 5.1.7) is plotted in fig. 5.33(b). The profile was acquired between 130 ms and 160 ms of ECRH discharge #24102. In (a), the electron density profile used as input for TRUBA and measured with the AM reflectometer is shown. The measurement region of the DR in this discharge is $\rho = 0.53$ – 0.78, one quarter of the total plasma radius. The measurement positions of the two innermost points in the profile had to be obtained by linearly extrapolating the density profile in (a). Due to the frequency programming mentioned above, each

point measured by one microwave channel is followed by a point measured by the other microwave channel. Nevertheless, the measurements are well aligned and continuous, suggesting that no hardware issues are present in the system. The error bars were calculated using the 3-ray method presented in sec. 5.7.2. An interesting characteristic is the minimum in the $u_\perp$ profile around $\rho = 0.73$. This effect has been investigated in detail and will be presented and interpreted in sec. 7.1.

5.8.4 Radial Electric Field Profiles

As mentioned in sec. 3.3, the perpendicular velocity measured by Doppler reflectometry is the superposition of the $E \times B$ plasma background velocity $v_{E\times B}$ and the phase velocity of turbulence v_{ph}:

$$u_\perp = v_{E\times B} + v_{\mathrm{ph}}. \tag{5.30}$$

If the phase velocity of turbulence is small compared to the $E \times B$-velocity,

$$v_{\mathrm{ph}} \ll v_{E\times B}, \tag{5.31}$$

its contribution to (5.30) can be neglected and the $E \times B$-velocity is measured directly by the DR. With knowledge of the magnetic field strength B, the radial electric field E_r can be calculated directly:

$$E_r = u_\perp B. \tag{5.32}$$

The validity of the inequality (5.31) has not been shown for TJ-II yet. Nevertheless in TJ-II a Heavy Ion Beam Probe (HIBP) is installed which measures the plasma potential ϕ_{p} and thus is able to provide the measurement of $E_r = -\mathrm{d}\phi_{\mathrm{p}}/\mathrm{d}r$.

In fig. 5.34 radial E_r profiles measured by HIBP (squares) and DR (circles) are shown. For the DR measurements, (5.31) was assumed to be true and E_r was calculated

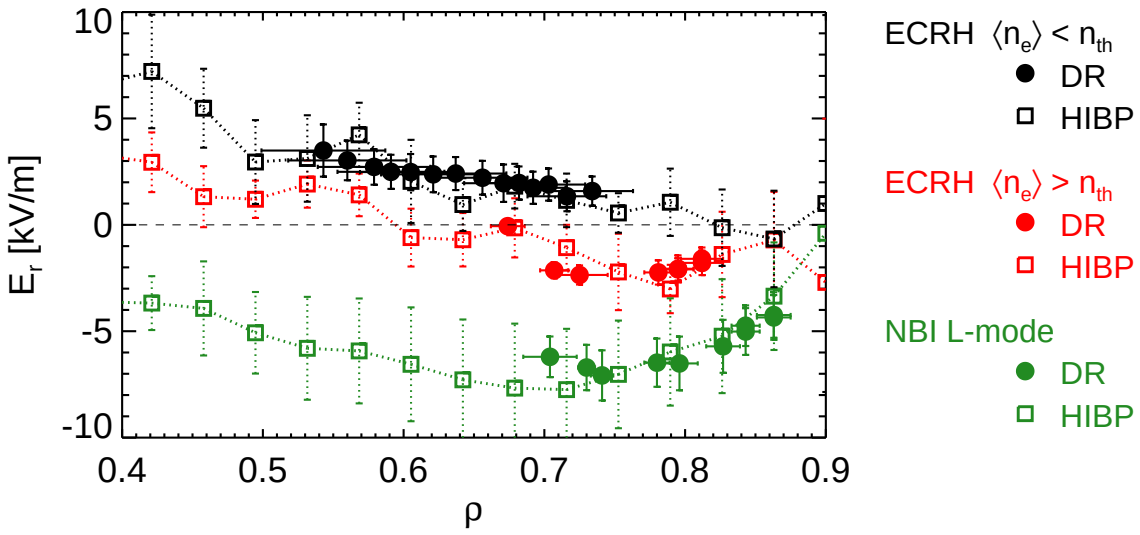

Figure 5.34: (#21872, #21909) Radial E_r profiles measured by HIBP (squares) and DR (circles) for three plasma scenarios: ECRH $\langle n_e\rangle < n_{\mathrm{th}}$ (black), ECRH $\langle n_e\rangle > n_{\mathrm{th}}$ (red) and NBI L-mode (green). The agreement is good in all cases.

according to (5.32). A trend observed in TJ-II since several years and discussed in detail in sec. 7.1 is reproduced by the measurements: If the line-average density $\langle n_e \rangle$ is above a certain threshold density $n_{\rm th}$, E_r becomes negative. For the low density ECRH case (black), E_r is positive in the whole measurement range, while for the mid-density ECRH case (red), the radial range $\rho > 0.7$ is dominated by a negative E_r. In the NBI plasma, $E_r < 0$ in the whole radial measurement range. In all three cases the agreement between HIBP and DR is remarkable, confirming (5.31) *a posteriori* for the observed plasmas.

Chapter 6

Data Analysis and Interpretation

This chapter gives an overview of the analysis methods used in this work. First a short introduction to quadrature phase detection is given followed by a presentation of numerical methods used to find the Doppler shift f_{D} of Doppler shifted spectra.

6.1 Quadrature Phase Detection

The heterodyne detection technique (for a review, see Ref. [92]) allows for the measurement of phase and amplitude information of a received microwave from the plasma. The signal received has two components, the *in-phase (I)* and *quadrature (Q)* terms:

$$I = A\cos\phi \tag{6.1}$$
$$Q = A\sin\phi. \tag{6.2}$$

These terms are combined to obtain the *complex amplitude signal*

$$V = I + iQ = A\cos\phi + iA\sin\phi = Ae^{i\phi}. \tag{6.3}$$

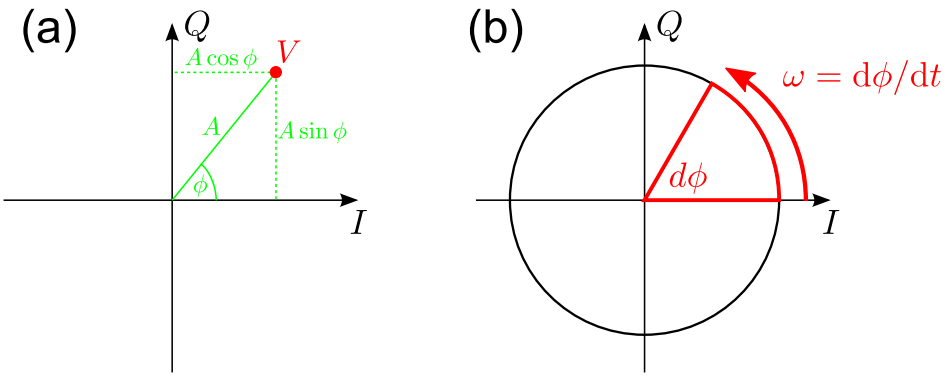

Figure 6.1: Schematic representation of heterodyne detection. (a) The position of the point S in the complex plane depends on amplitude and phase of the detected signal. (b) The temporal change in the phase can be expressed by the angular velocity.

As shown in fig. 6.1(a), the point V is located in the complex plane at $(A\cos\phi, A\sin\phi)$. To obtain amplitude and phase from V, the standard operations for complex numbers are used,

$$A = \sqrt{VV^*} = \sqrt{I^2+Q^2}, \tag{6.4}$$

$$\phi = \pm\arctan\frac{Q}{I}, \tag{6.5}$$

where V^* is the complex conjugate of V and the sign on the rhs of (6.5) has to be chosen appropriately so that $V = A\cos\phi + iA\sin\phi$.

For conventional reflectometry reflecting at a perfect mirror, the measurement of the phase ϕ then gives information on the position of the cutoff layer. In fact, if the microwave frequency is swept, the density profile can be reconstructed. If the cutoff layer moves due to turbulence, this movement is reflected in a change in ϕ, drawing a crescent shape in the IQ-plane.

Fig. 6.1(b) demonstrates the situation for a reflectometer subject to phase runaway (cf sec. 3.1), asymmetric density perturbations at the cutoff layer [60], or a Doppler reflectometer. The phase is increasing or decreasing in time, the *angular velocity* is given by $\omega = \mathrm{d}\phi/\mathrm{d}t$.

Since $V$is a complex number, the fluctuation spectra are two-sided, i.e. positive and negative frequencies are resolved. This gives the possibility to know in which direction the phase is evolving, which for Doppler reflectometry means the direction of propagation of the density fluctuations (the sign of $u_\perp$). Throughout all of the work, IQ-detection was used, so all spectra shown will be two-sided.

6.2 Analysis of Doppler Shifted Frequency Spectra

To check the reliability of different methods to obtain the Doppler shift f_D, an analytical Doppler shifted spectrum will be analyzed throughout this section. The shape of the spectrum is similar to an experimentally measured spectrum from the TJ-II DR. Both spectra are shown in fig. 6.2. It should be noted that the spectrum has a particularly strong $m = 0$ (zero-order reflection) component around 0 kHz, which in general is not the case for the TJ-II DR measurements. Nevertheless, the spectrum has been chosen in order to investigate the influence of the zero-order reflection on the different analysis methods. If a spectrum shows no zero-order reflection, all analysis methods yield the correct results.

Fig. 6.2 illustrates that the Doppler shifted peak is at about -500 kHz. The objective is to find the Doppler peak numerically and to extract its Doppler shift f_D, its height A_D, and its width Δf_D. The advantage of a synthetic spectrum is that the input parameters are known, so that the values obtained through the different methods can be cross-checked against the true ones.

The analytical spectrum is composed of a Lorentz function S_L representing the zero-order reflection, a Gaussian function S_G representing the Doppler peak and a noise component ξ.

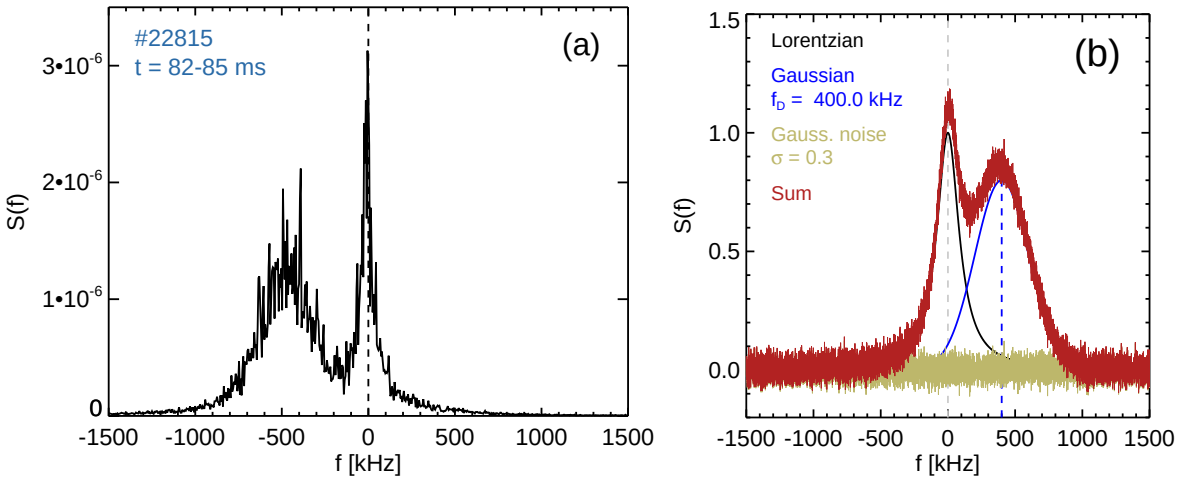

Figure 6.2: (a) Example spectrum of the TJ-II Doppler reflectometer in an ECRH plasma (`#22815, CH2, t=82-85 ms`). (b) Analytical spectrum (red) (with Lorentzian (black), Gaussian (blue) and noise (khaki) components) used to evaluate analysis methods.

The Lorentz function is defined

$$S_{\mathrm{L}}(A_{\mathrm{L}}, f_{\mathrm{L}}, \gamma, f) = \frac{A_{\mathrm{L}}}{1 + \left(\frac{f - f_{\mathrm{L}}}{\gamma}\right)^2}, \tag{6.6}$$

where f_{L}, called *location parameter*, specifies the location of the peak of the distribution and γ, called *scale parameter*, is the half width at half maximum (HWHM). A_{L} is the amplitude of the peak.

Furthermore, the Gaussian function is of the form

$$S_{\mathrm{G}}(A_{\mathrm{G}}, f_{\mathrm{G}}, \sigma, f) = A_{\mathrm{G}} e^{-\frac{(f - f_{\mathrm{G}})^2}{2\sigma^2}}. \tag{6.7}$$

Here, A_{G} is the amplitude of the peak, f_{G} the position of the center of the peak and σ controls the width of the peak, with about 68% of the area under the distribution within the interval $[f_{\mathrm{G}} - \sigma, f_{\mathrm{G}} + \sigma]$. The HWHM is $\sqrt{2 \ln 2}\sigma$.

The normally distributed noise component $\xi(\mu, \sigma)$ with zero mean $\mu = 0$ and standard deviation $\sigma = 0.03$, $\xi(0, 0.03)$, is added to simulate the noisy character of the spectra. The complete spectrum thus is

$$S(A_{\mathrm{L}}, f_{\mathrm{L}}, \gamma, A_{\mathrm{G}}, f_{\mathrm{G}}, \sigma, f) = S_{\mathrm{L}}(A_{\mathrm{L}}, f_{\mathrm{L}}, \gamma, f) + S_{\mathrm{G}}(A_{\mathrm{G}}, f_{\mathrm{G}}, \sigma, f) \ + \xi(0, 0.03). \tag{6.8}$$

Since the Lorentzian S_{L} describes the zero-order reflection, $f_{\mathrm{L}} = 0$. In addition a scale parameter of $\gamma = 100$ kHz is chosen, representing well the example spectrum in fig. 6.2(a). The Doppler peak amplitude and width are fixed at $A_{\mathrm{G}} = 0.8$ and $\sigma = 200$ kHz.

With the fixed values above in the following

$$S(A_{\mathrm{L}}, f_{\mathrm{L}}, \gamma, A_{\mathrm{G}}, f_{\mathrm{G}}, \sigma, f) = S(A_{\mathrm{L}}, 0, 100 \text{ kHz}, 0.8, f_{\mathrm{G}}, 200 \text{ kHz}, f). \tag{6.9}$$

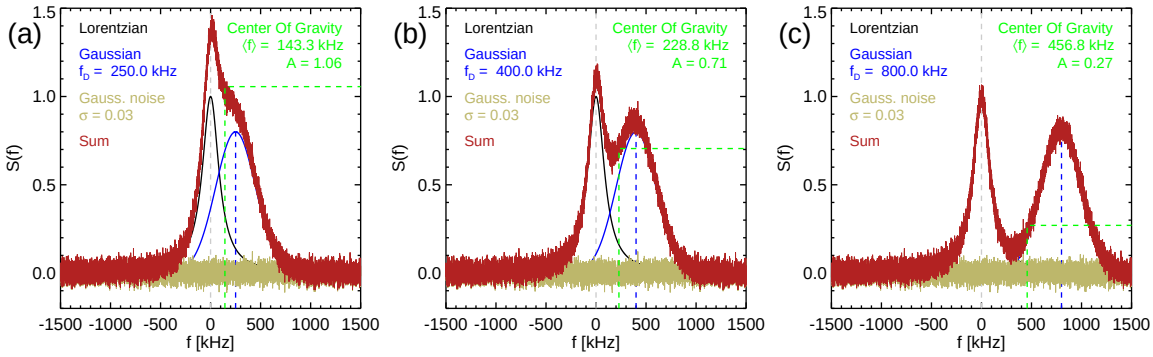

Figure 6.3: Analytical spectra with COG analysis result indicated in green. The influence of the zero-order reflection is strong in all cases (a)-(c). For details refer to the text.

In order to test the different methods, in each section three descriptive examples with $f_G = 250, 400$ and 800 kHz will be shown and a systematic study varying f_G from 100 to 1000 kHz and varying A_L from 0 to 1 is presented.

Three principal ways have been used throughout this work to obtain the Doppler shift f_D of a spectrum: calculation of the *center of gravity of the spectrum (COG)* (also called *weighted mean*), *fit to the power spectrum (SFIT)* $S(f)$ and *fit to the asymmetric part of the power spectrum (AFIT)* $S^*(f)$. They will be presented in the following along with their benefits and drawbacks. For clarity, in the three following sections (6.2.1 – 6.2.3) the Doppler shift and amplitude obtained by the different methods are called f_D and A_D, respectively. These values are compared to the input Doppler shift and amplitude f_G and A_G.

6.2.1 Center of Gravity

The center of gravity (COG), also called weighted mean, $\langle f \rangle$ of a spectrum $S(f)$ is defined

$$\langle f \rangle = \frac{\int_{-\infty}^{\infty} f S(f) \mathrm{d}f}{\int_{-\infty}^{\infty} S(f) \mathrm{d}f} \tag{6.10}$$

and is a measure for its asymmetry. If the spectrum consists only of a Gaussian, i.e. $S(f) = S_G(f)$, the COG yields the position of the center of the peak, i.e. $\langle f \rangle = f_G$. If the spectrum is not noisy, its value at $\langle f \rangle$ will then represent the amplitude of the Gaussian, i.e. $S(\langle f \rangle) = A_G$. However, as depicted in fig. 6.2(a), a zero-order reflection component can be existent in measured Doppler reflectometry spectra, with the effect that the frequency obtained by calculating the COG is not the value of the Doppler shift, but lies somewhere between 0 and the true Doppler shift f_G.

This effect is illustrated in fig. 6.3, where the Doppler shift is varied between 250 (a), 400 (b) and 800 kHz (c). In each plot the three components (S_L (black), S_G (blue), ζ (yellow)) are shown along with the resulting spectrum (red). For small f_D, the contribution from the Lorentzian influences the measurement and an amplitude

	f_G [kHz]	f_D/f_G	A_D/A_G
(a)	250	0.573	1.320
(b)	400	0.572	0.882
(c)	800	0.571	0.338

Table 6.1: Values obtained normalized to respective input values by COG analysis (cf fig. 6.3). The errors in Doppler shift and amplitude are large.

higher than A_G is obtained. For 800 kHz (c), the COG analysis yields a false Doppler shift close to the minimum between S_L and S_G. The f_D and A_D values obtained through COG analysis compared to their input equivalents are shown in tab. 6.1.

A more systematic analysis is shown in fig. 6.4. In (a), the Doppler shift f_G of the Gaussian is varied between 100 and 1000 kHz. The frequency obtained through COG analysis f_D normalized to the input Doppler shift f_G (blue circles) is below 1 (blue line), meaning $f_D < f_G$. The amplitude A_D normalized to the input amplitude A_G (magenta diamonds) is influenced by the Lorentzian distribution when f_G is small, yielding a value higher than the theoretical one ($A_D/A_G > 1$). As f_G increases, the amplitude yielded by the COG method is wrong, because f_D lies between 0 and f_G. The noisy character of A_D/A_G is due to the Gaussian noise ξ of the spectra. In fig. 6.4(b) the amplitude of the zero-order Lorentzian component A_L is varied between 0 and 1 while $f_G = 700$ kHz. If there is no central component in the spectrum, the COG analysis yields the correct values for f_G and A_G. However, as the amplitude of the central peak increases, the errors in f_D and A_D increase as well. The higher the zero-order reflection, the larger the errors the COG analysis yields.

In conclusion, the COG method is not suited to calculate the position and amplitude of the Doppler peak in the power spectrum if there is a zero-order component in the spectrum. However, most spectra measured with the TJ-II Doppler reflectometer show

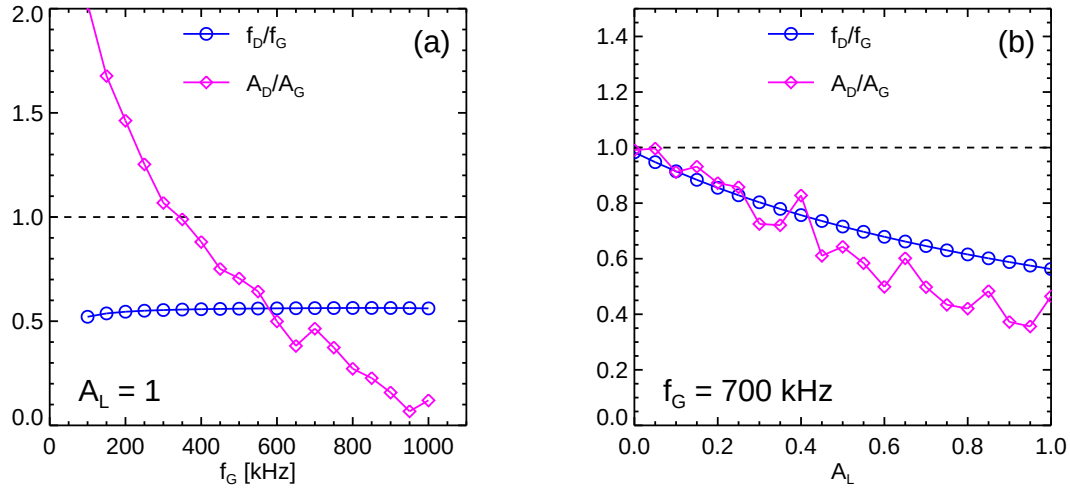

Figure 6.4: Mean frequency $\langle f \rangle$ and amplitude $S(\langle f \rangle)$ obtained through COG analysis. Values are normalized to the input values f_G and A_G. (a) Changing the input Doppler shift f_G and (b) changing the zero-order amplitude A_L.

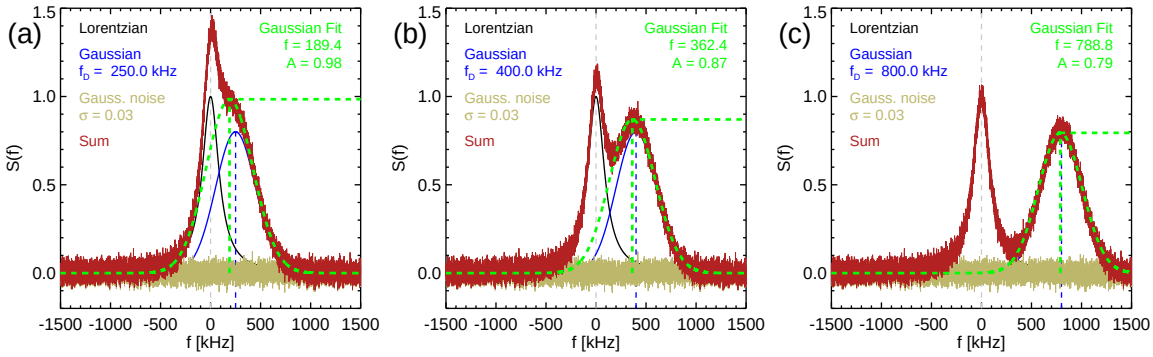

Figure 6.5: Analytical spectra and gaussian fits to obtain Doppler shift f_G and Doppler peak amplitude A_G. (a) If the Doppler shift is very small, the fitting method does not yield the correct values. (b-c) A well separated Doppler peak can be fitted and correct values are obtained.

no zero-order contribution. Despite its disadvantages, the COG method is reliable when used to extract the sign of the Doppler shift, which yields the direction of the plasma propagation [94, 95]. This can be done on fast timescales and therefore it can be used in the analysis of perpendicular velocity or radial electric field fluctuations [83, 116].

6.2.2 Fit to the Power Spectrum

Another way to obtain f_G and A_G and also the width of the Doppler peak is to fit a Gaussian (see (6.7)) to the power spectrum, hereafter called *SFIT* method. Throughout this entire work, the Levenberg-Marquardt method is used for fitting [117]. Fitting of a Gaussian is only possible when the Doppler peak is sufficiently separated from the zero-order reflection. Sufficiently means in this context that there has to be a minimum in the spectrum between zero-order reflection and Doppler peak. If this is the case, a fit to the power spectrum is a robust and direct method to obtain f_G and A_G.

Fig. 6.5 shows the three cases from fig. 6.3, analyzed by fitting a Gaussian (green) to the spectrum (red). To fit a gaussian to the spectrum, it has to be avoided that the zeroth order is fitted, so in the analysis the fitting is constrained to the frequencies $f > 150$ kHz. In (a), the Doppler shifted component of the spectrum is not separated sufficiently, and the gaussian fit does not yield the correct values of the Doppler component. It instead fits the righthand slope of the spectrum. In (b), the errors in f_D and A_D are about 10% because there is still a contribution from the lorentzian. The fit yields reasonably good values when the Doppler peak is well separated from 0 kHz, as can be seen in (c). The results are summarized in tab. 6.2.

The convergence of the resulting values to the input values is indicated in fig. 6.6, which is similar to fig. 6.4. In (a), the Doppler shift obtained by the fit normalized to the input Doppler shift (f_D/f_G) is plotted against the input Doppler shift f_G (blue circles). The magenta diamonds show the fit amplitude normalized to the input amplitude (A_D/A_G). As the Doppler shift becomes larger, the values obtained by fitting a Gaussian to the spectrum converge to the input values, as suggested by fig. 6.5. In fig. 6.6(b) the dependence of the obtained Doppler shift (input: $f_G = 700$ kHz)

	f_G [kHz]	f_D/f_G	A_D/A_G
(a)	250	0.758	1.231
(b)	400	0.906	1.088
(c)	800	0.986	0.993

Table 6.2: Values obtained normalized to respective input values by fitting a Gaussian to the power spectrum (cf fig. 6.5).

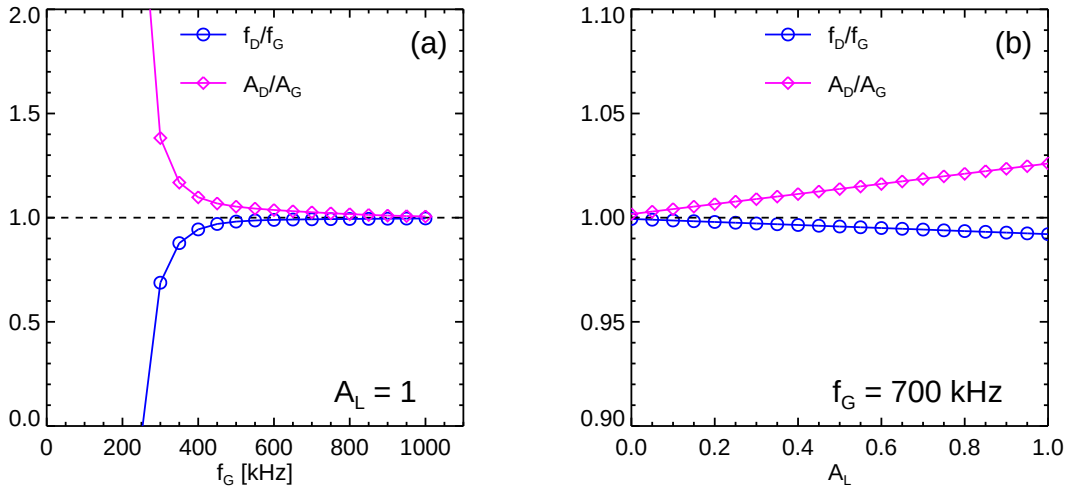

Figure 6.6: Doppler shift and Doppler peak amplitude normalized to their model values obtained through a gaussian fit to the power spectrum for (a) changing input Doppler shifts f_G and (b) changing zero-order amplitudes A_L.

and Doppler peak amplitude (input: $A_G = 0.8$) on the amplitude of the zero-order component is shown. Since there is a minimum between Doppler peak and zero-order component, the values obtained by fitting a Gaussian to the spectrum are good for small values of A_L. As A_L increases, its influence on the fit values becomes visible and the data deviate from the input Doppler shifts and amplitudes. Nevertheless, the error in the f_G and A_G determination is below 3%. Taking into account that the test spectrum chosen reflects a comparatively bad situation which is rather uncommon in the TJ-II DR measurements, these errors can be interpreted as upper limits in the Doppler peak estimation.

6.2.3 Fit to the Asymmetric Part of the Power Spectrum

Another way to obtain f_G, A_G and σ is the analysis of the asymmetric part of the power spectrum $S^*(f)$ (hereafter called *AFIT* method), defined

$$S^*(f) = S(f) - S(-f). \tag{6.11}$$

The advantage of this method is that only the asymmetric components of S will be contained in S^*. A schematic is depicted in fig. 6.7(a), where $S(f)$ (gray) contains a zero-order reflection. Subtracting $S(-f)$ (red) from $S(f)$, the asymmetric part of the

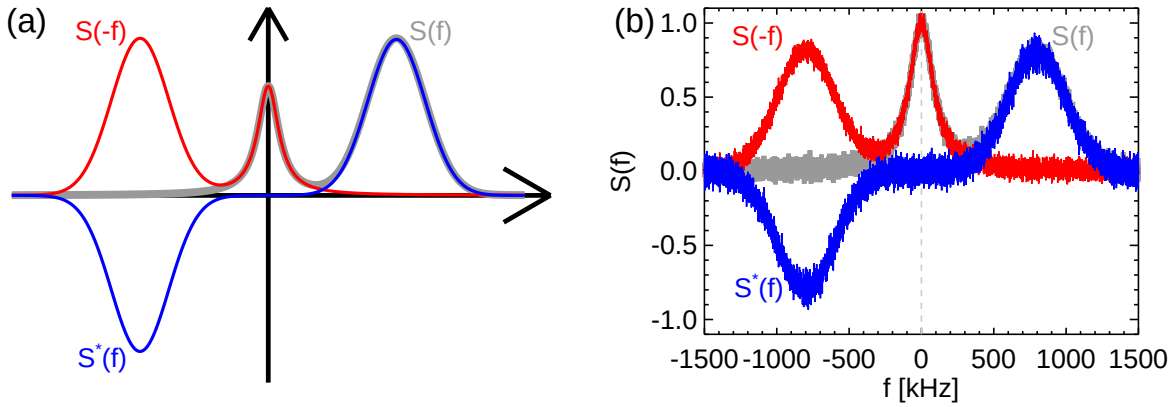

Figure 6.7: Doppler shifted spectra $S(f)$ (gray), mirrored $S(-f)$ (red) and the asymmetric part $S^*(f)$ (blue). (a) Schematic and (b) the example spectrum from fig. 6.3(c).

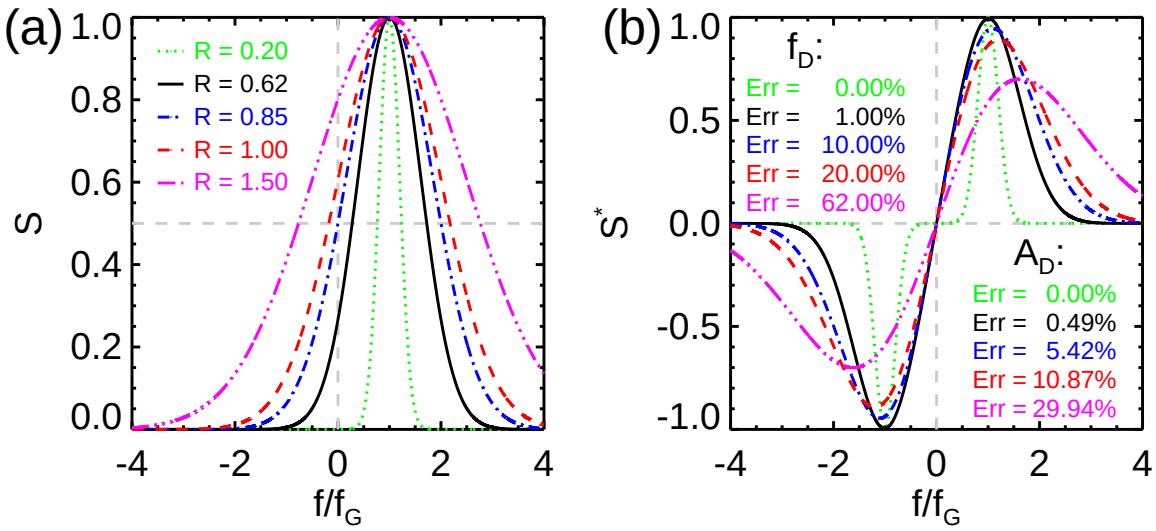

Figure 6.8: Evaluation of the applicability of the AFIT method. (a) Gaussians with different widths σ. The factor R denotes the relative width, $\sigma/|f_G|$. (b) Corresponding asymmetric spectra and errors in the determination of f_D and A_D. The larger the relative width, the larger the errors.

power spectrum $S^*(f)$ (blue) is obtained. As indicated by fig. 6.7(a), the zero-order reflection is canceled out. Fig. 6.7(b) shows the synthetic spectrum from fig. 6.3(c). The zero-order reflection has vanished and the Doppler shifted peak is still visible in the spectrum, with positive amplitude at $f = 800$ kHz and negative amplitude at $f = -800$ kHz.

However, it has to be taken into account that if the width of the Doppler peak is large compared to the Doppler shift, the AFIT method is subject to errors. For a quantitative analysis, the *relative width* of the Gaussian is defined

$$R = \frac{\sigma}{|f_G|}. \tag{6.12}$$

The meaning of the relative width is demonstrated in fig. 6.8(a), where five Gaus-

sians are plotted for different values of R (0.20, 0.62, 0.85, 1.00, 1.50). The frequency axis is normalized to the Doppler shift f_G. For small R the Gaussian is well separated from $f/f_G = 0$ and its flanks are steep. The larger the value of R becomes, the wider the distribution, and contributions to S in the negative frequency part become important. The impact on the asymmetric spectrum S^* is shown in fig. 6.8(b). For the smallest value of R (0.20, green), the asymmetric spectrum has two well-separated components in the negative and in the positive frequency part of the spectrum with a flat part between them. The error in this case for both the Doppler shift and the amplitude analysis is 0.00%. As the relative width increases (0.62, black), the flat part between negative and positive frequencies in the asymmetric spectrum vanishes and the analysis is subject to errors, for $R = 0.62$ the errors are 1.00% and 0.49% for the analysis of Doppler shift and amplitude, respectively. For larger relative widths, the peak in the asymmetric spectrum moves to frequencies higher than the Doppler shift and the amplitude decreases, falsifying the analysis. The error in the determination of the Doppler shift is above 20% for values of $R > 1$. The errors in the amplitude determination are always approximately half of the errors of the Doppler shift determination.

Fig. 6.9 shows the dependence of the error in the determination of f_G and A_G as a function of R. As seen in fig. 6.8(b), the error in the determination of A_G is smaller than the one for f_G. The plot shows that for $R \leq 0.6$, the errors are below 1%, which is acceptable in the analysis of Doppler shifted spectra.

Equation (6.12) has a singularity at $f_G = 0$ leading to $R \to \infty$, although the absolute width σ is finite. However, the fact that R goes to infinite for small f_G makes sense in the context of figs. 6.8 and 6.9. The spectrum is symmetric for $f_G = 0$, so it is not possible to analyze the asymmetric spectrum, because $S^*(f) = 0$ for $S = S(f_G = 0)$.

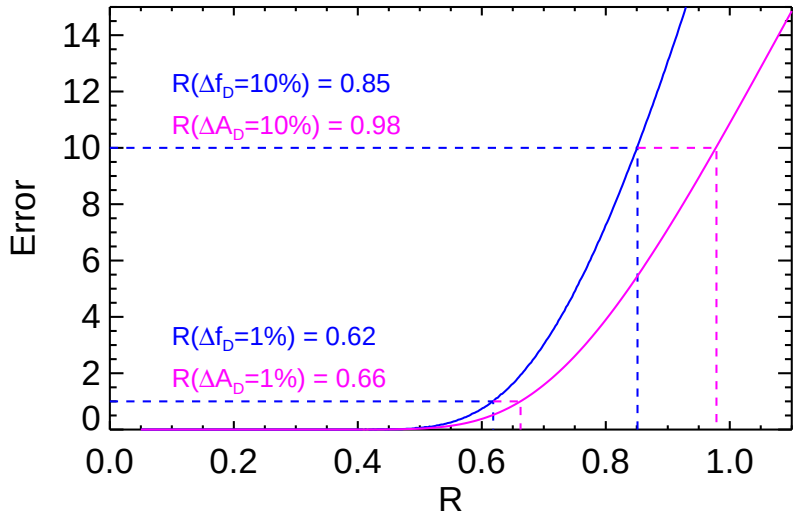

Figure 6.9: Dependence of the error in the determination of the Doppler shift (blue) and Doppler peak amplitude (magenta) on the relative width of the Doppler peak R.

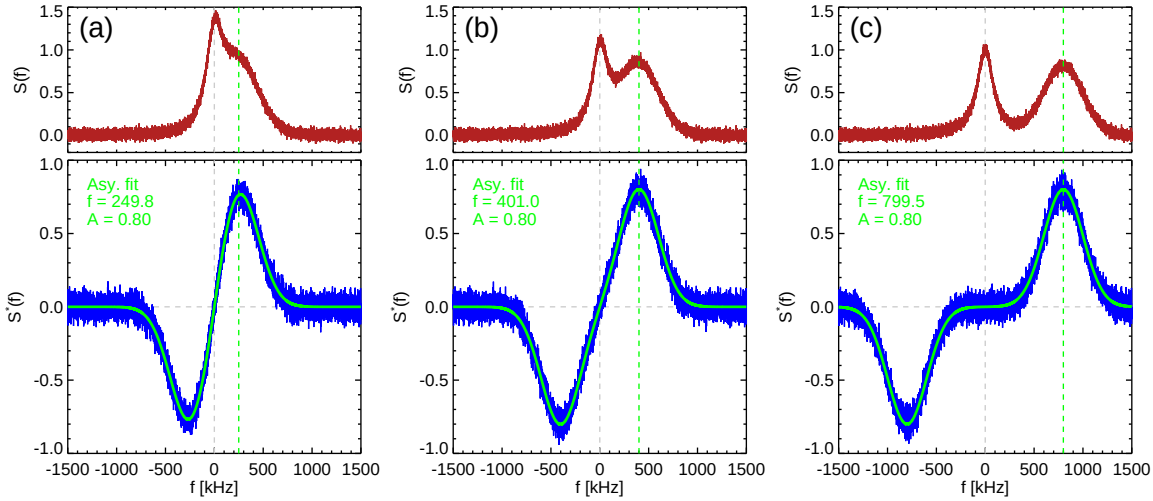

Figure 6.10: Analytical spectra and gaussian fits to the corresponding asymmetric spectra $S^*(f)$ to obtain Doppler shift f_G and Doppler peak amplitude A_G. (a-c) The resulting values have errors below 2% for all cases ($f_G = 250, 400$ and 800 kHz).

This analysis underlines the importance of a good spectral resolution of a Doppler reflectometer system (cf sec. 3.2.2). In the TJ-II Doppler reflectometer, values of R are normally around 0.35 and almost always below 0.5, depending on plasma characteristics, beam launch angle and microwave frequency, so the AFIT method is well-suited for the analysis of the Doppler shifted spectra in TJ-II. The experimental spectrum from fig. 6.2(a) has a relative width of $R = 0.338$ and thus lies in the range of fig. 6.9 where the errors can be neglected.

To analyze the asymmetric spectrum S^*, the superposition of two Gaussians – one positive and one negative but symmetric – has to be fitted to S^*, written

$$S_{\text{fit}}(f) = S_G(A_G, f_G, \sigma, f) - S_G(A_G, -f_G, \sigma, f). \tag{6.13}$$

Free parameters are A_G, f_G and σ. Note that S_{fit} is an odd function, $-S_{\text{fit}}(f) = S_{\text{fit}}(-f)$ and in particular $S_{\text{fit}} = 0$ for $f_G = 0$, i.e. if the spectrum is not Doppler shifted, the asymmetric spectrum is 0.

An analysis similar to sections 6.2.1 and 6.2.2 is demonstrated in fig. 6.10. The upper plots show the spectra S and in the lower plots the asymmetric parts of the spectra S^* are depicted. The asymmetric spectra S^* do not contain the Lorentzian contribution and the fits yield values close to the input values for Doppler shift f_D and Doppler peak amplitude A_D, shown in tab. 6.3.

The applicability of the gaussian fit to the asymmetric spectrum is demonstrated by fig. 6.11. In (a), f_D/f_G is plotted against f_G, while the amplitude of the zero-order reflection is maintained constant at $A_L = 1$. For all Doppler shifts larger than 200 kHz the method yields correct results with uncertainties below 2%. The points at 100 and 150 kHz are not correct, because the width of the Doppler peak is larger than its frequency $\sigma > f_G$, as discussed above. However, when $\sigma \leq f_G$ holds, both the Doppler shift and amplitudes values obtained through the fit to S^* yield correct

	f_G [kHz]	R	f_D/f_G	A_D/A_G
(a)	250	0.80	0.999	1.000
(b)	400	0.50	1.002	1.002
(c)	800	0.25	0.999	1.001

Table 6.3: Values obtained normalized to respective input values by fitting to S^*, the asymmetric part of the power spectrum (cf fig. 6.10).

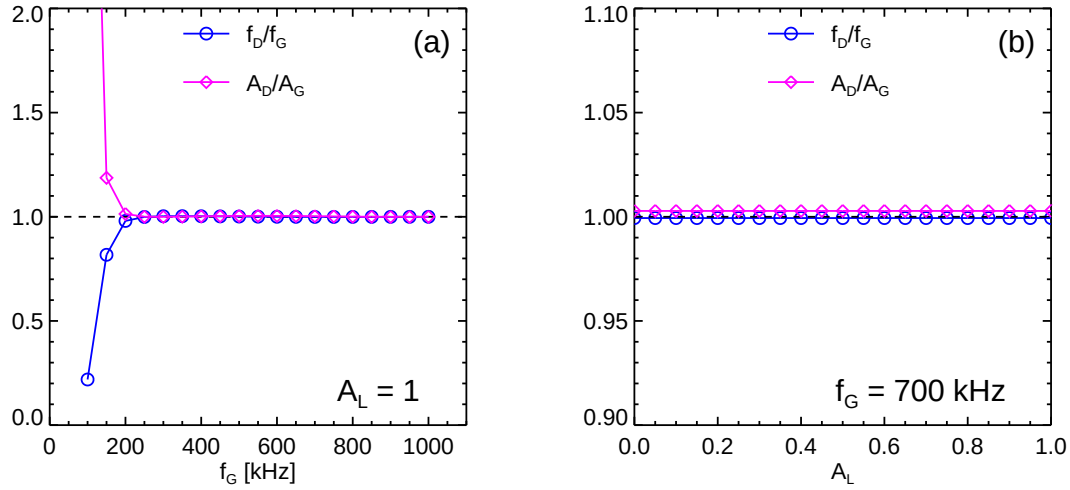

Figure 6.11: Doppler shift and Doppler peak amplitude normalized to their model values obtained through a gaussian fit to the asymmetric part of the power spectrum (AFIT) for (a) changing input Doppler shifts f_G and (b) changing the zero-order amplitude A_L.

values, underlining the reliability of the method.

Fig. 6.11(b) shows the same as (a) but the height of the Lorentzian is varied. Since the Lorentzian is eliminated in S^*, there is no dependence on A_L.

6.2.4 Summary of Analysis Methods

In conclusion, three methods suitable to extract the Doppler shift f_G and Doppler peak amplitude A_G have been presented in this section. They are

- Center of gravity (COG),
- Fit to the power spectrum (SFIT),
- Fit to the asymmetric part of the power spectrum (AFIT).

If the Doppler peak is sufficiently separated from $f = 0$ ($R < 0.6$), the AFIT method (cf sec. 6.2.3) can reliably be used. The method fits the asymmetric part of the power spectrum S^* and thus avoids any influence of the zero-order reflection. If $R < 0.6$ is provided, obtained results generally are subject to errors below 1%.

The SFIT (cf sec. 6.2.2) method can be used when the Doppler peak is separated from the zero-order reflection. However, if a zero-order reflection is present in the

spectrum, it will have an effect on the measured Doppler shift and amplitude. The advantage of the SFIT over the AFIT method is that if there is no zero-order reflection, it can be used for arbitrary values of R.

The COG method (cf sec. 6.2.1) is a simple method which gives reliable results if the spectrum has no zero-order reflection component or if interest is only paid to the sign of the rotation or to fast changes in rotation velocity. Hence the COG method is suited to analyze velocity fluctuations in the plasma on fast timescales. It should be noted that the example spectrum above is a particularly poor spectrum which is uncommon in the TJ-II DR measurements. In general, no zero-order reflection is visible and the COG method yields reliable results.

Chapter 7

Perpendicular Velocity of Density Fluctuations

The perpendicular velocity of density fluctuations $u_\perp$ is a magnitude of exceptional interest in magnetically confined fusion plasmas. As mentioned in sec. 2.2, turbulence theory predicts a possible tearing apart of turbulent structures (eddies) when the velocity shear is sufficiently large, resulting in a reduction of turbulence [24, 32]. Furthermore, zonal flows can suppress turbulence through self-regulating mechanisms [28, 29]. Measurement and interpretation of radial $u_\perp$ profiles and $u_\perp$ fluctuations is thus extremely important and can help to understand turbulence suppression and ultimately shed some light on the many questions regarding the complex processes involved in the L-H transition.

In this chapter, $u_\perp$ profiles obtained with the TJ-II Doppler reflectometer will be presented for different plasma conditions. In ECRH plasmas, both positive and negative $u_\perp$ profiles are observed, and the transition between the two is investigated in detail. The emergence of a strong $u_\perp$ shear is observed in TJ-II H-mode plasmas, strong enough to give rise to two Doppler peaks in the DR spectra. Furthermore, measurements at different $k_\perp$ yield the same $u_\perp$ values, meaning that either $v_{\rm ph} \ll v_{E\times B}$ or that $v_{\rm ph}$ does not depend on $k_\perp$.

Furthermore, high temporal resolution measurements of the L-H transition reveal a reduction of density fluctuations accompanied by an increase in the oscillating shear flow amplitude. The mean E_r shear starts rise about one millisecond after the L-H transition and is established roughly three milliseconds afterwards. Finally, close to the L-H transition threshold, a coupled oscillatory behavior of density turbulence and sheared flows is observed which shows a characteristic predator-prey relation.

7.1 Perpendicular Velocity Profiles in ECRH Plasmas

In this section $u_\perp$ profiles in ECRH plasmas measured with Doppler reflectometry are presented. They are put in context with previously published work treating the con-

nection between poloidal velocities, turbulence behavior and turbulence suppression. However, the previous findings did not cover the important density gradient region (Langmuir probes), lacked measurement precision (HIBP) or have not been able to provide absolute velocity values (conventional reflectometry).

The TJ-II Doppler reflectometer is able to provide $u_\perp$ measurements with high spatiotemporal resolution in the density gradient region, extending the before mentioned group of diagnostics and providing new information on the dynamic behavior of edge perpendicular velocities and density fluctuations.

7.1.1 Introduction

In TJ-II ECRH plasmas, the poloidal plasma velocity was investigated mainly with Langmuir probes [96]. It was found by Hidalgo *et al.* [118] that the development of edge poloidally sheared flows requires a threshold density $n_{\mathrm{th}} \approx 0.6 \times 10^{19}$ m^{-3}. The development of these edge sheared flows – which are connected to the development of a negative E_r – is accompanied by an increase in the level of edge turbulence and edge turbulent transport [118]. Furthermore, the increase in poloidal velocity shearing rate $\mathrm{d}v_\theta/\mathrm{d}r$ was shown to be connected to an increase in plasma density gradient, a driving term in plasma turbulence. In follow-up measurements, Pedrosa *et al.* discovered that once the sheared flow is fully developed, the turbulence level and turbulent transport decrease [119], while Alonso *et al.* used fast cameras to statistically investigate the shape and ordering of turbulent structures close to n_{th} [120]. Melnikov *et al.* confirmed the Langmuir probe findings on the E_r reversal close to n_{th} with heavy ion beam probe measurements covering a large radial range [121]. Furthermore, (conventional) reflectometry was used to investigate the velocity shear layer characteristics [94] and revealed that plasma collisionality is a key parameter in the $u_\perp$ reversal [93]. Simultaneous high temporal resolution measurements at two radial positions showed that the radial origin of the $u_\perp$ reversal is located at the radial position of maximum density gradient [95], explained in detail in sec. 7.1.3.

7.1.2 Doppler Reflectometry Measurements

Radial profiles of the flux surface averaged perpendicular velocity $\langle u_\perp \rangle$ for different line-densities $\langle n_e \rangle$ are plotted in fig. 7.1. The heating power in this experiment is $P_{\mathrm{ECRH}} = 500$ kW. The radial positions move outward as the density increases due to density profile steepening. For $\langle n_e \rangle < n_{\mathrm{th}}$, perpendicular velocities are positive in the whole radial range, corresponding to positive E_r. At the outermost measuring position, $\langle u_\perp \rangle \approx 3$ km/s. There is a small dip in $\langle u_\perp \rangle$ around $\rho = 0.77$, and towards the plasma center $\langle u_\perp \rangle$ increases up to values of roughly 4 km/s. In the high density case ($\langle n_e \rangle > n_{\mathrm{th}}$), $\langle u_\perp \rangle$ is negative in the whole radial measurement range. Strongest negative velocities (~ -3 km/s) are found close to the plasma edge, while further inside, the plasma slows down to about -1 km/s.

The two cases above and below n_{th} were well-known – although further in the edge – from previous measurements [118, 119] and theoretical estimations [122]. However, the

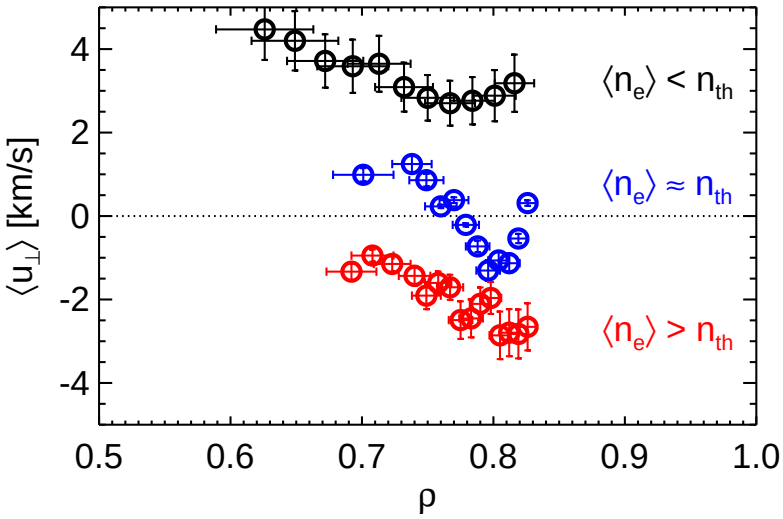

Figure 7.1: (#20281, #20285, #20294) Radial $\langle u_\perp \rangle$ profiles for $\langle n_e \rangle < n_{\rm th}$ (black), $\langle n_e \rangle \approx n_{\rm th}$ (blue) and $\langle n_e \rangle > n_{\rm th}$ (red). For $\langle n_e \rangle \approx n_{\rm th}$, negative $\langle u_\perp \rangle$ values are observed only at $\rho \approx 0.8$, while the remaining radial range shows positive perpendicular velocities.

intermediate case $\langle n_e \rangle \approx n_{\rm th}$ shows an interesting effect. The perpendicular velocity does not reverse its direction first in the plasma edge or center when $\langle n_e \rangle$ goes above $n_{\rm th}$, but at an intermediate position (here $\rho \approx 0.8$). This dip causes two velocity shear layers with strong $\langle u_\perp \rangle$ gradient at $\rho \approx 0.78$ and 0.82. It has been observed previously, that for the subsequent rise of line-average density, the turbulence amplitude slightly decays in spite of a steepening edge pressure gradient, a driving term in plasma turbulence [118, 119]. This effect could be interpreted as turbulence suppression through shear flows generated at $n_{\rm th}$. Possible generating mechanisms of the shear flows could be Reynolds stress [25, 32] or a spatial separation of ion- and electron-root regimes [123].

A detailed investigation on the dynamics of the perpendicular velocity reversal was done with conventional reflectometry before the DR was installed. It was found that not only the origin of the velocity reversal is at an intermediate radial position, but also the terminal point, when the velocity shear layer vanishes. The study is summarized in the following section.

7.1.3 Velocity Shear Layer Formation Investigations with Conventional Reflectometry

In order to investigate the formation of the edge velocity shear layer (VSL), the line-averaged density $\langle n_e \rangle$ was modulated. In this way, the formation and the disappearance of the VSL occurred in each discharge. In this experiment, the plasma was heated on-axis with $P_{\rm ECRH} = 420$ kW. The frequencies of the two-channel fast frequency hopping reflectometer (Sec. 4.3) were held fixed during each discharge, and changed on a shot-to-shot basis. Since the frequency of each channel corresponds to a radial measurement position, the sign of the perpendicular velocity of density fluctuations $u_\perp$ is monitored simultaneously at two different radial positions due to the slightly oblique incidence of

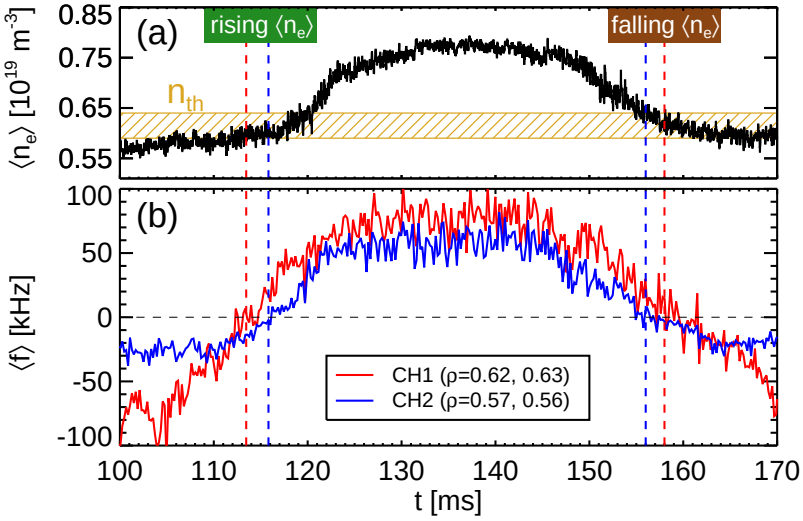

Figure 7.2: (#18917) (a) Time trace of $\langle n_e \rangle$, crossing twice the threshold density n_{th} (shaded area). (b) Respective center of gravity of the power spectra of the two reflectometer channels. The time instant of the perpendicular velocity reversal is indicated by vertical lines. The radial positions refer to the measurement position of the respective channel at the time instant of the crossing (and back-crossing) of n_{th}.

the reflectometer mentioned in Sec. 4.3. If t_{CH1} and t_{CH2} are the time instants at which $u_\perp$ reverses sign at channel 1 (CH1) and channel 2 (CH2), respectively, the time delay $\Delta t = t_{\mathrm{CH2}} - t_{\mathrm{CH1}}$ is positive if $u_\perp$ changes sign first at the radial position of CH1, and negative if the reversal occurs first at the position of CH2. In all discharges CH2 was the channel measuring at more interior positions than CH1. Their exact radial values ρ are determined for each discharge and corresponding time instant using the density profiles obtained by AM reflectometry (Sec. 4.2).

In fig. 7.2, a discharge representative for the discharges in the series is shown. In (a), the modulation of $\langle n_e \rangle$ is depicted. The approximate value of the threshold density n_{th} is represented by the shaded area. The line-density crosses n_{th} twice: First at $t \approx 115$ ms, the formation of the VSL takes place, while at $t \approx 157$ ms, it disappears. The center of gravity $\langle f \rangle$ of the power spectra of the two reflectometer channels is shown in fig. 7.2(b). Negative and positive $\langle f \rangle$ correspond to ion- and electron-diamagnetic velocity, respectively. When the VSL is formed, the perpendicular velocity reverses its sign first at $\rho = 0.62$ (CH1, red), then at $\rho = 0.57$ (CH2, blue), marked by vertical lines. The order of magnitude of the delay is of a few milliseconds. When the shear layer disappears, the reversal of the plasma velocity is first noted at $\rho = 0.56$ (CH2) and then at $\rho = 0.63$ (CH1). The values for ρ at the formation and at the vanishing of the VSL are similar due to similar density profiles at the transition point.

Fig. 7.3 shows the reconstructed phase ϕ of the two reflectometer channels for the same discharge as in fig. 7.2 when the VSL is established. Before the velocity reversal takes place, the plasma rotates in ion-diamagnetic direction (ϕ decreases). Reflectometer CH1 notes the velocity reversal approximately 2.5 ms before CH2, which is the minimum of the polynomial fits indicated by dashed lines. Afterwards, both

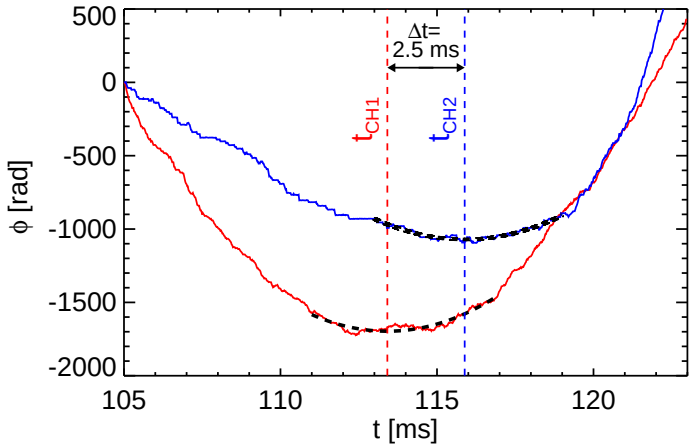

Figure 7.3: (#18917) Reconstructed phase ϕ for the discharge from fig. 7.2 at the first crossing ($t \approx 1115$ ms) of n_{th}. The second-grade polynomial fits are indicated by black dashed lines. Reflectometer CH1 (red) notes the velocity reversal approximately 2.5 ms before CH2 (blue).

channels are measuring rotation of the plasma in the electron-diamagnetic direction.

Fig. 7.4(a) shows the time delays Δt in dependence on the radial measurement position when $\langle n_e \rangle$ exceeds n_{th}, marked by circles, and when it falls below n_{th}, represented by diamonds. The values for t_{CH1} and t_{CH2} are obtained by fitting a second degree polynomial to the reconstructed phase (cf fig. 7.3) and calculating the minimum (emergence of the shear) or the maximum (disappearance of the shear) analytically using the first derivative. The vertical error bars are obtained by varying the length of the temporal window for the fit from 8 to 14 ms and calculating the standard deviation of the results. Each radial position corresponds to the mean of the two reflectometer measurement positions $\rho = (\rho_{\mathrm{CH1}} + \rho_{\mathrm{CH2}})/2$, obtained using the profiles from AM-reflectometry shown in fig. 7.4(c). The radial measurement error is shown for one point and is representative for the error in all measurements. When the density rises (emergence of the velocity shear), for radii $\rho > 0.68$, the perpendicular velocity reverses sign first at the more internal, and then at the more external positions, because $\Delta t < 0$. However, for $\rho < 0.68$, the contrary takes place: The change in perpendicular velocity is first noted by the exterior channel and then by the interior channel ($\Delta t > 0$). When $\langle n_e \rangle$ falls below the threshold density (disappearance of the VSL), the internal measurements show that the interior channel notes the change first, while the external measurements show that the exterior channel first measures the change in the $u_\perp$ sign.

This phenomenon can be explained as follows: when $\langle n_e \rangle$ goes above n_{th}, the VSL starts to form at $\rho \approx 0.68$. Since $\Delta t \approx 0$, this radius is the origin of the formation of the shear layer. For simplicity $\rho_0 = 0.68$ is defined. The formation of the shear layer continues, propagating outward for $\rho > \rho_0$ and inward for $\rho < \rho_0$. The process of disappearance of the VSL is the direct opposite: As $\langle n_e \rangle$ falls below n_{th}, the VSL starts to contract, the process ending at ρ_0. Hence the formation of the VSL as well as its disappearance occur at the same radial position.

The lower part of fig. 7.4 shows the density profiles (c) used for analysis and the

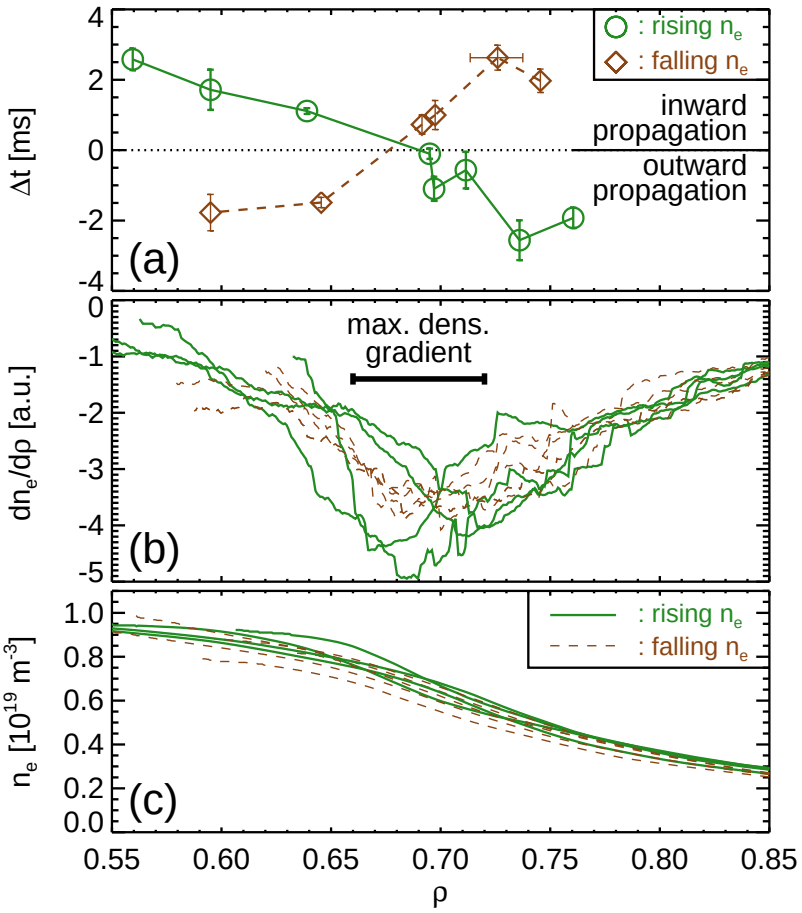

Figure 7.4: (#18907-11, #18916-18) (a) Time delays Δt of the formation and disappearance of the VSL. It forms at $\rho \approx 0.68$ and expands radially (circles). When the shear layer disappears (diamonds), it contracts and vanishes also at $\rho \approx 0.68$. The position of the origin and endpoint of contraction coincides with the position of maximum density gradient, shown in (b). The gradient is most pronounced at $\rho \approx 0.7$. (c) Density profiles when the VSL is established (continuous lines) and when it disappears (dashed lines).

corresponding density gradients (b). Continuous lines correspond to the density profiles when the VSL emerges while dashed lines show the density profiles at the moment when the line-density falls below the threshold density (disappearance of the VSL). The error in determining the radial position of the profile is $\Delta\rho = \pm 0.012$, depending on the initialization in the plasma edge. The value for $\Delta\rho$ is obtained by variation of the assumed edge density between $n_e(\rho = 1) = 0.03$ and 0.10×10^{19} m^{-3}. It should be noted that the profiles are very similar when the line-density crosses the threshold density. The region of maximum density gradient ($\rho = 0.66 - 0.72$) is marked in fig. 7.4(b) by the horizontal bar. The agreement between the origin (and terminal point) of the VSL ($\rho_0 = 0.68$) with the region of maximum density gradient is striking.

Fig. 7.5 shows the radial propagation velocity of the shear layer when it is formed (circles) and when it vanishes (diamonds). Positive and negative velocities correspond to outward and inward propagation, respectively. The velocity is calculated by obtain-

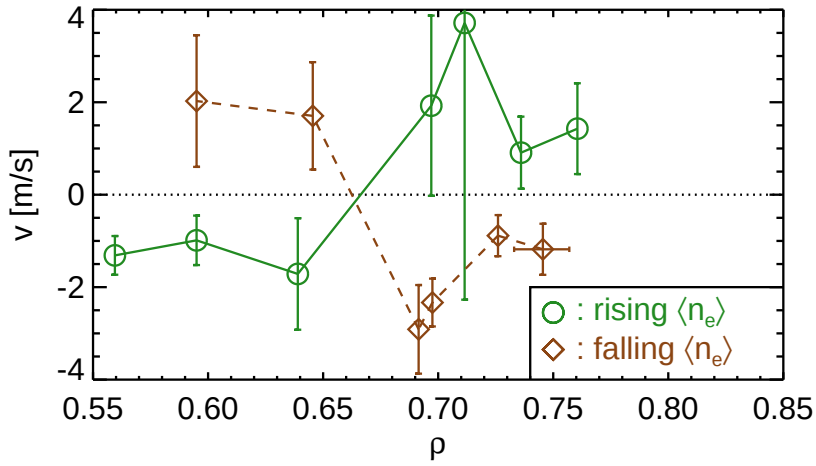

Figure 7.5: (#18907-11, #18916-18) Radial propagation velocity of the formation (circles) and the disappearance (diamonds) of the velocity shear. Positive velocities point radially outward, negative velocities point radially inward. The expansion while forming and the contraction while vanishing of the shear layer is apparent.

ing the absolute distance between the two measurement positions of the reflectometer and dividing by the time delay Δt (fig. 7.4(a)). The radial measurement error is the same as in fig. 7.4(a). Since both the radial distance of the measurements and the delays Δt are subject to errors, the error in the radial propagation velocity is calculated using the method of linear propagation of uncertainties. The shear layer starts to form at ρ_0 and expands from this point to exterior and interior regions of the plasma. The disappearance shows the inverse behavior of radial propagation velocity: the shear layer contracts radially in the direction of ρ_0. The radial velocities are of the order of some ms^{-1}. However, it has to be noted that this velocity depends on the density evolution. In the experiments, a slow density modulation was chosen in order to be able to capture the formation and disappearance of the VSL. If the density is ramped faster, the velocities in fig. 7.5 are higher.

In fig. 7.6, the mean crossphase γ between two poloidally separated Langmuir probes measuring the floating potential ϕ_{fl} at $\rho = 0.85$ is shown. The sign of γ corresponds to the sign of $u_\perp$. The upper part of the figure shows the total timeslice of a discharge where the reflectometer measures close to ρ_0 ($\rho_{\mathrm{CH1}} = 0.72$, $\rho_{\mathrm{CH2}} = 0.70$). The dashed and dotted vertical lines correspond to t_{CH1} and t_{CH2}, respectively. The propagation time of the VSL from the reflectometer channels to the probe is approximately 6 ms when the VSL forms. When it disappears, the exact time instant can not be exactly determined due to high fluctuations in the plasma edge. In the lower part, zooms to the mean crossphase when it reverses sign are shown for different discharges in which the reflectometer measurement position is between the origin of the VSL and the plasma edge. The time instant when the probe notes the velocity shear is t_{P}. In each case, the reflectometer measures the velocity reversal before the probe, meaning that the reversal occurred first at more internal positions. The radial propagation velocity of the emergence of the shear obtained from this measurement is $v = 2.9 \pm 1.0\ \mathrm{ms}^{-1}$, which

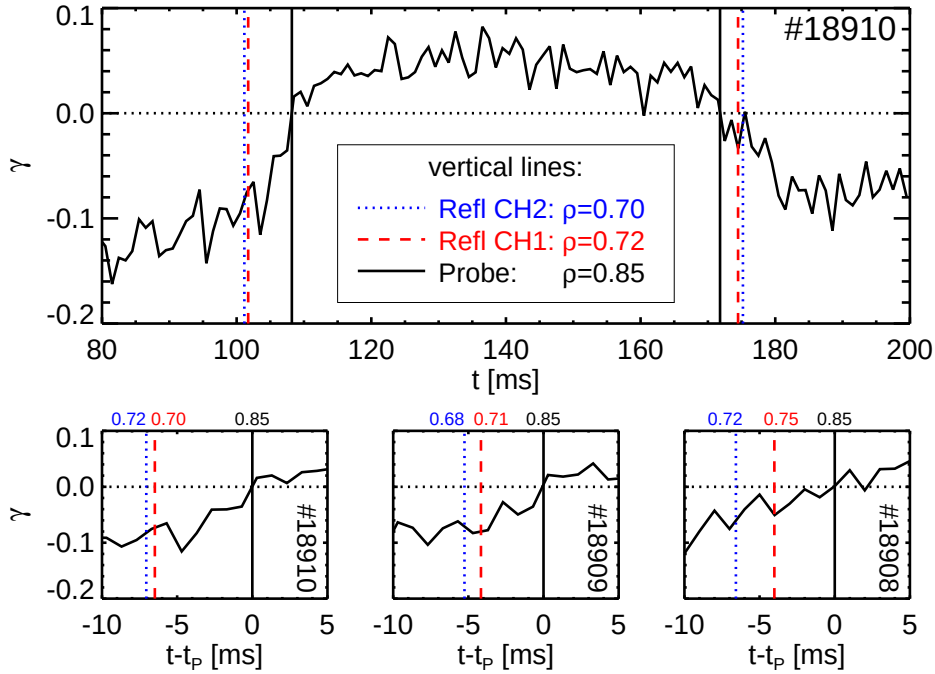

Figure 7.6: (#18908 - 10) Mean crossphase γ between two poloidally separated Langmuir probes measuring the floating potential ϕ_{fl}. The time instant at which the perpendicular velocity reversal is noted by reflectometer and probes is marked by vertical lines. Total time slice (upper part) and zoom to the time instant t_{P} when the probe notes the reversal of the perpendicular velocity (lower part). The numbers above the plots denote the radial position of the measurement.

is comparable to the radial velocities measured by reflectometry in fig. 7.5. However, the comparison with probe data does not only underline the results from reflectometry, but also shows that the origin of the VSL detected by reflectometry is the origin of the peripheral shear layer in TJ-II, which was proved to show universal properties familiar to all the shear layers of all fusion plasma experiments [118, 119].

Fig. 7.7 shows a schematic drawing of the sign of $u_\perp$ (upper part) and the corresponding plasma potential ϕ_{p} (lower part). It is assumed that $u_\perp = E_r/B = -\nabla_r \phi_p/B$ and the cases $\langle n_e \rangle < n_{\text{th}}$ (continuous lines), $\langle n_e \rangle \approx n_{\text{th}}$ (dashed lines) and $\langle n_e \rangle > n_{\text{th}}$ (dotted lines) are depicted. Reflectometer measurement positions at $\rho < \rho_0$ and $\rho > \rho_0$ are indicated by dotted vertical lines. Before the shear layer forms, $u_\perp$ is positive, as is the radial electric field E_r. As the shear layer develops and expands, the plasma velocity close to ρ_0 is negative, hence the local E_r is negative, caused by a dip in the plasma potential close to ρ_0. At this moment only CH1 of the interior measurement and CH2 of the exterior measurement note the reversal of $u_\perp$. When the shear layer is completely established, $u_\perp$ is negative in the whole radial region, so both channels are measuring negative E_r, independently of their positions in the plasma. This behavior resembles the behavior of the toroidal velocity shear reported in [124], where a qualitative physical explanation in terms of momentum conservation is given.

The influence of magnetic topology (low order rationals) in the development of edge

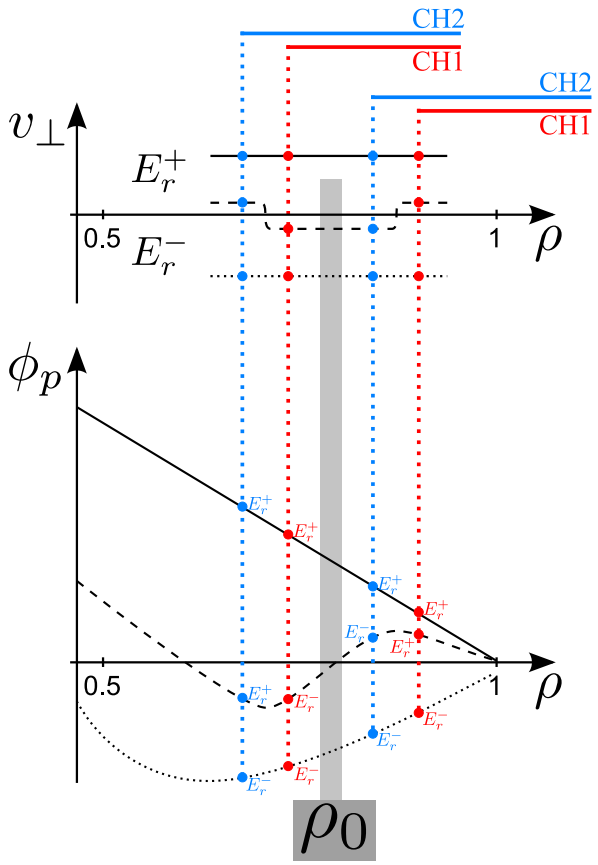

Figure 7.7: Schematic drawing of perpendicular velocities and corresponding plasma potential profiles for $\langle n_e \rangle < n_{\mathrm{th}}$ (continuous lines), $\langle n_e \rangle \approx n_{\mathrm{th}}$ (dashed lines) and $\langle n_e \rangle > n_{\mathrm{th}}$ (dotted lines). Reflectometer measurement positions at $\rho < \rho_0$ and $\rho > \rho_0$ are indicated by vertical dotted lines.

sheared flows has been shown both experimentally [125, 126] and theoretically [127]. Therefore it is important to cross-check whether rational ι-values play a role in the observed VSL formation. The experiment described above has been conducted in two other configurations, moving the rational $\iota = 8/5$ in a radial range of $\Delta\rho = 0.3$. The resulting values of ρ_0 (~ 0.7) are not related to the positions of $\iota = 8/5$ in these configurations. However, heating power could have an influence on the value of ρ_0. Doppler reflectometry results suggest $\rho_0 \approx 0.8$ (cf fig. 7.1), but were obtained at higher heating power ($P_{\mathrm{ECRH}} = 500$ kW) than the results shown here ($P_{\mathrm{ECRH}} = 420$ kW).

It should be pointed out that the formation of the VSL is triggered by a critical value of the density gradient, which leads to the conclusion that a critical diamagnetic velocity could be the responsible candidate for the process. The density profiles become steep just before the VSL is formed and do not change considerably during the phase where $\langle n_e \rangle > n_{\mathrm{th}}$. When the VSL is established, a large radial region independent of the gradient is affected and the perpendicular plasma velocity is in the electron-diamagnetic direction. The two phases (localized formation and existence in a large radial range) suggest a decoupling between the formation and the existence of the VSL.

It can be excluded that rational ι values are responsible for the VSL formation in TJ-II. These results show reliably that the radial origin and final points of the VSL formation and disappearance are directly connected to the region of maximum density gradient.

7.1.4 Summary on ECRH Plasma Velocity Profiles

The TJ-II DR has been employed to measure radial profiles of the perpendicular velocity $u_\perp$. The radial measurement range is $\rho = 0.55 - 0.85$, depending on the respective electron density profile. It was found that $u_\perp$ is positive (negative) when the line-averaged density $\langle n_e \rangle$ is below (above) the threshold density n_{th}. Close to n_{th}, the $u_\perp$ profile is mostly positive, but shows a dip reaching negative velocities at an intermediate radial position. Through investigation of the dynamics of the velocity shear layer formation and disappearance by conventional reflectometry, it has been found that its origin and terminal point are located at the radial position of maximum density gradient.

7.2 Perpendicular Velocity Profiles in NBI Plasmas

NBI plasmas in TJ-II reach higher densities than ECRH plasmas. One particular point of interest is the possibility to obtain discharges with low to high confinement transitions (L-H transitions). The H-mode confinement regime was first discovered by Wagner *et al.* in 1982 [21] and its causes and consequences have since been one of the central topics in magnetic confinement fusion research.

This section starts with a short introduction to TJ-II H-mode plasmas, followed by the presentation of $u_\perp$ profiles for both NBI L- and H-mode plasmas. The strong $u_\perp$ shear in H-mode plasmas causes two separated Doppler peaks to appear in the spectra, an effect which can be taken advantage of to localize the radial position of the H-mode velocity shear layer with excellent radial resolution.

Apart from the equilibrium $u_\perp$ measurements, the dynamics of radial electric field and density turbulence behavior at the L-H transition is investigated, revealing pronounced low frequency E_r shear oscillations at the transition. For discharges close to the L-H transition power threshold, a coupling between density turbulence level and E_r is observed which reveals evidence of predator-prey behavior.

7.2.1 Doppler Reflectometry Measurements

Since this section presents results from H-mode plasmas, it is appropriate to introduce the characteristics of the improved confinement regime of TJ-II. H-modes have been obtained in TJ-II since 2008 with lithium coated walls [128] with one (co) or two (co + ctr) NBI. H-mode characteristics are comparable to other devices, i.e. an increase of the energy confinement time τ_{E}, a decrease in H_α and density turbulence level, a steepening of the edge density profile gradient and an increase in the radial electric field (shear) [83] is observed. The electron temperature profile does not show significant changes.

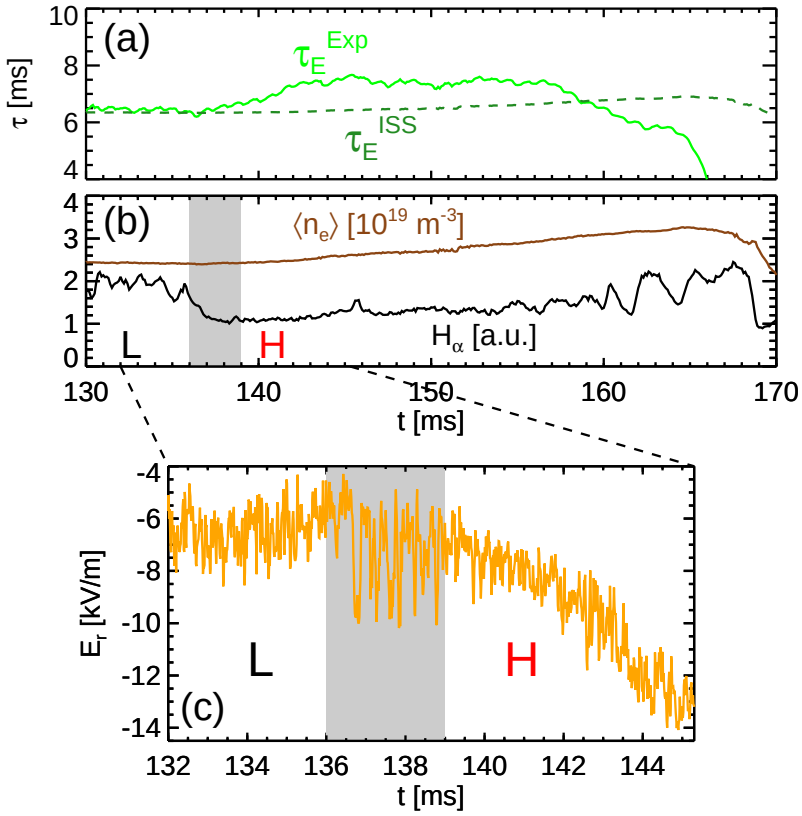

Figure 7.8: (#21319) Temporal evolution across an L-H transition in TJ-II. (a) In H-mode, the experimental energy confinement time τ_E^{Exp} increases about 25% w.r.t. the ISS predicted confinement time τ_E^{ISS} [129]. (b) In H-mode, the H_α level drops significantly w.r.t. L-mode. (c) E_r is roughly -6 kV/m in L-mode and increases in H-mode, after an oscillatory phase of about 3 ms marked by the gray stripe.

Fig. 7.8 shows the temporal evolution of several plasma parameters across an L-H transition, which takes place at roughly 136 ms. In (a), the experimental energy confinement time $\tau_E^{Exp} = W_{dia}/P_{abs}$ (W_{dia} and P_{abs} the diamagnetic energy and absorbed heating power, respectively) is compared to the energy confinement time τ_E^{ISS} calculated from the International Stellarator Scaling (ISS) [129]. As the plasma enters H-mode, τ_E^{Exp} rises by roughly 1.5 ms, and an increase of about 25% w.r.t. τ_E^{ISS} is observed, underlining the improved confinement properties after the transition. At 157 ms, the plasma starts to collapse, seen in the decrease in τ_E^{Exp}. In (b), the line-average density $\langle n_e \rangle$ is plotted along with the signal from an H_α detector. At 136 ms, the H_α signal decreases substantially, an indication of improved particle confinement. During the H-mode phase, $\langle n_e \rangle$ rises.

Fig. 7.8(c) shows a temporal zoom to the E_r evolution during the L-H transition measured by Doppler reflectometry. In L-mode, E_r is of roughly -6 kV/m and in H-mode an increase of up to -13 kV/m is observed. An increase of edge radial electric field has been observed in H-modes in many experiments and is believed to be intrinsically connected to the improved confinement in H-mode (cf sec. 2.2). The gray stripe marks

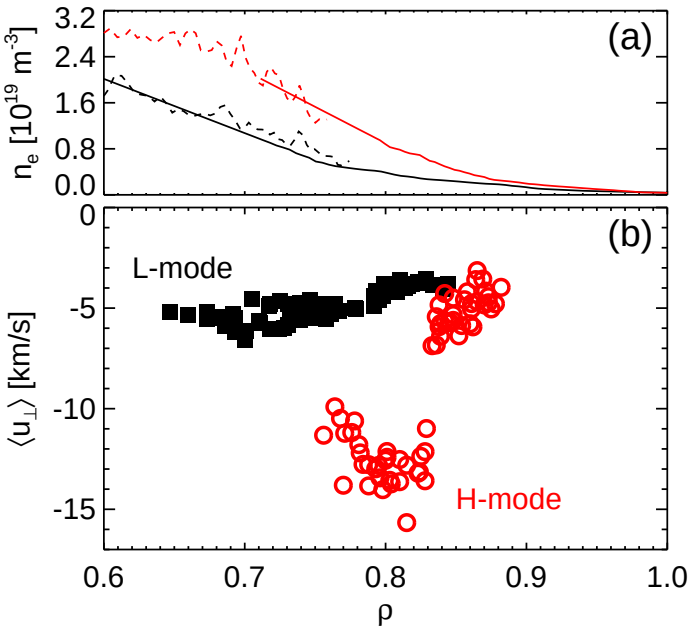

Figure 7.9: (#23013-51) (a) Representative density profiles in L- (black) and H-modes (red) obtained from AM reflectometry with linear extension (solid) and Thomson scattering (dashed). (b) Radial $\langle u_\perp \rangle$ profiles in L- and H-mode plasmas. In H-mode, a strong velocity shear layer is located at $\rho \approx 0.83$.

a 3 ms time window just at the L-H transition. A pronounced E_r oscillation is visible before the stronger H-mode E_r develops. This oscillation is observed when the heating power in TJ-II is close to the L-H transition threshold. The dynamical characteristics of the L-H transition are presented later in this chapter.

In order to measure the perpendicular velocity behavior in NBI plasmas of TJ-II, the DR channels are programmed to fixed frequencies during the whole discharge duration, and frequencies are changed on a shot-to-shot basis. This is done both because the density control in NBI plasmas is particularly difficult and because it allows spatiotemporally highly resolved studies of the L-H transition. With shot-to-shot measurements, equivalent time instants can be selected and the $u_\perp$ profile can be reconstructed or the radial (ρ) and scale ($k_\perp$) dependence of the L-H transition can be investigated.

Experiments were carried out in NBI co-heated (370 kW) plasmas pre-heated by off-axis ECRH (2×230 kW). An overlap of 10 ms between ECRH and NBI was used. The magnetic configuration was 101_42_64, a configuration previously identified as beneficial for L-H transitions [83]. Fig. 7.9 shows electron density profiles (a) and the flux surface averaged perpendicular velocity $\langle u_\perp \rangle$ profiles (b) for L- and H-mode plasmas in TJ-II. The density profiles are measured with AM reflectometry [89] (solid) and Thomson scattering [130] (dashed). To localize the Doppler reflectometry measurement positions a linear part is added to the AM profiles which are then used as input for `TRUBA`. The linear parts overlap well with the Thomson scattering profiles. In fig. 7.9(b) the velocity profile in L-mode is rather flat with values from -5 km/s in the edge region to -7 km/s

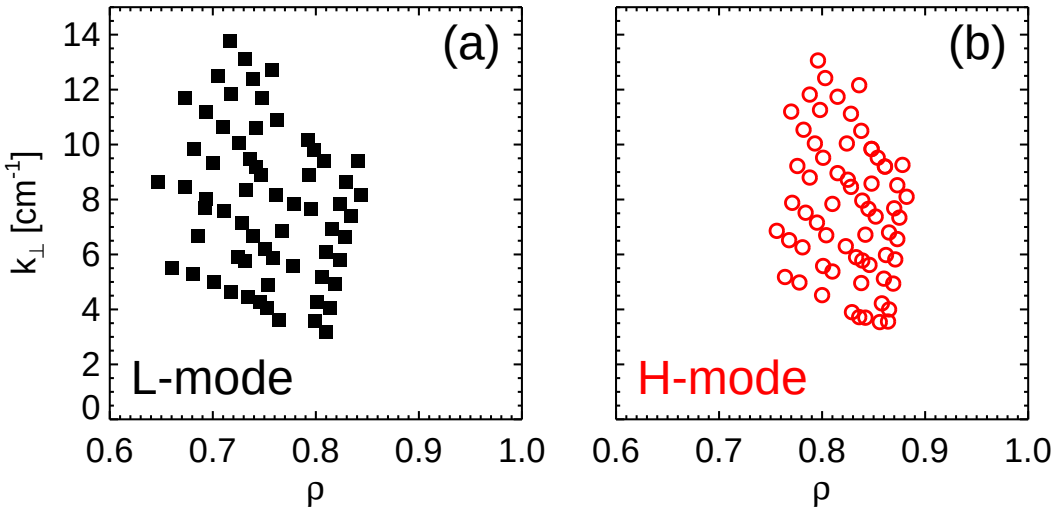

Figure 7.10: (#23013-51) Perpendicular wavenumbers of density turbulence probed during the measurement of fig. 7.9(b). In both (a) L- and (b) H-mode, $k_\perp$ ranges from about 4 to 14 cm^{-1}.

further inside. However, in H-mode plasmas, a strong velocity shear layer is observed at $\rho_{\mathrm{shear}} \approx 0.83$. Velocities in the edge are similar to those in L-mode, while inside the VSL ($\rho < \rho_{\mathrm{shear}}$) values of up to -15 km/s are reached. Further inside, $\langle u_\perp \rangle$ decreases to about -10 km/s. Note that the innermost measurement points are measured with $f_0 = 50$ GHz, and hence mark the technical limits of the TJ-II DR. It would be of particular interest to measure the $\langle u_\perp \rangle$ profiles further inside, which would require either the possibility of O-mode operation or a second DR in X-mode operating in a higher frequency band (e.g. V-band: 50 – 75 GHz).

The radial dependence of the $k_\perp$ space scanned in this experiment is depicted in fig. 7.10 for (a) L- and (b) H-mode. In (a), the measurement points are further inside the plasma than in (b), which is due to the shallower density profile in L-mode (cf fig. 7.10(a)). In both cases, $k_\perp$ ranges from about 4 to 14 cm^{-1}, corresponding to turbulent structure sizes between 0.4 and 1.6 cm.

The velocity profiles from fig. 7.9(b) are plotted again in fig. 7.11 with color-coded $k_\perp$ of density turbulence that the microwave beam probed (cf fig. 7.10). It is observed that the $u_\perp$ measurement does not depend on the value of $k_\perp$. This can either mean that $v_{\mathrm{ph}} \ll v_{E\times B}$ or that v_{ph} does not depend on the value of $k_\perp$, conclusions of particular importance not only for Doppler reflectometry, but also for turbulence investigations. In general, in turbulence theory, v_{ph} does depend on $k_\perp$. In drift wave turbulence the wavenumber dependence of the phase velocity is due to the polarization drift, in particular for small structures $k_\perp \rho_{\mathrm{s}} > 1$. The above supports the conclusion that $v_{\mathrm{ph}} \ll v_{E\times B}$, already seen for ECRH and NBI L-mode plasmas in sec. 5.8.4.

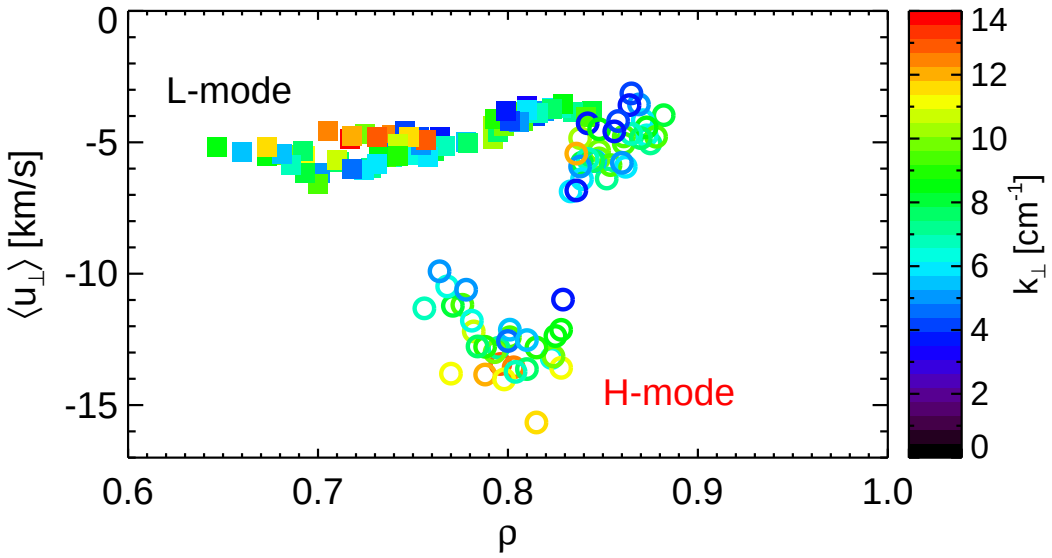

Figure 7.11: (#23013-51) Perpendicular velocity profiles as in fig. 7.9(b) with color-coded $k_\perp$ of density turbulence as probed by the microwave beam.

7.2.2 The Role of Spectral Resolution in Velocity Shear Measurements

The Doppler shift, as shown in sec. 3.2.1, depends on the perpendicular velocity of density fluctuations $u_\perp$ and the turbulence scale probed by the microwave beam $k_\perp$. The relative width of the Doppler peak R, defined in sec. 6.2.3, can be written

$$R = \frac{\sigma}{|f_\mathrm{D}|} = \frac{\Delta u_\perp}{|u_\perp|} + \frac{\Delta k_\perp}{k_\perp}, \tag{7.1}$$

where $\Delta u_\perp$ can be due to spatial or temporal variations in $u_\perp$ and $\Delta k_\perp$ is the spectral resolution introduced in sec. 3.2.2. Eq. (7.1) shows that the spectral resolution of a Doppler reflectometer has immediate influence on the width of the Doppler peak. An experimental observation in TJ-II shows that in H-mode plasmas with strong velocity shear, two Doppler shifted peaks are observed close to the $u_\perp$ shear layer [67]. This observation is presented in the following, followed by a numerical study of the influence of the spectral resolution on the capability to distinguish the two Doppler peaks.

Three Doppler shifted spectra measured at different radial positions of the H-mode $u_\perp$ profile from fig. 7.9(b) are plotted in fig. 7.12. In (c), made at $\rho = 0.87 > \rho_\mathrm{shear}$, only one Doppler peak with low Doppler shift is present. However, the spectrum in (b), acquired at $\rho = 0.83 \approx \rho_\mathrm{shear}$ shows two distinct Doppler shifted peaks, one at low f_D (∼750 kHz) and one at higher f_D (∼1800 kHz). Since the backscattering process has a certain radial extension, the backscattered signal contains information from both regions of the velocity profile, the low- and the high velocity regions. Spectrum (a) is measured further inside, at $\rho = 0.79 < \rho_\mathrm{shear}$, and only one (high frequency) Doppler peak is visible at roughly 1900 kHz.

As a reference, fig. 7.13(a) shows again the perpendicular velocity profiles for L-

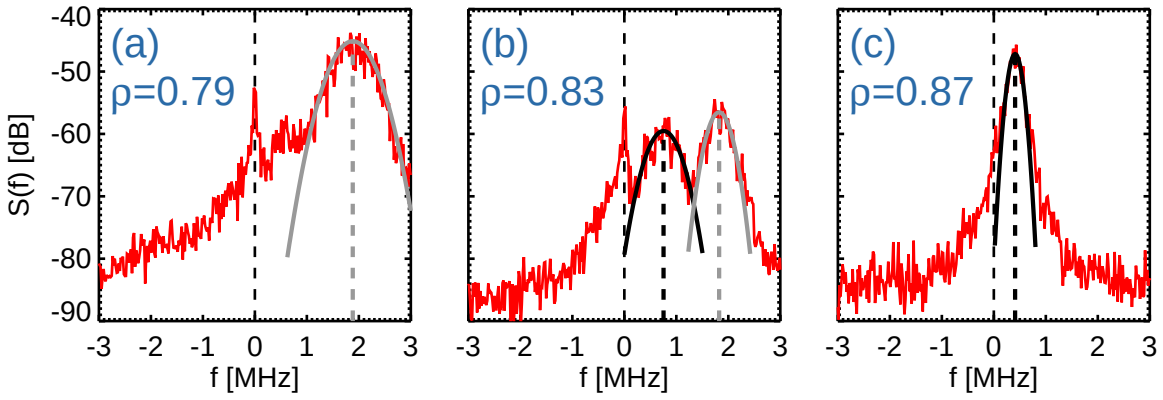

Figure 7.12: (#23024, #23043, #23051) Doppler shifted spectra with respective fits at different radial positions in a TJ-II H-mode plasma: (a) inside the shear layer, (b) close to the velocity shear layer, (c) in the edge.

and H-mode from the previous section. The velocity shear layer (VSL) is indicated at $\rho_{\text{shear}} \approx 0.83$. Fig. 7.13(a) suggests that the radial extension of the VSL is smaller than the probing wavelength λ_0 (6 – 9 mm). The labels (a, b, c) refer to the radial positions of the Doppler shifted spectra in Fig. 7.12(a-c). The ratios of the amplitudes of the two peaks $S(f_{\text{high}})/S(f_{\text{low}})$ are plotted for several radial positions across the VSL in Fig. 7.13(b). Close to the VSL, the ratio is close to one (cf Fig. 7.12(b)). While at the

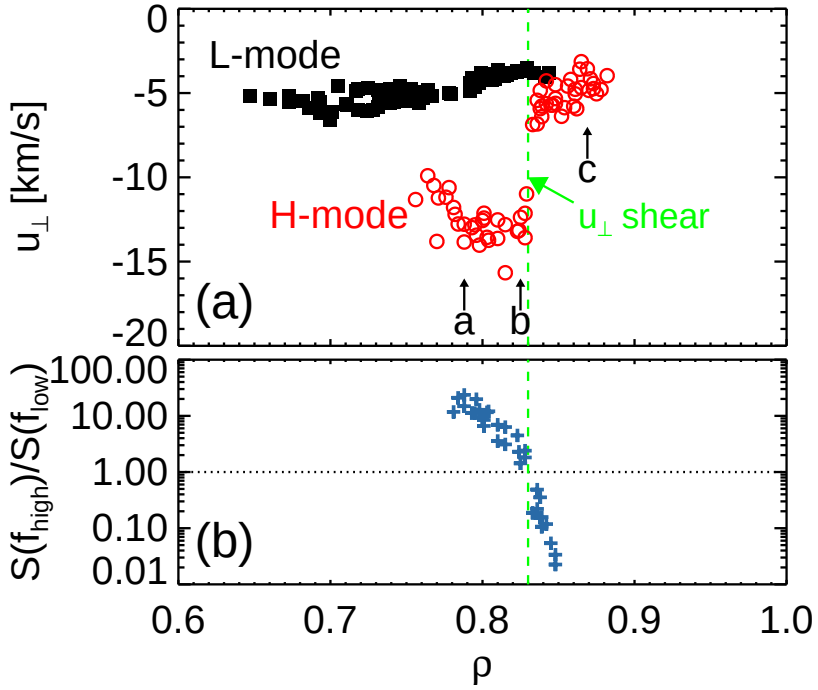

Figure 7.13: (#23013-51) (a) Perpendicular velocity profiles as in fig. 7.9(b). The labels a, b and c indicate the radial positions where the power spectra from fig. 7.12 are measured. (b) Ratio of Doppler peak amplitudes close to ρ_{shear}.

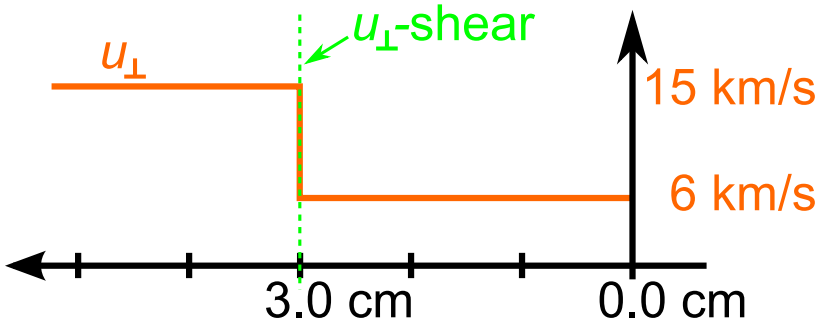

Figure 7.14: Input velocity profile for the 2D full wave simulation. The $u_\perp$ shear at $x = 3$ cm is instantaneous. Note the x-axis is reversed.

plasma edge the peak at low frequency dominates (cf Fig. 7.12(c)), the predominance of the high frequency peak becomes clearer as the measurement moves from the VSL towards the plasma center (cf Fig. 7.12(a)).

2D Full Wave Simulation Results

In order to delve deeper into the obtained results, two-dimensional full wave simulations [101] have been conducted. X-mode propagation in plasma slab geometry is used. The plasma is considered to move perpendicularly to the magnetic field with velocities of 6 km/s and 15 km/s, values that are close to the experimentally measured ones. Refer to fig. 7.14 for clarity, where the x-axis is reversed. The velocity profile has a discontinuity at $x_{\text{shear}} = 3$ cm, i.e. $u_\perp = 6$ km/s for $x < x_{\text{shear}}$ and 15 km/s for $x \geq x_{\text{shear}}$. The gaussian antenna is located at the plasma edge at $x = 0$ cm and its tilt angle is 20°. The beam waist w_0 in the antenna is scanned from $w_0 = 0.70$ cm to $w_0 = 2.85$ cm. As deduced by Holzhauer and Massig, the larger the beam size, the better the spectral resolution in scattering experiments [79]. This result is valid for Doppler reflectometry in plasma slab geometry.

Fig. 7.15(a-c) shows three spectra obtained with beam waist size $w_0 = 1.35$ cm, for radial positions $x = 3.9$ cm (a), $x = 3.0$ cm (b) and $x = 2.3$ cm (c). The trend observed in the experiment (cf Fig. 7.12) is reproduced. In Fig. 7.15(d-f) the corresponding spectra for poorer spectral resolution ($w_0 = 0.70$ cm) are depicted. The Doppler peak is generally broader with the consequence that close to the VSL the two peaks blend into one (e).

The ratio of Doppler peak heights $S(f_{\text{high}})/S(f_{\text{low}})$ across the VSL is shown in Fig. 7.15(g). Again the x-axis is reversed. Since the peaks are not always separable, the curves are of different lengths. In particular, in the $w_0 = 0.70$ cm case, it is not possible at all to distinguish the two peaks. If the backscattering position is close to x_{shear}, then the heights of the Doppler peaks are comparable. When the measurement position is separated a few mm from the VSL, the difference in Doppler peak heights is an order of magnitude and becomes larger as the measurement moves further away from the VSL. This result confirms the interpretation of the experimental results in Fig. 7.13(b). Note that the better the spectral resolution, the larger the radial region where two peaks

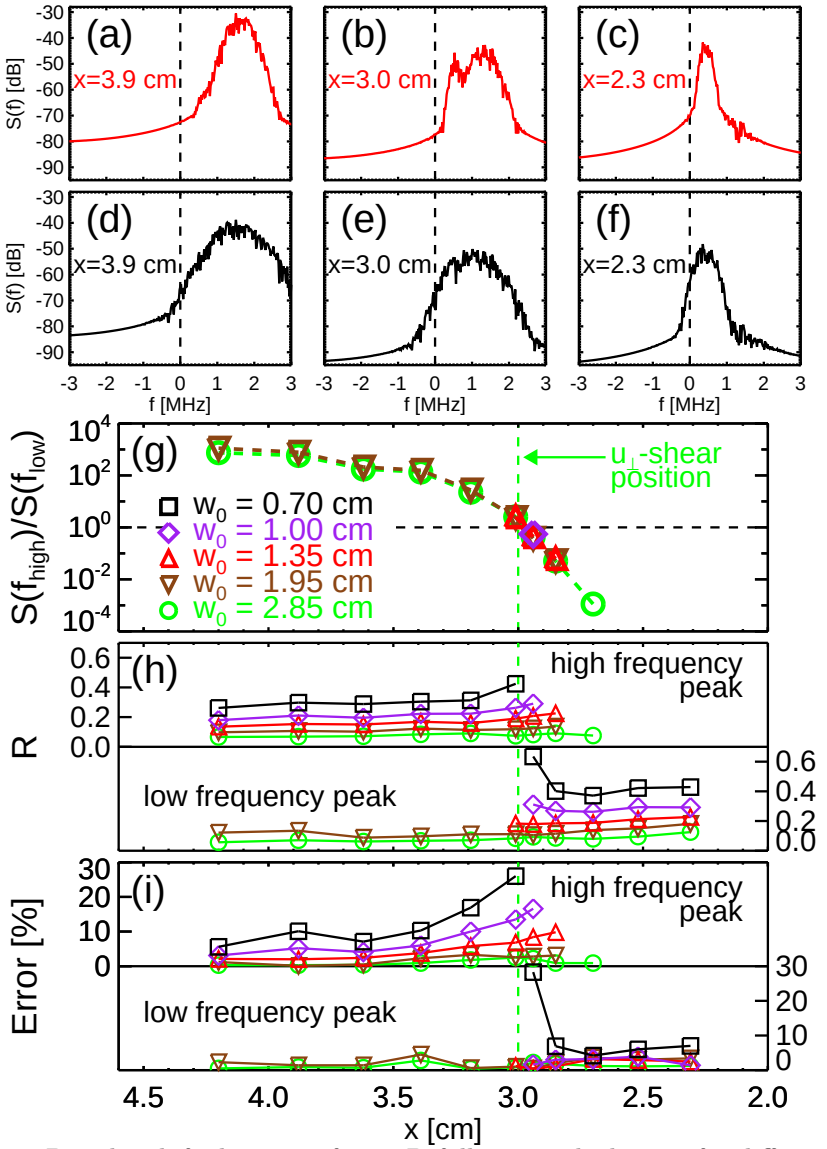

Figure 7.15: Doppler shifted spectra from 2D full wave calculations for different radial positions for $w_0 = 1.35$ cm (a-c) and $w_0 = 0.70$ cm (d-f). (g) Ratio of Doppler peak heights for different cutoff positions and beam waists at the antenna. (h) R for low and high frequency Doppler peaks. (i) Error in the perpendicular velocity determination.

can be observed in the Doppler shifted spectra. This affects the length of curves in Fig. 7.15(g-i). In Fig. 7.15(h) the relative width of the Doppler peak (cf (6.12) in sec. 6.2.3) is depicted for the high and low frequency peaks (upper and lower parts, respectively). As w_0 reduces ($\Delta k_\perp$ increases), the Doppler peaks broaden and eventually blend into a single peak close to the VSL, see Fig. 7.15(e). Since the simulation input velocities are known, the errors in their determination can be calculated. Fig. 7.15(i) shows these for the high velocity part ($x > x_{\mathrm{shear}}$, upper part) and the low velocity part ($x \leq x_{\mathrm{shear}}$, lower part) of the profile. The analysis yields correct values in the outer part of the plasma, when the wave has not yet reached the VSL. If measurement positions are

close to the VSL and further inside, the high velocity can be measured if the spectral resolution of the system is good (beam waist $w_0 \geq 1.35$ cm). In the case of poor spectral resolution (black and purple lines) the measurement is error-prone due to the mixing of the two peaks (cf Fig. 7.15(e)).

An important point is that if the spectral resolution is good enough to distinguish the two peaks, the VSL can be localized with high spatial resolution. This is illustrated in Fig. 7.15(g), where the ratio of Doppler peak heights is unity at the VSL radial position. For cases of poor spectral resolution ($w_0 = 0.70$ cm, black points), it is impossible to distinguish the two Doppler peaks.

The two peaks are also lost in simulations with $w_0 = 1.35$ cm (as in fig. 7.15(b)) and a broader shear layer width (close to λ_0), which supports the statement above that the radial extension of the VSL in TJ-II H-mode plasmas is smaller than the probing beam wavelength ($\lambda_0 = 6$ – 9 mm).

This section has shown that when the spectral resolution of a DR is insufficient, i.e. the peaks cannot be separated, the measurements can be misinterpreted. These results highlight the need for the careful design and adaptation of a Doppler reflectometer to the given experimental conditions in order to obtain reliable results. If a Doppler reflectometer is optimized, however, it is suited to localize the perpendicular velocity shear layer with excellent radial resolution. Since H-mode plasmas usually show a strong velocity shear layer, Doppler reflectometry is a diagnostic capable of investigating perpendicular velocities, radial electric fields and density fluctuation levels across the shear layer with high accuracy.

7.2.3 Summary on NBI Plasma Velocity Profiles

Radial profiles of the perpendicular velocity of density fluctuations have been presented for NBI plasmas in TJ-II. In L-mode, the $u_\perp$ profile is rather flat with values between -5 km/s in the plasma edge ($\rho > 0.8$) and -7 km/s further inside ($\rho = 0.7$). In H-mode plasmas, a strong velocity shear develops at $\rho = 0.83$. Velocities inside this shear (towards the plasma center) of up to -15 km/s are observed. From the shear towards the plasma edge, $u_\perp$ is in the range of -6 km/s, which is comparable to the velocities measured in L-mode.

These results are in agreement with results obtained in H-modes on other experiments, where strong $u_\perp$ (or E_r) shears are measured [33, 97, 131–135].

Furthermore, a diagnostic peculiarity has been encountered. Doppler reflectometry measurements can be affected by strong $u_\perp$ shears, which can give rise to two Doppler peaks. This has been confirmed by 2D full wave simulations and it has been shown that the separation of the two peaks is only possible when the spectral resolution of the DR is sufficient, which in general demands that the DR is optimized. If it is not possible to separate the two peaks, the data can be subject to misinterpretation, underlining the importance of spectral resolution optimization. Nevertheless, the presence of two Doppler peaks can be exploited. It has been shown that a high precision spatial localization of the $u_\perp$ shear layer is possible by making use of the Doppler peak heights. Their ratio is unity when the radial measurement location is at the shear layer.

7.3 Dynamics of the L-H Transition

The L-H transition is a sub-millisecond process, and it is a challenge for experimentalists to obtain time-resolved measurements which follow the evolution of plasma parameters during the transition. One of the advantages of Doppler reflectometry is good spatiotemporal resolution of the diagnostic, which can be utilized to investigate the temporal evolution of both E_r and $\tilde{n}_e$ and a possible coupling of both during the transition [83].

The basic question which has not been answered in more than one quarter century of H-mode research is what exactly is the reason for the confinement transition into H-mode. Is the background radial electric field shear strong enough to "push" the plasma into H-mode? Could an oscillating E_r shear be the candidate? Or does the plasma enter the H-mode for another reason and the strong E_r shear develops later, as a consequence of a strong pressure gradient ∇p in (2.13)? These are basic questions which are of great interest to the magnetic confinement fusion community.

In TJ-II, the L-H-transition shows different characteristics which can depend on the magnetic configuration [136] and heating power. In the following, the dynamics of two L-H transitions will be presented, one with higher heating power (co + ctr NBI) and one with heating power close to the transition threshold power (co NBI).

7.3.1 Evolution of Mean and Oscillating Shear Flows during the L-H Transition

The plasma investigated in this section is heated by both NBI injectors (co + ctr) with a total port-through power of 900 kW and has a line-average density of $\langle n_e \rangle \approx 2.0 \times 10^{19}$ m^{-3} at the L-H transition, which takes place at $t = 90.6$ ms.

Since the evolution of the density fluctuation level $\tilde{n}_e$ and E_r can be followed on fast timescales with Doppler reflectometry, it is possible to measure density and E_r fluctuation spectra. The density and E_r fluctuation spectra for L- and H-mode are plotted in fig. 7.16. In (a), the density fluctuations are reduced over a broad frequency range from L-mode (black) to H-mode (red). The increase of density fluctuations between 2 and 5 kHz is not yet fully understood, but it could be conjectured that a possible shearing apart of turbulence structures by perpendicular sheared flows could result in a stretching of the structures in the perpendicular direction, as suggested by the rightmost plot of fig. 2.6. Nevertheless, a clear reduction of density fluctuations at all frequencies above 5 kHz is evident, underlining that density turbulence is suppressed in the H-mode plasma.

Fig. 7.16(b) shows the radial electric field fluctuation spectra in L- and H-modes. In contrast to the density fluctuations, the low frequency E_r fluctuations between 1 and 10 kHz increase in H-mode w.r.t. the L-mode plasma. For the high frequency part of the spectrum, no change can be observed.

The temporal evolution of several magnitudes during the L-H transition of the discharge from fig. 7.16 is illustrated in fig. 7.17. The time instant of the L-H transition is marked by the vertical dashed line. It has been obtained by searching for the time

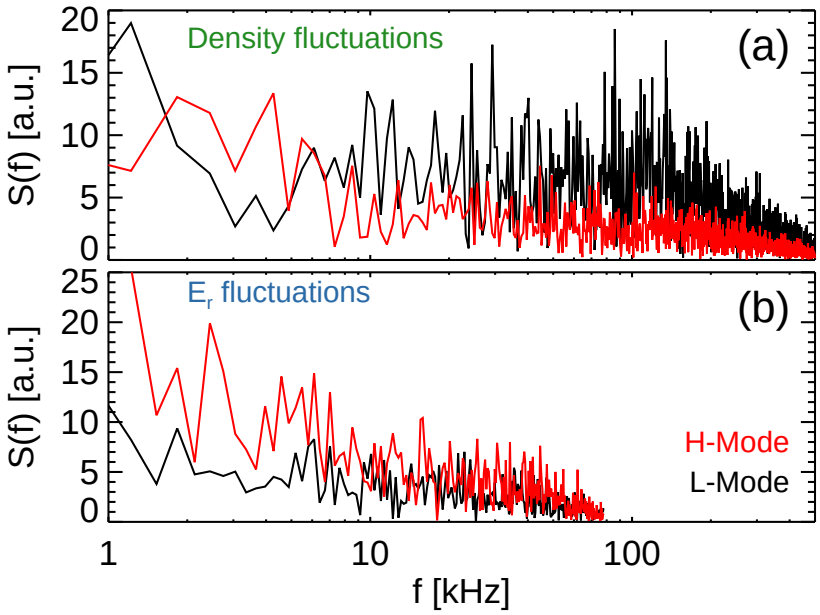

Figure 7.16: (#21620) (a) Density fluctuation and (b) radial electric field fluctuation spectra in L-mode (black) and H-mode (red) for 2 ms time windows just before and after the L-H transition. While the density fluctuation level is reduced in almost the whole frequency range in H-mode, the low frequency E_r fluctuation level increases in H-mode.

instant where the density fluctuation level measured by Doppler reflectometry is drastically decreased. For comparison, the H_α emission is shown in (a), which drops at this time instant.

In (b), the radial electric field E_r measured by the two DR channels is depicted. The measurement position of CH1 is at $\rho = 0.85$ in L-mode and moves to $\rho = 0.87$ in H-mode due to the density profile steepening in H-mode. CH2 moves from $\rho = 0.82$ (L-mode) to $\rho = 0.85$ (H-mode). In L-mode ($t < 90.6$ ms), the two channels measure a low E_r of roughly -3 kV/m. The E_r at $\rho = 0.82$ is slightly stronger than the E_r further outside. From $t \approx 87$ ms E_r starts to become stronger at both measurement positions until in H-mode they reach $E_r \approx -6$ kV/m in the edge and $E_r \approx -14$ kV/m slightly further inside. Note that in this discharge, the appearance of the strong $u_\perp$ shear is measured by CH2 while CH1 measures the edge which does not show a strong E_r increase as observed in sec. 7.2.1.

Fig. 7.17(c) plots the mean E_r difference between the two channels $\Delta E_r = E_r^{\mathrm{CH2}} - E_r^{\mathrm{CH1}}$ (red). In L-mode ΔE_r is constant at roughly -1 kV/m. This value is maintained until about 1 ms after the L-H transition, when ΔE_r starts to increase, until it reaches -6 kV/m about 3 ms after the transition. In the lower part of (c), the high-frequency density fluctuations filtered between 100 and 200 kHz are suppressed when the plasma goes into H-mode.

In fig. 7.17(d) the behavior of the low frequency oscillating E_r shear, filtered between 1 and 10 kHz, is depicted. The magnitude is obtained through the E_r difference between the two DR channels divided by their distance. To guide the eye, the standard deviation

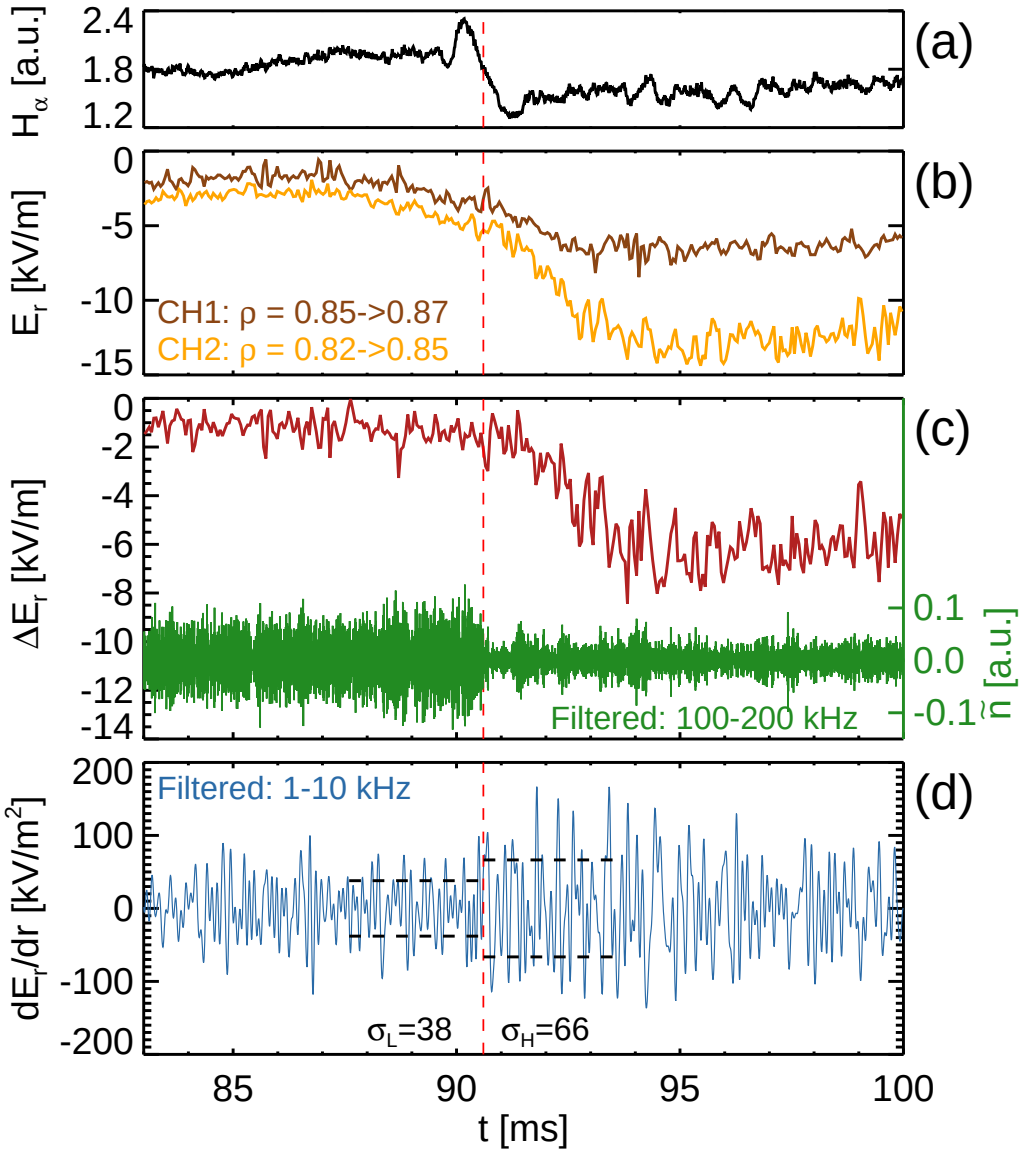

Figure 7.17: (#21620) Temporal evolution of an L-H transition. (a) E_r of the two DR channels, (b) H_α emission, (c) mean E_r difference (red) and density fluctuations (green), (d) oscillating E_r shear. For details refer to the text.

is indicated just before and after the L-H transition by the dashed lines. Note the increase in the oscillating E_r shear takes place just at the time instant of the L-H transition, when the density fluctuation level decreases. Later in the discharge, the amplitude of the oscillating shear flow decreases slightly.

It has to be stressed that figs. 7.16 and 7.17 show examples of an L-H transition where the density fluctuation level is reduced simultaneously with an increase in the oscillating sheared radial electric field, i.e. oscillating shear flow. The mean radial electric field shear starts to develop roughly one millisecond after the L-H transition and is completely established several milliseconds later, an observation which resembles

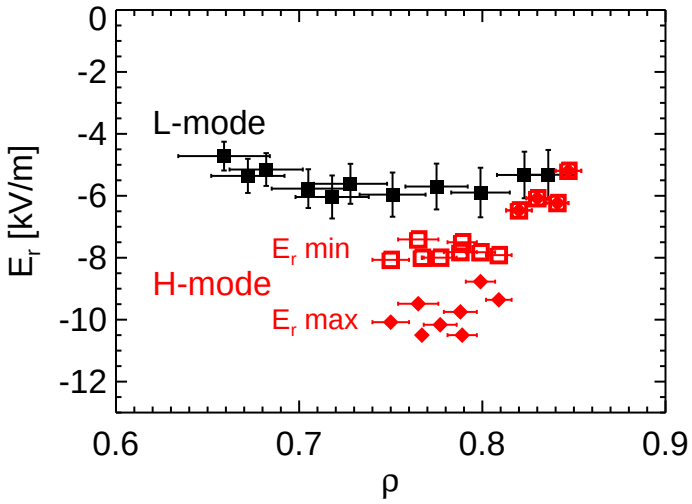

Figure 7.18: (#23473, 78, 79, 81-83) Radial E_r profiles in L- (black) and H-mode (red) visualizing the E_r minima and maxima during the oscillating H-mode phase from fig. 7.19.

a recently published work from JET [42].

The results presented here point towards Zonal Flows (ZFs) as a possible explanation for the turbulence suppression which could ultimately trigger the L-H transition. ZFs are a candidate for turbulence regulation via time-varying sheared flows [28]. The steepening of the edge pressure gradient is a result of the turbulence regulation by the ZF and can drive a mean sheared flow, which can then act as the turbulence regulation mechanism in the established H-mode [35]. It is tempting to speculate that the established mean E_r shear (fig. 7.17(c), $t > 94$ ms) could be the suppression mechanism of density turbulence in the established H-mode and thus damp the oscillating sheared flow in this phase of the discharge.

Experimentally, with Langmuir probes long-range toroidal correlations in ϕ_p but not n_e have been detected during the L-H transition [137] in TJ-II. To gain more insight into these ϕ_p fluctuations, a second HIBP system will be installed toroidally separated from the existing one in TJ-II, allowing measurements of electrostatic fluctuations and their radial dependence similar to those done at CHS, where the first direct experimental evidence of ZFs was obtained in 2004 by Fujisawa *et al.* [138].

7.3.2 Experimental Evidence for Predator-Prey Behavior of Turbulence

The plasma presented in this section is heated with one NBI (co) and the L-H transition takes place at a line-average density $\langle n_e \rangle \approx 2.5 \times 10^{19}$ m^{-3}. During the transition, a coupled oscillating behavior of density turbulence level and radial electric field can be observed [139].

The radial E_r profile measured in the discharge series is depicted in fig. 7.18. Like in sec. 7.2.1, the L-mode profile is rather flat with values between -5 and -6 kV/m. The H-mode E_r profile oscillates inside the shear layer (here $\rho \approx 0.82$) between -8 and -10

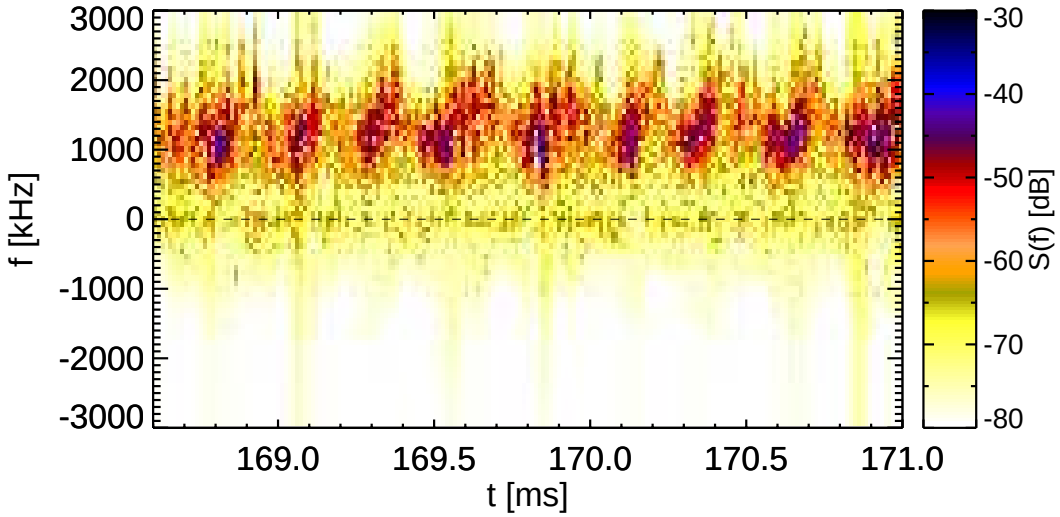

Figure 7.19: (#23473) Doppler reflectometer spectrogram during the oscillating phase of an H-mode transition.

kV/m, while it remains static at -6 kV/m in the plasma edge. This has the effect that the E_r shear oscillates as well, being approximately twice as strong in the maximum E_r case as in the minimum E_r case. As in sec. 7.2.1, the edge values of the E_r profile are comparable to the L-mode values.

Fig. 7.19 shows a spectrogram of a 2.4 ms time window during the oscillating phase of the H-mode transition. The oscillation frequency is of roughly 4.5 kHz. Due to the high density NBI plasma, f_{D} is positive (negative E_r). Each time the density fluctuation level is rising and reaches about -50 dB (color-coded), E_r starts to increase. This E_r increase lasts roughly 200 μs and is accompanied by a decrease in density fluctuations, until an abrupt E_r decrease takes place and the density fluctuation level starts to rise again.

The temporal evolution of $S(f_{\mathrm{D}})$ and $|E_r|$ obtained applying the SFIT method to the spectrogram from fig. 7.19 is plotted in fig. 7.20(a) and (b), respectively. For simplicity, the absolute E_r value is plotted. A periodic behavior can be detected where E_r (and its shear, see above) follows the density fluctuation level with a 90° phase difference. The gray vertical stripes mark the time instants when the turbulence level is maximum. Starting at the stripe at $t = 170.1$ ms, the turbulence level is maximum and the E_r shear has already started to increase. With the increase of E_r shear, the turbulence level drops and reaches its minimum value when the E_r shear is maximum.

The blue region in (b) marks the time window used for the plot of $|E_r|$ against $S(f_{\mathrm{D}})$ in (c). The gray circle corresponds to the situation marked by the vertical stripes in (a) and (b), i.e. the turbulence level is maximum and E_r (sheared flow) is increasing. In phase ① the shear flow increases, which suppresses the density turbulence level. When the turbulence level is minimum, it cannot maintain the sheared flow anymore, which decreases drastically (②). Hereafter, the turbulence level increases again due to the absence of turbulence suppression by sheared flows, and eventually, from about -50 dB,

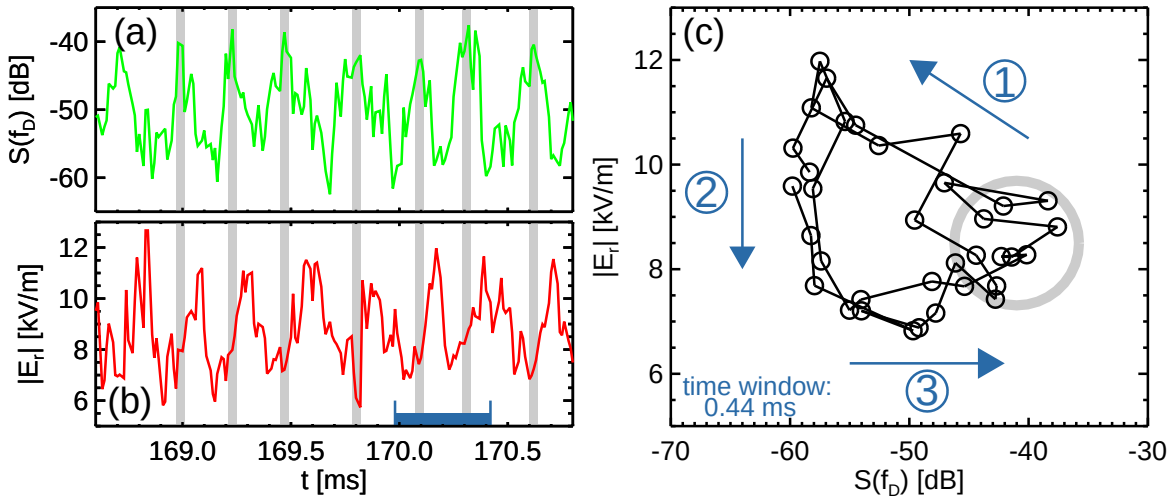

Figure 7.20: (#23473) Temporal behavior of (a) density fluctuation level and (b) absolute electric field amplitude. (c) Dependence of $|E_r|$ on density fluctuation level for two cycles of (a) and (b) indicated by the blue bar.

is strong enough to generate the sheared flow again.

This process can be interpreted as a predator-prey mechanism [27], where the sheared flow is the predator and the density turbulence level is the prey. When the prey population has grown, the predator population can feed on it and itself starts to increase in number. This reduces the number of preys (①), which has the effect that the predator population will decrease because there is not enough prey to feed on any more (②). When the predator population is at its minimum, the prey population can rise again (③).

This type of coupling between turbulence and sheared flows has been proposed theoretically [26]. Experimentally, it was investigated in DIII-D power scan experiments during the so-called IM-mode [140]. Sheared flow and electron temperature fluctuations seem to follow a predator-prey behavior, however, the sheared flow is not measured directly but inferred from Beam Emission Spectroscopy data.

The outstanding advantage of the measurements presented in this section is the simultaneous measurement (with one diagnostic) of the radial electric field and the density fluctuation level with high spatiotemporal resolution.

7.4 Summary

The previous section underlines the successful operation of the TJ-II Doppler reflectometer. It is possible to measure $u_\perp$ profiles in plasmas with different heating schemes, confinement regimes, magnetic configurations (not shown here, see Ref. [136]). In fact, as of today, no plasma has been encountered in which a Doppler reflectometry measurement was not possible due to whatever reason.

In ECRH plasmas, basically three types of $u_\perp$ profiles can be observed. At low line-average density $\langle n_e \rangle < n_{\rm th}$, $u_\perp$ is positive, while at $\langle n_e \rangle > n_{\rm th}$, $u_\perp$ is negative.

The third case ($\langle n_e \rangle \approx n_{\mathrm{th}}$) is an intermediate case, where $u_\perp$ is mainly positive but reaches negative values close to the radial position of maximum density gradient. From observations with conventional reflectometry, it is known that the edge velocity shear layer appearance and disappearance has its radial origin and terminal point at this position.

In NBI plasmas, the $u_\perp$ profile is negative in the whole radial measurement range of the DR. In L-mode plasmas, the profile is rather flat with values ranging from -5 km/s in the plasma edge ($\rho = 0.85$) to -7 km/s further inside ($\rho = 0.65$). In H-mode, a strong $u_\perp$ shear layer develops at $\rho_{\mathrm{shear}} \approx 0.83$, with highly increased $u_\perp$ values of up to -15 km/s inside ($\rho < \rho_{\mathrm{shear}}$), but comparable values to L-mode outside ($\rho > \rho_{\mathrm{shear}}$).

In detailed investigations of the Doppler spectra close to the $u_\perp$ shear layer, two Doppler shifted peaks are visible, corresponding to velocities inside and outside the shear layer. This interpretation has been confirmed by 2D full wave simulations, which also showed that the two peaks are only distinguishable when the spectral resolution of the DR is good, i.e. the DR is optimized. For poor spectral resolution, simulation results show that the two peaks blend into one and yield an intermediate and incorrect velocity.

High spatiotemporal resolution measurements of the dynamics of the L-H transition reveal that the decrease of density fluctuations is accompanied by an increase in the low frequency oscillating shear flow. Furthermore, the mean electric field shear begins to form roughly one millisecond after the L-H transition and is completely established about 3 ms after the transition into H-mode. This observation is in accordance with recent L-H transition theories [28, 35], but no definite conclusions can be drawn. Furthermore, a predator-prey type behavior between radial electric field shear and density fluctuation level has been identified during an L-H transition which shows oscillating behavior, consistent with the model proposed by Diamond *et al.* [26].

Chapter 8

Perpendicular Wavenumber Spectra

Since in toroidal fusion experiments the plasma is magnetized, the movement of any particle species can in general be decoupled into movement parallel to the magnetic field, which is mainly of *thermal* character, and movement perpendicular to the magnetic field, which mostly consists of *drifts*. Effects like collisions depend on plasma density and temperature, and introduce secondary effects.

Hence when measuring perpendicular density turbulence wavenumber spectra, normally the findings are compared using the terminology of fluid turbulence introduced in sec. 2.1.2. As pointed out earlier, the spectral indices can depend on several factors, as for example:

Interacting fluids
: The plasma consists of ions and electrons which interact and even act back on the confining magnetic field, and can in general not be compared to a neutral fluid.

Energy injection scale
: In sec. 2.1.2 it is assumed that energy is injected at one distinct wavenumber k_i. In a fusion plasma, there are several sources of energy, there can be several instabilities present at the same time. If there is a range k_i of different energy injection scales, no knee will be detectable in the spectrum, instead a smoother transition between inertial ranges is to be expected.

Non-Gaussian PDF
: For the derivation in the K41- and 2D-theories, Gaussian PDFs of turbulence are explicitly assumed. As mentioned in sec. 2.1.2, a non-Gaussian PDF of turbulent fluctuations will provoke deviations from the predicted spectral indices.

2D turbulence
: The separation of the movements parallel and perpendicular to the magnetic field is correct as long as parallel dynamics do not influence the perpendicular ones. Nevertheless, drift wave dynamics has three-dimensional character, hence the resulting spectral shape can be distinct from the ones shown in sec. 2.1.2.

Nevertheless, a question about the degree of influence the effects above can have on the spectra is legitimate. The principal features should be expected to be measured, e.g. a turbulence decrease with increasing $k_\perp$ and the existence of inertial ranges. An identification of the viscous cutoff can give an idea of the scales at which turbulence energy is fed back into the system.

8.1 System Calibration

A microwave generator working with variable frequency will produce a different power output at each frequency generated. Apart from that, the transmitted power through waveguides, twists, bends, attenuators, isolators etc. will also depend slightly on the frequency. Therefore, a power calibration of a Doppler reflectometer is indispensable if wavenumber spectra are to be measured. This section starts with general remarks on calibration followed by the system calibration used for the wavenumber spectra measurements presented later in this chapter.

8.1.1 General Remarks

Several methods of system calibration have been investigated during the course of this work. The first method consisted in measuring the power returned by the vessel wall when launching the beam towards the central conductor (combination of circular coil and helical coil) or towards a point slightly displaced from the central conductor. The results were extremely erratic, a problem which could be due to increased reflection of certain frequencies at different parts of the vessel. Furthermore, by reflection at the vessel wall non-symmetric wavefronts can return to the ellipsoidal mirror, resulting in a deformed wave received by the antenna.

A second way to calibrate the system was to measure the received power with closed antenna shutter. This method would not include the calibration of the ellipsoidal mirror. However, the results compared to the method above did not improve, which could be due to reflected beam deformations at the antenna mouth.

For this reason, a further attempt was undertaken which yielded the most reliable and reproducible results. The launching and receiving waveguides were disconnected from the antenna and joined by a 180° turn which included a variable attenuator to protect the system from saturation. In this way, the emitted power is transferred directly into the receiving part of the system, which increases the reliability of the measurement at the cost of the loss of the emitting and receiving part (antenna and mirror). The directivity of the antenna varies only about 2.5 dB in the whole frequency range (cf fig. 5.12(c)), and the 2D full wave simulation results of the mirror do not indicate a strong frequency dependence of the latter (cf fig. 5.20). Ideally, the characteristics of the mirror-antenna system should be measured as well and combined with the microwave oscillator calibration. However, due to time restrictions, it was not possible to characterize mirror and antenna in the laboratory. Nevertheless, the microwave components most susceptible to frequency variations are components such

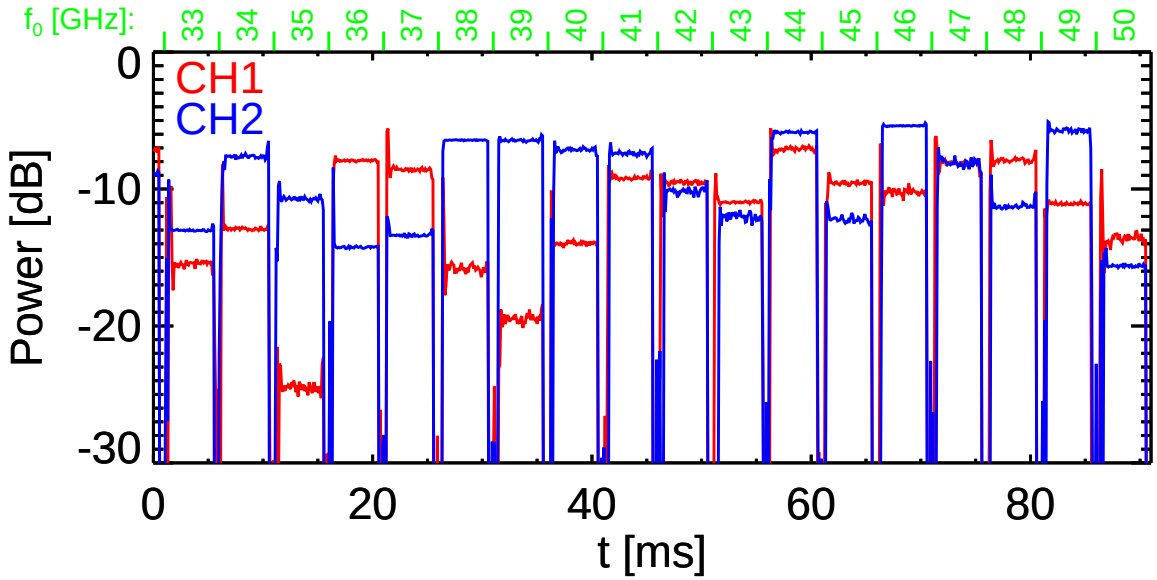

Figure 8.1: (#200052) Doppler reflectometer amplitude of CH1 (red) and CH2 (blue) with emitting and receiving waveguides connected and 20 dB attenuation.

as oscillators, multipliers, mixers, filters etc. Since these components are measured by the above method, the calibration will not be perfect, but at least reliable. An a posteriori confirmation of this assumption is made later in this chapter (cf sec. 8.2.4).

The question arises to the observant reader as to why the present section was not included in the general description of the TJ-II DR, chapter 5. This is because chapter 5 presents general properties and characteristics of the DR. However, as mentioned above, the calibration is particularly susceptible to the configuration of the waveguide system. If the waveguides are disconnected and connected again or the microwave oscillator configuration is altered, it can be expected that the calibration values change. Hence the system calibration is actually part of the experimental measurement of wavenumber spectra, and should be done on the same day, therefore the inclusion in the experimental results chapter.

It should also be noted that the system calibration is not necessary for Doppler shift- and therefore $u_\perp$- and E_r-measurements, because the f_D extraction is independent of its height, so the results from the previous chapter are not impaired by the above.

8.1.2 Calibration Results

Fig. 8.1 plots the power measured with the 180° turn method for microwave frequencies $f_0 = 33 - 50$ GHz in steps of $\Delta f_0 = 1$ GHz against acquisition time. Each 5 ms, f_0 is increased by Δf_0. Note the respective f_0 is indicated on top of the plot. In a time window of 90 ms, the frequencies to be used in the measurements are scanned. Technically, the acquisition is 180 ms long, the first 90 ms for CH1 (where CH2 is fixed at $f_0 = 33.5$ GHz) and then 90 ms for CH2 (CH1 at $f_0 = 33.5$ GHz), since one channel has to be characterized at a time.

f_0 [GHz]	33	34	35	36	37	38	39	40	41	...
P_{CH1} [dB]	-15.3	-12.8	-24.4	-8.0	-8.6	-15.9	-19.2	-14.0	-9.1	
P_{CH2} [dB]	-13.2	-7.5	-10.8	-14.4	-13.6	-6.4	-6.4	-7.1	-7.3	

... f_0 [GHz]	42	43	44	45	46	47	48	49	50
P_{CH1} [dB]	-9.6	-11.1	-7.1	-9.6	-10.2	-8.2	-8.0	-11.1	-13.6
P_{CH2} [dB]	-10.2	-12.0	-5.8	-12.0	-5.4	-8.2	-11.4	-5.7	-15.4

Table 8.1: (#200052) Calibration of DR channels for the measurement of perpendicular wavenumber spectra.

A general observation is the strong power variation in both channels. The received power for CH1 varies between -24.4 and -7.1 dB, i.e. a difference of 17.3 dB. CH2 is slightly more constant, with values ranging from -15.4 to -5.7 dB, a difference of 9.7 dB. Each power for each frequency in both channels $P_{\mathrm{CH1,CH2}}(f_0)$ in combination with the gain of each channel $G_{\mathrm{CH1,CH2}}$ is then used to calibrate the measurement. The calibration values are listed in tab. 8.1.

The measured Doppler peak height $S(f_{\mathrm{D}})$ can then be calibrated to obtain a comparable value (in dB)

$$S(f_{\mathrm{D}})_{\mathrm{real}} = S(f_{\mathrm{D}}) - G - P(f_0), \tag{8.1}$$

where G is the gain defined in dB for the DR and $P(f_0)$ is the power from the calibration in tab. 8.1. In this way, measurements of different frequencies and channels can be compared to each other, giving the possibility to measure the density turbulence level at different $k_\perp$, thus enabling the measurement of perpendicular wavenumber spectra.

8.2 Wavenumber Spectra in L- and H-modes

The usual process of measuring a $k_\perp$-spectrum is that for a launch angle of the microwave beam θ_{l} (cf (5.24)), a radial profile is measured, i.e. f_0 is scanned between 33 and 50 GHz, and the backscattered signal is measured. After this frequency scan, θ_{l} is set to a new value and the process is repeated. For the wavenumber spectra shown in this section and the $u_\perp$ profiles from sec. 7.2.1, a total of 33 comparable plasma discharges were measured and analyzed. Taking into account the availability of two DR channels, this results in more than 60 measurements for both L- and H-modes.

8.2.1 Determination of Radial Measurement Regions

For clarity, the $u_\perp$ profiles from sec. 7.2.1 are repeated in fig. 8.2, separated for (a) L- and (c) H-modes. Four different radial regions are identified in each velocity profile. In L-mode, the choice of intervals is determined by the number of samples available. Sufficient statistics are obtained when the radial range is divided into four regions with intervals of $\Delta\rho = 0.05$, as indicated in fig. 8.2(a) by the vertical dotted lines. This partitioning results in about 15 points for each $k_\perp$ spectrum, except for the most

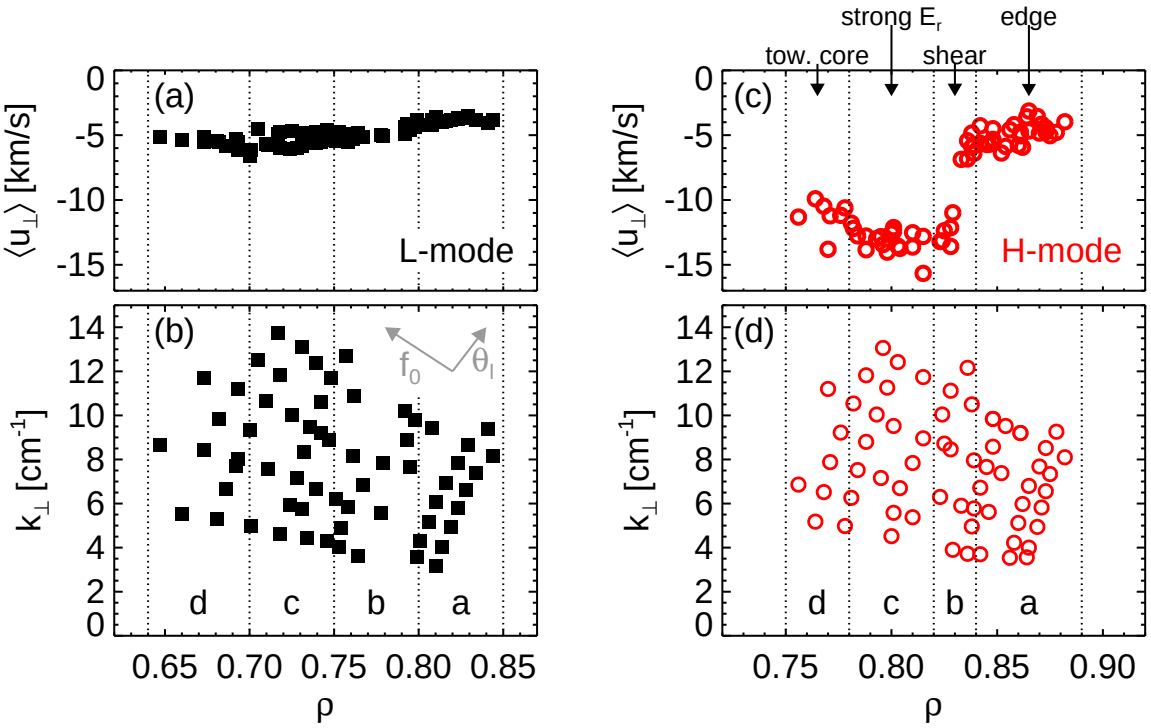

Figure 8.2: (#23013-51) (a, c) L- and H-mode $u_\perp$ profiles measured with the TJ-II DR and labeling of different regions. (b, d) Corresponding wavenumber spaces spanned by variation of f_0 and θ_l.

internal one (here: $\rho = 0.64 - 0.70$), where ten measurement points are available. The corresponding $k_\perp$ space is depicted in fig. 8.2(b). As can be expected from (3.1) the probed perpendicular wavenumbers increase towards the plasma center for fixed θ_l, because f_0 (hence k_0) increases. An additional effect can be attributed to the fact that the angle of incidence of the microwave beam with the cutoff layer normal increases as the beam enters more into the plasma. See fig. 5.27(a) for an illustrative example. The launch angle scan spans the wavenumber space in the other direction, as indicated by the arrows in the upper right corner. Fig. 8.2(b) visualizes that in the outer part of the measured region, wavenumbers from around 3 to 10 cm^{-1} will be scanned, while further inside, the wavenumber range can increase up to between 4 and 15 cm^{-1}. The labels (a, b, c, d) at the bottom of the plot identify the wavenumber spectra plotted below in fig. 8.3.

In the H-mode profile, the situation is slightly different. Here the $u_\perp$ profile must be classified in four different sections from a physics point of view. They are marked in fig. 8.2(c) by the vertical dotted lines and labeled (see above plot) the *edge* region ($\rho = 0.84 - 0.89$), the *shear* region with strong $u_\perp$ shear ($\rho = 0.82 - 0.84$), the *strong* E_r region with high E_r values between $\rho = 0.78$ and 0.82, and finally the *tow. core* region (towards core, $\rho = 0.75 - 0.78$), where E_r starts to decrease towards the plasma center. The fact that the shear region is narrow does not result in a reduced number of measurement points. In fact it is compensated by the strong density

gradient at the same radial position, leading to an accumulation of measurements. A reduced fluctuation level should be expected due to shear decorrelation (cf sec. 2.2.2) of turbulence in the *shear* region. The four radial regions are marked in the $k_\perp$ space plot in fig. 8.2(d). As for L-mode, in the edge, the accessible $k_\perp$ values are slightly lower than further inside, resulting in wavenumber spectra for slightly larger scales. For the innermost region only few points are available. The labels (a, b, c, d) at the bottom of the plot identify the wavenumber spectra plotted below in fig. 8.4.

For both L- and H-modes the corresponding normalized wavenumbers are in the range $k_\perp \rho_s \approx 0.5$ – 2.5, where $\rho_\mathrm{s} = \sqrt{2 m_i T_e}/eB = \rho_i \sqrt{T_e/T_i}$ is the ion Larmor radius evaluated at electron temperature.

8.2.2 Experimental Results

The L-mode wavenumber spectra for the radial regions defined in fig. 8.2(a, b) are plotted in fig. 8.3. The horizontal dashed line at -40 dB serves to guide the eye. In each plot, the $u_\perp$ profile is shown where the respective measurement region is indicated by a gray stripe. From (a) to (d), the measurement region moves from the plasma edge towards the plasma center. A general observation is that from large towards small scales the density turbulence level decreases, which is observed as well in 2D and 3D neutral fluid turbulence (cf sec. 2.1.2). Furthermore, apart from the innermost spectrum, which shows a large scatter, an inertial range can be identified. Beginning with the outermost spectrum (a), there is a flat region from $k_\perp = 3$ to 5 cm^{-1}, where the spectral fall-off starts. The spectral index of the inertial range is $\alpha = -2.9$. The absence of data at $k_\perp > 10$ cm^{-1} prohibits an identification of the dissipative range in the edge $k_\perp$ spectrum. Further inside ((b) and (c)) the spectral index in the $k_\perp$ range between 4 and 9 cm^{-1} is comparable to the edge spectral index with values of $\alpha = -2.4$ and -2.8. Furthermore, a fall-off at higher $k_\perp$ becomes apparent, separated from the low $k_\perp$ inertial range by a spectral knee at around 9 cm^{-1}. The spectral index of the high $k_\perp$ inertial range in (b) is $\alpha = -11.3$. In the innermost $k_\perp$ spectrum (d) the scatter of data is large, so no conclusions are drawn apart from the spectral fall-off towards small scales.

Following the theory from sec. 2.1.2 the inertial range identified in (a)-(c) could be interpreted as the enstrophy cascade. However, caution is necessary in the interpretation of the data, as explained above. The underlying theory is based on one energy injection scale and 2D neutral fluid turbulence, which – as explained above – is not the case in the measurements presented here.

In the H-mode measurements (fig. 8.4), the turbulence level decrease with decreasing structure scale can be confirmed as for the L-mode measurements. In the edge $k_\perp$ spectrum (a), an inertial range with $\alpha = -3.3$ can be identified followed by a pronounced spectral fall-off towards higher $k_\perp$ with α between -10 and -14 (large data scatter). In the shear region (b), the spectral index is comparable, but the turbulence level has dropped about one order of magnitude in comparison with the edge measurement and also in comparison with the L-mode spectra. The spectral index of the high $k_\perp$ inertial range is $\alpha = -6.8$, which is lower than the high $k_\perp$ spectral index in L-mode

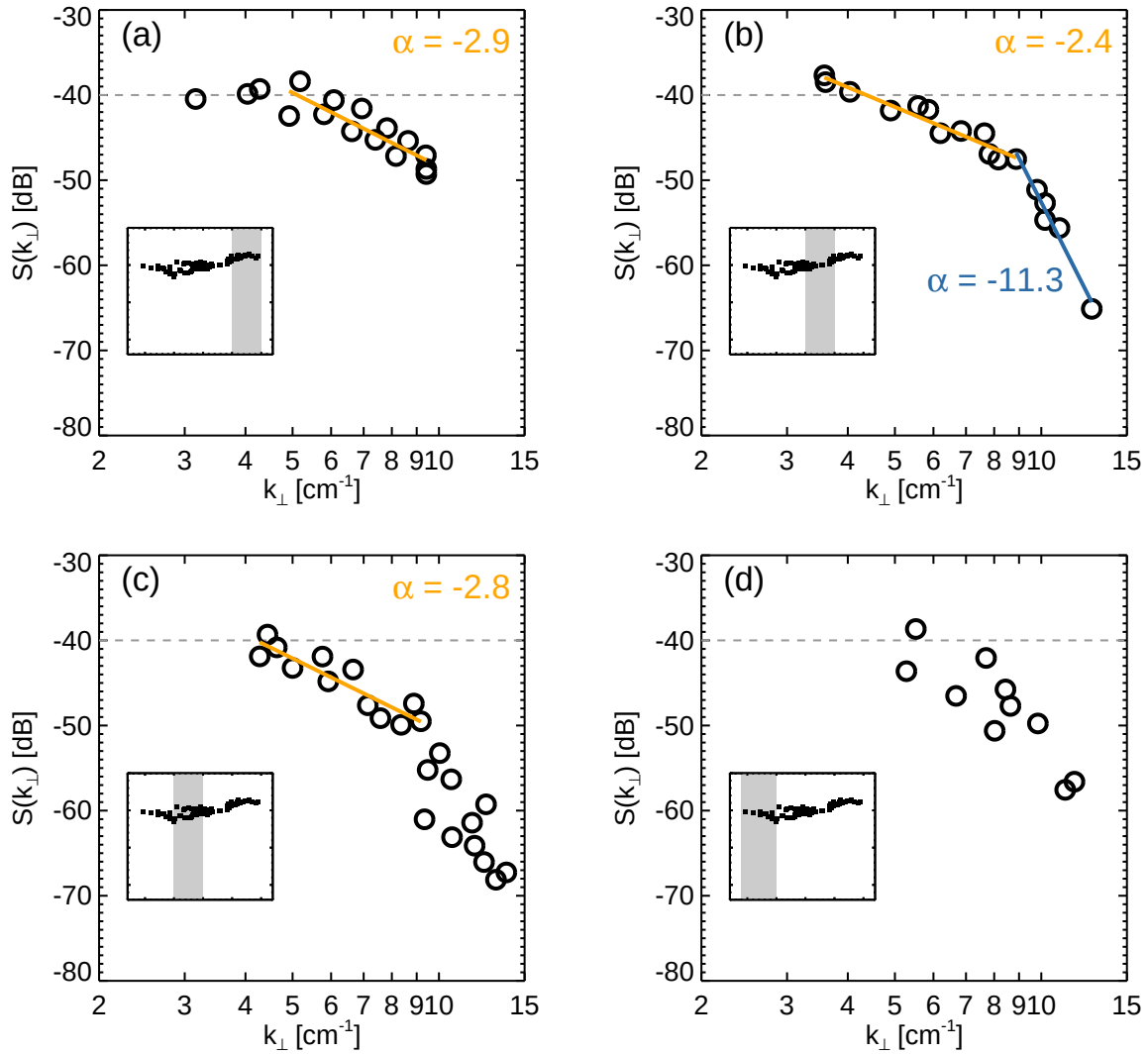

Figure 8.3: (#23013-51) L-mode wavenumber spectra for different radial regions indicated in the inset $u_\perp$ profile at the bottom left of each plot. The dashed line at -40 dB serves to guide the eye. For details refer to the text.

(cf fig. 8.3(b)), indicating that turbulence reduction is most effective at intermediate turbulence scales. The turbulence reduction in this region could be due to the shear decorrelation mechanism, where turbulent structures are torn apart by sheared plasma flows. In the region of strong E_r (c), the turbulence level is reduced as well (and lower than in L-mode). However, it increases slightly w.r.t. the shear layer measurement (b). The inertial range shows a spectral index of $\alpha = -3.2$, comparable to the measurements further outside. The data scatter at high $k_\perp$ is very large, so no conclusions can be drawn. For the most internal measurements (d), the turbulence level is comparably high, and no inertial ranges can be identified.

It should be noted that the appearance of two Doppler peaks close to the $u_\perp$ shear layer (cf sec. 7.2.2) influences the measurement of the Doppler peak amplitude A_D. Although the higher of the two peaks is used to analyze the spectra, some of the

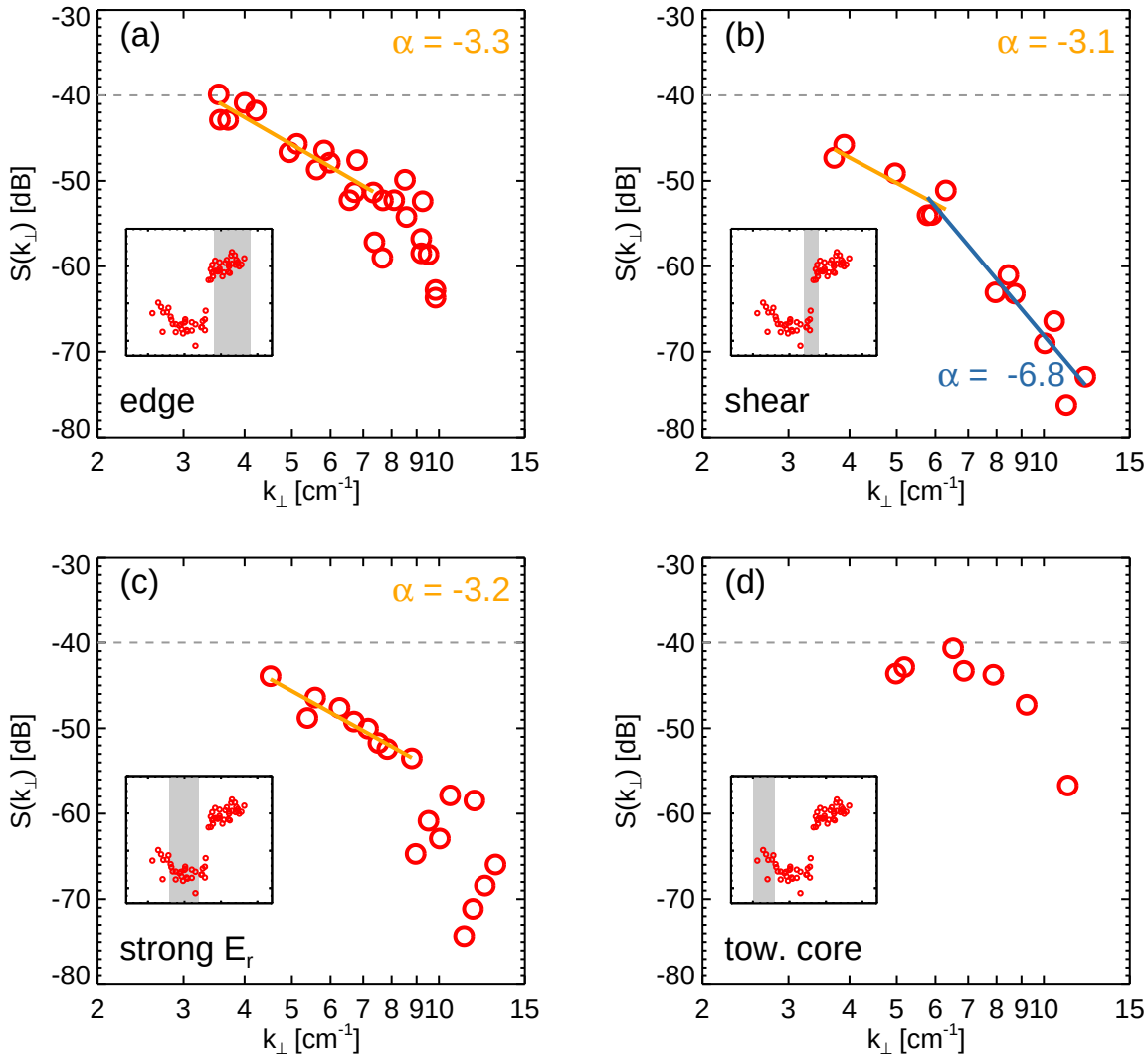

Figure 8.4: (#23013-51) Same as fig. 8.3 for H-mode.

backscattered power is lost to the other Doppler peak. Nevertheless, in the worst case, when the two Doppler peaks have comparable amplitudes, this results in a factor of 1/2 (or -3 dB), an effect which is limited to a narrow radial range (cf fig. 7.13). Since the observed turbulence amplitude reduction in the H-mode shear region is roughly one order of magnitude (or -10 dB), it can not be explained alone by the double Doppler peak effect. Obviously some turbulence suppression mechanism, probably E_r shear, acts on the turbulence.

8.2.3 Interpretation

Comparing L- and H-mode measurements, it becomes apparent that the identified inertial range in H-mode ($\alpha < -3$) is slightly more pronounced than that in L-mode ($\alpha > -3$). From shear decorrelation theory, it is expected that the power at high wavenumbers should increase while at low wavenumbers it should decrease, because

small structures are "born" out of larger ones. This would result in less pronounced inertial ranges in H-mode. This is not observed here. However, since the difference in α is small (≈ 0.5), an interpretation of this effect is arguable. Nevertheless, the fact that turbulence in the whole wavenumber range is reduced in H-mode w.r.t. the L-mode plasma in the region of maximum $u_\perp$ shear (and not in the edge or at the innermost measurement position), is a strong hint that the shear decorrelation mechanism is effective and reduces the edge turbulence level in TJ-II H-mode plasmas.

The first far-infrared (FIR) measurements in a tokamak plasma (Mictrotor tokamak) were made in 1980 by Semet *et al.* and yielded $\alpha = -3.5$ in the range $6\ \mathrm{cm}^{-1} < k_\perp < 20\ \mathrm{cm}^{-1}$ [141], a result comparable to the one obtained here. Devynck *et al.* investigated $k_\perp$ spectra in 1993 in the Tore Supra tokamak with collective infrared laser scattering and obtained spectral indices $\alpha = -3$ at $k_\perp > 6\ \mathrm{cm}^{-1}$ [142]. Furthermore, in the results at hand, only in one $k_\perp$ spectrum a maximum is found (fig. 8.3(a)) at roughly $k_\perp = 5\ \mathrm{cm}^{-1}$. For the other spectra this leads to the conclusion that the maximum is below $k_\perp = 4\ \mathrm{cm}^{-1}$, a result similar to the one found by Devynck *et al.* in the same work [142]. The results of Devynck *et al.* were confirmed by Zou *et al.* through the first $k_\perp$ spectrum measurement by Doppler reflectometry in 1999 for the $k_\perp > 4\ \mathrm{cm}^{-1}$ range, where $\alpha = -2.8$ was measured [44]. Note this value is also measured in the TJ-II L-mode plasma. Weisen *et al.* found that $k_\perp$ spectra peaked at roughly $k_\perp = 1.3\ \mathrm{cm}^{-1}$ in the TCA tokamak [143], supporting the above statement. Truc observed a peaking of the wavenumber spectrum at $k_\perp = 5\ \mathrm{cm}^{-1}$ and $\alpha = -4$ [144].

Fyfe and Montgomery obtained a dual cascade through numerical simulations with spectral indices $\alpha = -7/3$ and -3 for Hasegawa-Mima electrostatic drift-wave turbulence [145]. Hasegawa and Wakatani showed through simulations as well that $\alpha = -3$ for resistive drift-wave turbulence [146].

There is more work in literature than mentioned here, but a summary of all the results is out of the scope and not the main interest of this work. In summary, theoretical predictions and experimental and numerical results have been observed with Doppler reflectometry in TJ-II as well. The possibility to measure $k_\perp$ spectra in several radial regions is a benefit of Doppler reflectometry.

8.2.4 On Calibration Quality

With the measured wavenumber spectra, the questions from sec. 8.1 can be answered. The outermost L-mode $k_\perp$ spectra from fig. 8.3 are plotted again in fig. 8.5. The probing beam frequencies f_0 and microwave channels are color-coded. In (a), a systematic offset of roughly 2 dB for the CH1, 34 GHz measurement (orange) causes a separation of the measurements. Nevertheless, the spectral index deduced above is not affected strongly by the separation of the measurements. In the $k_\perp$ spectrum in (b), measurements from both channels and a total of six different probing beam frequencies are mixed. Although this is a large sample of necessary calibration values, with power variations of up to 8 dB in the respective channels, the measurements coincide and complement each other remarkably well, which is a confirmation that the calibration of the electronics part of the DR excluding the antenna/mirror combination is reliable.

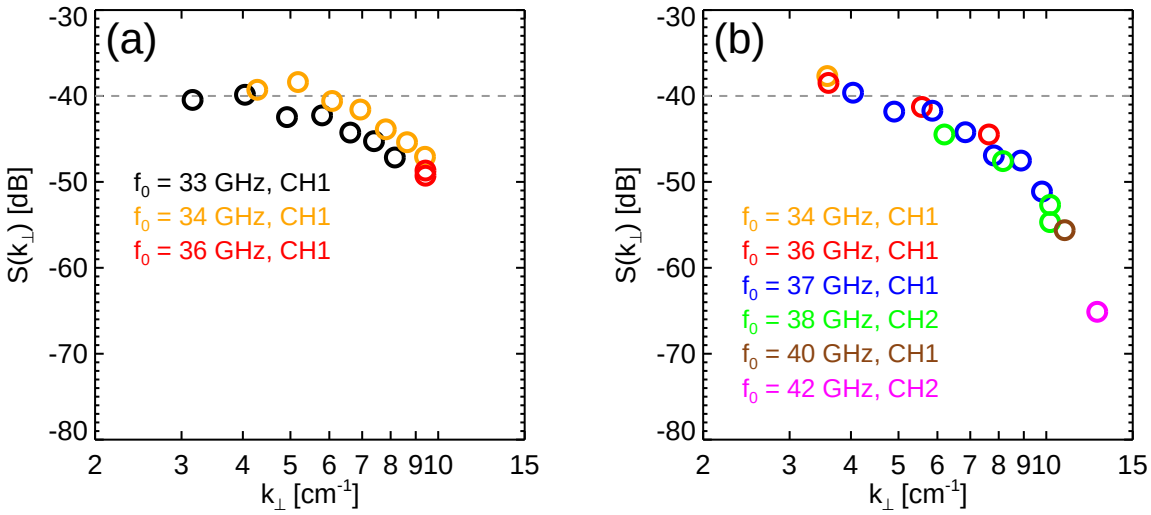

Figure 8.5: (#23013-51) Perpendicular wavenumber spectra from fig. 8.3(a-b) with color-coded frequency and microwave channel information. (a) The 34 GHz measurement points show an offset of roughly 2 dB w.r.t. the other measurements. (b) The measurements of all frequencies and channels overlap.

8.3 Radial Dependence of Turbulence Reduction

To calculate the wavenumber spectra of sec. 8.2, the data were grouped into different radial regions, and the $k_\perp$-spectrum plotted for each region. Another representation is to group the measured data into different wavenumber ranges and plot the radial turbulence level dependence. In particular, the turbulence level in H-mode $\tilde{n}_\mathrm{H}$ can be compared to the turbulence level measured in L-mode $\tilde{n}_\mathrm{L}$ for each channel in each respective discharge with no need for calibration.

Fig. 8.6 plots $\tilde{n}_\mathrm{H}$ normalized to $\tilde{n}_\mathrm{L}$ for different turbulence scales, which reflects the reduction of turbulence in H-mode at each scale. A strong reduction close to the $u_\perp$ shear layer can be observed, confirming the results from the wavenumber spectrum investigations in sec. 8.2.2. Furthermore, a stronger reduction of intermediate scale turbulence ($k_\perp = 6 - 11$ cm^{-1}, corresponding to $k_\perp \rho_\mathrm{s} = 0.9 - 1.7$) compared to the larger and smaller scales can be identified, again confirming the results above. An interpretation of this effect has not been found yet. Nonetheless, it is tempting to conjecture that the turbulence decorrelation in the radial direction (L_r decrease) results in a structure elongation in the perpendicular direction, as can be observed in the right plot of fig. 2.6. This could feed turbulence energy back into the larger $k_\perp$ scales.

8.4 Summary

Perpendicular wavenumber spectra have been measured and compared for the first time in L- and H-mode plasmas in TJ-II. To be able to compare density fluctuation levels at different microwave probing beam frequencies, the system has been calibrated. Best results have been obtained when the emitting and receiving parts of the system

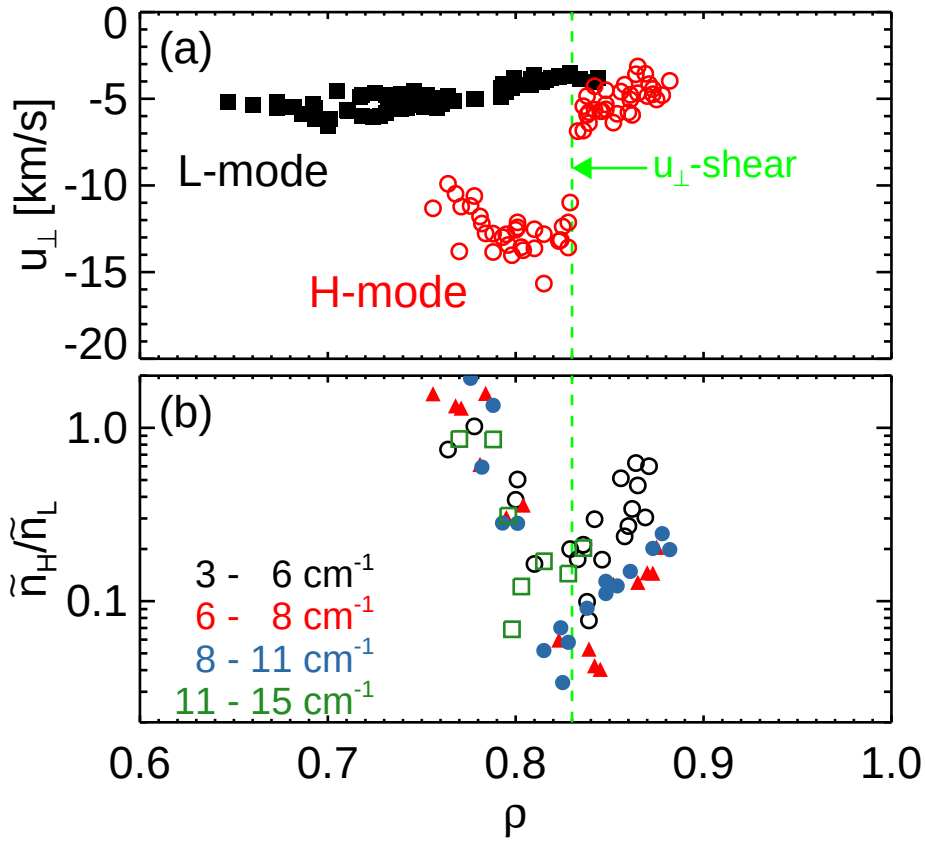

Figure 8.6: (#23013-51) (a) $u_\perp$ profile in L- and H-mode, same as fig. 7.9. (b) Radial dependence of scale-resolved density fluctuation level reduction from L- to H-mode. At the $u_\perp$-shear location, the reduction is strongest. In general, of the scales investigated, the intermediate scales are reduced most effectively.

electronics were connected, which enabled a precise characterization of the system response. However, due to time restrictions, it has not been possible to calibrate the transceiving part of the system (antenna – mirror), which should be done in the future to characterize the system completely.

Nevertheless, with the results from simulation of both antenna and mirror that the frequency dependence of the transceiving part is negligible, $k_\perp$ spectra have been measured in L- and H-modes with radial resolution. For each confinement regime, several spectra have been obtained at different radial regions, while the choice of regions depended on physics characteristics of the velocity profiles (mainly in H-mode).

The L-mode spectra show a decrease of turbulence energy towards small scales, which is seen in both 2D and 3D isotropic Navier-Stokes neutral fluid theory. No maximum can be detected in the spectra. Inertial ranges can be identified in all L-mode spectra except for the innermost one, where data scatter is large. Spectral indices α lie between -2.4 and -2.9. The spectra hint that the dissipative range should be at $k_\perp > 10$ cm^{-1}, although a clear identification would require a diagnostic measuring at even higher $k_\perp$.

In H-mode, the density turbulence level decreases towards small scales as well,

leading to the same conclusions as in the L-mode case. The inertial ranges are slightly more pronounced with α between -3.1 and -3.3. Close to the $u_\perp$ shear layer, the turbulence energy is decreased preferably at intermediate scales by about one order of magnitude in comparison to the L-mode measurement, in accordance with the shear decorrelation mechanism. Further inside, where E_r is strong, $S(k_\perp)$ is reduced as well, but not as much as at the $u_\perp$ shear ($\rho = 0.82 - 0.84$). At even more internal radii, the turbulence energy is level with the L-mode measurement.

Chapter 9

Conclusions and Outlook

A Doppler reflectometer has been designed and installed in the TJ-II stellarator. Particular attention has been paid to the requirements imposed by the complex three-dimensional structure of the TJ-II magnetic field and plasma. The in-vessel part of the TJ-II Doppler reflectometer consists of a choked-corrugated antenna and an ellipsoidal steerable mirror used to focus the beam with a well-defined beam waist to the cutoff layer in the plasma. The variable tilt angle of the probing beam provides flexibility to measure at different density turbulence scales ($k_\perp = 3 - 15$ cm^{-1}) and to use the system in perpendicular incidence (conventional reflectometry). The system has been aligned perpendicular to the magnetic field in order to minimize the parallel wavenumber contribution. Two-dimensional full wave simulations and three-dimensional ray-tracing calculations confirm the correct adaptation of the system to the given requirements. The reliable operation of the diagnostic has been demonstrated in different types of plasmas (ECRH, NBI L- and H-mode).

Edge profiles of the perpendicular velocity of density fluctuations $u_\perp$ have been measured both in L-mode (ECRH / NBI) and H-mode (NBI) plasmas in TJ-II. In ECRH plasmas, $u_\perp$ is positive (ion-diamagnetic direction) for low line-average densities $\langle n_e \rangle$ and becomes negative (electron-diamagnetic direction) when $\langle n_e \rangle$ exceeds a threshold density. As this threshold value is approached, the $u_\perp$ reversal is first observed close to the radial position of maximum density gradient. The $u_\perp$ profiles in NBI plasmas are negative over the whole radial measurement range. The L-mode profile is rather flat with $u_\perp$-values between -7 and -5 km/s. In H-mode $u_\perp$ increases up to -15 km/s and a pronounced $u_\perp$ shear develops at $\rho \approx 0.8$, where a strong suppression of density fluctuations is observed. The pronounced $u_\perp$ shear can give rise to two separated Doppler peaks, corresponding to the high and low velocity parts of the profile. It has been shown by two-dimensional full wave simulations that the peaks can be separated only if the spectral resolution of a Doppler reflectometer is sufficient, underlining the importance of Doppler reflectometer optimization. The occurrence of the two Doppler peaks can be exploited to localize the $u_\perp$ shear layer with excellent radial resolution.

The TJ-II Doppler reflectometer has allowed first-time high spatiotemporal resolution measurements of the L-H transition in TJ-II. It is observed that the reduction of density fluctuations is simultaneous with an increase in the low-frequency oscillating

shear flow. Furthermore, the mean radial electric field shear (E_r shear) starts to develop roughly one millisecond after the L-H transition and it takes several milliseconds until the strong H-mode E_r shear is completely established, pointing to zonal flows as a responsible candidate for triggering the L-H transition. In L-H transitions with heating power close to the power threshold, an oscillatory coupled behavior between density fluctuations and E_r shear is observed. Here the E_r shear follows the density fluctuations with a phase difference of 90°, resembling predator-prey behavior, where the density fluctuations are the prey and the E_r shear is the predator. These experimental observations are consistent with L-H transition models based on turbulence induced sheared / zonal flows.

Perpendicular wavenumber spectra of density fluctuations have been measured in L- and H-mode NBI plasmas for the first time in TJ-II. Both L- and H-mode spectra show a decrease of turbulence energy towards small scales. Inertial ranges have been identified with spectral indices α between -2.4 and -2.9 in L-mode, while in H-mode slightly stronger spectral indices of -3.1 to -3.3 are observed. The density turbulence reduction, when going from L- to H-mode, is most pronounced (by about one order of magnitude) in the radial region of maximum E_r shear. Moreover, intermediate turbulence scales (0.5 – 1.0 cm) have been observed to be suppressed predominantly.

The experimental results give an overview of the applicability of Doppler reflectometry in the TJ-II stellarator. However, the results presented do not exploit all of the possibilities the new diagnostic provides. Apart from the results of this work, the TJ-II Doppler reflectometer has been successfully applied to further physics studies:

- A Master's thesis was carried out which investigated the influence of rational surfaces on the edge radial electric field [84].
- Particular regard is paid to the influence of heating power and magnetic configuration on the characteristics of both the H-mode and the L-H transition, work which has partly been published [136] and is still ongoing.

Future plans include correlation measurements which could yield information on the scale-dependence of the radial correlation length L_r, which is predicted to be reduced by sheared flows (BDT theory). Comparative measurements between L- and H-modes could yield information of the L_r reduction during the L-H transition.

Furthermore, the results obtained with the Doppler reflectometer have motivated the decision to install a second Doppler reflectometer in a higher frequency band, which will permit measurements at more internal radial positions. It will be of great interest to measure the radial evolution of perpendicular velocities, radial electric fields and wavenumber spectra towards the plasma center.

In a wider context, Doppler reflectometry is a diagnostic technique with a remarkable potential for future fusion experiments such as W7-X or ITER. In fact, for both experiments, Doppler reflectometers are planned and first designs are available. Due to the higher densities expected, higher probing beam frequencies will be needed in

these experiments. This will not only reduce the size of the employed waveguides and antennas, but also improve the radial resolution of the diagnostic.

Appendix A

Gaussian Beam Propagation

A.1 The Paraxial Wave Equation in Cartesian Coordinates

The wave equation (Helmholtz equation) in cartesian coordinates $\{xyz\}$ is given by

$$\left(\nabla^2 - \frac{1}{c^2}\frac{\partial^2}{\partial t^2}\right) u = 0, \tag{A.1}$$

where $\nabla^2 = (\partial^2/\partial x^2 + \partial^2/\partial y^2 + \partial^2/\partial z^2)$ is the (vector) Laplacian, c is the speed of light and u represents either the electric field $\mathbf{E}$ or the magnetic field $\mathbf{H}$ of the wave. By choosing the ansatz

$$E = A(x, y, z)e^{i\omega t}, \tag{A.2}$$

(A.1) reduces to

$$\left(\Delta + k^2\right) A = 0, \tag{A.3}$$

where $k = \omega/c$. If the direction of propagation of the wave is the z-direction, i.e.

$$A = a(x, y, z)e^{-ikz}, \tag{A.4}$$

(A.3) can be evaluated and yields

$$\frac{\partial^2 a}{\partial x^2} + \frac{\partial^2 a}{\partial y^2} + \frac{\partial^2 a}{\partial z^2} - 2ik\frac{\partial a}{\partial z} = 0. \tag{A.5}$$

Assuming the axial variation of the beam to be small in comparison to the perpendicular variation,

$$\left|\frac{\partial^2 a}{\partial z^2}\right| \ll \left|\frac{\partial^2 a}{\partial x^2}\right| \quad \text{and} \quad \left|\frac{\partial^2 a}{\partial z^2}\right| \ll \left|\frac{\partial^2 a}{\partial y^2}\right|, \tag{A.6}$$

and assuming also that the variation along the direction of propagation will be small over a distance comparable to a wavelength,

$$\left|\frac{\Delta\frac{\partial a}{\partial z}}{\Delta z}\right| \lambda \ll \frac{\partial a}{\partial z}, \tag{A.7}$$

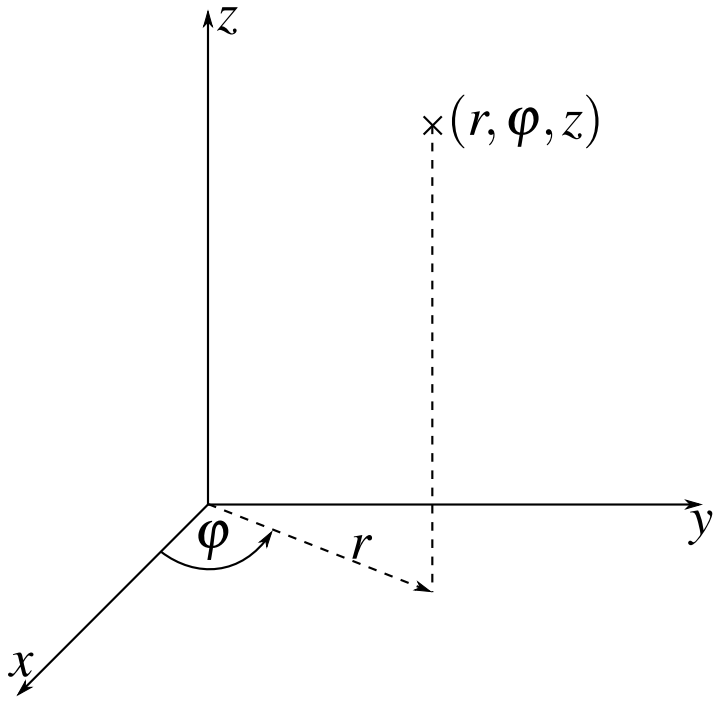

Figure A.1: Cylindrical coordinate system used for the calculation of gaussian beam parameters.

the third term in (A.5) becomes negligible in comparison to the other ones and the form of the *paraxial wave equation* wave equation is obtained:

$$\frac{\partial^2 a}{\partial x^2} + \frac{\partial^2 a}{\partial y^2} - 2ik\frac{\partial a}{\partial z} = 0. \tag{A.8}$$

A.2 The Paraxial Wave Equation in Cylindrical Coordinates

Since the following will treat of axially symmetric beams, it is convenient to go over to a cylindrical coordinate system $\{r\varphi z\}$, as shown in Fig. A.1. r represents the perpendicular distance from the axis of propagation, taken to be the z-axis. The angular coordinate is φ and varies over $[0, 2\pi)$.

The paraxial wave equation (A.8) in cylindrical coordinates takes the form ($a \equiv a(r, \varphi, z)$)

$$\frac{\partial^2 a}{\partial r^2} + \frac{1}{r}\frac{\partial a}{\partial r} + \frac{1}{r^2}\frac{\partial^2 a}{\partial \varphi^2} - 2ik\frac{\partial a}{\partial z} = 0. \tag{A.9}$$

If the beam is assumed to be axially symmetric, the third term in (A.9) vanishes and the *axially symmetric paraxial wave equation* is obtained:

$$\frac{\partial^2 a}{\partial r^2} + \frac{1}{r}\frac{\partial a}{\partial r} - 2ik\frac{\partial a}{\partial z} = 0. \tag{A.10}$$

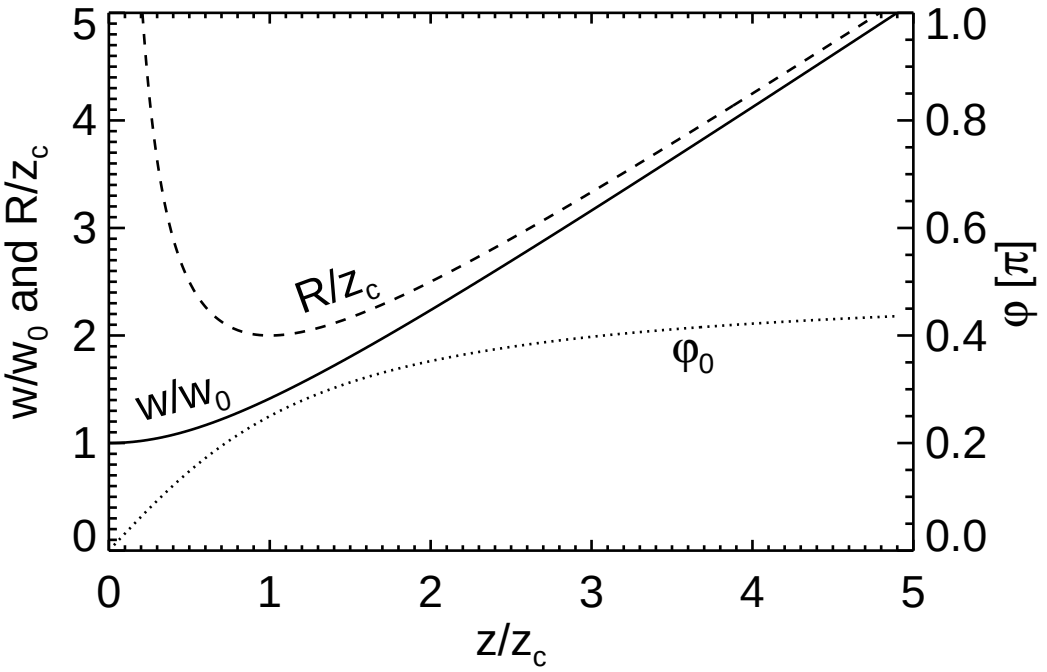

Figure A.2: Illustration of the (gaussian) beam parameters. Going from the near field ($z < z_c$) to the far field ($z > z_c$) region, the beam parameters change their behavior. For details refer to the text.

The solution to this equation is straightforward and can be read in detail in [98]. The normalized solution to (A.10) is the electric field distribution of a gaussian beam in cylindrical coordinates

$$E(r,z) = \sqrt{\frac{2}{\pi w^2}} \exp\left(-\frac{r^2}{w^2} - ikz - i\frac{\pi r^2}{\lambda R} + i\phi_0\right). \tag{A.11}$$

Here, the definitions

$$z_c = \frac{\pi w_0^2}{\lambda} \tag{A.12}$$

$$w = w_0\sqrt{1+\left(\frac{z}{z_c}\right)^2} \tag{A.13}$$

$$R = z + \frac{z_c^2}{z} \tag{A.14}$$

$$\phi_0 = \tan^{-1}\left(\frac{z}{z_c}\right) \tag{A.15}$$

are used. z_c is called the *confocal distance*, w is the *beam waist*, R the radius of curvature of the beam and ϕ_0 is the *gaussian beam phase shift*.

The confocal distance or confocal parameter z_c has significant meaning in beam propagation. It can be seen in (A.13) - (A.15) that the behavior of the beam parameters

w, R and ϕ_0 is different for $0 < z < z_c$ and $z > z_c$. Therefore, two different regions are defined, the "near field" for $z \ll z_c$ and the "far field" for $z \gg z_c$, in which the beam parameters behave differently. This is illustrated in Fig. A.2. The distance from the beam waist z, normalized to the confocal distance z_c, is shown on the abscissa.

$z < z_c$: The beam radius normalized to the beam waist (w/w_0, solid line) remains collimated, the increase in beam waist up to the confocal distance is very small. The radius of curvature nomalized to the confocal distance (R/z_c, dashed line) decreases from infinity, which is its value at $z = 0$, since the wavefronts are plane at the beam waist. The phase shift increases almost linearly.

$z = z_c$: At this position the beam radius is $w = \sqrt{2}w_0$, the radius of curvature is minimum $R = 2z_c$ and the phase shift is $\phi_0 = \pi/4$.

$z > z_c$: In the far field, both the beam waist and the beam radius grow linearly with z. The phase shift converges to a value of $\pi/2$.

Appendix B

Acronyms / Abbreviations / Symbols

Acronyms / Abbreviations

AFIT	Gaussian fit to the asymmetric part of the power spectrum
CH1, CH2	Channel 1 and 2 of the Doppler reflectometer
COG	Center Of Gravity of the power spectrum
CXRS	Charge Exchange Recombination spectroscopy
DR	Doppler Reflectometry
DBS	Doppler Backscattering
ECE	Electron Cyclotron Emission
ECRH	Electron Cyclotron Resonance Heating
ELM	Edge Localized Mode
fig.	Figure
FIR	Far-Infrared
GAM	Geodesic Acoustic Mode
HIBP	Heavy Ion Beam Probe
HWHM	Half Width at Half Maximum
ISS	International Stellarator Scaling
ITG	Ion temperature gradient
lhs, rhs	Left hand side, right hand side
NBI	Neutral Beam Injection
PDF	Probability Density Function
PRA	Phase Runaway
rhs, lhs	*see* lhs, rhs
RTP	Ray turning point
SFIT	Gaussian fit to the power spectrum
SOL	Scrape-Off Layer
tab.	Table

continued on next page...

VSL	Velocity Shear Layer
w.r.t.	with respect to
WKB	Wentzel-Kramers-Brillouin approximation (Geometrical optics)
ZF	Zonal Flow

Latin alphabet

`#12345`	TJ-II Shot number 12345
a	Minor plasma radius
A_D	Doppler peak amplitude
A_G	Gauss function amplitude
A_L	Lorentz function amplitude
$\mathbf{B}$	Magnetic field strength
B	Magnetic field strength, absolute value
B_0	Magnetic field strength (on-axis)
D	(Peak) directivity
E	Energy
$\mathbf{E}$	Electric field
E_r	Radial electric field
$\tilde{E}_r$	Radial electric field, fluctuating part
f_0	Microwave frequency
$\langle f \rangle$	Center of gravity or mean frequency of power spectrum
f_D	Doppler shift of power spectrum
Δf_D	Width of Doppler peak
f_G	Location parameter for Gaussian
f_L	Location parameter for Lorentzian
f_Ny	Nyquist-frequency
$\mathbf{k}$	Wave vector
k_0	Wave number in vacuum
$k_\perp$	Perpendicular wavenumber of density turbulence
$\Delta k_\perp$	Spectral resolution
$k_{\perp,i}$	Perpendicular wavenumber of ray (ray tracing)
L_r	Radial correlation length
n_α	Plasma density of species α
n_c	Cutoff-density
$\langle n_e \rangle$	Line-averaged plasma electron density
n_th	Threshold density for the development of a negative E_r
N	Refractive index
$N_\perp$	Refractive index (perpendicular component)
$N_\parallel$	Refractive index (parallel component)
P_abs	Absorbed heating power
P_ECRH	Heating power (ECRH)
P_NBI	Heating power (NBI)

continued on next page...

P_{th}	Threshold heating power for the L-H transition
$p = nT$	Plasma pressure
qc	Number of counts (stepper motor)
$R = \sigma / f_{\mathrm{D}}$	Relative width of Doppler peak
R_{B}	Curvature radius of microwave beam
R_{C}	Curvature radius of plasma
R_e	Reynolds number
r	Minor radius
$r_{\mathrm{HX}}^{\mathrm{sw}}$	Helical coil swing radius
r_{TF}	Toroidal field coil swing radius
S	Power spectrum
S^*	Asymmetric part of power spectrum
S_{G}	Gaussian distribution
S_{L}	Lorentzian distribution
$S(k_\perp)$	Wavenumber spectrum
T_α	Temperature of species α
$u_\perp$	Perpendicular velocity
u_θ	Poloidal velocity
$\tilde{u}_\perp$	Perpendicular velocity, fluctuating part
$v_{E\times B}$	$E \times B$-velocity
v_{ph}	Phase velocity of density fluctuations
w	Beam size
w_0	Beam waist
W_{dia}	Diamagnetic energy
w_{opt}	Optimum beam waist (in plasma)
z_c	Confocal distance

Greek alphabet

α	Spectral index, particle species
Γ	Particle flux
γ	Crossphase
γ_p	Magnetic field pitch angle
μ	Mean value
ν	Viscosity
ω_{D}	Doppler shift of the power spectrum (angular)
ϕ	Phase of reflectometer measurement, beam wavefront phase
ϕ_{fl}	Floating potential
ϕ_{p}	Plasma potential
φ	Toroidal angle
Ψ	Normalized poloidal magnetic flux
ρ	Normalized plasma radius
ρ_0	Radial origin of low density velocity shear layer

continued on next page...

ρ_α	Charge density of plasma species α
ρ_{eff}	Effective curvature radius (DR spectral resolution)
$\rho_{m,\alpha}$	Mass density of plasma species α
$\rho_{\text{p},\alpha}$	Poloidal gyroradius of species α
ρ_{RTP}	Ray turning point
ρ_{s}	Ion Larmor radius at electron temperature
ρ_{shear}	Radial position of velocity shear layer
σ	Standard deviation, width of Gaussian distribution
$\tau_{\text{E}}^{\text{Exp}}$	Energy confinement time (experimental)
$\tau_{\text{E}}^{\text{ISS}}$	ISS predicted energy confinement time
θ	Poloidal angle
θ_0	Tilt angle of microwave beam
θ_{H}	Mirror angle w.r.t. horizontal
θ_{l}	Launch angle of the microwave beam
$\xi(\mu, \sigma)$	Gaussian noise with mean μ and standard deviation σ

Bibliography

[1] U. Frisch, *Turbulence* (University of Cambridge, The Pitt Building, Trumpington Street, Cambridge, United Kingdom, 1995).

[2] U. Stroth, *Einführung in die Plasmaphysik* (Universität Stuttgart, Stuttgart, 2008).

[3] J. Wesson, *Tokamaks* (Oxford University Press Inc., New York, 2004).

[4] D. A. Hartmann, Fusion Sci. Technol. **49**, 43 (2006).

[5] C. Alejaldre *et al.*, Fusion Technol. **17**, 131 (1990).

[6] A. N. Kolmogorov, Dokl. Akad. Nauk SSSR **30**, 301 (1941), (reprinted in Proc. R. Soc. Lond. A **434**, 9 (1991)).

[7] A. N. Kolmogorov, Dokl. Akad. Nauk SSSR **32**, 16 (1941), (reprinted in Proc. R. Soc. Lond. A **434**, 15 (1991)).

[8] R. H. Kraichnan, Phys. Fluids **10**, 1417 (1967).

[9] F. H. Champagne, J. Fluid Mech. **86**, 67 (1978).

[10] J. Sommeria, J. Fluid Mech. **170**, 139 (1986).

[11] J. Maurer, P. Tabeling, and G. Zocchi, Europhys. Lett. **26**, 31 (1994).

[12] R. H. Kraichnan, J. Fluid Mech. **47**, 525 (1971).

[13] M. G. Shats, H. Xia, and H. Punzmann, Phys. Rev. E **71**, 046409 (2005).

[14] J. Paret and P. Tabeling, Phys. Fluids **10**, 3126 (1998).

[15] M. G. Shats, H. Xia, H. Punzmann, and G. Falkovich, Phys. Rev. Lett. **99**, 164502 (2007).

[16] H. Xia, H. Punzmann, G. Falkovich, and M. G. Shats, Phys. Rev. Lett. **101**, 194504 (2008).

[17] T. Happel *et al.*, Phys. Rev. Lett. **102**, 255001 (2009).

[18] G. Xu *et al.*, Nuclear Fusion **49**, 092002 (2009).

[19] B. Nold *et al.*, Plasma Phys. Control. Fusion **52**, 065005 (2010).

[20] X. Garbet *et al.*, Nucl. Fusion **39**, 2063 (1999).

[21] F. Wagner *et al.*, Phys. Rev. Lett. **49**, 1408 (1982).

[22] F. Ryter *et al.*, Nucl. Fusion **49**, 062003 (2009).

[23] S.-I. Itoh and K. Itoh, Phys. Rev. Lett. **60**, 2276 (1988).

[24] H. Biglari, P. H. Diamond, and P. W. Terry, Phys. Fluids **2**, 1 (1990).

[25] P. H. Diamond and Y.-B. Kim, Phys. Fluids B **3**, 1626 (1991).

[26] P. H. Diamond, Y.-M. Liang, B. A. Carreras, and P. W. Terry, Phys. Rev. Lett. **72**, 2565 (1994).

[27] V. Volterra, Nature **118**, 558 (1926).

[28] P. H. Diamond, S.-I. Itoh, K. Itoh, and T. S. Hahm, Plasma Phys. Control. Fusion **47**, R35 (2005).

[29] K. Itoh *et al.*, Phys. Plasmas **13**, 055502 (2006).

[30] A. Fujisawa, Nucl. Fusion **49**, 013001 (2009).

[31] B. Lehnert, Phys. Fluids **9**, 1367 (1966).

[32] P. W. Terry, Rev. Mod. Phys. **72**, 109 (2000).

[33] R. J. Groebner, K. H. Burrell, and R. P. Seraydarian, Phys. Rev. Lett. **64**, 3015 (1990).

[34] B. Scott, Phys. Plasmas **7**, 1845 (2000).

[35] E. Kim and P. H. Diamond, Phys. Plasmas **10**, 1698 (2003).

[36] A. M. Dimits *et al.*, Phys. Plasmas **7**, 969 (2000).

[37] R. Schrittwieser *et al.*, Plasma Phys. Control. Fusion **44**, 567 (2002).

[38] J. Adamek *et al.*, Czech. J. Phys. **55**, 235 (2005).

[39] R. Balbín *et al.*, Rev. Sci. Instrum. **63**, 4605 (1992).

[40] N. Mahdizadeh *et al.*, Plasma Phys. Control. Fusion **47**, 569 (2005).

[41] K. Ida, Plasma Physics and Controlled Fusion **40**, 1429 (1998).

[42] Y. Andrew *et al.*, Europhys. Lett. **83**, 15003 (2008).

[43] M. Hirsch, E. Holzhauer, J. Baldzuhn, and B. Kurzan, *Doppler Reflectometry for the Investigation of poloidally propagating Density Perturbations* (Proc. 4th International Reflectometry Workshop, Cadarache, France, 1999), report EUR-CEA-FC-1674.

[44] X. L. Zou *et al.*, *Poloidal Rotation Measurement in Tore Supra by Oblique Reflectometry* (Proc. 4th International Reflectometry Workshop, Cadarache, France, 1999), report EUR-CEA-FC-1674.

[45] V. V. Bulanin, S. V. Lebedev, L. S. Levin, and V. S. Roytershteyn, Plasma Phys. Rep. **26**, 813 (2000).

[46] A. C. C. Sips, Ph.D. thesis, Eindhoven University of Technology, Netherlands, 1991.

[47] J. Sánchez, T. Estrada, and H. J. Hartfuss, *Broadband Heterodyne Reflectometry: Application to the W7-AS stellarator* (Proc. 1st International Reflectometry Workshop, Abingdon, United Kingdom, 1992).

[48] G. Hanson *et al.*, Nucl. Fusion **32**, 1593 (1992).

[49] E. Mazzucato and R. Nazikian, Phys. Rev. Lett. **71**, 1840 (1993).

[50] V. O. Aleksandrov, V. V. Bulanin, D. O. Korneyev, and A. A. Sergeyev, *Study of the plasma turbulence by means reflectometry in TUMAN-3 and FT-2 tokamaks* (Proc. 19th EPS Conference on Contr. Fusion and Plasma Phys., Innsbruck, Austria, 1992), p. I-111.

[51] V. V. Bulanin and D. O. Korneev, Plasma Phys. Rep. **20**, 14 (1994).

[52] R. Nazikian and E. Mazzucato, Rev. Sci. Instrum. **66**, 392 (1995).

[53] E. Mazzucato *et al.*, Phys. Rev. Lett. **77**, 3145 (1996).

[54] A. Ejiri, K. Kawahata, and K. Tanaka, Fusion Eng. Des. **34-35**, 429 (1997).

[55] K. Shinohara *et al.*, Jpn. J. Appl. Phys. **36**, 7367 (1997).

[56] B. Brañas, M. Hirsch, J. Sánchez, and V. Zhuravlev, Rev. Sci. Instrum. **70**, 1025 (1999).

[57] J. H. Irby, S. Horne, I. H. Hutchinson, and P. C. Stek, Plasma Phys. Control. Fusion **35**, 601 (1993).

[58] J. H. Irby and P. Stek, Rev. Sci. Instrum. **61**, 3052 (1990).

[59] Y. Umul, Opt. Express **12**, 4959 (2004).

[60] G. D. Conway, Plasma Phys. Control. Fusion **41**, 65 (1999).

[61] M. Hirsch *et al.*, Plasma Phys. Control. Fusion **43**, 1641 (2001).

[62] G. D. Conway *et al.*, Plasma Phys. Control. Fusion **46**, 951 (2004).

[63] P. Hennequin *et al.*, Rev. Sci. Instrum. **75**, 3881 (2004).

[64] T. Happel *et al.*, Rev. Sci. Instrum. **80**, 073502 (2009).

[65] J. C. Hillesheim *et al.*, Rev. Sci. Instrum. **80**, 083507 (2009).

[66] E. Blanco and T. Estrada, Plasma Phys. Control. Fusion **50**, 095011 (2008).

[67] T. Happel, E. Blanco, and T. Estrada, Rev. Sci. Instrum. **81**, 10D901 (2010).

[68] V. L. Ginzburg, *Propagation of Electromagnetic Waves in Plasma* (Gordon and Breach, New York, 1961), p. 364.

[69] M. Hirsch, E. Holzhauer, J. Baldzuhn, and B. Kurzan, Rev. Sci. Instrum. **72**, 324 (2001).

[70] N. Mahdizadeh *et al.*, Plasma Phys. Control. Fusion **49**, 1005 (2007).

[71] C. P. Ritz *et al.*, Rev. Sci. Instrum. **59**, 1739 (1988).

[72] J.-N. Leboeuf *et al.*, Phys. Fluids **3**, 2291 (1991).

[73] S. J. Zweben and S. S. Medley, Phys. Fluids B **1**, 2058 (1989).

[74] R. E. Slusher and C. M. Surko, Phys. Fluids **23**, 472 (1980).

[75] R. L. Watterson, R. E. Slusher, and C. M. Surko, Phys. Fluids **28**, 2857 (1985).

[76] E. Holzhauer, G. Dodel, and the ASDEX Team, Rev. Sci. Instrum. **61**, 2817 (1990).

[77] C. Fanack *et al.*, Plasma Physics and Controlled Fusion **38**, 1915 (1996).

[78] V. Bulanin and M. Yafanov, Plasma Phys. Rep. **32**, 47 (2006).

[79] E. Holzhauer and J. H. Massig, Plasma Physics **20**, 867 (1978).

[80] Y. Lin, R. Nazikian, J. H. Irby, and E. S. Marmar, Plasma Phys. Control. Fusion **43**, L1 (2001).

[81] M. Hirsch and E. Holzhauer, Plasma Phys. Control. Fusion **46**, 593 (2004).

[82] J. Schirmer *et al.*, Plasma Phys. Control. Fusion **49**, 1019 (2007).

[83] T. Estrada *et al.*, Plasma Phys. Control. Fusion **51**, 124015 (2009).

[84] O. Bondarenko *et al.*, Contrib. Plasma Phys. **50**, 605 (2010).

[85] T. Estrada *et al.*, Plasma Phys. Control. Fusion **44**, 1615 (2002).

[86] F. Castejón *et al.*, Nucl. Fusion **42**, 271 (2002).

[87] T. Estrada *et al.*, Plasma Phys. Control. Fusion **46**, 277 (2004).

[88] J. Herranz *et al.*, Phys. Rev. Lett. **85**, 4715 (2000).

[89] T. Estrada *et al.*, Plasma Phys. Control. Fusion **43**, 1535 (2001).

[90] H. Bottollier-Curtet and G. Ichtchenko, Rev. Sci. Instrum. **58**, 539 (1987).

[91] L. Cupido, J. Sanchez, and T. Estrada, Rev. Sci. Instrum. **75**, 3865 (2004).

[92] H. J. Hartfuss, T. Geist, and M. Hirsch, Plasma Phys. Control. Fusion **39**, 1693 (1997).

[93] L. Guimarais *et al.*, Plasma and Fusion Research **3**, S1057 (2008).

[94] T. Estrada *et al.*, Nucl. Fusion **46**, S792 (2006).

[95] T. Happel, T. Estrada, and C. Hidalgo, Europhys. Lett. **84**, 65001 (2008).

[96] M. A. Pedrosa *et al.*, Rev. Sci. Instrum. **70**, 415 (1999).

[97] M. Hirsch *et al.*, Plasma Phys. Control. Fusion **48**, S155 (2006).

[98] P. F. Goldsmith, *Quasioptical Systems - Gaussian Beam Quasioptical Propagation and Applications* (IEEE Press, Piscataway, NJ, 1998).

[99] J. Teniente, C. del Río, D. Goni, and R. Gonzalo, *Horn Antenna Combining Horizontal and Vertical Ridges*, 2003, patent WO03100907.

[100] J. Teniente, R. Gonzalo, and C. del Río, IEEE Antennas and Wireless Prop. Lett. **5**, 380 (2006).

[101] E. Blanco, T. Estrada, and J. Sánchez, Plasma Phys. Control. Fusion **48**, 699 (2006).

[102] T. S. Chu, IEEE Trans. Antennas Propag. **31**, 614 (1983).

[103] E. Blanco *et al.*, Rev. Sci. Instrum. **75**, 3822 (2004).

[104] Y. A. Kravtsov and Y. I. Orlov, Sov. Phys. Usp. **23**, 750 (1980).

[105] E. Poli, A. G. Peeters, and G. V. Pereverzev, Comput. Phys. Commun. **136**, 90 (2001).

[106] C. Honoré, P. Hennequin, A. Truc, and A. Quéméneur, Nucl. Fusion **46**, S809 (2006).

[107] G. Conway *et al.*, Nucl. Fusion **46**, S799 (2006).

[108] M. A. Tereshchenko *et al.*, *Development and Use of 3D Ray/Beam Tracing Code for Plasma Heating by EBW in the TJ-II Stellarator* (Proc. 30$^{\text{th}}$ EPS Conference on Contr. Fusion and Plasma Phys., St. Petersburg, Russia, 2003), Vol. 27A, p-1.18.

[109] F. Castejón *et al.*, Fusion Sci. Technol. **46**, 327 (2004).

[110] F. Castejón *et al.*, Fusion Sci. Technol. **52**, 230 (2007).

[111] F. Castejón, A. Cappa, M. Tereshchenko, and A. Fernández, Nucl. Fusion **48**, 075011 (2008).

[112] H. Bindslev, Plasma Phys. Control. Fusion **34**, 1601 (1992).

[113] S. Klenge, Ph.D. thesis, Institut für Plasmaforschung, Universität Stuttgart, Germany, 2005.

[114] J. Schirmer *et al.*, Nucl. Fusion **46**, S780 (2006).

[115] P. Hennequin *et al.*, Nucl. Fusion **46**, S771 (2006).

[116] G. D. Conway *et al.*, Plasma Phys. Control. Fusion **47**, 1165 (2005).

[117] W. H. Press, S. A. Teukolsky, W. T. Vetterling, and B. P. Flannery, *Numerical Recipes in C (2nd ed.): The Art of Scientific Computing* (Cambridge University Press, Cambridge, 1992), p. 683.

[118] C. Hidalgo, M. A. Pedrosa, L. Garca, and A. Ware, Phys. Rev. E **70**, 067402 (2004).

[119] M. A. Pedrosa *et al.*, Plasma Phys. Control. Fusion **47**, 777 (2005).

[120] J. A. Alonso *et al.*, Plasma Phys. Control. Fusion **48**, B465 (2006).

[121] A. V. Melnikov *et al.*, Fusion Sci. Technol. **51**, 31 (2007).

[122] V. Tribaldos, Phys. Plasmas **8**, 1229 (2001).

[123] U. Stroth *et al.*, Phys. Rev. Lett. **86**, 5910 (2001).

[124] A. Bortolon, B. P. Duval, A. Pochelon, and A. Scarabosio, Phys. Rev. Lett. **97**, 235003 (2006).

[125] C. Hidalgo *et al.*, Plasma Phys. Control. Fusion **42**, A153 (2000).

[126] K. Ida *et al.*, Phys. Rev. Lett. **88**, 015002 (2002).

[127] L. Garcia *et al.*, Phys. Plasmas **8**, 4111 (2001).

[128] F. L. Tabarés *et al.*, Plasma Phys. Control. Fusion **50**, 124051 (2008).

[129] H. Yamada *et al.*, Nucl. Fusion **45**, 1684 (2005).

[130] C. J. Barth *et al.*, Rev. Sci. Instrum. **70**, 763 (1999).

[131] K. Ida *et al.*, Phys. Rev. Lett. **65**, 1364 (1990).

[132] E. J. Doyle *et al.*, Phys. Fluids B **3**, 2300 (1991).

[133] K. H. Burrell, Phys. Plasmas **4**, 1499 (1997).

[134] H. Matsumoto *et al.*, Plasma Phys. Control. Fusion **34**, 615 (1992).

[135] H. Punzmann and M. G. Shats, Phys. Rev. Lett. **93**, 125003 (2004).

[136] T. Estrada *et al.*, Contrib. Plasma Phys. **50**, 501 (2010).

[137] C. Hidalgo *et al.*, Europhys. Lett. **87**, 55002 (2009).

[138] A. Fujisawa *et al.*, Phys. Rev. Lett. **93**, 165002 (2004).

[139] T. Estrada *et al.*, Europhys. Lett. (2010), *submitted*.

[140] R. J. Colchin *et al.*, Phys. Rev. Lett. **88**, 255002 (2002).

[141] A. Semet *et al.*, Phys. Rev. Lett. **45**, 445 (1980).

[142] P. Devynck *et al.*, Plasma Phys. Control. Fusion **35**, 63 (1993).

[143] H. Weisen, C. Hollenstein, and R. Behn, Plasma Phys. Control. Fusion **30**, 293 (1988).

[144] A. Truc, Plasma Phys. Control. Fusion **26**, 1045 (1984).

[145] D. Fyfe and D. Montgomery, Phys. Fluids **22**, 246 (1979).

[146] A. Hasegawa and M. Wakatani, Phys. Rev. Lett. **50**, 682 (1983).

Publications in Refereed Journals / Awards

As First Author:

T. Happel, E. Blanco, and T. Estrada
On the role of spectral resolution in velocity shear layer measurements by Doppler reflectometry
Rev. Sci. Instrum. **81**, 10D901 (2010)

T. Happel, T. Estrada, E. Blanco, V. Tribaldos, A. Cappa, and A. Bustos
Doppler reflectometer system in the stellarator TJ-II
Rev. Sci. Instrum. **80**, 073502 (2009)

T. Happel, F. Greiner, N. Mahdizadeh, B. Nold, M. Ramisch, and U. Stroth
Generation of Intermittent Turbulent Events at the Transition from Closed to Open Field Lines in a Toroidal Plasma
Phys. Rev. Lett. **102**, 255001 (2009)

T. Happel, T. Estrada, and C. Hidalgo
First experimental observation of a two-step process in the development of the edge velocity shear layer in a fusion plasma
Europhys. Lett. **84**, 65001 (2008)

As Second Author:

O. Bondarenko, T. Estrada, R. Jiménez-Gómez, D. López-Bruna, T. Happel, J. Romero, A. López-Fraguas, E. Ascasíbar, and E. Blanco
Influence of Low-Order Rational Surfaces on the Radial Electric Field of TJ-II ECH Plasmas
Contrib. Plasma Phys. **50**, 605 (2010)

G. D. Conway, E. Poli, T. Happel, and the ASDEX Upgrade Team
Interaction of mean and oscillating plasma flows across confinement mode transitions
Plasma and Fusion Research (2010), *In press*

T. Estrada, E. Ascasíbar, T. Happel, C. Hidalgo, E. Blanco, R. Jiménez-Gómez, M. Liniers, D. López-Bruna, F. Tabarés, and D. Tafalla
L-H Transition Experiments in TJ-II
Contrib. Plasma Phys. **50**, 501 (2010)

T. Estrada, T. Happel, C. Hidalgo, E. Ascasbar, E. Blanco and the TJ-II Team
Experimental observation of coupling between turbulence and sheared flows during L-H transitions in a toroidal plasma
Europhys. Lett. (2010), *Submitted*

B. Nold, G. D. Conway, T. Happel, H. W. Müller, M. Ramisch, V. Rohde, U. Stroth, and the ASDEX Upgrade Team
Generation of blobs and holes in the edge of the ASDEX Upgrade tokamak
Plasma Phys. Control. Fusion **52**, 065005 (2010)

M. Ramisch, G. Birkenmeier, T. Happel, A. Köhn, N. Mahdizadeh, P. Manz, B. Nold, R. Wilcox, D. T. Anderson, and U. Stroth
Investigation of Turbulent Transport and Shear Flows in the Edge of Toroidal Plasmas
Contrib. Plasma Phys. **50**, 718 (2010)

T. Estrada, T. Happel, L. Eliseev, D. López-Bruna, E. Ascasíbar, E. Blanco, L. Cupido, J. M. Fontdecaba, C. Hidalgo, R. Jiménez-Gómez, L. Krupnik, M. Liniers, M. E. Manso, K. J. McCarthy, F. Medina, A. Melnikov, B. v. Milligen, M. A. Ochando, I. Pastor, M. A. Pedrosa, F. L. Tabarés, D. Tafalla, and the TJ-II Team
Sheared flows and transition to improved confinement regime in the TJ-II stellarator
Plasma Phys. Control. Fusion **51**, 124015 (2009)

J. Sánchez, M. Acedo, A. Alonso, J. Alonso, P. Álvarez, E. Ascasíbar, A. Baciero, R. Balbín, L. Barrera, E. Blanco, J. Botija, A. Bustos, E. de la Cal, I. Calvo, A. Cappa, J. Carmona, D. Carralero, R. Carrasco, B. Carreras, F. Castejón, R. Castro, G. Catalán, A. Chmyga, M. Chamorro, L. Eliseev, L. Esteban, T. Estrada, A. Fernández, R. Fernández-Gavilán, J. Ferreira, J. Fontdecaba, C. Fuentes, L. García, I. García-Cortes, R. García-Gómez, J. García-Regana, J. Guasp, L. Guimarais, T. Happel, J. Hernanz, J. Herranz, C. Hidalgo, J. Jiménez, A. Jiménez-Denche, R. Jiménez-Gómez, D. Jiménez-Rey, I. Kirpitchev, A. Komarov, A. Kozachok, L. Krupnik, F. Lapayese, M. Liniers, D. López-Bruna, A. López-Fraguas, J. López-Razola, A. López-Sánchez, S. Lysenko, G. Marcon, F. Martin, V. Maurin, K. J. McCarthy, F. Medina, M. Medrano, A. Melnikov, P. Mendez, B. v. Milligen, E. Mirones, I. Nedzelskiy, M. A. Ochando, J. Olivares, J. d. Pablos, L. Pacios, I. Pastor, M. A. Pedrosa, A. d. l. Pena, A. Pereira, G. Perez, D. Perez-Risco, A. Petrov, S. Petrov, A. Portas, D. Pretty, D. Rapisarda, G. Rattá, J. Reynolds, E. Rincon, L. Rios, C. Rodríguez, J. Romero, A. Ros, A. Salas, M. Sánchez, E. Sánchez, E. Sánchez-Sarabia, K. Sarksian, J. Sebastian, C. Silva, S. Schchepetov, N. Skvortsova, E. Solano, A. Soleto, F. Tabarés, D. Tafalla, A. Tarancon Y. Taschev, J. Tera, A. Tolkachev, V. Tribaldos, V. Vargas, J. Vega, G. Velasco, J.

Velasco, M. Weber, G. Wolfers, and B. Zurro
Confinement transitions in TJ-II under Li-coated wall conditions
Nucl. Fusion **49**, 104018 (2009)

L. Guimarais, T. Estrada, E. Ascasíbar, M. E. Manso, L. Cupido, T. Happel, E. Blanco, F. Castejón, R. Jiménez-Gómez, M. A. Pedrosa, C. Hidalgo, I. Pastor, and A. López-Fraguas
Parametric Dependence of the Perpendicular Velocity Shear Layer Formation in TJ-II Plasmas
Plasma and Fusion Research **3**, S1057 (2008)

Awards

Sep. 2010:
Journal article "First experimental observation of a two-step process in the development of the edge velocity shear layer in a fusion plasma" (Europhys. Lett.) chosen for the "Best of 2009" articles collection by readers via the number of paper downloads.

Jul. 2009:
Winner of the 5$^{\text{th}}$ Itoh Project Prize in Plasma Turbulence at the 36$^{\text{th}}$ European Physical Society Conference on Plasma Physics, 2009, Sofia, Bulgaria.

Dec. 2008:
Journal article "First experimental observation of a two-step process in the development of the edge velocity shear layer in a fusion plasma" (Europhys. Lett.) chosen as a highlight by the Co-Editor.

Acknowledgments

During the preparation of this thesis, a large number of people contributed both scientifically and non-scientifically to its progress. But preparing a Ph.D. thesis is not only about scientific achievements, it also depends on factors like a good atmosphere at work as well as making and having friends.

First of all I would like to express my deep gratitude to Teresa Estrada, who was the supervisor of this thesis and who motivated and encouraged me throughout the almost four years I was at Ciemat. Her scientific excellence and motivation have been, are, and will be of a standard that I will always struggle to achieve. I must say that not only on a professional level, but also on a personal level, Teresa is one of the most marvelous persons I have ever worked with.

A sincere thanks is given to Emilio Blanco, who had to suffer my many questions, particularly at the beginning of my Ph.D. He introduced me step by step into the theory of microwave reflectometry and interpretation of data. His dedication in the development of the ellipsoidal mirror and the double peak simulations was exemplary and is highly appreciated.

Furthermore, I profoundly appreciate the enlightening discussions, ideas and the exceptional support of Carlos Hidalgo. The enthusiasm and kindness Carlos always shows, in spite of his unimaginable workload, are exemplarily and always an inspiration.

I am deeply indebted to Garrard Conway and the whole staff of the Max-Planck-Institut für Plasmaphysik in Garching bei München, Germany. I was given the possibility to work with, and interpret, Doppler reflectometry data before the TJ-II Doppler reflectometer was installed. The reception I received was very friendly and I am thankful for the opportunity to go to the Ringberg Seminar, where I got to know many of the nice AUG staff.

I would also like to thank Sanae-I. Itoh for the invitation to Japan and giving me the possibility to visit Kyushu University and the National Institute for Fusion Science (NIFS). The reception I received was of exceptional warmth, which was not least because of the hospitality and kindness of Shigeru Inagaki. Enlightening discussions at NIFS with Kimitaka Itoh, Katsumi Ida, Kenji Tanaka and Tokihiko Tokuzawa are highly appreciated. The acknowledgment and encouragement of the work of young scientists is very special and the trip to Japan was a unique experience for me.

I appreciate the insistence of Uli Stroth concerning the publication of an article which was pending since my Diploma thesis in Kiel. His support made this work possible, which is highly acknowledged. In a wider context, Uli is the person who brought me into the exciting field of fusion science, and I will always be in his debt.

I appreciate the critical suggestions of Boudewijn van Milligen during the last weeks of the thesis writing. Kieran McCarthy helped me a lot with questions concerning the English language, this help is highly acknowledged.

Ramón Solís always dedicated an immense effort to help me out with whatever problems came up when I had to clarify things with the Universidad Carlos III de Madrid, Spain. He would always find solutions when there were none.

With Víctor Tribaldos I had the most didactic conversations ever. His pool of knowledge of stellarator theory seems infinite (I think it actually is), and he allowed me to exploit that during the design phase of the Doppler reflectometer.

Of course, the design of a diagnostic system is not finished once the theoretical part has been established. The tremendous work done by the Ciemat draftsmen and workshops, pushed forward with an incredible commitment by Antonio Bravo and Luis Melón, is highly recognized and made the Doppler reflectometer a reality. At this point I would like to thank Enrique Ascasíbar for his outstanding detective work, which led to the localization of a stainless steel block that was adequate for installation as the ellipsoidal mirror in TJ-II.

The work of the Antenna Group of the Universidad de Navarra, Spain, is highly appreciated. Carlos del Río and Jorge Teniente provided an antenna with beam characteristics much better than we could ever have imagined.

After the system was installed I was only able to analyze the data because of the dedicated help of Álvaro Cappa and José Manuel García with the `TRUBA` ray tracing code. Modification of the source code by José was indispensable and made my life much easier.

Quite a large number of people is needed to operate TJ-II. My thanks to the whole TJ-II team for conducting the experiments, and for obtaining the plasmas I was aiming for.

Without Ana Portas and Augusto Perreira, no data would have traveled from the experiment hall to the control room. Whenever problems came up, they were able to help immediately.

The organizing ability of Doralice Aranda and Sabina Moreno has to be underlined in these acknowledgments. The were always able to help me out whenever I approached them with whatever bureaucratic questions.

Furthermore, the time I had in Ciemat would not have been the same if it were not for my officemates Luis Esteban (Luiz), Andres de Bustos (Antez de Bastos, Antezno, Aceituno, Ranadrilo) and Daniel Alegre (Daniz, Zapadaniz, El Coletas). Luiz, Daniz and I (Timz) talking about Formula 1 with the reaction of Antez putting on his earphones was a classic since the first day. Daniz trying to partition his hard drive by means of installing (mechanically) a floppy drive was priceless (N.B.: he never succeeded). Guys, you made my day.

A warm thank you to all the people from edificio 20. The atmosphere in the "aisle" was great and we had quite some laughs. But also the others from edificios 6 and 66 made life in Ciemat a worthwhile experience.

I am most thankful to my family for the support not only during the whole time of the thesis, but also before. Without their constant backing of my plans and ideas my

Ph.D. in Madrid would not have been possible.

Finally I want to mention Thamara Nover, the one person who bravely endured all the ups and downs I encountered in the course of this work. Your voice at the end of the day was most precious and comforting and I would always look forward to hearing it. The thought of being with you makes the future brighter than ever.